MODELLING OF THE THERMAL BEHAVIOUR OF A TWO-PHASE CLOSED THERMOSYPHON

A thesis submitted for the degree of Doctor of Philosophy (PhD)

By

Bandar Fadhl

Department of Mechanical, Aerospace and Civil Engineering

College of Engineering, Design and Physical Sciences

Brunel University London

March 2015

ABSTRACT

Interest in the use of heat pipe technology for heat recovery and energy saving in a vast range of engineering applications has been on the rise in recent years. Heat pipes are playing a more important role in many industrial applications, especially in increasing energy savings in commercial applications and improving the thermal performance of heat exchangers. Computational techniques play an important role in solving complex flow problems for a large number of engineering applications due to their universality, flexibility, accuracy and efficiency. However, up to now, computational studies on heat pipes are still at an early stage due to the complexity of multiphase flow characteristics and heat and mass transfer phase changes. Therefore, the main objective of this study is to develop a CFD modelling that includes the complex physical phenomena of both the heat transfer processes of evaporation and condensation and the mass transfer process of phase change during the pool boiling and film condensation.

In this thesis, two novel numerical models were developed in ANSYS FLUENT. In the first, a two-dimensional CFD model was developed to visualise the two-phase flow and the evaporation, condensation and heat transfer phenomena during the operation of a wickless heat pipe, that otherwise could not be visualised by empirical or experimental work. An in-house code was developed using user-defined functions (UDFs) to enhance the ability of FLUENT to simulate the phase change occurring inside the heat pipe. Three different fluids, water, R134a and R404a, were selected as the working fluids of the investigated wickless heat pipe. The cooling system of the condenser section was simulated separately as a three-dimensional CFD model of a parallel-flow double pipe heat exchanger to model the heat transfer across the condenser section's heat exchanger and predict the heat transfer coefficients. The overall effective thermal resistance along with the temperature profile along the wickless heat pipe have been investigated. An experimental apparatus was built to carry out a thermal performance investigation on a typical wickless heat pipe for the purpose of validating the CFD simulation. A theoretical model based on empirical correlations was developed to predict the heat transfer thermal resistances in the evaporator and the condenser section.

The second model was developed to combine the two-dimensional CFD simulation of the wickless heat pipe and the three-dimensional CFD simulation of the condenser section's heat exchanger to simulate the two-phase flow phenomena of boiling and condensation and the cooling system of the condenser section through a comprehensive three-dimensional CFD model of a wickless heat pipe. Two fluids, water and R134a, were selected as the working fluids of the investigated wickless heat pipe. This model was validated using a transparent glass wickless heat pipe to visualise the phenomena of pool boiling and comparing the results with the three-dimensional CFD flow visualisation.

This study demonstrated that the proposed CFD models of a wickless heat pipe can successfully reproduce the complex physical phenomena of both the heat transfer process of evaporation and condensation and the mass transfer process of phase change during the pool boiling that takes place in the evaporator section and the filmwise condensation that takes place in the condenser section. The CFD simulation was successful in modelling and visualising the multiphase flow characteristics for water, R134a and R404a, emphasising the difference in pool boiling behaviour between these working fluids. The CFD simulation results were compared with experimental measurements, with good agreement obtained between predicted temperature profiles and experimental temperature data.

PUBLICATIONS

Published Journal Papers

Fadhl B, Wrobel LC, Jouhara H. Numerical modelling of the temperature distribution in a two-phase closed thermosyphon. *Applied Thermal Engineering* 2013; 60: 122-131.

Fadhl B, Wrobel LC, Jouhara H. CFD modelling of a two-phase closed thermosyphon charged with R134a and R404a. *Applied Thermal Engineering* 2015; 78: 482-490.

Jouhara H., Fadhl B, Wrobel LC. Three dimensional CFD simulation of geyser boiling in a two-phase closed thermosyphon, accepted for publication in *International Journal of Hydrogen Energy*

Published Conference Papers

Fadhl, B., Wrobel, L.C., CFD modelling of a closed two-phase thermosyphon. *ECCOMAS International Conference on Numerical Heat Transfer, Wroclaw, POLAND, 2012.*

Fadhl, B., Wrobel, L.C., Jouhara, H. Modelling of the thermal behaviour of heat pipes. *7th International Conference on Computational and Experimental Methods in Multiphase and Complex Flow, LA Coruna, SPAIN*, 2013.

Fadhl, B., Wrobel, L.C., Jouhara, H. Three-dimensional CFD modelling of two-phase flow in a wickless heat pipe. *8th International Conference on Sustainable Energy & Environmental Protection, Paisley, UK, 2015.*

ACKNOWLEDGEMENTS

First of all, I would like to thank Almighty Allah who has guided me during my PhD and given me the strength and ability to succeed in finishing my PhD thesis and without his immeasurable blessing and favours none of this could have been possible.

I would like to express my profound sense of gratitude to my supervisor Professor Luiz Wrobel for the many years of guidance and invaluable assistance in every aspect of this work. I have been very fortunate to have had the opportunity to work so closely with an advisor that has so much to offer and is willing to share his knowledge and years of experience enthusiastically. I sincerely appreciate his keen advice, encouragement and patience.

I would like to express my sincere appreciation to Dr. Hussam Jouhara for sharing his knowledge. I truly thank him for his valuable comments and suggestions. Without his support it would have been much difficult to accomplish this work.

I would like to thank ANSYS UK Training Centre in Sheffield for their trainings and support with FLUENT package. In particular, I wish to thank Dr. Adam Anderson.

I am thankful to my best friend Lesh for his practical advice and helping me with FLUENT issues. I am also very grateful to my good friend Hassan for his assistance and helping me in the experimental apparatus.

Most importantly, acknowledgments attached to my beloved family, especially my lovely mother Haniah and my sister Sabah for their great and never-ending support accompanying with me all the way.

Finally, I truly cannot find the words to thank my wonderful wife Budor and my great son Amin whose constant moral and emotional support was the major factor in the completion of this work. With all my heart and all my soul, I thank them for all sacrifices over this long and arduous period. I dedicated this thesis to my mother, Haniah and my wife and my son, Budor and Amin.

Table of Contents

List of Figures

List of Tables

NOMENCLATURE

A_{evp_out}	surface area of the outer wall of the evaporator section	m^2
A_{evp_in}	surface area of the inner wall of the evaporator section	m^2
A_{con_out}	surface area of the outer wall of the condenser section	m^2
A_{con_in}	surface area of the inner wall of the condenser section	m^2
A_e	surface area of the evaporator section	m^2
A_c	Surface area of the condenser section	m^2
a_c	accommodation coefficient	
$C_{v,l}$	specific heat of the liquid phase	J/kg.K
$C_{v,v}$	specific heat of the vapour phase	J/kg.K
$C_{p,w}$	specific heat of the cooling water	J/kg.K
C_{sf}, C_{cr}, n	constants obtained by experimental measurements depends on the fluid and surface-fluid combination	
$C_0, C_1 \dots C_5$	physical properties coefficients	
D_{out}	diameter of the outer wall	m
D_{in}	diameter of the inner wall	m
D_c	inner diameter of the condenser section	m
D_e	inner diameter of the evaporator section	m
D_e	inner diameter of the evaporator section	m
D_{sm}	Sauter mean diameter	m
e	internal energy	
F_{CSF}	continuum surface force	
g	gravitational acceleration	m/s^2
h_{fg}	latent heat of vaporisation	J/kg
h	heat transfer coefficient	$W/m^2.K$
h_{evp_out}	heat transfer coefficient at the outer wall of the evaporator section	$W/m^2.K$
h_{evp_in}	heat transfer coefficient at the inner wall of the evaporator section	$W/m^2.K$
h_{con_out}	heat transfer coefficient at the outer wall of the condenser	$W/m^2.K$

	section	
h_{con_in}	heat transfer coefficient at the inner wall of the condenser section	W/m^2.K
h_{film}	average heat transfer coefficient of the liquid film	W/m^2.K
h_{NPB}	heat transfer coefficient of the nucleate pool boiling in the evaporator section	W/m^2.K
I	unit tensor	
$I_{electric}$	electric current flow	amp
k_{wall}	wall thermal conductivity	W/m.K
k_l	thermal conductivity of the liquid phase	W/m.K
L_{evp}	length of evaporator section	m
L_{con}	length of condenser section	m
L_{adia}	length of adiabatic section	m
l_e	length of the evaporator section	m
l_c	length of the condenser section	m
M	molecular weight	kg/kmole
$\dot{m}$	mass flow rate	kg/s
$\dot{m}_w$	mass flow rate of the cooling water	kg/s
m_f	net mass flux over vapour-liquid interface	kg/ m^2.s
p	pressure	Pa
P_v	vapour pressure	Pa
P_{atm}	atmospheric pressure	Pa
p_{sat}	Saturation pressure	Pa
Pr_l	prandtl number of the liquid phase	
$\dot{Q}$	overall rate of heat transfer	W
Q_c	rate of heat transfer from the condenser section	W
Q_e	rate of heat transfer to the evaporator section	W
$q_{.NBP}$	rate of heat flux in the nucleate pool boiling regime	W/m^2
$q_{critical}$	maximum heat flux	W/m^2
r	radius	m
R	overall thermal resistance	K/W

R_{HP}	predicted overall thermal resistance of wickless heat pipe	K/W
R_e , R_3	thermal resistance associated with the evaporation in the evaporator section	K/W
R_c , R_8	thermal resistance associated with the condensation in the condenser section	K/W
R_{CFD}	overall thermal resistance of the CFD simulation	K/W
R_{EXP}	overall thermal resistance of the experimental results	K/W
Re_{film}	reynolds number of the liquid film	
R_u	universal gas constant	J/mole.K
S_m	mass source term in the continuity equation	
t	time	s
T	temperature	K
T_{sat}	saturation temperature	K
T_s	surface temperature	K
T_v	temperature of the saturated vapour	K
T_c	temperature of the condenser wall	K
ΔT_{lm}	logarithmic mean temperature difference	K
$T_{c,av}$	average temperature of the condenser section	K
$T_{e,av}$	average temperature of the evaporator section	K
$T_{w,outlet}$	temperature of the outlet of the cooling water jacket	K
$T_{w,inlet}$	temperature of the inlet of the cooling water jacket	K
Te_{CFD}	average wall temperature of the evaporator section	K
Tc_{CFD}	average wall temperature of the condense r section	K
u	velocity	m/s
U	velocity of the inlet of the cooling water jacket	m/s
v_l	Kinematic viscosity of the liquid phase	m^2/s
$\mathbf{V}$	velocity vector	m/s
$\dot{V}$	volume flow rate of the cooling water	m^3/s
V_{vol}	heater voltage	volt
$\dot{W}$	rate of work done by pressure force	
Z_1, Z_9	heat transfer resistances for heating a solid surface	K/W

Z_2 , Z_8	thermal resistances of the heat pipe wall	K/W
Z_3, Z_7	thermal resistances of the wick structure	K/W
Z_4, Z_6	thermal resistance corresponding to the vapour liquid surfaces	K/W
Z_5	the thermal resistance of the saturated vapour	K/W
Z_{10}	axial conduction thermal resistance through the heat pipe wall	K/W

GREEK SYMBOLS

μ_l	dynamic viscosity of the liquid phase	kg/m.s
ρ	density	kg/m^3
ρ_l	density of the liquid phase	kg/m^3
ρ_v	density of the vapour phase	kg/m^3
ρ_w	density of the cooling water	kg/m^3
α	volume fraction	
α_l	volume fraction of the liquid phase	
α_v	volume fraction of the vapour phase	
σ	surface tension of liquid-vapour interface	N/m
Δ	increment	
ΔT_{excess}	excess of the temperature above the saturation temperature	K
ΔT_w	temperature difference between the cooling water inlet and outlet	K
ΔT_{e-c}	temperature difference between average wall temperature of the evaporator section and average temperature of the condenser section	K
ΔV_{vol}	voltage difference	volt

SUBSCRIPTS

av	average
evp	evaporator
adia	adiabatic
atm	atmospheric
c	condenser
con	condenser

CSF	continuum surface force
CFD	CFD simulation
e	evaporator
e-c	average temperature between evaporator and condenser
excess	temperature excess
EXP	experimental
electric	electric flow
critical	maximum
fg	fluid to gas
film	liquid film
HP	heat pipe or thermosyphon
in	inner wall
inlet	water inlet
l	liquid phase
lm	logarithm
m	mass
NPB	nucleate pool boiling
out	outer wall
outlet	water outlet
s	surface
sat	saturation
v	vapour phase
vol	voltage
w	cooling water
wall	wall

CHAPTER 1 INTRODUCTION AND MOTIVATION

In this study, the motivation of developing a CFD model is to provide a deeper understanding of the fluid mechanics and thermodynamics within a heat pipe, allowing the performance of heat pipes to be enhanced for many different applications. Furthermore, modelling the complicated two-phase flow of boiling and condensation have been done and validated in this study for a simple configuration of a straight heat pipe; however, boiling and condensation, specially boiling, does not depend on the actual shape of the surface. Therefore, this model can be applied to much more complicated heat exchanger structures. The developed CFD model can reduce the amount of experimental work necessary to predict the performance of the system, which can then be optimised. The performance of the final optimised model can then be verified through experiments, substantially reducing the design costs.

1.1 General Background

Generally speaking, a heat pipe is a device with high thermal conductance. Gaugler was the first scientist to suggest the idea of the heat pipe in 1942 and in the early 1960s Grover established an independent invention and illustrated its effectiveness as a high-performance heat transfer device, named it the "heat pipe", and developed its applications. The heart of the heat pipe is the existence of a wick structure in the system to transfer heat against the force of gravity by an evaporation-condensation process. However, many heat pipe applications are independent on this feature; and the Perkins tube, which was established decades before the heat pipe, is basically a wickless tube that is still being used today. The Perkins tube was invented and improved upon by the Perkins family from the mid-19th to the 20th century. The Perkins tube was designed as a closed tube that includes a small amount of water working in either a single or two-phase cycle to transfer heat from a furnace to a boiler, as illustrated in Figure 1.1. This system was basically a closed tube boiler in which water is circulated in tubes between the furnace and the steam drum, providing an indirect heating system. The expansion tube was fitted with a removable air plug to allow the air to escape when the boiler is being filled. This system was used in baking ovens in which heat is transferred from the

flames to the baking chamber by the vapour contained inside the tubes. The Perkins tube became an important element in the history of the heat pipe [1,2].

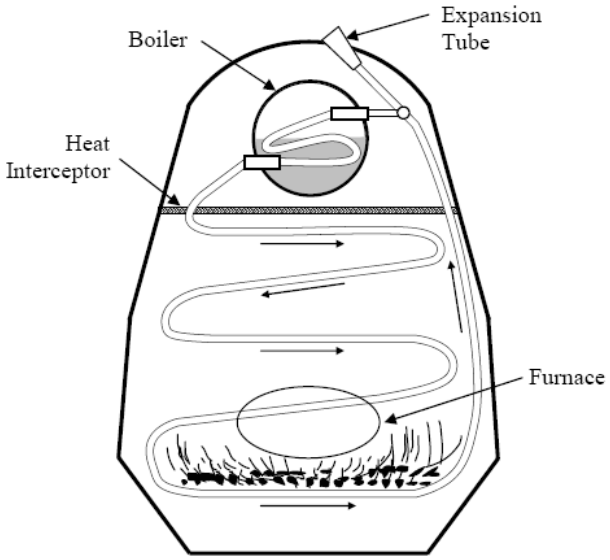

Figure 1.1: Basic Perkins tube [2]

In a wickless heat pipe, heat is added to the evaporator where a liquid pool exists, changing the liquid into vapour and thus increasing the liquid temperature and pressure. The high temperature and pressure cause the vapour to flow and pass through the adiabatic (transport) section, which is located in the middle between the evaporator and condenser, toward the condenser. A heat pipe may or may not have adiabatic section depending on specific applications and design. The vapour adjacent to the condenser's wall gives up its latent heat that is absorbed in the evaporator section. The condensed liquid is then transported back to the evaporator due to gravity [3].

The demand for waste heat energy recovery in engineering applications with commercial use is increasing due to the effect of greenhouse gases on the environment and the adoption of the Kyoto Agreement by many industrial countries [4,5]. The Kyoto Agreement is a protocol of the United Nations Framework Convention on Climate Change that commits the countries under this agreement to achieve their targets of reducing greenhouse gas emissions [6].

Heat pipes have been successfully used for waste heat energy recovery in a vast range of engineering applications, such as heating, ventilation, and air conditioning (HVAC)

systems [7], ground source heat pumps [8], water heating systems [9] and electronics thermal management [10]. This is mainly because of their simple structure, special flexibility, high efficiency, good compactness, and excellent reversibility [11-14].

1.2 Identification of Research Gap and Scope of the Thesis

Heat pipe technology is now receiving high attention and the optimisation of heat pipe performance is being investigated. Wickless heat pipe have three sections, which are the evaporator at the bottom end, where heat is added and the liquid is vaporised, the condenser at the top end, where heat is released and the vapour is condensed, and an adiabatic section in the middle between the evaporator and condenser [15]. However, up to now, computational studies developed on wickless heat pipe, displaying the complex two-phase flow of pool boiling in the evaporator section and liquid film condensation in the condenser section during the operation of the wickless heat pipe are at an early stage.

Only a limited number of CFD simulation studies on wickless heat pipes have been published [3,16-19]. A range of numerical codes have been developed to simulate their multiphase flow behaviour. The overall temperature profiles along the wickless heat pipe have been determined for different working fluids and parameters. However, these studies have limitations, as some studies have not included the phase change during the evaporation process, so the formation of bubbles during the pool boiling has not been simulated accuracy [3,17,18]. Inaccurate correlations have been used to determine the overall thermal performance [19]. Some models treated the flow inside the pipe as a single phase [18]. To the best of our knowledge, a CFD simulation of a wickless heat pipe charged with refrigerant that considers all the details of heat transfer phenomena has not yet been reported in the literature.

Consequently, there is an obvious gap in the published literature on CFD simulations of two-phase heat transfer/flow within a heat pipe. Hence, the main objectives of this study will be as follows:

- Developing a CFD model that includes the complex physical phenomena of the heat transfer processes of evaporation and condensation
- Modelling the mass transfer process of phase change during the pool boiling and film condensation.
- Modelling the pool boiling in the evaporator section.
- Modelling the liquid film-wise condensation near the inner face of the condenser section wall.
- Investigating the performance of a heat pipe by testing different sets of parameters.
- Reducing the amount of experimental work necessary to predict the performance of the system.

~~Modelling the complicated two-phase flow of boiling and condensation have been done and validated in this study for a simple configuration of a straight heat pipe, however boiling and condensation, specially boiling, does not depend on the actual shape of the surface. Therefore, this model can be applied to much more complicated heat exchanger structures.~~

In order to achieve the objectives of this study, the following processes will be conducted:

i. Using ANSYS Fluent as a numerical solver
ii. Building model geometry and mesh.
iii. Using different mesh sizes to test grid-independence.
iv. Using the Volume of Fluid technique (VOF) to track the interface between the liquid and vapour phases.
v. Using appropriate correlations that have been covered in the literature to model mass transfer during the evaporation and condensation processes that are not included in the CFD FLUENT code.

vi. Developing a user-defined function (UDF) by adding the mass transfer correlations to employ phase change material during the evaporation and condensation processes.
vii. Modelling the two-phase flow and heat and mass transfer during the operation of a wickless heat pipe.

The above characteristics will be coupled to each other and used to build a proper and accurate CFD model that describes flow and heat transfer in a closed two-phase thermosyphon. Further, each process will be discussed in detail. Finally, the predicted model will be validated using experimental work.

This thesis consists of seven chapters**. Chapter 1** provides a background and the main aims and objectives of the project, as well as a general description of each chapter carried out in this study. **Chapter 2** reviews the heat pipe technology including its applications. The published literature in a broad area is reviewed including wickless heat pipes or thermosyphons and wick heat pipes. The basic heat pipe theory is described first. Then, the working fluids as well as shell materials of the heat pipes are reviewed. Different and special types of heat pipes such as loop heat pipes are reviewed. Heat pipe heat exchangers are also reviewed. In addition, studies of two-phase heat pipes and heat pipe heat exchangers have also been covered in this chapter.

Chapter 3 focuses on the heat transfer of boiling and condensation. This chapter consists of three parts. The first part deals with the physics behind the boiling process that takes place in the evaporator section and the condensation process that takes place in the condenser section. The second part deals with the correlations of the heat transfer coefficient of pool boiling and film condensation, which are used to predict the heat transfer thermal resistances of the thermosyphon. The third part presents the procedures for applying the theoretical model, described in the second part, used to predict the thermal resistances in the evaporator and condenser section. The theoretical calculations are assessed using the experimental work.

Chapter 4 describes the experimental apparatus that was built to carry out a thermal performance investigation on a typical wickless heat pipe. A set of experiments have been carried out for the purpose of validating the theoretical calculations described in

Chapter 3, as well as the CFD simulations of the thermosyphon described in Chapter 5, in order to demonstrate the accuracy of the simulation results.

Chapter 5 introduces the CFD theory and approaches of modelling multiphase flows. The chapter introduces the developed UDF techniques to complete the existing multiphase model, used to simulate the phase change during the evaporation and condensation processes. This chapter also describes a novel CFD model used to simulate the details of the two-phase flow and, heat and mass transfer phenomena during the operation of a thermosyphon, including evaporation and condensation processes. The cooling system of the condenser section is simulated separately as a parallel-flow double pipe heat exchanger to model the heat transfer across the condenser section's heat exchanger and predict the heat transfer coefficients. This chapter also introduces the CFD simulation findings of the flow visualisation of pool boiling and liquid film condensation processes that take place in the evaporator and condenser, respectively. The temperature profiles along the thermosyphon, as well as the thermal performance are also presented. The CFD model is validated using experimental measurements described in Chapter 4.

Chapter 6 combines the CFD simulation of the two-phase flow in a thermosyphon and the CFD simulation of the condenser water jacket described in Chapter 5 by developing a comprehensive three-dimensional CFD modelling of a two-phase closed thermosyphon, including the simulation of the two-phase flow phenomena of boiling and condensation and the simulation of the cooling system. For a reduced CPU time, an experimental investigation of a small thermosyphon carried out by Jouhara and Robinson [20] has been selected for this model and the same configuration of the thermosyphon described in [20] has been adopted.

Chapter 7 concludes the research work by introducing and discussing the outcomes of the project, and provides recommendations for further CFD modelling work in this field.

CHAPTER 2 HEAT PIPE THEORY

In order to understand the operation of heat pipes and the modelling of two-phase heat transfer in heat pipes, especially the determination of heat transfer coefficients (h) associated with boiling and condensation, as explained in Chapter 3, it is important to discuss the physics behind the boiling that takes place in the evaporator section, as well as the condensation that takes place in the condenser section [15,21].

2.1 Pool boiling heat transfer

In this mechanism of boiling, the heated fluid does not flow by external forces, and any fluid movement is caused by natural convection. The purpose of pool boiling is therefore to transform some, or all, of the fluid from the liquid phase to the vapour phase.

In case where a pipe is filled by water, the water will initially be at about 300 K, which is far less than the saturation temperature of 373 K at atmospheric pressure. After applying heat to the pipe by an external source, the water is heated from a subcooled state to a saturated state. During this stage, the water temperature is raised and chunks of liquid water move up and down because of natural convection currents, followed by the formation of vapour bubbles. These bubbles then start rising towards the top of the water pool, and then smash in the cooler water above. This is called subcooled boiling, where the bulk of the liquid pool is still below the saturation temperature. Eventually, the overall temperature of the liquid pool reaches the saturation temperature and the number and size of the vapour bubbles increase and the bubbles then reach the top region of the pool. This is saturated boiling [15,21].

2.2 Pool boiling regimes

The values of the measured excess temperature play an important role in determining the type of pool boiling regimes. On basis of the excess temperature range, different regimes have been observed, which are natural convection boiling, nucleate boiling, transition boiling and film boiling. These regimes are illustrated in Figure 2.1, which shows a plot of boiling heat transfer flux versus the excess temperature to give what is

called the boiling curve. The boiling curve given in this figure is for water at atmospheric pressure [15,21].

2.2.1 Natural convection boiling regime

By applying heat to the pipe filled with water, heat is transferred from the pipe wall into a subcooled water by natural convection. Once the water reaches the saturation temperature, it begins to move to the top surface of the liquid pool by natural convection currents. At this stage, no vapour bubbles form until the water is heated to a few degrees above the saturated temperature, and the excess temperature is very low. The natural convection boiling regime is illustrated on the boiling curve in Figure 2.1 between Point 0 and Point A. [15,21].

2.2.2 Nucleate boiling regime

Following the natural convection boiling, vapour bubbles start to form in the water as a result of increasing the excess temperature. By continuous boiling, isolated vapour bubbles are formed and rise to the top of the liquid pool resulting in an increase in the heat flux as illustrated on the boiling curve in Figure 2.1 between Points A and B. With a further increase in the excess temperature, the isolated vapour bubbles start to merge and coalesce forming columns and slugs of vapour. These columns and slugs of vapour bubbles rise all the way up to the top of the liquid pool and break up releasing their vapour content. This state is illustrated on the boiling curve between Points B and C.

Further formation of vapour bubbles near the heating surface makes the liquid difficult to reach the surface and cause a reduction in the convection heat transfer, thus causing the slope of the boiling curve to reduce gradually. Consequently, the excess temperature increases with increasing the heat flux until it reaches a maximum value. This value is called the critical heat flux and illustrated at Point C in Figure 2.1.

Nucleate boiling regime is the most important regime in pool boiling, as high heat transfer rates can be achieved with relatively small values of excess temperature [15,21].

2.2.3 Transition and film boiling regimes

In these regimes, a vapour film forms above the heating surface and insulates the surface from the liquid phase, due to the low thermal conductivity of the vapour compared to the liquid. Thus, the heat flux decreases until it reaches the minimum value, which can be seen at Point D on the boiling curve in Figure 2.1. The vapour film thickness then grows and the heat flux begins to increase again due to radiation heat transfer [15,21].

2.3 Flow boiling mechanism (or Forced convection boiling)

In flow boiling, the liquid being boiled inside the tube is forced to flow by an external source, which is not the case in a thermosyphon. Both the liquid phase and the vapour phase in this boiling regime are forced to move together, therefore no free surface exists for the vapour to escape. Different flow boiling regimes have been observed on the basis of the relative amounts of the liquid phase and the vapour phase. Figure 2.2 illustrates four different flow boiling regimes in a pipe under forced convection [15,21].

Eventually, the flow becomes saturated of the vapour phase. The change in the heat transfer coefficient throughout the processes of theses regimes is also illustrated in Figure 2.2.

2.4 Filmwise condensation heat transfer

As the condenser in the thermosyphon involves laminar flow for the liquid film condensation along the inner surface of the condenser section, Nusselt filmwise condensation correlation is used [20,22] to predict the heat transfer coefficient associated with the film condensation in the condenser section.

The thin liquid film begins to form at the top of the inner surface of the condenser wall of the thermosyphon and then falls back to the evaporator section under the force of gravity. During the condensation process, heat in the form of the latent heat of vaporisation is released by the vapour and transfers through the liquid film to the inner surface of the cold condenser wall [22].

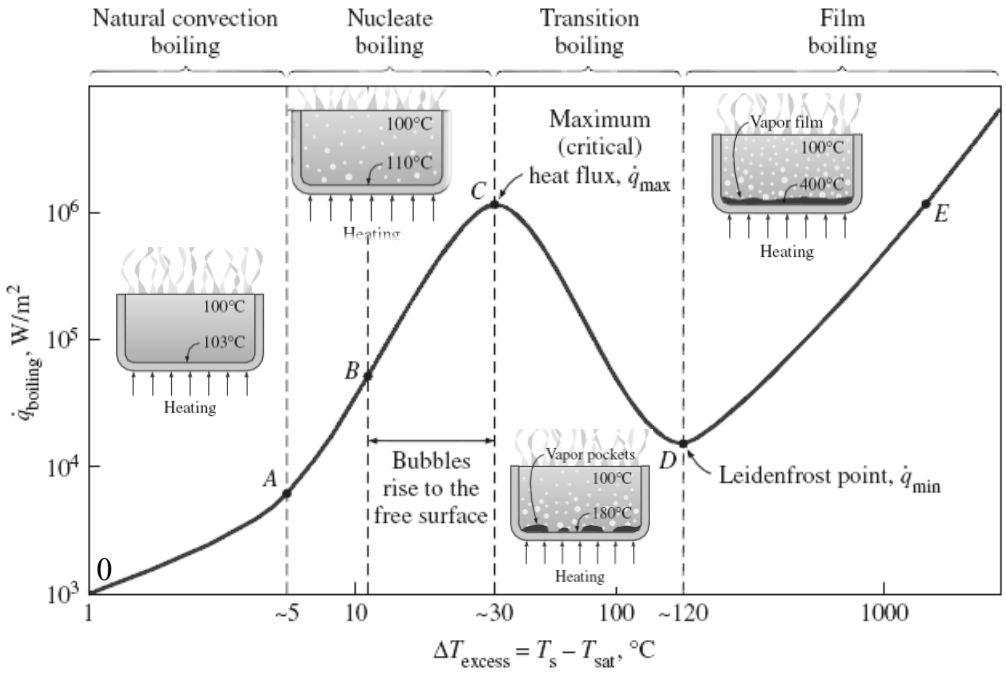

Figure 2.1: Pool boiling regimes and boiling curve for water [15]

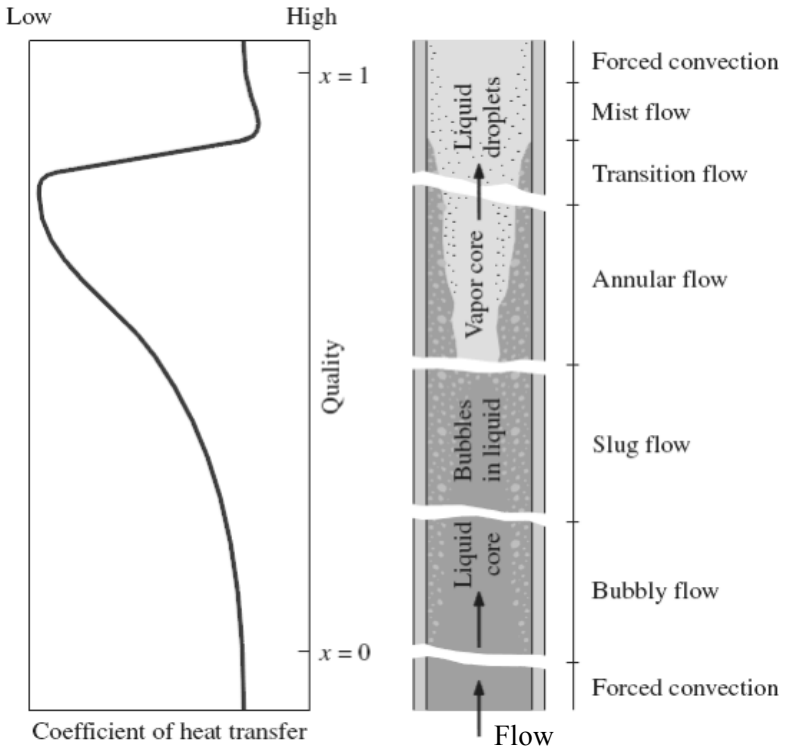

Figure 2.2: Flow boiling regimes versus heat transfer coefficient [15]

2.5 Operation Principle of Heat Pipes

A heat pipe is a two-phase heat transfer device with a highly effective heat transfer rate through evaporating and condensing a fluid that is circulating in a sealed container. The pipe can be in different sizes and of different configurations [23]. A schematic diagram of a heat pipe is shown in Figure 2.3.

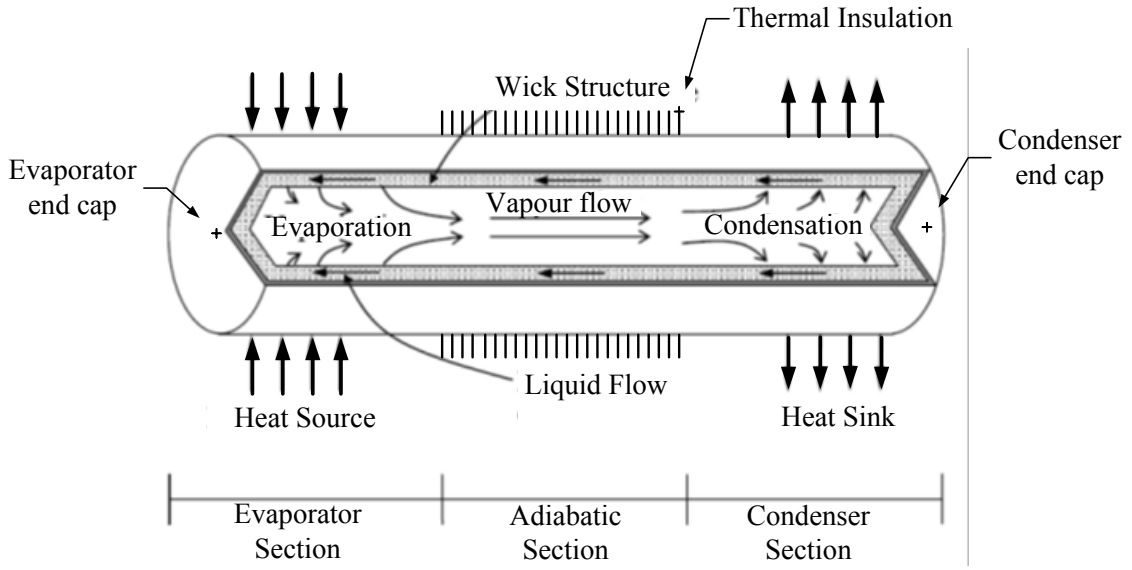

Figure 2.3: Schematic of a heat pipe showing the components and the principle of operation [23]

The heat pipe is filled with a working fluid, such as water. The working fluid will be at saturation condition because heat pipes operate on a two-phase closed cycle, and pure vapour and liquid phases are present inside the heat pipe. When heat is added to the evaporator section by an external source where a liquid pool exists, the working fluid is heated until it starts boiling and changes to vapour. The resulting vapour pressure cause the vapour to flow through the adiabatic section towards the condenser section, which is the colder section. The wall of the condenser section will be at a lower temperature; therefore, the vapour adjacent to this wall gives up its latent heat. The condensed liquid is then transported back to the evaporator section by the capillary wicks or by gravity in a wickless heat pipe [3]. This cycle will continue transporting heat from the evaporator to the condenser as latent heat. The amount of latent heat that can be transported is much larger than that which can be transported as sensible heat in a conventional system. The temperature difference in a heat pipe needed to transport heat is less than in

other systems, thus it is also referred to as a super conductor as the thermal conductivity for the heat pipe is much larger than any known solid with the same size [24]. In particular, heat pipes can have a thermal conductivity ninety times higher than that of a copper bar of the same size [25].

As illustrated in Figure 2.3, a heat pipe consists of three main sections: an evaporator where heat is added and the liquid is evaporated, a condenser where heat is released and the vapour is condensed, and an adiabatic section in the middle between the evaporator and condenser. Size, type, material, construction, heat transfer rate and working fluid are the factors that play an important role in the heat pipe characteristics [24].

2.6 Applications of Heat Pipes

Heat pipes are playing a more important role in many industrial applications, particularly in improving the thermal performance of heat exchangers and increasing energy savings in applications with commercial use. Heat pipes have been successfully used for waste heat energy recovery in a vast range of engineering applications, such as heating, ventilation, and air conditioning (HVAC) systems [7], ground source heat pumps [8], water heating systems [9] and electronics thermal management [10]. This is mainly because of their simple structure, special flexibility, high efficiency, good compactness, and excellent reversibility [11-14].

The list of applications is quite long and growing, thus selected published applications will be discussed and they can be classified into four categories [23] as follows:

- **Heat transfer applications:** where heat pipes are used as heat exchangers to transfer large rates of heat transfer, such as thermal energy recovery and HVAC applications as seen in Figure 2.4 [26,27].
- **Isothermal applications:** where heat pipes are used in an isothermal furnace to eliminate pre-existing temperature gradients, such as ovens and furnaces applications as seen in Figure 2.5 [28].
- **Temperature control applications:** where heat pipes are used to control the temperature of a system, such as electronic equipment applications as seen in Figure 2.6 [29].

- **Transformation of heat flux applications:** where heat pipes are used for applications that need variable heat fluxes at the heat source and the heat sink, such as circuit breakers and solar desalination plants as seen in Figure 2.7 [30].

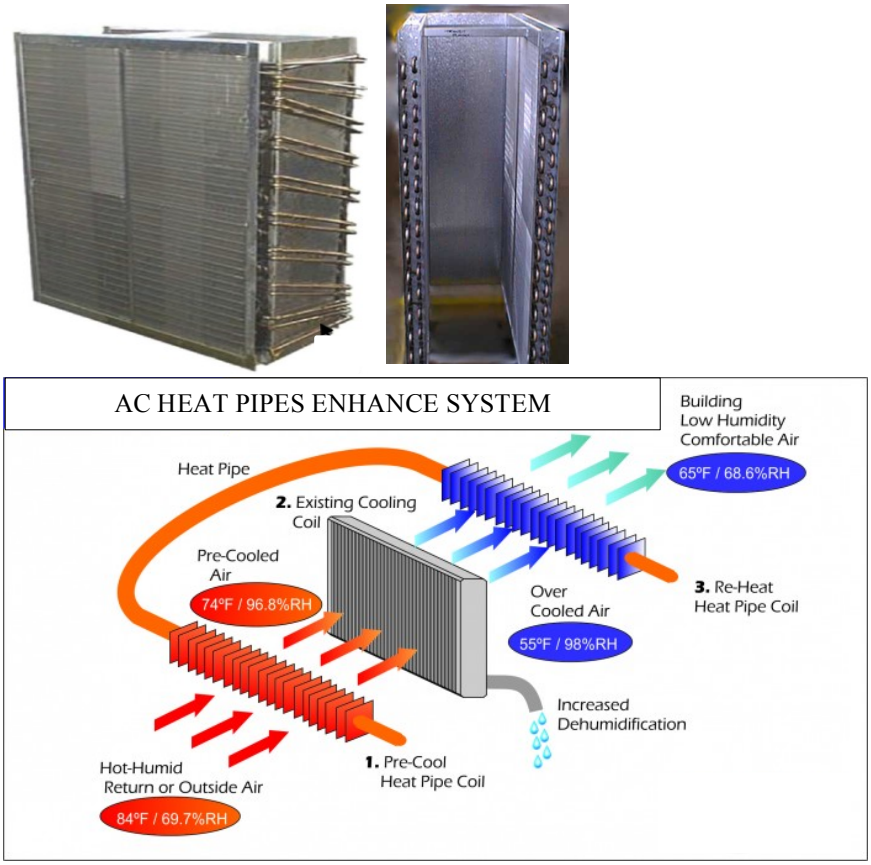

Figure 2.4: Heat pipe heat exchanger for heat recovery [26,27]

Figure 2.5: Steam pipes deck oven [28]

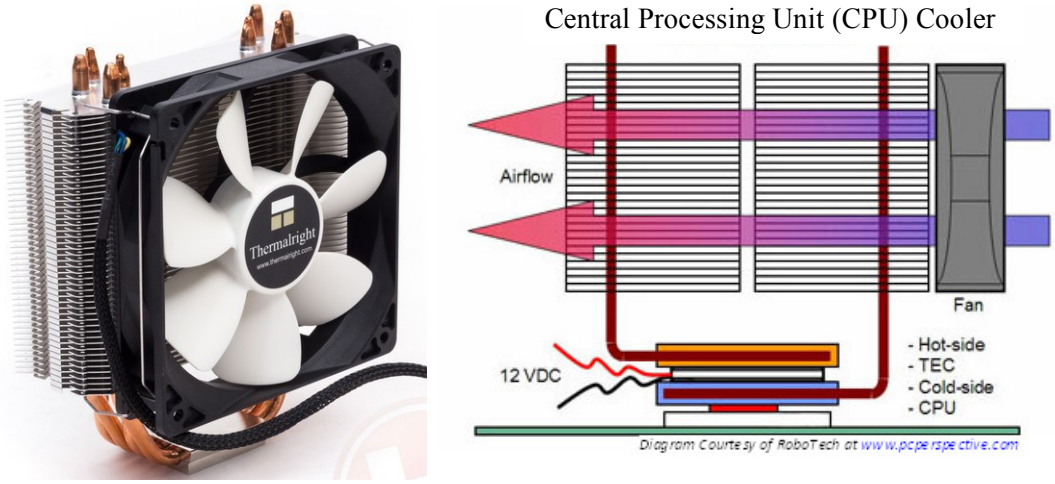

Figure 2.6: Heat pipe cooling system for electronic components [29]

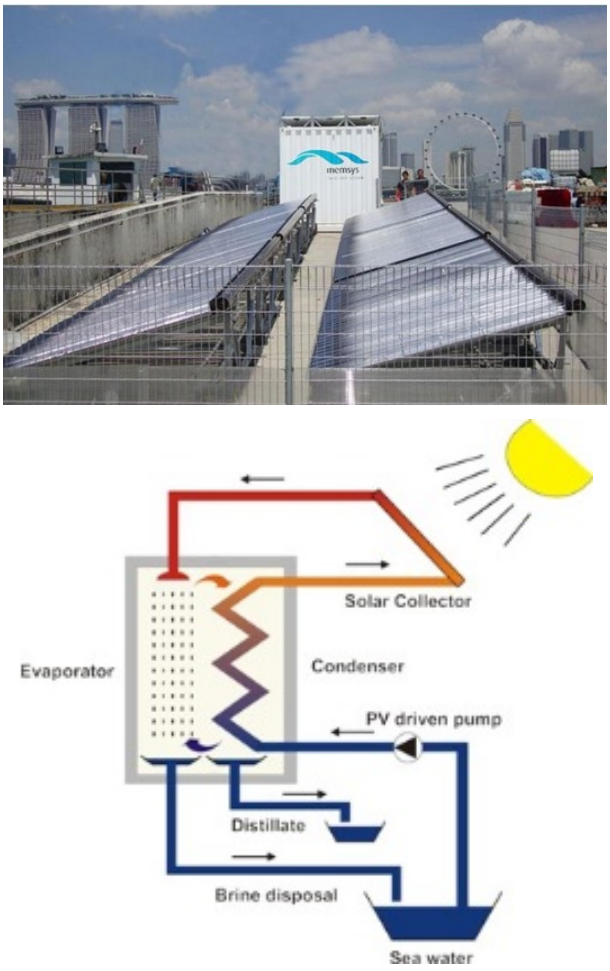

Figure 2.7: Thermosyphon for solar desalination system [30]

2.7 The Working Fluid

The working fluid is an important part of the heat pipe, and this is due to each heat pipe application having a specific temperature range in which the heat pipe is required to operate. Consequently, the design of a heat pipe must take into account the intended temperature range by selecting a proper working fluid. The shell material of the heat pipe is another important parameter as the heat pipe container material needs to be compatible with the working fluid. The reason behind this is that the heat pipe shell material can react chemically with the working fluid and thus non-condensable gases (NCG) can be produced, which affect the heat pipe performance [25]. Therefore, the working fluids and shell materials compatibility for a heat pipe will be discussed below, based on the published literature.

According to Reay and Kew [2], the operating vapour temperature range is the most important element in the determination of a suitable working fluid. The most important characteristics to consider in identifying suitable working fluids are as follows:

- Compatibility and wet ability with wick and wall materials
- Good thermal stability
- High latent heat
- High thermal conductivity
- High surface tension
- Low viscosities for both liquid and vapour

Heat pipe intermediate temperature working fluids can be categorised into three groups: elements, organic fluids and halides [31]. The intermediate temperature region is generally defined as a temperature range of 177^{O}C to 477^{O}C. Generally, water is a better working fluid due to its beneficial transport properties; in the past, it was used as a working fluid for heat pipes at temperatures up to 153^{O}C. In recent times, water has been used at temperatures up to 277^{O}C with shell materials of Titanium [32]. Additionally, it was found that Titanium/water two-phase closed thermosyphons increased the heat transfer coefficient in the condenser section about 2-3 times more than Copper/water two-phase closed thermosyphons [33]. Nevertheless, water is not suitable as a working fluid for heat pipes for temperatures over 277^{O}C, because of the

increase in the vapour pressure and decrease in the surface tension [34,35]. Copper heat pipes are compatible with water for many applications, such as electronics cooling, although they encounter some performance problems with high-temperature electronics. Titanium and Monel heat pipes have the ability to solve these problems with high-temperature electronics [36]. Furthermore, water at low temperature is compatible with Nickel and incompatible with Aluminium due to the generation of NCG at all temperatures. Moreover, water is incompatible with Stainless Steel due to the generation of gas at elevated temperatures [2].

For high temperature range, Cesium is used as a working fluid for heat pipes. It was found that Cesium is compatible with shell material of CP-2 Titanium at temperature ranges of 277^{O}C to 467^{O}C. For temperatures above 467^{O}C, Cesium becomes not suitable as a working fluid with shell materials of CP-2 Titanium and 70-30 Copper/Nickel due to copper transport from the condenser section to the evaporator section [34,37].

For low temperature applications, ammonia and various refrigerants such as R134a, R22 and R410a have been used as working fluids with copper, steel, aluminium and other compatible metals as shell materials. [8,38].

The three groups of fluids used as intermediate temperature range working fluids in a heat pipe will be described below:

2.7.1 Elements fluids

Elements include three main working fluids: Sulphur, Sulphur Iodine mixture and Mercury. Mercury has several disadvantages as a working fluid because of its toxicity and high density that transforms into increased mass, and the difficulty combined in wetting the wick and shell material without corrosion [2,31].

Viscosity is essential in a wickless heat pipe because it influences the ability of the fluid to transport from the condenser to the evaporator. Sulphur has high viscosity, which is a disadvantage in the temperature range of 177^{O}C to 477^{O}C. Therefore, adding a small percentage of Iodine (10% I) can reduce the viscosity of Sulphur to a suitable level for practical heat pipe operation. Pure Sulphur is compatible with shell material of 3003 Aluminium at a temperature of 600^{O}C [31,39]. Pure Iodine is not used in a heat pipe

because of two main problems: low thermal conductivity and corrosiveness caused by its highly reactive properties [39]. A mixture of Sulphur and 10% of Iodine is compatible with 304 Stainless Steel and not compatible with 5052 Aluminium, Ti-6A1-4V, and the mixture of Niobium and 1% of Zirconium at a temperature of 350^{O}C. In addition, it is also incompatible with CP-2 Titanium at a temperature of 250^{O}C [31].

2.7.2 Organic fluids

Organic working fluids have two main disadvantages: polymerization and dissociation. Polymerized working fluids cause decrease in the circulation of the fluid in a heat pipe because of the increase in liquid viscosity that also leads to a decrease in the heat transport capacity of the heat pipe. Dissociation produces NCG, which are located in the condenser section. Therefore, the temperature of non-condensable gases will be increased. Additionally, organic fluids begin to decompose when the temperature is increased. The maximum operating temperature for the organic fluid depends on the NCG and heat pipe operating lifetime [31].

The best three organic fluids that have been tested for life are as follows:

- Toluene
- Naphthalene
- Dipheny1, Dipheny1 Oxide, and Eutectic Dipheny1/Dipheny1 Oxide (Dowtherm A, Therminol VP, Diphy1)

Toluene has three main advantages: compatibility with many shell materials, a melting temperature of -95^{O}C, and lower saturation pressure. Toluene is compatible with shell materials of Copper-Nickel at a temperature of 280^{O}C, 6061 Aluminium at a temperature of 137^{O}C, as well as Mild Steel, 316 Stainless Steel and Titanium at a temperature of 250^{O}C [31].

Naphthalene is compatible with shell materials of 316 Stainless Steel, Copper-Nickel, CP-Titanium and Titanium for temperatures above 320^{O}C. It is also compatible with 6061 Aluminium at a temperature of 215^{O}C and with Mild Steel at a temperature of 270^{O}C. Fluoride compounds are more steady than hydrogen compounds; however, this observation requires life test validation. Monochloronaphthalene, Octafluoronaphtalene

and 1-Fluoronaphthalene are not compatible with Stainless Steel or Mild Steel due to some generation of NCG [31,40,41].

Dipheny1, Dipheny1 Oxide, and Eutectic Dipheny1/Dipheny1 Oxide for temperatures between 300 and 400^{O}C are normally suitable for short tests about 400 ^{O}C and long tests about 300^{O}C. These working fluids generate NCG for temperatures over 400^{O}C [31]. Diphney1 was found compatible with 304 Stainless Steel and Black Iron for long duration tests at a temperature of approximately 250^{O}C. It was also found compatible with 316 Stainless Steel for life tests at a temperature of 350^{O}C. On the other hand, Diphney1 was found incompatible with 304 Stainless Steel for a temperature above 400^{O}C.

Dipheny1 Oxide was found compatible with 347 Stainless Steel and 304 Stainless Steel at a temperature of 300^{O}C [31,41]. An Eutectic mixture of Dipheny1/Dipheny1 Oxide is traded under the names of Dowtherm A and Therminol VP. It was tested for life with shell materials of 304 Stainless Steel and CP-Titanium for a temperature range of 350 to 450^{O}C; Dowtherm A was found to be compatible with 304 SS at 350^{O}C and incompatible with 304 SS, and CP-Ti at 400^{O}C and 450^{O}C, due to the non-condensable gas generation [34]. Further, Dowtherm A and Therminol VP were also used as working fluids in a wickless heat pipe with shell material of 316 Stainless Steel for an operating temperature range of 200 to 450^{O}C; they were also found compatible with 316 SS [5].

2.7.3 Halides fluids

A halide is a compound between element or organic fluids and fluorine, chlorine, bromine, iodine or astatine. The halides family include Tin Tetrachloride ($SnCl_4$), Titanium Tetrachloride ($TiCl_4$), Gallium Trichloride ($GaCl_3$), Titanium Tetrabromide ($TiBr_4$), Aluminium Tribromide ($AlBr_3$), Antimony Tribromide ($SbBr_3$) and Antimony Trichloride ($SbCl_3$). Halides are suggested as potential heat pipe fluids due to their stability at high temperatures up to 400^{O}C, which is higher than organic fluids. The compatibility of halides with shell materials is summarised in Table 2-1. Halides life tests are still being researched [34,35,39,41].

Table 2-1 presents a summary of the working fluids and their useful temperature ranges including their compatibility and incompatibility with different shell materials as

discussed above. In addition, it includes organic working fluids other than those discussed above.

Table 2-1: Summary of working fluids and temperarue ranges [2,5,8,31-41]

Working Fluids	Melting Point (^{O}C)	Temperature Range (^{O}C)	Recommended Shell Materials	
			Compatible	Incompatible
Water (H_2O)	0	20-277	Copper Titanium Monel	Aluminium Stainless Steel
Cesium (Cs)	29	277-467	CP-2 Titanium	
		Above 467		CP-2 Titanium Monel 400 70-30 Copper/Nickel
R134a	-101	(-80) - 50	Copper Steel Aluminium	
Elements				
Mercury (Hg)	- 39	-	Not in use any more	
Sulphur (S)	113	600	3003 Aluminium	-
Iodine (I_2)	114	-	Not used	
Sulphur-10% Iodine	117	250		CP-Titanium
		350	304 Stainless Steel	5052 Aluminium Niobium-1%Zr Ti-6A1-4V
Organic Fluids				
Toluene (C_6H_5CH3)	- 95	137	6061Aluminium	
		250	Mild Steel 316 Stainless Steel Titanium	
		280	Copper-Nickel	
Naphthalene ($C_{10}H_8$)	80	215	6061Aluminium	
		270	Mild Steel	
		320	Copper-Nickel 316 Stainless Steel CP-Titanium Titanium	

Monochloronaphthalene ($C_{10}H_7Cl$)	-2.3	287		Stainless Steel
Octafluoronaphtalene ($C_{10}F_8$)	-	215		Mild Steel
1-Fluoronaphthalene ($C_{10}H_7F$)	-	257		304 Stainless Steel
Dipheny1 ($C_{12}H_{10}$)	70	225-250	Aluminium, Mild Steel	
		250-400	304 Stainless Steel Black Iron 316 Stainless Steel	Mild Steel
		Above 400		304Stainless Steel
Dipheny1 Oxide ($C_{12}H_{10}O$)	27	300	347 Stainless Steel 304 Stainless Steel	
Dowtherm A ($C_{12}H_{10}$)	12	200		Copper
		250	Mild Steel	Copper-Nickel
		300		Mild Steel
		350	304 Stainless Steel	
		200-450	316 Stainless Steel	
		400-450		CP-Titanium 304 Stainless Steel
N-Octane (C_8H_8)	-57	230	Mild Steel	
		250	321 Stainless Steel	
Dowtherm E($C_6H_4C_{l2}$)	-17	220	Mild Steel	
Phenol (C_6H_6O)	41			
O-Terpheny1($C_{18}H_{14}$)	58	272	Mild Steel	
		307		6061 Aluminium
		325-380	316 Stainless Steel	
Decafluorobipheny1($C_{12}F_{10}$)	26	325-380	316 Stainless Steel	
Quinoline (C_9H_7N)	-17	325-380		316Stainless Steel
Formy1-piperidune($C_6H_{11}NO$)	-	280		304Stainless Steel

P-terpheny1 ($C_{18}H_{14}$)	215	450		304Stainless Steel
Ortho-&meta-terpheny1 ($C_{18}H_{14}$)	-	320		Mild Steel
		350		316Stainless Steel
		400		Mild Steel 316Stainless Steel
Dipheny1, ortho-&meta-terpheny1 ($C_{18}H_{14}$)	-	350		Mild Steel 316Stainless Steel
		400		Mild Steel 316Stainless Steel
Halides				
Tin Tetrachloride ($SnCl_4$)	-33	156	Mild Steel	
		159		6061 Aluminium
		280		Hastealloy
Titanium Tetrachloride ($TiCl_4$)	-30	159	Mild Steel	
		165		6061 Aluminium
		227	CP-Titanium	
		300	Hastealloy	
Gallium Trichloride ($GaCl_3$)	-22	340		CP-Titanium
		360		Hastealloy
Titanium Tetrabromide ($TiBr_4$)	39	380	CP-Titanium	
Aluminium Tribromide ($AlBr_3$)	97	227		5052 Aluminium 6061 Aluminium CP2-Titanium
		400	Hastealloy	
Antimony Tribromide (SbBr3)	97	227		6061 Aluminium
Antimony Trichloride (SbCl3)	73	203		Mild Steel
		227		6061 Aluminium

2.8 Heat Pipe Thermal Resistance

Heat enters the heat pipe from a heat source and leaves the heat pipe through a heat sink by conduction, convection, or thermal radiation. Further, electron bombardment or eddy currents can be used to heat the heat pipe, and electron emission can be used for cooling. A temperature difference will take place by thermal conduction through the evaporator and condenser walls. Thermal resistance exists at both vapour and liquid surfaces. Heat pipe performance can be considered in terms of the overall thermal resistance [2,23,42]. Thermal resistances and an equivalent circuit are shown in Figure 2.8.

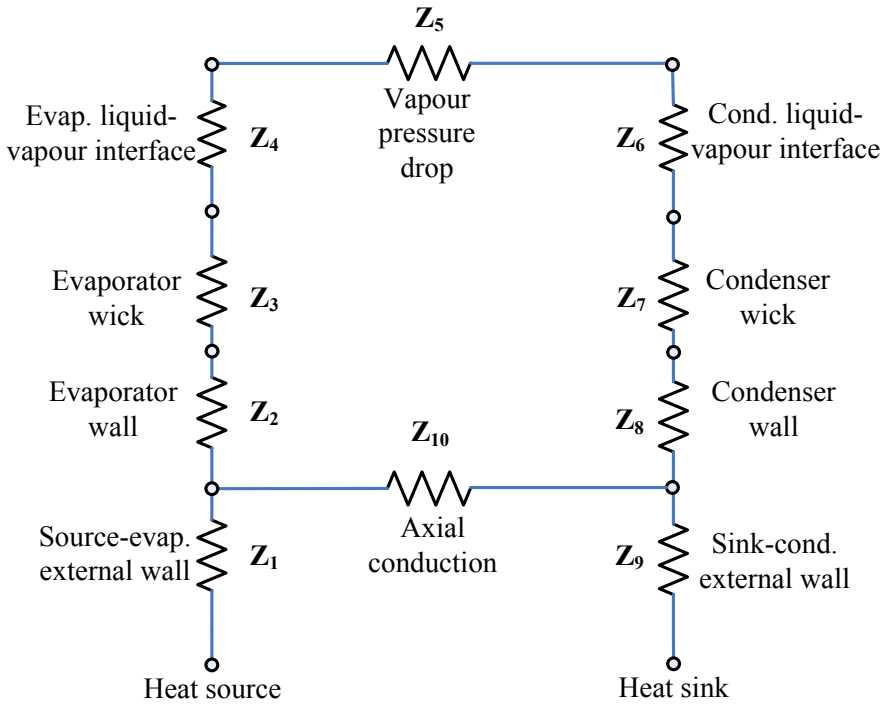

Figure 2.8: Thermal resistance in a heat pipe

- Z_1 and Z_9 are heat transfer resistances for heating a solid surface.
- Z_2 and Z_8 are the thermal resistances of the heat pipe wall.
- Z_3 and Z_7 are the thermal resistances of the wick structure.
- Z_4 and Z_6 represent the thermal resistance corresponding to the vapour-liquid surfaces.
- Z_5 is the thermal resistance of the saturated vapour.
- Z_{10} is the axial conduction thermal resistance through the heat pipe wall.

2.9 Operating Limits

Heat pipes are subject to a number of heat transfer limitations, called operating limits. These limits are illustrated in Figure 2.9 and will be explained in the next sections [2,23].

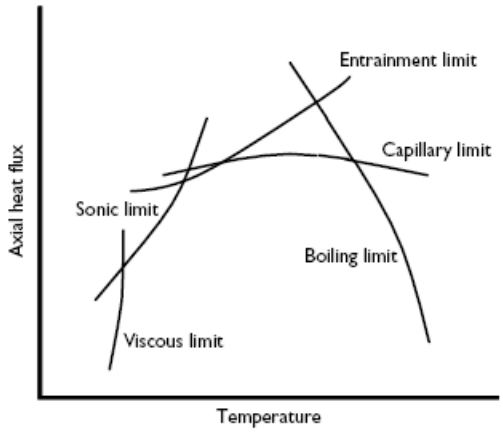

Figure 2.9: Limitation to heat transport in a heat pipe [2]

2.9.1 Vapour pressure limit

The vapour pressure limit, also called the "viscous limit", occurs at a low operating temperature when the vapour pressure difference between the evaporator and the condenser is lower than the viscous forces. As a result, the vapour does not flow to the condenser, and the rate of heat transfer along the pipe is limited. Basically, the maximum vapour pressure must occur at the end of the evaporator and the minimum vapour pressure must occur at the end of the condenser, as shown in Figure 2.10. Hence, when the vapour pressure at the end of the evaporator becomes very low, the vapour pressure drop also becomes very low. Therefore, the rate of heat transfer can be limited [23].

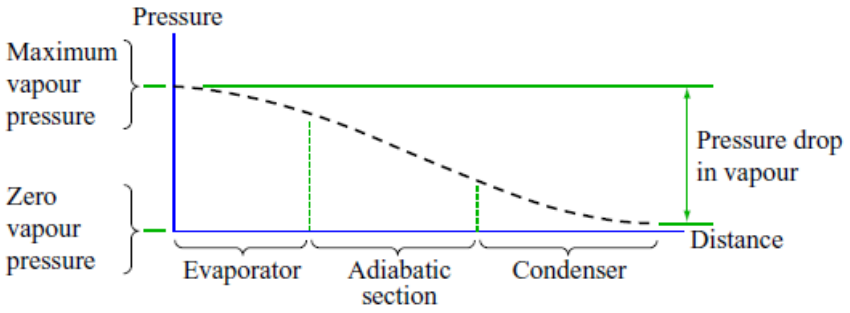

Figure 2.10: Distribution of vapour pressure along the heat pipe [23]

2.9.2 Sonic limit

In a heat pipe, the mass flow of the vapour basically increases and decreases as a result of the vapour addition in the evaporator, due to evaporation and removal in the condenser due to condensation. Hence, the vapour velocity varies in a heat pipe [23,24]. At low temperatures in the operational range during the start-up operation, the vapour velocity reaches the local speed of sound at a point in the flow path and, therefore, the flow is choked and the overall rate of heat transfer can be limited to a value called the sonic limit. The sonic limit is the highest possible heat transport rate that can be sustained in a heat pipe for a specific vapour temperature at the evaporator end of the heat pipe. Since there is a substantial temperature drop along the evaporator length in the vicinity of the sonic limit, heat pipes are usually designed to operate well below this value. However, the sonic limit may be encountered during the start-up of liquid metal heat pipes. According to ESDU [22], the value of the sonic limit during the start-up operation, can be be determined by the maximum overall rate of heat transfer,

$$Q_{max} = 0.5\, A\, h_{fg} \sqrt{(P_v\, \rho_v)}$$

2.9.3 Entrainment limit

At the liquid-vapour interface, a shear force exists due to the liquid and vapour moving in opposite directions. When the vapour velocity is quite high, the condensed liquid will be torn off the wick's surface and entrained in the vapour flowing to the condenser, causing the condensed liquid not to return to the evaporator. This phenomena causes dry out of the evaporator and the rate of the heat transfer at which this takes place is called the entrainment limit [23,24].

2.9.4 Boiling limit

Generally, conductive heat transfer is the main mode of heat transfer in the evaporator and condenser sections. The boiling limit occurs when the radial heat flux in the evaporator causes the liquid in the evaporator wick structure to boil. Because vapour bubbles are generated inside the wick, they have difficulty in moving from the wick so that they combine with the liquid, and the wick can dry out [24].

2.9.5 Circulation limit

In a wicked heat pipe, the working fluid starts boiling in the evaporator, vapour flows upward to the condenser and the condensed liquid returns to the evaporator in the wick by capillary force. During the above operation, two pressure gradients exist, one in the vapour flow passage and the other in the condensed liquid passage. In order to maintain the circulation of the working fluid, it is necessary that along the heat pipe the pressure associated with the vapour flow is different from that associated with the liquid flow. This pressure difference is called the capillary pressure. The circulation limit can also be called the "capillary limit" and it occurs when the capillary pressure becomes too low to supply enough liquid to the evaporator. This can lead to limiting the ability of the capillary to circulate the working fluid, and then the heat pipe will not operate properly [23,24].

2.10 Types of Heat Pipe

Heat pipes have been manufactured with different sizes and configurations to transfer heat during the evaporation and condensation of a working fluid circulating within a sealed cavity. All heat pipes have three main regions, evaporator where the working fluid is evaporated, condenser where the vapour is condensed and adiabatic to separate the previous two regions by a distance suitable to the intended application. The working fluid circulates inside the heat pipe by either capillary forces in a porous wick or gravitational forces. Depending on the purpose of the heat pipe, it is built with different diameters and lengths varying from about three millimetres up to almost a thousand millimetres. There are four main heat pipe configurations: capillary-driven heat pipe or wick heat pipe, flat-plate heat pipe, rotating heat pipe, and wickless heat pipe or two-phase closed thermosyphon [23]. These types will be explained in the next sections.

2.10.1 Wick or capillary-driven heat pipe

In this type of heat pipe, the working fluid moves in the wick by the forces of capillary and gravitation. The positive aspect of this type is that there is no limitation on the orientation of the heat pipe. In other words, the heat pipe can operate independent of gravity. Figure 2.11 illustrates a schematic diagram of the wick heat pipe.

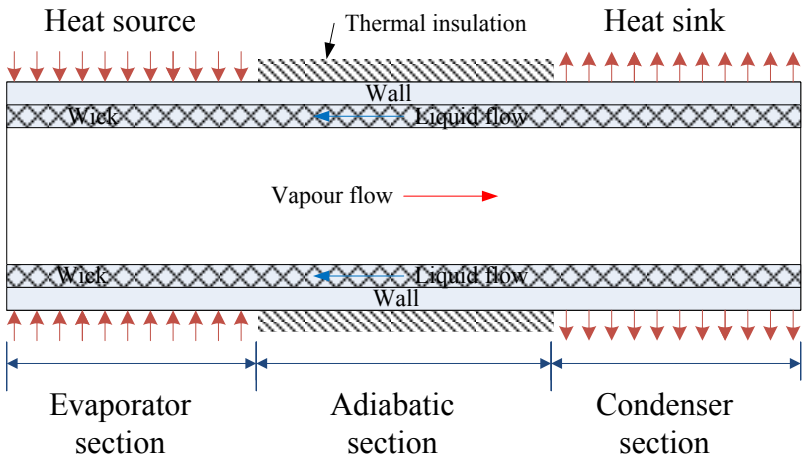

Figure 2.11: Schematic of a wick heat pipe

2.10.1.1 Wick structure of the heat pipe

The main purpose of the wick is to provide a path for the return of condensed liquid from the condenser to the evaporator. There are three properties of wicks that play an important role in the wick heat pipes, which are maximum effective thermal conductivity, minimum capillary radius and maximum permeability.

As shown in Figure 2.12, there are four common wick structures: axial groove, which is a rectangular, circular, triangular, or trapezoidal groove; fine fibre, which is stacked between wall and coil; screen mesh, which is multiple wraps of wire screen mesh; and sintering (powder), which is packed spherical particles, felt metal fibres or powder. A comparison between these structures based on the above three properties of wicks is listed in Table 2-2 [23,43].

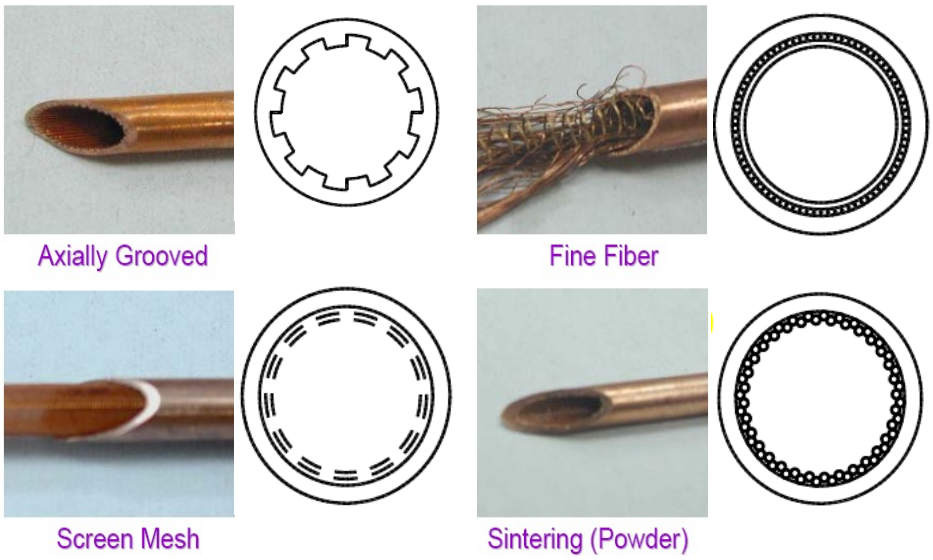

Figure 2.12: Wicking structures [43]

Table 2-2: Wicking structures comparison [43]

Wicking material	Conductivity	Overcome gravity	Thermal resistance	Stability	Conductivity lost (bend & flatten)
axial groove	good	poor	low	good	average
fine fibre	average	average	average	average	low
screen mesh	poor	good	high	poor	average
sintering (powder)	average	excellent	high	average	high

2.10.1.2 Studies of wick heat pipes

A group of researchers carried out experimental and numerical investigations on a wick heat pipe. Legierski et al. [3] provided experimental measurements and CFD modelling of the heat and mass transfer in a horizontal wick heat pipe. They investigated the effectiveness of the heat pipe thermal conductivity in a transient state during the start up of the pipe operation and during temperature increases.

Ghajar et al. [44] developed a model to predict the behaviour of a micro loop heat pipe (MLHP), including identifying the heat transfer to and from the micro compensation chamber (CC). The results showed that increasing the evaporator or width of the vapour line and decreasing the length of the vapour line increased the heat removal capability.

Rahmat and Hubert [45] used ANSYS CFX-5.7.1 to model a three-dimensional two-phase flow in a triangular micro heat pipe. For both phases along the micro heat pipe, the effective thermal conductivity, pressure, and velocity, as well as the influence of the liquid filling ratio on the effective length of the heat pipe, were studied and compared to the literature. The authors pointed out that CFX-5.7.1 software has the ability to simulate two-phase flow.

The theory of two-phase laminar flow in a heated micro channel was investigated by Yarin et al [46]. The authors analysed the effects of inertia, pressure, gravity, friction forces, capillary pressure, and thermal and dynamical interactions of liquid and vapour phases.

2.10.2 Flat-plate heat pipe

As illustrated in Figure 2.13, additional wick material can be located between the evaporator and condenser wicks to make the working fluid move back to the evaporator better. The flat-plate heat pipe is called the “vapour chamber” or “flat two-phase thermosyphon” in some papers.

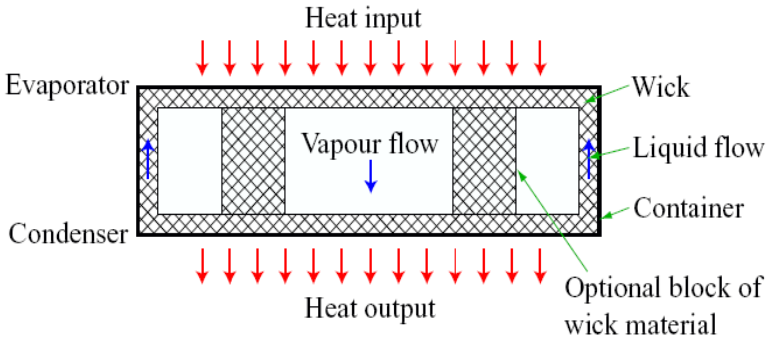

Figure 2.13: Flat-plate heat pipe [23]

Several research studies have been done on this type of heat pipe. Zhang et al. [47] developed a two-dimensional heat and mass transfer model for the disk-shaped flat two-phase thermosyphon. The authors compared the predicted model with experimental results to determine the factors that affected the axial thermal resistance of a thermosyphon. They measured and analyzed the temperatures inside the flat thermosyphon.

2.10.3 Rotating heat pipe

In this type of heat pipe, the working fluid is centrifuged and returned to the evaporator along the tapered inner wall of the cavity; this heat pipe is also wickless. Figure 2.14 shows a rotating heat pipe.

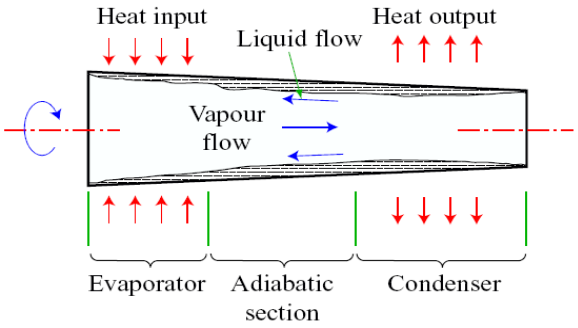

Figure 2.14: Rotating heat pipe [23]

2.11 Special Types of Heat Pipe

According to Reay & Kew [2], there are various other types of heat pipes, in terms of their geometry, function, and the methods used to transport the working fluid from the condenser to the evaporator. Some types have become less popular such as the flat-plate heat pipe, and other types of heat pipes have become more popular because of the increasing demand for instant loop heat pipes (LHP), micro-heat pipes, and pulsating heat pipes. Among these heat pipes, LHP will be briefly discussed.

2.11.1 Loop Heat Pipes (LHP)

A loop heat pipe is an effective and efficient two-phase device with capillary pumping of fluid [48]. It could offer an advantage for solving the problem of traditional heat pipes, which is the limitation of transport capabilities over long distances. The first loop heat pipe was established in 1972 by two scientists, Gerasimov and Maydanik from the Ural Polytechnical Institute [49]. Figure 2.15 presents the basic scheme of a loop heat pipe.

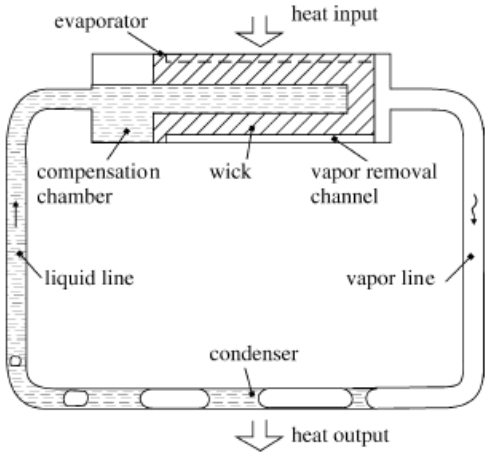

Figure 2.15: Basic scheme of LHP [2]

2.11.1.1 Studies of loop heat pipe

Wan et al. [50] studied the effect of a loop heat pipe air handling coil on the energy savings in a central air conditioning system with return air. The study was applied to an office building. By applying the loop heat pipe technology in the system, the results showed that the rate of energy savings was 23.5-25.7% for the cooling load and 38.1-40.9% for total energy consumption in the range of 22-26^{O}C indoor design and 50% relative humidity. The researchers also found that the rate of energy saving of the loop heat pipe air conditioning system increased when the indoor design temperature was increased and the indoor relative humidity was decreased.

2.12 Wickless Heat Pipe or Two-Phase Closed Thermosyphon

The difference between a wick heat pipe and a thermosyphon is that in the wick heat pipe, the working fluid is returned by capillary forces from the condenser to the evaporator, but the thermosyphon depends on gravity for the condensate liquid to return to the evaporator. Therefore, the condenser section is always above the evaporator section. A cross section of a thermosyphon is shown in Figure 2.16.

2.12.1 Overall thermal resistance in thermosyphon

The performance of a thermosyphon can be characterised by the overall thermal resistance. The overall rate of heat transfer to the system $\dot{Q}$ is proportional to the effective temperature difference between the heat source to the evaporator and the heat sink from the condenser, and inversely proportional to the equivalent thermal resistance to heat transfer between the two regions. The overall rate of heat transfer can be defined as:

$$\dot{Q} = \frac{T}{R} \tag{2-1}$$

The overall thermal resistance R is illustrated by the network of thermal resistances as shown in Figure 2.17 and can be calculated by the total sum of the thermal resistances [22,51]. The descriptions and formulas of the thermal resistances shown in Figure 2.17 are listed in Table 2-3.

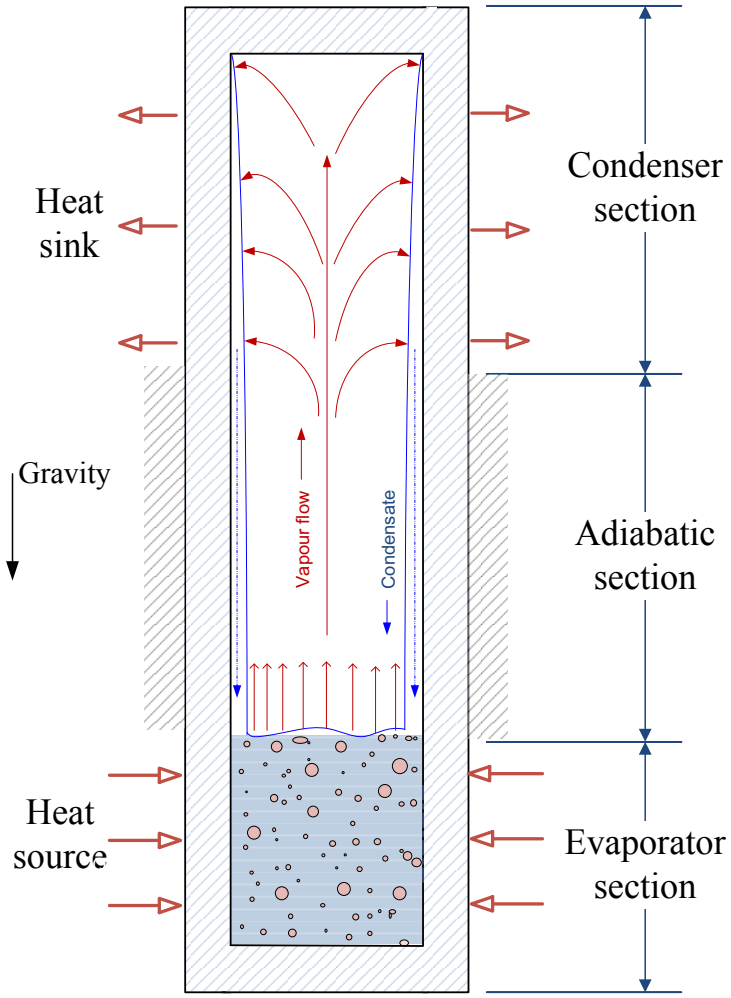

Figure 2.16: Two-phase closed thermosyphon (wickless heat pipe)

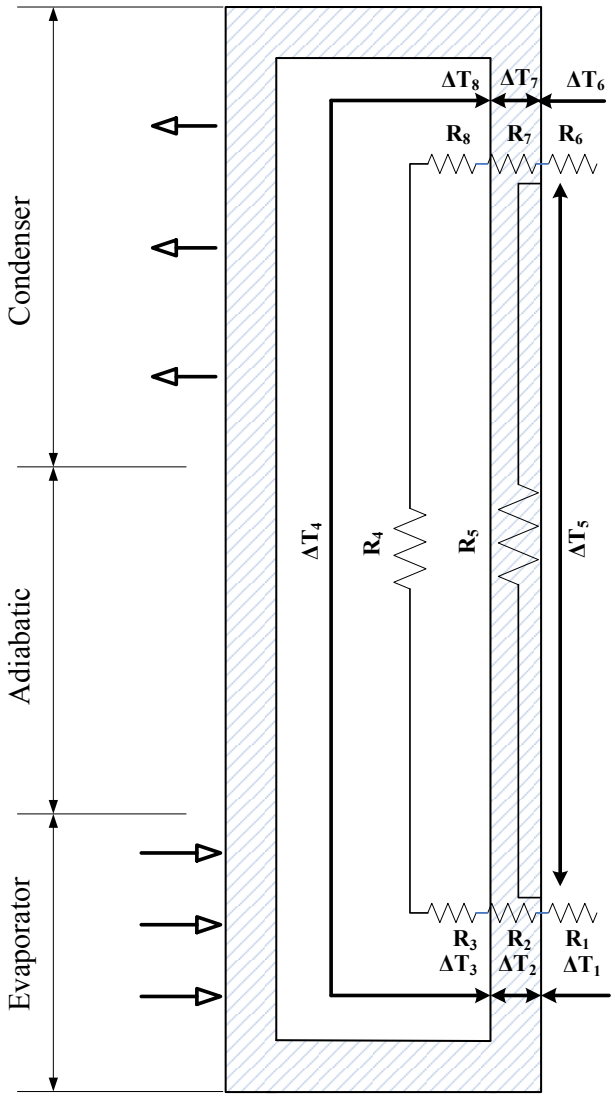

Figure 2.17: Thermosyphon thermal resistance network

Table 2-3: The descriptions and formulas of the thermal resistance network [22,51]

Description	Formula
The resistance between the evaporator external wall and the heater (R_1)	$R_1 = \frac{1}{h_{evp\_out} A_{evp\_out}}$ (2-2)
The resistance across the solid wall in the evaporator (R_2)	$R_2 = \frac{\ln(D_{out} / D_{in})}{2\ L_{evp} k_{wall}}$ (2-3)
The internal resistance of the boiling liquid (R_3)	$R_3 = \frac{1}{h_{evp\_in} A_{evp\_in}}$ (2-4)
The resistance due to the vapour pressure drop flowing from evaporator to condenser (R_4)	$R_4 = \frac{T_{sat\_evp\ con}}{\dot{Q}}$ (2-5)
The axial resistance of the wall (R_5)	$R_5 = \frac{(0.5L_{evp} + L_{adia} + 0.5L_{con})}{k_{wall} A_{wall}}$ (2-6)
The resistance between the condenser external wall and the heat sink (R_6)	$R_6 = \frac{1}{h_{con\_out} A_{con\_out}}$ (2-7)
The resistance across the solid wall in the condenser (R_7)	$R_7 = \frac{\ln(D_{out} / D_{in})}{2\ L_{con} k_{wall}}$ (2-8)
The internal resistance of the condensing liquid (R_8)	$R_8 = \frac{1}{h_{con\_in} A_{con\_in}}$ (2-9)

It should be noted that the overall thermal resistance in thermosyphons will be discussed in Chapter 3 and Chapter 5.

2.12.2 Heat transfer limitation in thermosyphon

Although thermosyphons are very effective heat transfer elements, which became increasingly applied in heat recovery systems, their performance is restricted by a number of heat transfer limitations. Different types of heat transfer limitations that may occur in a thermosyphon depend on the thermosyphon geometry, fill ratio of working fluid and radial heat input [52,53]. Among these factors, the fill ratio of working fluid has a significant influence on the thermosyphon performance.

2.12.2.1 Dry-out limit

The dry-out limit occurs when the filling ratio of the working fluid in the evaporator is not sufficient for the circulation of the condensed liquid inside the pipe. Thus, most of the falling condensed liquid from the condenser would have evaporated before reaching the liquid pool in the evaporator, causing an increase in the evaporator wall temperature. Figure 2.18 shows the process of dry-out in a thermosyphon [22,53,54].

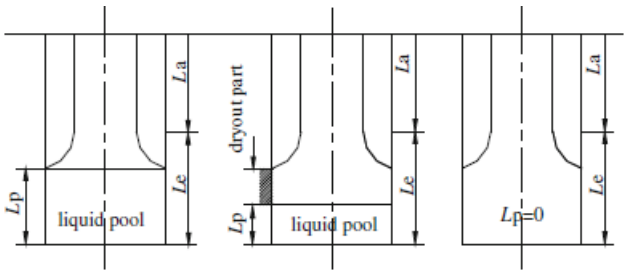

Figure 2.18: Schematic process of dry-out limitation [54]

2.12.2.2 Boiling limit

This limit occurs at relatively large fill ratios of the working fluid and high radial evaporator heat flux. In this limit, bubbles are formed in the liquid pool of the evaporator creating a film of vapour between the working fluid and the wall of the evaporator. Due to the poor thermal conductivity of the vapour film, a small amount of the heat input to the evaporator is transferred to the working fluid and the rest of the heat input is transferred to the evaporator wall, causing a sudden increment in the evaporator wall temperature. Hence, a significant reduction in the rate of heat transfer occurs in the thermosyphon [23,53].

2.12.2.3 Flooding limit

At large fill ratios of the working fluid, small radial evaporator heat flux and high axial heat flux, a high speed occurs between the liquid and vapour flows and therefore a rise in the shear stress occurs at the liquid-vapour interface. As a result, the liquid drops can be entrained from condensed liquid to vapour flow and transported again to the condenser and, consequently, prevent the condensed liquid reaching the evaporator. Therefore, the evaporator can become dry resulting in an increase in wall temperature [53,54].

2.12.3 Heat Pipe Heat Exchangers (HPHX)

Figure 2.19 introduces the basic heat pipe heat exchanger, which consists of a bank of finned heat pipes. The process of the heat pipe affects the transfer of heat from the evaporator in the duct carrying the gas, from which heat is required to be recovered, to the condenser in the duct carrying the air which is to be preheated [2].

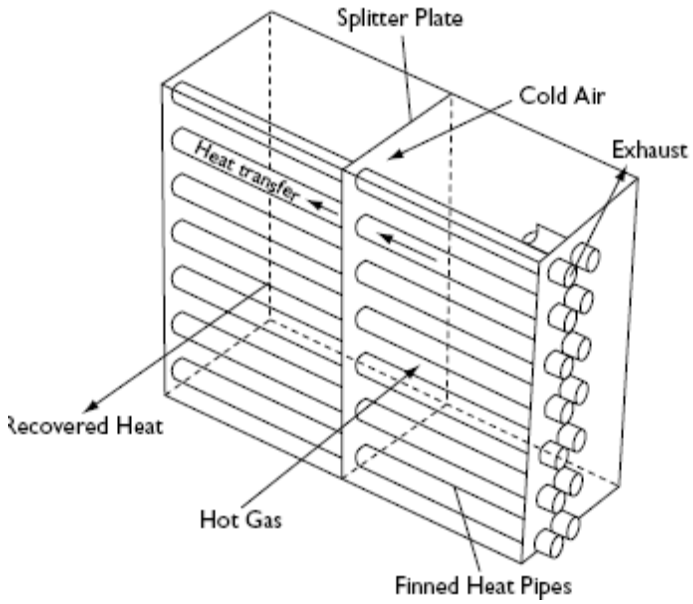

Figure 2.19: Basic heat pipe heat exchanger showing concept of heat transfer [2]

The bank of heat pipes in the heat pipe heat exchanger can be horizontal or vertical with the evaporators under the condensers. Further, the heat pipes' orientation can be adjusted as a means of controlling the heat transfer, and that concept is a positive aspect in air-conditioning applications [55].

Heat pipe heat exchangers are a useful tool in industrial heat recovery applications, and their main advantages are as follows:

- HPHX have high reliability as they have no moving parts and no external power requirements to circulate the working fluid [52,53].
- HPHX eliminate any risk of cross-contamination as the hot and cold gas streams are completely separated by a solid wall [52,53].
- HPHX provide a wide range of sizes.

- HPHX are totally reversible as they have the ability to transfer heat in both directions [2].

Heat pipe heat exchanger applications can be grouped into three categories [55] as follows:

- Heat recovery in air-conditioning applications.
- Recovery of heat from a process exhaust stream to preheat air for heating.
- Recovery of waste heat such as preheating of combustion air.

Figure 2.20 shows a heat pipe heat exchanger made by a UK company.

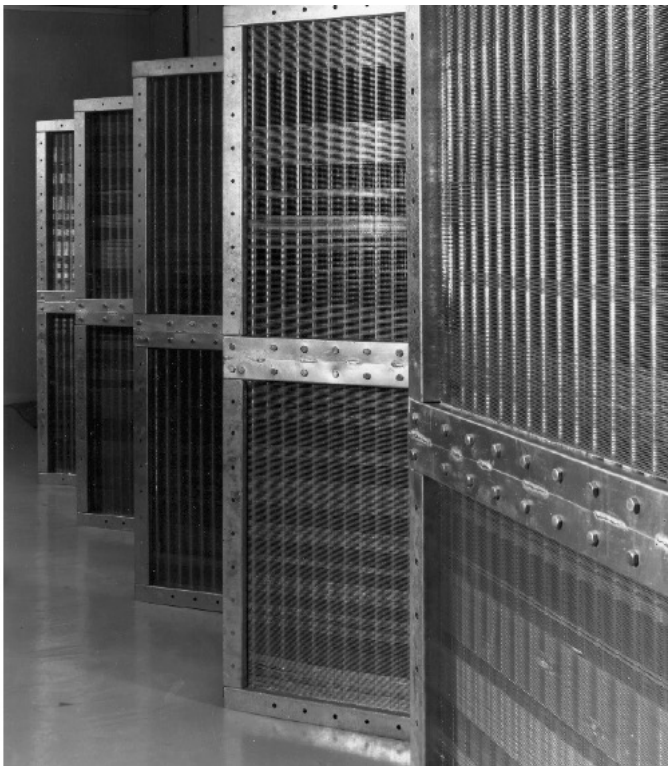

Figure 2.20: Heat pipe heat exchanger made in the UK by Thermacore Europe [2]

2.12.4 Studies of closed two-phase thermosyphons

Closed two-phase thermosyphons have received more research attention in the literature, and have been investigated experimentally by various researchers. Jouhara and Robinson [20] provided an experimental study of the performance of a small diameter thermosyphon charged with four different working fluids: water, FC-3283, FC-77 and FC-84. The authors used a copper thermosyphon that was 200 mm long with an inner diameter of 6 mm. They found that the effective thermal performance resistance and maximum heat transport capabilities of the water-charged thermosyphon were better than those of the other working fluids. They also pointed out that all of the examined Fluorinert liquids were suitable for sensitive electronics cooling applications because they were dielectric fluids. It should be noted that dielectric fluids are electrically insulating and used for cooling electronic applications.

Another investigation, presented by Jouhara and Robinson [5], was carried out to investigate a small diameter wickless heat pipe charged with environmentally sound and commercially available working fluids. The investigators used a thermosyphon 209 mm long with an inner diameter of 6 mm. They considered two working fluids, Dowtherm A and Themonol VPI, for thermosyphons with operating temperatures of between 200 ^{o}C and 450 ^{o}C. The experimental results were compared with Rohsenow's pool boiling correlation and found to be in good agreement.

Kalogirou and Papamarcou [56] used TRNSYS to model a thermosyphon solar water heating system. They validated their model by conducting simple experiments. Water temperature measurements in the storage tank were gathered by using actual weather data. They then implemented the experimental measurements in TRNSYS and carried out an economic analysis for the system. The economic analysis showed that the payback time of the system was eight years, and the present worth of life-cycle savings was £ 161.

An experimental investigation and a mathematical model were carried out by Jiao et al. [57], in which they investigated the effect of the filling ratio on the heat transfer performance of a vertical thermosyphon. The effects of the heat input, operating pressure and geometry of the thermosyphon were studied. Three types of flow patterns and two types of transition were considered in the model according to the distribution of

the liquid pool and liquid film. The results showed that the range of the filling ratio that can keep the thermosyphon steady and effective was enclosed within the upper boundary EFR (liquid pool fills entire evaporator) and the lower boundary CFR (minimum value of liquid film thickness). They also noted that unsteady violent boiling in the liquid pool was not considered.

Abreu and Colle [58] carried out an indoor experimental investigation of the transient thermal behaviour of two-phase closed thermosyphons with an unusual geometry, characterized by a semicircular condenser and a straight evaporator. The authors used an electrical skin heater to simulate the solar radiation. The length of the evaporator, fill ratio of the working fluid, cooling temperature, and evaporator slope were analysed for different heat fluxes. They also investigated the effects of these parameters on the overall thermal resistance.

A numerical study was introduced by Nayak et al. [59] to study the boiling flow instability of a reactor thermosyphon system. The researchers used the MONA code to solve the conservation equations of mass, momentum, and energy.

2.12.5 Studies of HPHX

In terms of energy management and heat recovery, applications of the loop heat pipe in order to control temperature and humidity level in conditioned spaces have been investigated by a number of researchers. The potential for energy and cost saving that can be realized through the incorporation of a wraparound heat pipe heat exchanger into the apparatus of a conventional means of dehumidification was investigated by Jouhara [11]. The author used loop heat pipe technology in the air handling unit for the purpose of energy saving. The actual weather data was recorded for Dubai where the climates are hot and humid and a year-round energy/cost analysis has been considered. The economic analysis showed that the annual energy saving was 134 MWh, and the author also reported that the cost of using the heat pipe technology was marginal compared with the cost savings. The study demonstrated that the loop heat pipe design was the most suitable for the application in terms of simplicity of incorporation, initial cost, and superiority of operation.

Another investigation, introduced by Jouhara & Meskimmon [8] carried out an experimental study on the thermal performance of a wraparound loop heat pipe heat exchanger used in air handling units for the purpose of energy savings. The investigators examined the relationship between heat pipe effectiveness and velocity of air flow through the heat exchanger. A schematic diagram of the experimental test rig reported by the authors is shown in Figure 2.21.

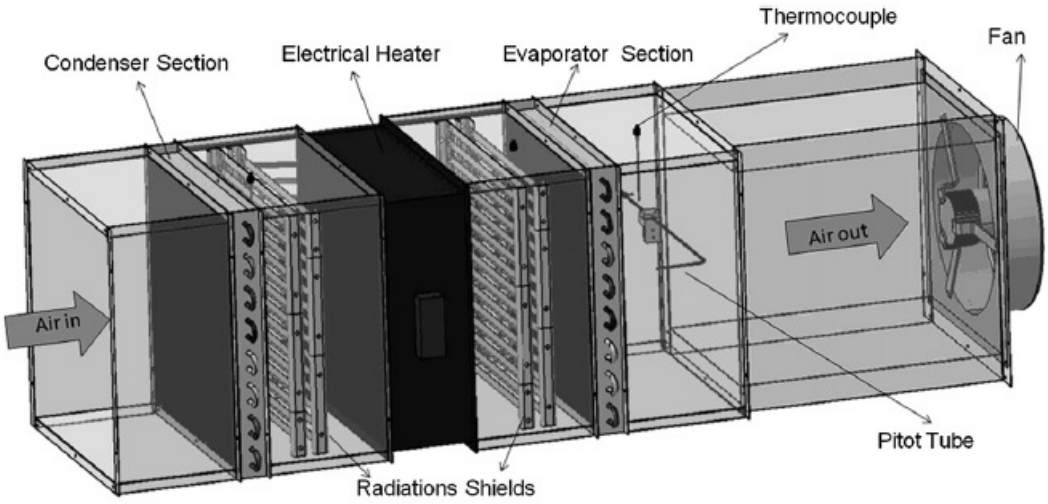

Figure 2.21: Schematic diagram of experimental test rig [8]

The heat pipe heat exchanger consisted of seven loop heat pipes charged with refrigerant R134a as the working fluid. The authors used aluminium fins in the evaporator and condenser sections. They used thermocouples in different positions to monitor the temperatures of the heat pipe surface and the air temperatures in the test duct. Six different air volume flow rates were examined for the experimental work. The economic analysis showed that, by installing the heat pipe heat exchanger in the air handling units, the total annual energy saving was 133.563 MWh.

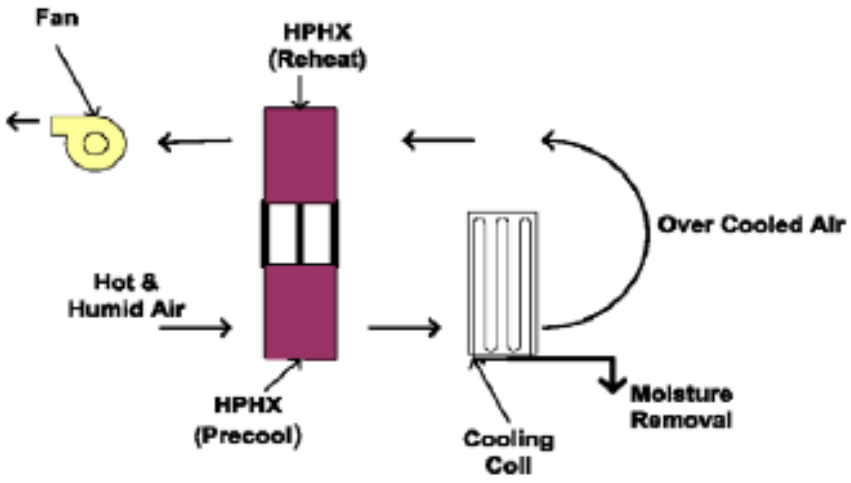

Figure 2.22: Schematic diagram for HVAC system running with HPHX [60]

An eight-row vertical thermosyphon heat pipe heat exchanger for building HVAC systems in a tropical climate was investigated experimentally by Yau [60]. The research examined the influence of three key parameters of the inlet air state: dry bulb temperature, relative humidity and air velocity in the sensible heat ratio (SHR) of the eight-row thermosyphon heat pipe heat exchanger.

Figure 2.22 illustrates the thermosyphon HPHX evaporator section as a pre-cooler and the condenser section as a reheating coil. By adding the HPHX to the HVAC system, the author found that overall the SHR of the HVAC system was decreased from 0.688 to 0.188 as the dry bulb temperature inlet for the evaporator was increased. He also found that the SHR was reduced from 0.856 to 0.188 as the relative humidity inlet for the evaporator was increased. The study demonstrated that tropical HVAC systems should be installed with heat pipe heat exchangers for dehumidification enhancement. The author recommended that the results be used to create a HPHX model by using TRNSYS.

In another research provided by Yau [61], an eight-row thermosyphon-based heat pipe heat exchanger for tropical building HVAC systems was studied with the HPHX inclined at a 30^{o} angle. The investigator analyzed whether condensates forming on the fins of the HPHX would influence its effectiveness. The results showed that the HPHX in a vertical configuration could perform equally as well as at an inclined angle. This is

because the possibly adverse influence of condensates forming on the fins of the HPHX was negligible.

In another study presented by Yau [62], a double heat pipe heat exchanger (HPHX) for reducing the energy consumption of treating ventilation air in an operating theatre located in Kuala Lumpur, Malaysia, was simulated by using the TRNSYS program. The simulation model was used to estimate the air states in addition to the entire typical meteorological year's energy consumption of the theatre. A schematic diagram for installing two heat pipe heat exchangers in the HVAC system is shown in Figure 2.23. The results showed that, through the installation of two HPHX in the HVAC system, the annual energy saving was 51 MWh. Further, the moisture removal capability (dehumidification) of the cooling coil was increased from 0.24 to 0.54. The research demonstrated that the double HPHX in the air handler unit (AHU) was suitable for application to the tropical climate, for instance in an HVAC system operating in a hospital environment.

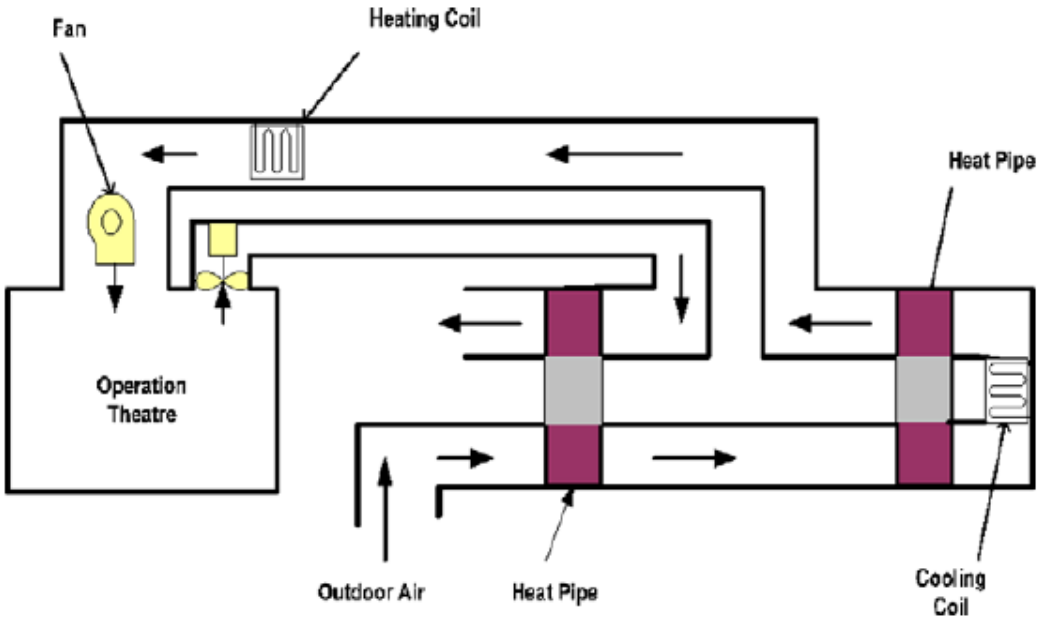

Figure 2.23: Schematic diagram of two HPHX in HVAC [62]

Riffat and Gan [63] investigated the effectiveness of a heat pipe heat exchanger for naturally ventilated buildings. The authors examined the performance of three types of heat pipe heat recovery units in a two-zone chamber with a horizontal dividing wall. The first type of heat pipe heat recovery unit was a bank of seven externally finned heat pipes; the second type was a bank of cylindrical spine fins, and the third type was made of two rows of staggered heat pipes. They used CFD to calculate the pressure loss characteristics of HPHX units. The experimental results demonstrated that air velocity had a major influence on the effectiveness of heat pipe heat recovery. The authors found that at the same velocity, the heat recovery was between 16% and 17% more efficient when double banks of heat pipes with plain fins were used than when one bank was used. They suggested that in naturally ventilated low rise buildings without the wind effect, the design's mean air velocity should be less than 1 m/s.

CHAPTER 3 BOILING AND CONDENSATION HEAT TRANSFER

~~In order to understand the modelling of two-phase heat transfer in thermosyphons, especially the determination of heat transfer coefficients (*h*) associated with boiling and condensation, it is important to discuss the physics behind the boiling that takes place in the evaporator section, as well as the condensation that takes place in the condenser section [15,21]~~.

In this chapter, theoretical calculations are performed to predict the effective overall thermal resistance associated with pool boiling in the evaporator section and liquid film condensation in the condenser section. The experimental data related to the thermal performance of the thermosyphon, which is explained in Chapter 4, have been used for the purpose of validating the theoretical calculations.

3.1 Theoretical Calculations of Boiling and Condensation

In the current study, theoretical calculations are performed to predict the effective overall thermal resistance associated with pool boiling in the evaporator section and liquid film condensation in the condenser section. The experimental data of the thermal performance of the thermosyphon have been used for the purpose of validating the theoretical calculations. The experimental apparatus and procedure carried out in this study are discussed in Chapter 4. The experimental results will also be used to validate the CFD simulations of the thermosyphon. The CFD model of this study will be discussed in detail in Chapter 5.

3.1.1 Predicted heat transfer thermal resistance of a thermosyphon

In order to predict the thermal resistances of a thermosyphon, the analogy network between electric and thermal circuit is applied for thermosyphon as presented in Figure 2.17, Chapter 2 [22,64]. In this figure, R_2 and R_7 are related to the radial heat conduction through the solid wall of the evaporator and condenser regions, respectively; R_3 is the thermal resistance associated with the evaporation, and consists of two sub regions: the pool boiling resistance and the nucleate film boiling resistance; R_8 is the

thermal resistance associated with the condensation; R_5 is related to the axial heat conduction through the solid wall of the pipe; R_4 is related to the vapour flow inside the pipe from evaporator to condenser region; R_1 and R_6 are the thermal resistances between the heat source and the external surface of the evaporator and between the external surface of the condenser and the heat sink, respectively. In addition, there are thermal resistances associated with the interface vapour-liquid, for the evaporator and condenser regions, respectively, which are usually neglected.

For simplification, the conduction thermal resistance in the axial direction along the thermosyphon wall is negligible. The thermal resistance due to the pressure drop of the vapour as it flows from evaporator to condenser is not considered as it is assumed there is no drop in the saturation temperature between the evaporator and condenser. The thermal resistance of the radial heat conduction through the thickness of the evaporator and condenser wall is very small, so it is neglected. Since a uniform heat flux has been presented in the evaporator and condenser walls, the thermal resistances associated with the external surface are not considered.

Based on the above discussion, the predicted overall thermal resistance of the thermosyphon (R_{HP}) consists of the thermal resistance associated with the evaporation in the evaporator section (R_e) and the thermal resistance associated with the condensation in the condenser section (R_c) as these two sections are thermally in series, thus:

$$R_{HP} = R_3 + R_8 = R_e + R_c \tag{3-1}$$

It is important to note that the thermal resistances associated with the evaporation and condensation processes are determined with the use of empirical correlations for the heat transfer coefficient obtained from the literature, as discussed in the next sections.

3.1.1.1 Correlations of predicted heat transfer thermal resistance in the evaporator

As a result of circulation of the working fluid in a closed thermosyphon, complex fluid flow and heat transfer behaviours occur in the evaporator section, particularly nucleate boiling heat transfer in the pool and liquid film regions [33,65]. The internal thermal

resistance of the evaporator section consists of the thermal resistance of both the nucleate pool boiling in the liquid pool and the nucleate film boiling in the thin liquid film.

In order to determine the evaporator thermal resistance, the internal heat transfer coefficient (h_{NPB}) of the nucleate pool boiling is calculated and then the following expression is used to determine the evaporator internal thermal resistance:

$$R_e = \frac{1}{h_{NPB} \cdot A_e} \tag{3-2}$$

where A_e is the surface area of the evaporator, calculated as:

$$A_e = \pi D_e l_e \tag{3-3}$$

where D_e is the evaporator internal diameter and l_e is the evaporator length.

No set of theoretical correlations has been developed to determine the nucleate pool boiling heat transfer coefficient in thermosyphons. However, some correlations have been developed experimentally by several researchers for nucleate boiling in thermosyphons [20,66-70]. According to Rohsenow [67], the correlation used to calculate the nucleate pool boiling heat transfer coefficient (h_{NPB}) in the evaporator section is:

$$h_{NPB} = \frac{q^{2/3}}{\frac{C_{sf} h_{fg}}{C_{pl}} \left\{ \frac{1}{h_{fg} \mu_l} \left(\frac{\sigma}{g[\rho_l - \rho_v]} \right)^{1/2} \right\}^{0.33} Pr_l^n} \tag{3-4}$$

Meanwhile, the correlation produced by Shiraishi et al. [68] to predict the boiling heat transfer coefficient in the evaporstor section is:

$$h_{NPB} = 0.32 \left(\frac{\rho_l^{0.65} {k_l}^{0.3} C_{pl}^{0.7} g^{0.2} q^{0.4}}{\rho_v^{0.25} h_{fg}^{0.4} \mu_l^{0.1}} \right) \left(\frac{P_v}{P_{atm}} \right)^{0.23} \tag{3-5}$$

where P_v is the vapour pressure and P_{atm} is the atmospheric pressure.

According to Labuntsov [69], the correlation used to calculate the evaporator heat transfer coefficient in the region of the liquid pool is:

$$h_{NPB} = 0.075\left(1 + 10\left(\frac{\rho_v}{\rho_l - \rho_v}\right)^{0.67}\right)\left(\frac{k_l^2}{v_l \sigma T_{sat}}\right)^{0.33} (q)^{0.67} \quad (3\text{-}6)$$

where k_l is the thermal conductivity of the liquid and v_l is kinematic viscosity of the liquid, while the correlation introduced by Kruzhilin [70] is:

$$h_{NPB} = 0.082\left(\frac{h_{fg}\, q}{gT_{sat}k_l}\frac{\rho_v}{\rho_l - \rho_v}\right)^{0.7}\left(\frac{C_{pl}\sigma\rho_l T_{sat}}{\rho_v^2 h_{fg}^2}\right)^{0.33}\left(\frac{1}{[\sigma/g(\rho_l - \rho_v)]^{0.5}}\right)^{0.33}\left(\frac{k_l}{[\sigma/g(\rho_l - \rho_v)]^{0.5}}\right)(Pr_l)^{-0.4} \quad (3\text{-}7)$$

Other researchers [71,72] reported additional correlations, as follows:

Imura's correlation [71]

$$h_{NPB} = 0.32\left(\frac{\rho_l^{0.65} k_l^{0.3} C_p^{0.7} g^{0.2} q^{0.4}}{\rho_v^{0.25} h_{fg}^{0.4} \mu_l^{0.1}}\right)\left(\frac{P_v}{P_{atm}}\right)^{0.3} \quad (3\text{-}8)$$

Kutateladze's correlation [72]

$$h_{NPB} = 0.44\left(\frac{1x10^{-4}\, qP_v}{gh_{fg}\rho_v\mu_l}\frac{\rho_l}{\rho_l - \rho_v}\right)^{0.7}\left(\frac{k_l}{\left(\sigma/g\left(\rho_l - \rho_v\right)\right)^{0.5}}\right)(Pr_l)^{0.35} \quad (3\text{-}9)$$

Jouhara and Robinson [20] compared the above correlations [67-72] with experimental results for a two-phase closed thermosyphon charged with water, as well as FC-3283, FC-77 and FC-84, and found that the Labuntsov's correlation best matched the data reported for the thermosyphon over the range of heat fluxes examined. In particular, of all the correlations tested, Labuntsov's correlation shows the best agreement with the experimental measured data for low and high thermal resistance levels for water-charged thermosyphon. Other correlations under-predict the experimental measurements for low thermal resistances and over-predict the measurements for high thermal resistances.

The above correlations, which are developed specifically for nucleate pool boiling in thermosyphons, are listed in Table 3-1.

Table 3-1: Nucleate pool boiling heat transfer coefficient correlations

Author	Correlation (h_{NPB})	
Rohsenow's correlation [67]	$\frac{q^{2/3}}{\frac{C_{sf}h_{fg}}{C_{pl}}\left\{\frac{1}{h_{fg}\mu_l}\left(\frac{\sigma}{g[\rho_l-\rho_v]}\right)^{1/2}\right\}^{0.33} Pr_l^n}$	(3-4)
Shiraishi's correlation [68]	$0.32\left(\frac{\rho_l^{0.65}k_l^{0.3}C_{pl}^{0.7}g^{0.2}q^{0.4}}{\rho_v^{0.25}h_{fg}^{0.4}\mu_l^{0.1}}\right)\left(\frac{P_v}{P_{atm}}\right)^{0.23}$	(3-5)
Labuntsov's correlation [69]	$0.075\left(1+10\left(\frac{\rho_v}{\rho_l-\rho_v}\right)^{0.67}\right)\left(\frac{k_l^2}{v_l\sigma T_{sat}}\right)^{0.33}(q)^{0.67}$	(3-6)
Kruzhilin's correlation [70]	$0.082\left(\frac{h_{fg}\,q}{gT_{sat}k_l}\frac{\rho_v}{\rho_l-\rho_v}\right)^{0.7}\left(\frac{C_{pl}\sigma\rho_l T_{sat}}{\rho_v^2 h_{fg}^2}\right)^{0.33}\left(\frac{1}{[\sigma/g(\rho_l-\rho_v)]^{0.5}}\right)^{0.33}\left(\frac{k_l}{(\sigma/g(\rho_l-\rho_v))^{0.5}}\right)(Pr_l)^{-0.45}$	(3-7)
Imura's correlation [71]	$0.32\left(\frac{\rho_l^{0.65}k_l^{0.3}C_p^{0.7}g^{0.2}q^{0.4}}{\rho_v^{0.25}h_{fg}^{0.4}\mu_l^{0.1}}\right)\left(\frac{P_v}{P_{atm}}\right)^{0.3}$	(3-8)
Kutateladze' s correlation [72]	$0.44\left(\frac{1x10^{-4}\,qP_v}{gh_{fg}\rho_v\mu_l}\frac{\rho_l}{\rho_l-\rho_v}\right)^{0.7}\left(\frac{k_l}{(\sigma/g(\rho_l-\rho_v))^{0.5}}\right)(Pr_l)^{0.35}$	(3-9)

For nucleate liquid film boiling, Nusselt's theory of filmwise condensation on a vertical flat plate can be applied to predict the average heat transfer coefficient of the nucleate liquid film boiling (h_{NFB}) [20] using the following expression;

$$h_{NFB} = 0.707\left(\frac{\rho_l(\rho_l-\rho_v)gk_l^3h_{fg}}{\mu_l(T_v-T_c)l_c}\right)^{\frac{1}{4}} \quad (3\text{-}10)$$

3.1.1.2 Correlations of predicted heat transfer thermal resistance in the condenser

The thermal resistance of the condenser section (R_c) is determined by calculating the heat transfer coefficient of the liquid film condensation (h_{film}) and then using the following expression:

$$R_c = \frac{1}{h_{film}\,.A_c} \quad (3\text{-}11)$$

where A_c is the surface area of the condenser, calculated as:

$$A_c = \pi D_c l_c \tag{3-12}$$

where D_c is the condenser internal diameter and l_c is the condenser length.

Filmwise condensation occurs at the condenser section of a closed thermosyphon. For Reynolds numbers of the liquid film in the laminar flow regime [22], a theoretical correlation was derived by Nusselt for average heat transfer coefficient in film condensation on a vertical plate is applied [20,33,65]. This correlation is as follows:

$$h_{film_{Nusselt}} = 0.943 \left\{ \frac{h_{fg} \rho_l g {k_l}^3 (\rho_l - \rho_v)}{\mu_l l_c (T_v - T_c)} \right\}^{\frac{1}{4}} \tag{3-13}$$

where T_v is the temperature of the saturated vapour, which is taken as the wall temperature of adiabatic, and T_c is the temperature of the condenser wall.

Filmwise condensation has also been studied experimentally for vertical two-phase closed thermosyphons. Hashimoto and Kaminaga [73] reported the correlation they used to model the condensation heat transfer coefficient, which is as follows:

$$h_{film} = 0.802 \, {Re_{film}}^{0.1} \, exp\left\{ -6.7x10^{-5} \left(\frac{\rho_l}{\rho_v} \right) - 0.6 \right\} x \, h_{film_{Nusselt}} \tag{3-14}$$

Jouhara & Robinson [20] performed a regression analysis using Hashimoto and Kaminaga's correlation to produce a correlation for the heat transfer coefficient as follows:

$$h_{film} = 0.802 \, {Re_{film}}^{0.1} \, exp\left\{ -6.7x10^{-5} \left(\frac{\rho_l}{\rho_v} \right) - 0.14 \right\} x \, h_{film_{Nusselt}} \tag{3-15}$$

The previous correlations are summarised in Table 3-2.

Table 3-2: Liquid film condensation heat transfer coefficient correlations

Author	Correlation (h_{film})
Nusselt's correlation [20]	$0.943 \left\{\frac{h_{fg}\rho_l g {k_l}^3(\rho_l-\rho_v)}{\mu_l l_c(T_v-T_c)}\right\}^{1/4}$ (3-13)
Hashimoto's correlation [73]	$0.802\ {Re_{film}}^{0.1}\ exp\left\{-6.7x10^{-5}\left(\frac{\rho_l}{\rho_v}\right)-0.6\right\}\ x\ h_{film_{Nusselt}}$ (3-14)
Jouhara's correlation [20]	$0.802\ {Re_{film}}^{0.1}\ exp\left\{-6.7x10^{-5}\left(\frac{\rho_l}{\rho_v}\right)-0.14\right\}\ x\ h_{film_{Nusselt}}$ (3-15)

The procedure of comparing the above correlations for predicting the heat transfer coefficients associated with pool boiling in the evaporator section and film condensation in the condenser section with the experimental measurements will be explained in the next section.

3.2 Theoretical Calculations Validation

Theoretical calculations are performed to predict the effective overall thermal resistance associated with pool boiling and liquid film condensation. The experimental results of the thermal resistance have been used to validate the theoretical calculations. The correlations described in the previous sections for predicting the heat transfer coefficients associated with pool boiling in the evaporator section, listed in Table 3-1, and film condensation in the condenser section, listed in Table 3-2, are used to compare with the experimental data. Then, the characteristics of the thermal performance of the working fluids, namely water, R134a and R404a are compared using Eq. (3-1).

The relevant physical properties of the working fluids such as the density of the liquid ρ_l and vapour phase ρ_v, thermal conductivity of the liquid phase k_l, surface tension σ, specific heat of the liquid phase C_{Pl} and dynamic viscosity of the liquid phase μ_l are fitted into functions of temperature in the form of high-order polynomials, as shown by

$$Y(T) = \sum_{i=0}^{n=6} C_i\ .\ T^i \tag{3-16}$$

where *C* is the physical properties coefficients and *Y(T)* is the physical property.

A 6th order polynomial has been used to describe the physical properties. The data source of the physical properties of the working fluids is the NIST REFPROP program [74] and Table 3-3 has been provided to present the coefficients in Eq. (3-16) of all physical properties of the working fluids used in the correlations.

Table 3-3: Physical properties coefficients of Eq. (3-16) for the working fluids

R134a							
Temperature Range (193.15 – 370.15 K)							
Y(T)	C_0	C_1	C_2	C_3	C_4	C_5	C_6
ρ_l	3952.80165	-25.9914729	0.09482745	-1.2904E-04	0	0	0
ρ_v	32208.2368	-440.625398	2.25653915	-0.00513332	4.386E-06	0	0
C_{Pl}	60790.2103	-1191.47206	9.9247559	-0.04417109	1.1088E-04	-1.489E-07	8.366E-11
k_l	0.29569779	-0.00124086	2.5284E-06	-2.62E-09	0	0	0
μ_l	0.02538293	-0.00031338	1.483E-06	-3.1464E-09	2.507E-12	0	0
σ	0.04929242	-8.3485E-05	-3.9522E-07	7.0711E-10	0	0	0
h_{fg}	876230.5681	-6951.1566	26.2489	-0.03613503	0	0	0
R404a							
Temperature Range (230 – 340 K)							
Y(T)	C_0	C_1	C_2	C_3	C_4	C_5	C_6
ρ_l	-23723.1556	380.3528019	-2.14135611	0.005318375	-4.9654E-06	0	0
ρ_v	633721.7339	-13943.7975	127.5225882	-0.62051790	0.00169450	-2.462E-06	1.488E-09
C_{Pl}	39077454.02	-855080.092	7773.868807	-37.5856296	0.10192853	-1.470E-04	8.818E-08
k_l	0.987502394	-0.01176052	5.99537E-05	-1.4041E-07	1.23327E-10	0	0
μ_l	0.004578005	-3.9165E-05	1.18505E-07	-1.2476E-10	0	0	0
σ	0.031213813	7.10867E-05	-9.8202E-07	1.48539E-09	0	0	0
h_{fg}	- 156245458	3444577.407	-31507.4895	153.31432	- 0.4186728	0.00060845	-3.677E-07
Water							
Temperature Range (247.15 – 499.15 K)							
Y(T)	C_0	C_1	C_2	C_3	C_4	C_5	C_6
ρ_l	717.8565500	2.393232923	-0.00572608	2.794E-06	0	0	0
ρ_v	64.82116603	-0.82278540	0.003953797	-8.5492E-06	7.03911E-09	0	0
C_{Pl}	10730.91329	-68.4392134	0.269993767	-0.00048293	3.36345E-07	0	0
k_l	-2.09036300	0.021701761	-6.4525E-05	8.87081E-08	-4.9257E-11	0	0
μ_l	0.997984244	-0.01487354	9.23461E-05	-3.0523E-07	5.65978E-10	-5.578E-13	2.282E-16
σ	0.083433652	1.04637E-04	-5.7238E-07	3.104E-10	0	0	0
h_{fg}	3341285.876	-4428.00355	7.952601452	-0.01510904	2.15849E-05	-2.396E-08	0

3.2.1 R134a-charged thermosyphon

In the following sub-sections, a thermosyphon charged with R134a filling the total volume of the evaporator section is theoretical examined to develop an understanding of how to predict the thermal resistance associated with pool boiling and liquid film condensation.

3.2.1.1 Pool boiling heat transfer

As mentioned earlier, no set of correlations has been theoretically developed to determine the heat transfer coefficient of the nucleate pool boiling in thermosyphons. Instead, it is general practice to choose one or more correlation for the nucleate pool boiling heat transfer coefficients proposed by some researchers [67-72] and compare them with the experimental measurements. Therefore, the empirical correlations stated in Table 3-1 have been applied to select one correlation to compare with the experimental measurements. The selected correlation to determine the heat transfer coefficient for pool boiling is then used to determine the predicted thermal resistance (R_e) in the evaporator section using Eq. (3-2).

The experimental measurements shown in Figure 3.1 come from the experimental data explained in Chapter 4. Figure 3.1 shows a comparison between the experimentally measured and the predicted thermal resistance values for different pool boiling heat transfer coefficient correlations (h_{NPB}). The experimental thermal resistance for the evaporator section is determined using the following expression;

$$R_{e,Expr} = \frac{T_{e,av} - T_v}{\dot{Q}} \tag{3-17}$$

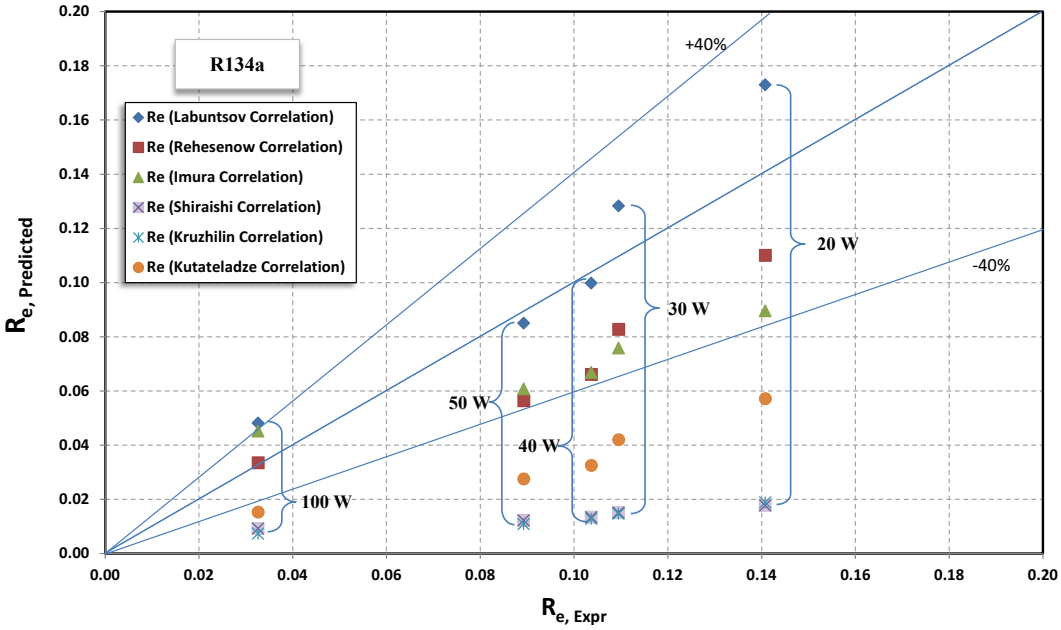

Figure 3.1: Predicted and experimentally determined thermal resistance in the evaporator section for R134a-filled thermosyphon

From the figure, it seems that the predictions and experiments show reasonable agreement with most of the points being within the range of ± 40%. The Shiraishi's, Kruzhilin's and Kutateladze's correlations under-predict the experimental measurements when the thermal resistance is low. For lower heating power loads, these correlations give high thermal resistance, thus the agreement is worsened.

The Rohsenow's correlation shows good agreement with the experimental measurements but for the lowest thermal resistance. For high thermal resistance, Rohsenow's and Imura's correlations still agree well with the experimental data. It should be noted that the constants $C_{s,f}$ and n in the Rohsenow's correlation are taken as 0.013 and 1, respectively [4], for R134a-copper combination. The Labuntsov's correlation is selected for the determination of the pool boiling heat transfer coefficient as it shows the best agreement over the tested range of heating power loads.

3.2.1.2 Film condensation heat transfer

As liquid film condensation heat transfer appears in the condenser section, the theoretical and empirical correlations to determine the film heat transfer coefficient (h_{film}), stated in Table 3-2, have been examined by a relation between Nusselt number (Nu) and the film Reynolds number (Re_{film}) [20], defined as,

$$Nu = \frac{h_{film}\, l_c}{k_l} \tag{3-18}$$

$$Re_{film} = \frac{4\,\dot{Q}}{\pi D \mu_l h_{fg}} \tag{3-19}$$

The experimental film heat transfer coefficients are determined using the following expression;

$$h_{film_{Expr}} = \frac{\dot{Q}}{A_c\,(T_v - T_{c,av})} \tag{3-20}$$

where $\dot{Q}$ is the power throughput .

The selected correlation to determine the heat transfer coefficient for film condensation is then used to determine the predicted thermal resistance (R_c) in the condenser section using Eq. (3-11).

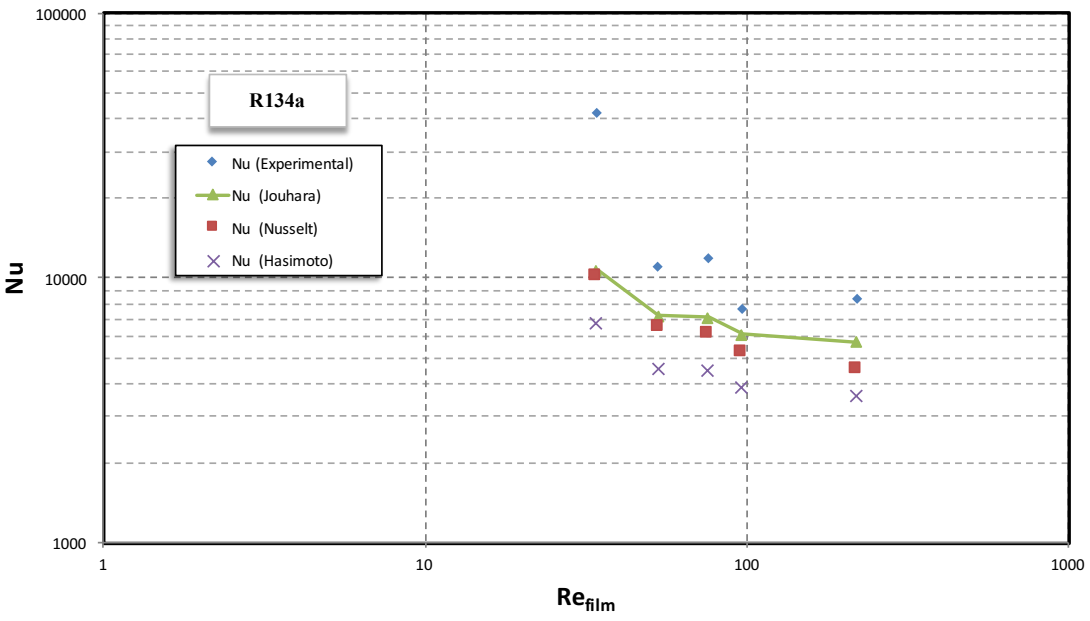

Figure 3.2: Predicted and experimentally determined Nusselt number for the condenser section for R134a-filles thermosyphon

Figure 3.2 illustrates a comparison between the experimental and predicted film heat transfer coefficients for the condenser section. As can be seen from the figure, Jouhara and Nusselt predicted heat transfer correlations are both close to the experimental heat transfer coefficients. In particular, the agreement with Jouhara's correlation is ~~quite~~ good.

3.2.1.3 Overall thermal resistance

After examining different correlations to predict the heat transfer coefficients for pool boiling in the evaporator section and film condensation in the condenser section, the selected correlations are used to determine the predicted overall thermal resistance of the thermosyphon, based on the discussion in Section 3.1.1, by adding the predicted thermal resistances of the evaporator (R_e), Eq. (3-2) and condenser (R_c), Eq. (3-11) sections using Eq. (3-1), as follows:

$$R_{HP} = \frac{1}{h_{NPB} \,.\, A_e} + \frac{1}{h_{film} \,.\, A_c} \tag{3-21}$$

For clarification, the selected correlations used in the above expression are Labuntsov's correlation for determining the predicted pool boiling heat transfer coefficient (h_{NPB}) and Jouhara's correlation for determining the predicted film condensation heat transfer coefficient (h_{film}).

The experimental overall thermal resistance of the thermosyphon is determined using the following expression;

$$R_{EXP} = \frac{T_{e,av} - T_{c,av}}{\dot{Q}} \tag{3-22}$$

The correlations and the experimental overall thermal resistance for the thermosyphon for the R134a-charged thermosyphon are plotted in Figure 3.3; from this figure, it is evident that the agreement between them is very good.

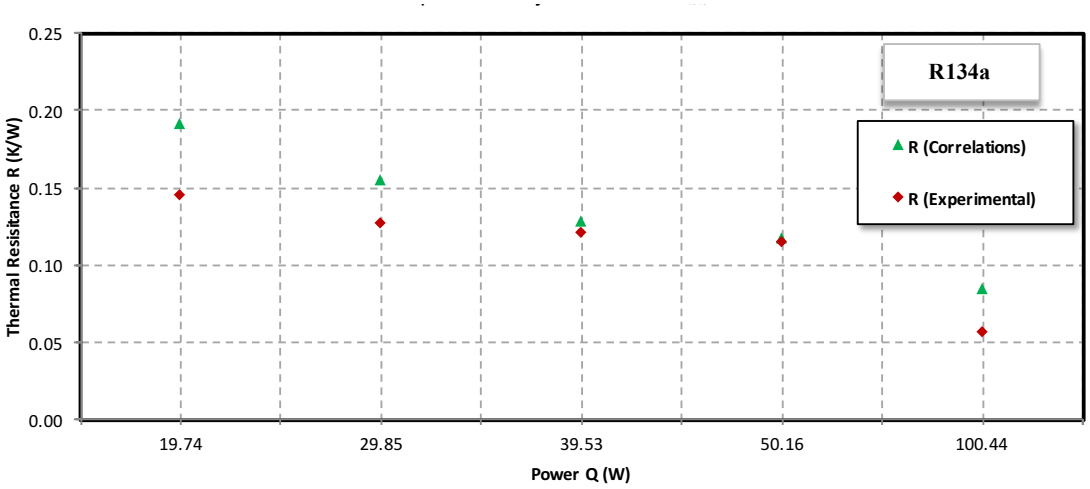

Figure 3.3: Predicted and experimental thermal resistance values for the thermosyphon charged with fill ratio of 1.0 of R134a

3.2.2 R404a and water charged thermosyphon

The selected correlations, for a thermosyphon charged with R134a, to predict the heat transfer coefficients for pool boiling in the evaporator and for film condensation in the condenser section are also used for the other working fluids, namely R404a and water.

Figure 3.4 illustrates the correlations and experimental overall thermal resistance for the thermosyphon charged with the refrigerant R404a, Figure 3.4 (a), as well as water, Figure 3.4 (b). It should be noted that for the thermosyphon charged with water, the fill ratio is 0.5. As a result, the evaporator section consists of the thermal resistance of both the nucleate pool boiling occurring in the liquid pool as well as the nucleate film boiling occurring in the thin liquid film. The correlation of Nusselt is used to predict the heat transfer coefficient for the nucleate film boiling.

It is apparent from Figure 3.4 (b) that the thermal resistance for water is under predicted, especially for the heat load of 100 W. It is thus suggested that suppressed activity of the nucleate boiling, in the experiment, that takes place in the evaporator is the main cause of the deteriorating thermal resistance with decreasing the power loads. Apart from that issue, the selected correlations showed they are capable of reproducing the trend of data for predicting the pool boiling and film condensation in the thermosyphon charged with R404a and water.

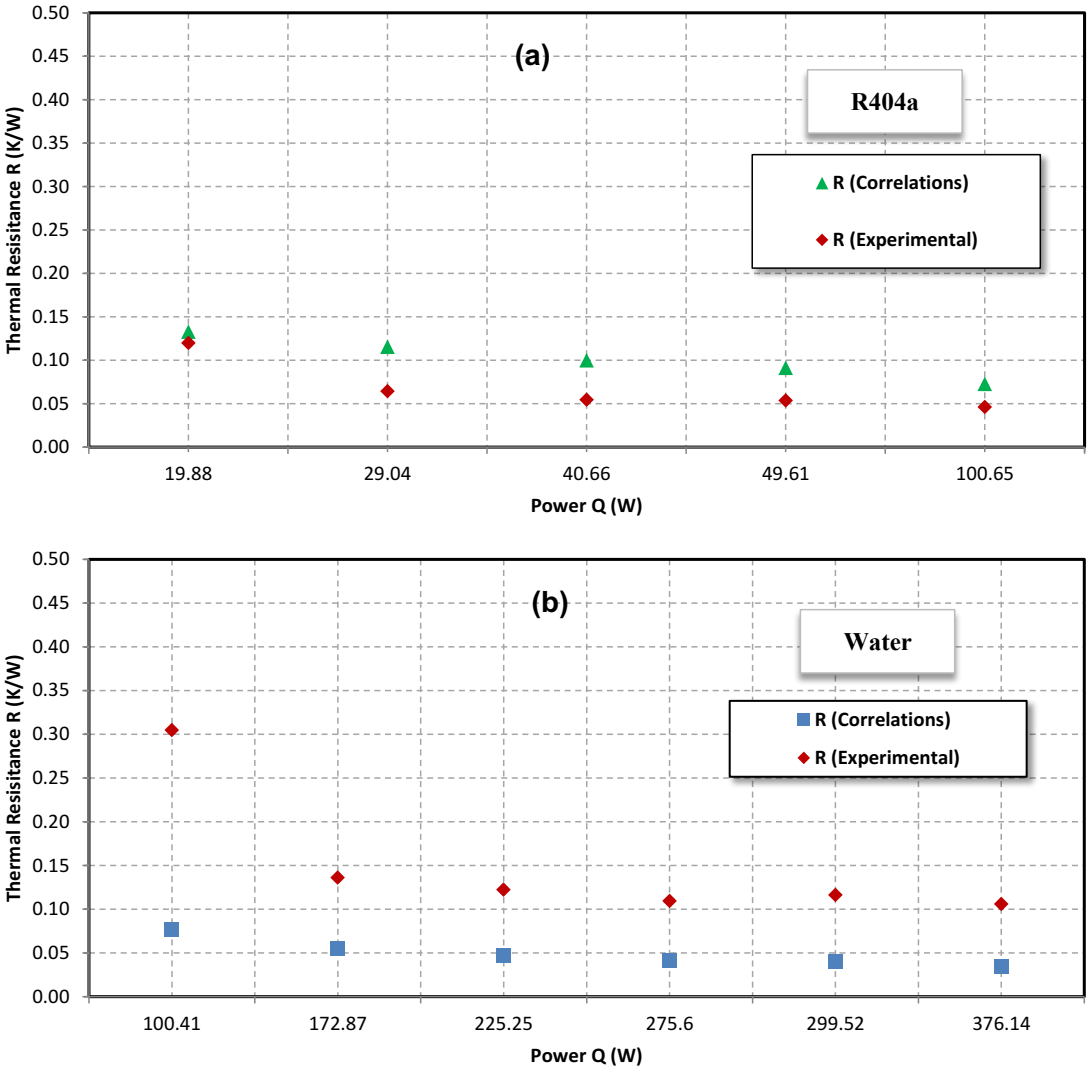

Figure 3.4: Predicted and experimental thermal resistance values for the thermosyphon charged with fill ratio of 1.0 of R404a (a) and 0.5 of water (b)

CHAPTER 4 EXPERIMENTAL PROCEDURE

In order to validate the CFD findings, an experimental apparatus was built to carry out a thermal performance investigation on a typical wickless heat pipe. A set of experiments have been carried out for the purpose of validating the theoretical calculations, as described in Chapter 3. Thus, for the purpose of this study, the experimental results will also be used to validate the CFD simulations of the thermosyphon, as discussed in Chapter 5, in order to assess the accuracy of the simulation results.

The experimental apparatus and procedure will be the same for the different working fluids. Thus, only one of the working fluids will be discussed below, which is a water-charged thermosyphon. The experimental procedure for the water-charged thermosyphon has been published in [75].

4.1 Experimental Apparatus

The experimental apparatus is shown in Figure 4.1. The apparatus consists of a two-phase closed thermosyphon (TPCT), a rope heater, the cooling water circuit, and instrumentation. The apparatus was fixed on a framework to insure vertical orientation under all test conditions.

As can be seen in Figure 4.2, the thermosyphon was manufactured with a 22mm outer diameter, 500mm-long smooth copper tube with a wall thickness of 0.9mm. It contains a 200mm-long evaporator section, a 100mm-long adiabatic section and a 200mm-long condenser section.

The evaporator section was heated by a rope heater with a maximum power output of 500 W at 220V, which was evenly wrapped and not directly positioned above any of the thermocouples that are used to measure the surface temperature of this section. The energy output of the heater was controlled by a variac, which is a variable voltage transformer used to control the supplied electrical power to the evaporator heater. The evaporator section was wrapped in a layer of fire-proof insulation before it was wrapped with suitable thermal insulation layers to reduce any heat losses to the ambient. The evaporator and adiabatic sections were wrapped with several layers of high-temperature thermal ceramic insulation to certify that no heat energy interactions take place with the

ambient. The condenser section was cooled using a double pipe concentric heat exchanger with an insulated outer surface using layers of thermal ceramic insulation. The insulated adiabatic section wall temperature was used as an indicator of the thermosyphon working temperature. The thermosyphon was charged with water.

The cooling water circuit provided the condenser's heat exchanger with the cooling fluid at predefined conditions for the inlet temperature and flow velocity. A constant-head water circuit was used to supply the water in order to provide constant mass flow rate through the heat exchanger of the condenser section. A chilled water coil was used to remove the heat from the water leaving the condenser's heat exchanger before it was returned to the main reservoir using a dedicated pump, as can be seen in Figure 4.1. A proportional-integral-derivative control system (PID) was used to control the chiller system to ensure water supply at the heat exchanger inlet was constant throughout the testing programme. A flow meter and a valve arrangement were used to control and measure the inlet volume flow rate into the shell of the heat exchanger.

The experimental apparatus was equipped with calibrated instrumentations to measure the power throughputs, temperatures and flow rate data.

The temperature distribution along the thermosyphon surface was observed using eight thermocouples. As shown in Figure 4.1, two thermocouples, labelled as Te_1 and Te_2, were used to monitor the evaporator section and were placed 40mm and 160mm from the bottom. Another thermocouple, labelled as Ta, was positioned at the centre of the adiabatic section, while the condenser section was monitored using five, evenly spaced, thermocouples, labelled as Tc_1 to Tc_5. These five thermocouples were also used to confirm the non-existence of non-condensable gases (NCGs) within the heat pipes throughout the conducted tests. The presence of NCGs would block a portion at the top region of the condenser section as a result of NCGs being be swept by the vapour toward the top area of the condenser section. In this case, the effective condenser length would be decreased, and thus the thermal resistance would be increased. Two additional thermocouples were also used to observe the input and the output water temperatures from the condenser's heat exchanger, labelled as $T_{w,inlet}$ and $T_{w,outlet}$. These two thermocouples were stainless steel shielded and were positioned at the centre of the flow using two compression fittings.

The thermocouples were K-type (NiCr/NiAl). DataScan system with 32-channel was used to read and monitor the thermocouples and was connected to a dedicated PC for an online data recording at 1Hz scanning frequency. An inline flow meter was used to measure the cooling water flow rate.

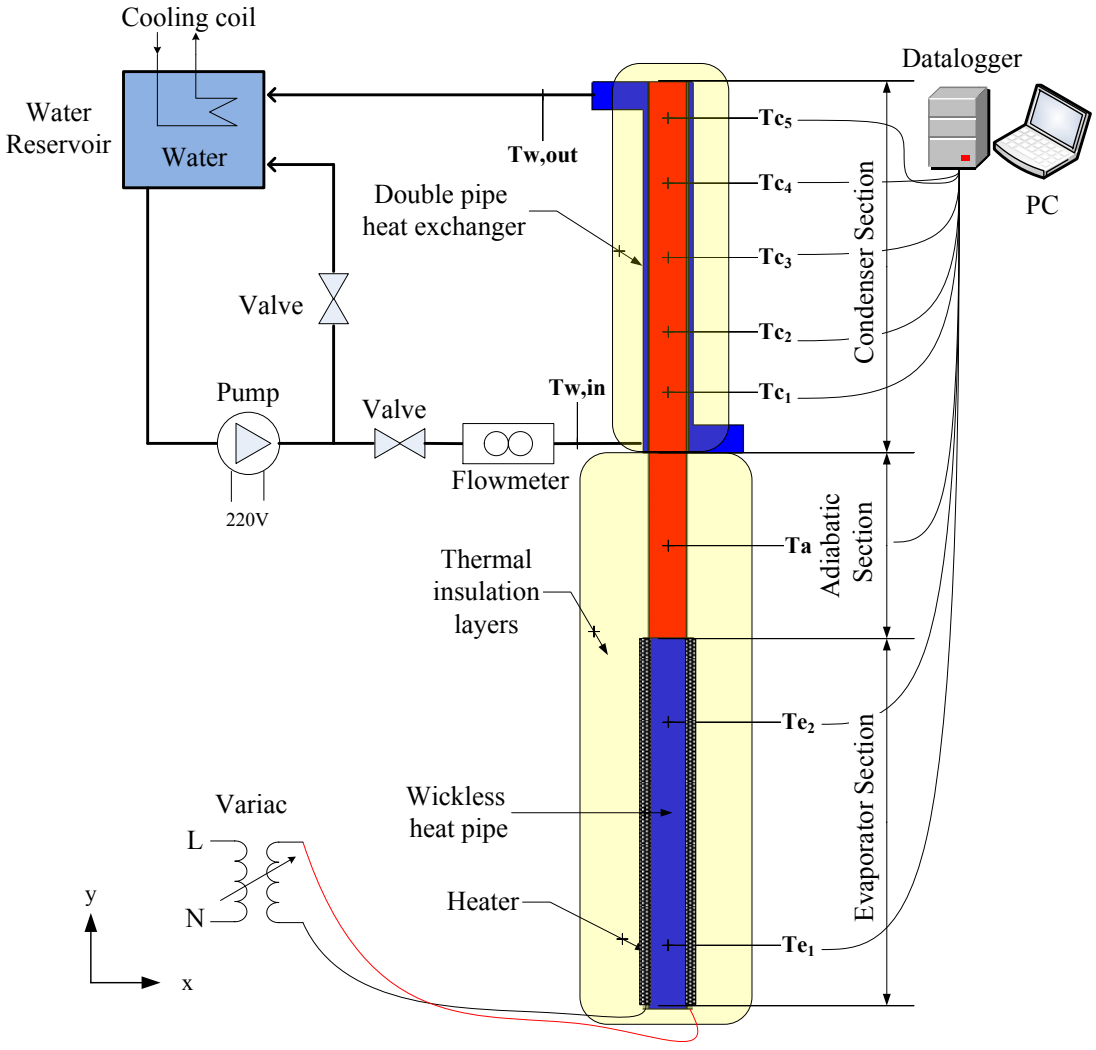

Figure 4.1: The experimental apparatus

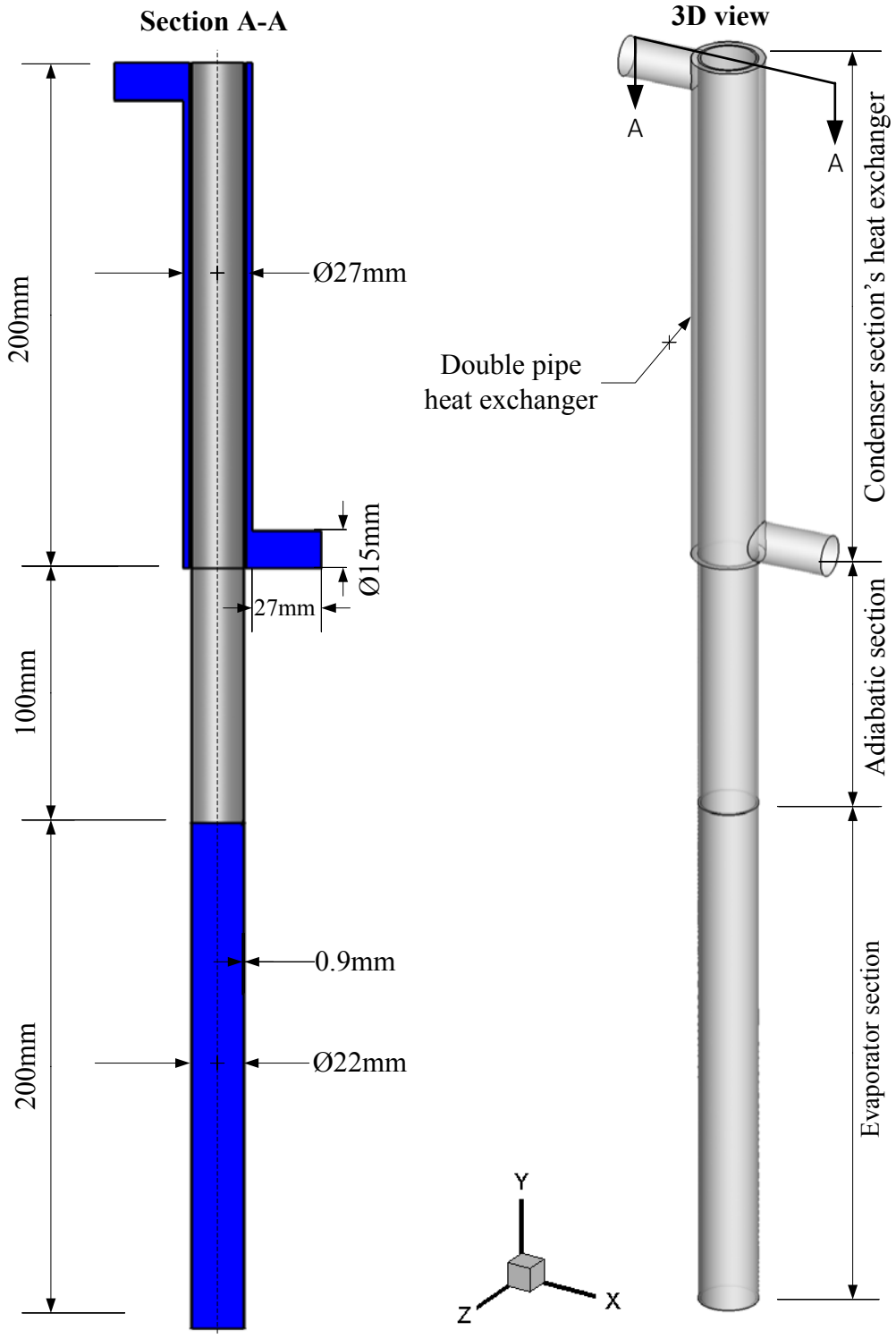

Figure 4.2: Three-dimensional view and cross-section of tested TPCT

4.2 Experimental Procedure

At the start of each experiment, and after fixing the water flow rate to the desired value, the electrical heat input was set at a level of 50 W. Before any readings were taken, the equipment was given 30 minutes in order to reach steady state, when all the energy was dissipated and no further changes occurred in the internal energy. In particular, the adiabatic section was insulated to ensure no heat energy interactions are taking place with the ambient. This has allowed the use of its wall temperature as an indicator of the heat pipe working temperature. Once the adiabatic wall temperature stops changing, so there is a balance between heat in to the evaporator section and heat out from the condenser section. In this case, the heat pipe has reached steady state and the adiabatic wall temperature becomes uniform with a temperature range of $\pm 2\ ^{o}C$. Temperature readings from all the thermocouples were then monitored using the data logger. The procedure was repeated for various electrical power throughputs between 50 and 400 W. In order to confirm repeatability, each test was repeated three times for each power throughput. After the whole power range was covered, the repeated tests were done to confirm stable thermal characteristics of the thermosyphon after a prolonged operational time.

4.3 Data Reduction

The effective overall thermal resistance of the thermosyphon was determined by applying the electrical analogue in the form:

$$R_{EXP} = \frac{\Delta T_{e-c}}{\dot{Q}_e} \tag{4-1}$$

where $\Delta T_{e-c} = T_{e,av} - T_{c,av}$; $T_{e,av} = \frac{T_{e1} + T_{e2}}{2}$ and $T_{c,av} = \frac{T_{c1} + T_{c2} + T_{c3} + T_{c4} + T_{c5}}{5}$ are the average internal wall temperatures in the evaporator and condenser sections, respectively, and $\dot{Q}_e$ is the power throughput. The internal wall temperatures of the thermosyphon were measured after considering the thermal conduction across the shell wall.

An energy balance across the sections was performed by determining the energy added and removed at the evaporator and condenser, respectively. Consequently, the power throughput to the evaporator was calculated from the power analyser, as follows:

$$\dot{Q}_e = V_{vol}.I_{electric} \tag{4-2}$$

The rate of heat transfer removal from the condenser section's heat exchanger was calculated as follows:

$$\dot{Q}_c = \dot{m}_w.Cp_w.\left(T_{w,outlet} - T_{w,inlet}\right) = \rho_w.\dot{V}.Cp_w.\Delta T_w \tag{4-3}$$

where $\dot{m}_w$ and Cp_w are the cooling water mass flow rate and specific heat, respectively, $T_{w,outlet}$ and $T_{w,inlet}$ are the cooling water inlet and outlet temperatures, respectively, ρ_w is the cooling water density, $\dot{V}$ is the cooling water volume flow rate and ΔT_w is the temperature difference from the cooling water inlet and outlet.

4.4 Error and Uncertainty Analysis

In engineering experiments, the term "error" does not mean mistake, it means the unavoidable uncertainty that attends all experimental measurements [76]. Error can be propagated due to equipment usage. In this case, equipment suppliers establish an expected percentage error in their equipment specifications for certain usage conditions when experimenting. Thus, the error associated with values calculated from expected percentage errors showed with the equipment can be determined using the equations listed in Table 4-1 [76].

The main source of uncertainty for the calculated R came from the temperature readings, which were measured using K-type thermocouples with a measurement error of ±(0.05% rdg + 0.3°C).

The propagation of uncertainties associated with the calculated R (S_R) can be estimated from the following equation, according to Taylor [76]:

$$S_R = R\sqrt{\left(\frac{S_{\Delta T_{e-c}}}{\Delta T_{e-c}}\right)^2 + \left(\frac{S_{Q_e}}{\dot{Q}_e}\right)^2} \tag{4-4}$$

where:

$S_{\Delta T_{e-c}} = \sqrt{\left(S_{T_{e,av}}\right)^2 + \left(S_{T_{c,av}}\right)^2}$: The error associated with $T_{e\ c}$

$S_{\dot{Q}_e}$: The error associated with the reading of the energy throughput $\dot{Q}_e$

The equations used to estimate the propagation of uncertainties associated with the calculated variables $\dot{Q}_e$, $\dot{Q}_c$, $T_{e,av}$, $T_{c,av}$, ΔT_w and $T_{w,av}$ have been listed in Table 4-2.

Table 4-1: Error analysis equations

Operation	Associated error
Uncertainty in sums and differences $(y = a + b + \cdots)$	$S_y = \sqrt{(S_a)^2 + (S_b)^2 + \cdots}$ (4-5)
Uncertainty in product and quotient $(y = a * b/c)$	$S_y = y\sqrt{\left(\frac{S_a}{a}\right)^2 + \left(\frac{S_b}{b}\right)^2 + \left(\frac{S_c}{c}\right)^2}$ (4-6)
Uncertainty in exponentiation $(y = a^b)$	$S_y = y * b * \left(\frac{S_a}{a}\right)$ (4-7)

where:

y is the result of the calculation,

S_q is the uncertainty associated with the result,

a, b and c are the individual numbers used for the calculations,

S_a, S_b and S_c are the uncertainties associated with the individual numbers for the calculation of the result.

Table 4-2: Error analysis equations used to estimate the propagation of uncertainties

Variable	Associated error
$\dot{Q}_e$	$S_{Q_e} = \dot{Q}_e\sqrt{\left(\frac{S_{I_{electric}}}{I_{electric}}\right)^2 + \left(\frac{S_{V_{vol}}}{V_{vol}}\right)^2}$ (4-8)
$\dot{Q}_c$	$S_{Q_c} = \dot{Q}_c\sqrt{\left(\frac{S_{\Delta T_w}}{\Delta T_w}\right)^2 + \left(\frac{S_{\dot{V}}}{\dot{V}}\right)^2}$ (4-9)
$T_{e,av}$	$S_{T_{e,av}} = \sqrt{\left(S_{T_{e1}}\right)^2 + \left(S_{T_{e2}}\right)^2}$ (4-10)
$T_{c,av}$	$S_{T_{c,av}} = \sqrt{\left(S_{T_{c1}}\right)^2 + \left(S_{T_{c2}}\right)^2 + \left(S_{T_{c3}}\right)^2 + \left(S_{T_{c4}}\right)^2 + \left(S_{T_{c5}}\right)^2}$ (4-11)
ΔT_w	$S_{\Delta T_w} = \sqrt{\left(S_{T_{w,inlet}}\right)^2 + \left(S_{T_{w,outlet}}\right)^2}$ (4-12)
$T_{w,av}$	$S_{T_{w,av}} = \sqrt{\left(S_{T_{w,inlet}}\right)^2 + \left(S_{T_{w,outlet}}\right)^2}$ (4-13)

where:

$$\Delta T_w = (T_{w,outlet} - T_{w,inlet}),\ T_{w,av} = \frac{T_{w,outlet} + T_{w,inlet}}{2}$$

An energy balance testing was conducted for the tested thermosyphon using Eq. (4-3) and demonstrated that the maximum percentage of uncertainty of the energy removal from the condenser section was less than 5.7% of the energy into the evaporator section, which is generally within the expected uncertainty of the experiments. The reason behind this difference might be the small heat losses to the ambient in the adiabatic section. Consequently, due to the low experimental uncertainty associated with the power analyser, the energy values into the evaporator section obtained from Eq. (4-2) were considered to be the power throughput of the thermosyphon and used to calculate *R*. The uncertainties associated with calculating $\dot{Q}_e$, $\dot{Q}_c$ and *R* are given in Table 4-3.

By calculating S_R, for the whole experimental range, the maximum uncertainty associated with the resulting *R* values was found to be around 4.1%, as shown in Table 4-3, which is an acceptable uncertainty value in engineering applications.

Table 4-3: Results of error analysis for water-charged thermosyphon

$\dot{Q}_e$	$S_{Qe}\pm$	Error±	$\dot{Q}_c$	$S_{Qc}\pm$	Error±	R	$S_R\pm$	Error±
W	W	%	W	W	%	℃/W	℃/W	%
100.41	1.7040396	1.70	95.11	5.415666	5.69	0.304626	0.009982	3.28
172.87	2.9337249	1.70	162.55	6.036538	3.71	0.136113	0.005496	4.04
225.25	3.8226769	1.70	192.21	6.382825	3.32	0.122307	0.004373	3.58
275.59	4.6770531	1.70	236.61	6.964004	2.94	0.109398	0.003678	3.36
299.52	5.0830585	1.70	254.78	7.220691	2.83	0.116319	0.003524	3.03
376.13	6.3832260	1.70	336.62	8.467227	2.52	0.105999	0.002961	2.79

CHAPTER 5 CFD SIMULATION OF A TWO-PHASE CLOSED THERMOSYPHON

Basically, numerical modelling employs a set of mathematical correlations that describe the dynamic behaviour of a real system. Numerical models are commonly employed in engineering applications for different purposes, particularly interpretative, design or predictive studies. Interpretation is applied when numerical models are used to explain the logic behind field or laboratory data. Design is applied when numerical models are used to compare the relative performance of different systems, with less emphasis on the final predicted performance. Prediction is applied when numerical models are used to reflect the efficacy of the experimental data of the actual system [77].

Validation processes involve an iterative procedure in which the model outcomes are compared with experimental data, until both the numerical modelling and experimental measurements give good accuracy [78].

5.1 Introduction to Computational Fluid Dynamics (CFD)

CFD is a numerical technique to solve the set of governing mathematical equations in order to predict approximate solutions of fluid dynamics, heat and mass transfer, chemical reaction and related phenomena. There are basically three approaches used to solve heat and mass transfer and fluid flow problems, which are analytical, experimental, and computational approach [79,80].

In the analytical approach, analytical solutions of the governing equations of continuity, momentum and energy are found. However, analytical solutions are only possible for a limited range of problems and their derivation requires substantial mathematical efforts. Despite of that, analytical approaches play an important role to help engineers understanding the fundamental laws controlling the behaviour of many engineering applications. Further, the analytical approach can also be used as an initial step in the validation of CFD models [79,80].

In the experimental approach, the relevant equipment and measurement tools are required in certain applications to predict the physical phenomena. However, full-scale

experiments can take a long time to set-up and run, and are also technically difficult or very expensive to perform. Experimental approaches play a significant role in engineering applications as reliable computational models require reliable experimental data for validation [79,80].

In the computational approach, CFD techniques have emerged and play an important role in solving complex flow problems for a large number of engineering applications due to their universality, flexibility, accuracy and efficiency. They can also provide a complete set of relevant information through a particular domain, which is mostly limited in the experimental approach [79,80].

CFD is usually based on the finite volume method that solves numerically the discretised form of the governing equations to obtain solution fields describing the fluid dynamics throughout the computational domain. The basic process of the CFD approach for the current research is outlined in Figure 5.1.

5.2 Modelling of Multiphase Flows

There are three main parts that need to be considered before modelling multiphase flows [81], as follows:

- Number of phases and expected flow regimes.
- Governing equations that describe the multiphase flow. This is because the numerical simulation is dependent on the solution of the conservation of mass, momentum and energy equations.
- The solution of the governing equations involved in modelling the multiphase flow

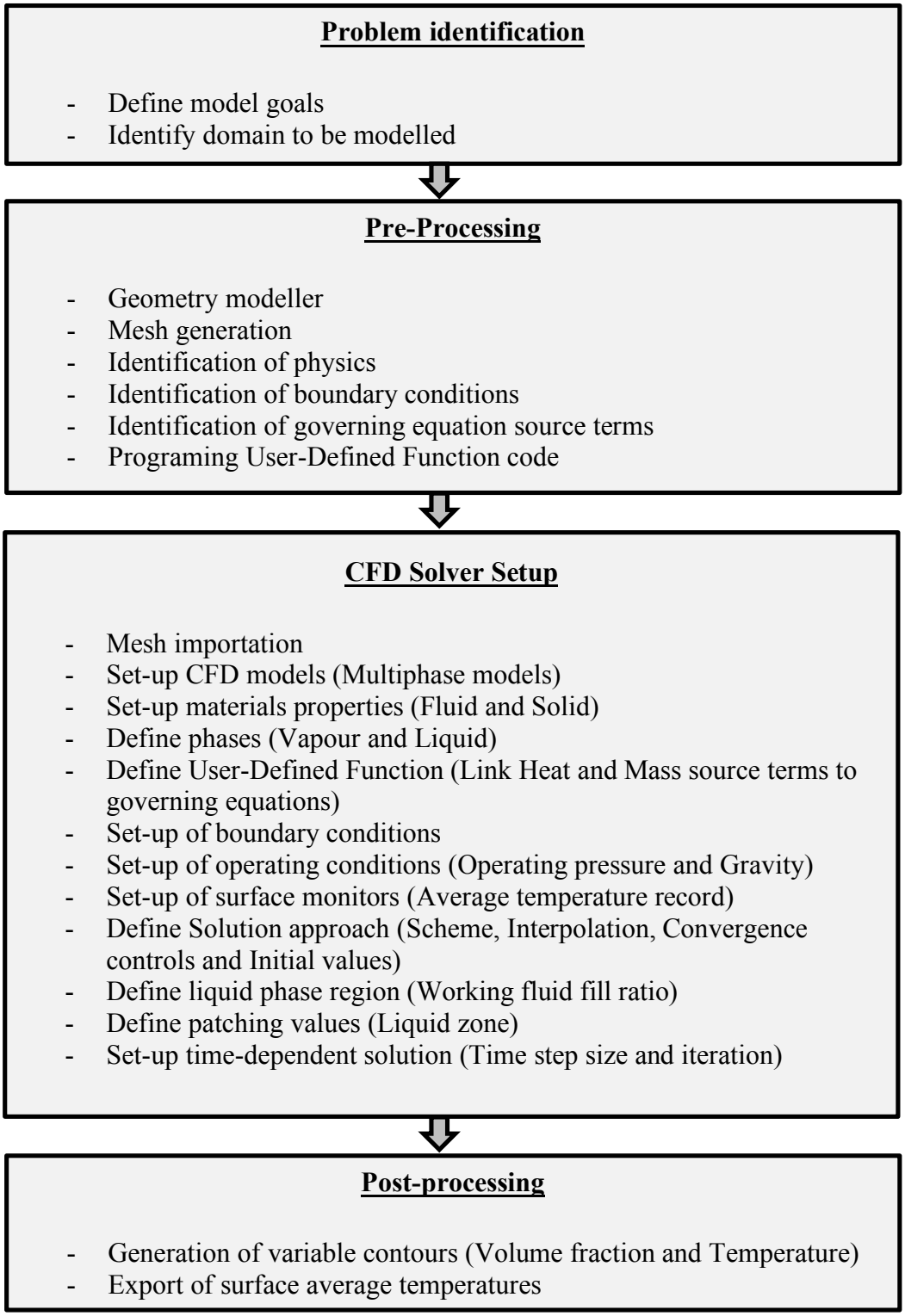

Figure 5.1: Schematic of CFD solution process

5.2.1 Limitation of modelling two-phase flows

Since more than one type of flow can occur, such as gas-liquid and liquid-liquid, a number of flow patterns can also exist within each type of flow, and two-phase flow is a complex physical phenomenon. There is also a lack in the development of the mathematical solution of the phenomena existing in the two phases. Therefore, there is no complete agreement on the governing equations. Defining the distribution of the liquid and the gas phases in the flow field is still one of the main problems in the modelling [82,83]. In spite of the above limitations, the CFD technique has been successful in the calculation of two-phase flow regimes [81].

5.2.2 Studies of multiphase flows by using the CFD technique

Multiphase flows have received considerable interest in the literature, and they have been investigated by numerous researchers in order to understand the characteristics of different flow patterns. Further, numerous numerical investigations using the volume of fluid method (VOF) have been used to model the multiphase process. De Schepper et al. [81] introduced a CFD simulation to model gas/vapour-liquid, two-phase horizontal flow patterns. They compared the results of their model with experimental data predicted by the Baker chart. The authors used the VOF technique to predict seven different flow regimes. They concluded that the CFD technique has the ability to simulate all horizontal two-phase horizontal flow regimes that were predicted by the Baker chart.

In another study provided by De Schepper et al. [82], a three-dimensional model was developed to simulate the evaporation process of a hydrocarbon feed stock in a heat exchanger in the convection section of a steam cracker. They used the VOF method in their simulation and validated their model by comparing it with results from the literature.

A CFD model and experimental studies were presented by Parvareh et al. [84] to model the interface between gas and liquid, in addition to the fluid flow movement of different two-phase regimes inside horizontal and vertical tubes. They concluded that the predicted model was validated by experimental results.

Another investigation, presented by Liu et al. [85], was carried out using electrical capacitance tomography (ECT) to measure the thickness of the liquid film in a two-phase closed thermosyphon. The authors carried out a CFD simulation to provide further comparisons with the measured results.

An experimental study, CFD model, and artificial neural networks (ANN) were created by Alizadehdakhel et al. [86] in order to investigate two-phase flow regimes and pressure drops in a tube. They used CFD codes to model two-phase flow (gas-liquid) in an experimental tube, and ANN to evaluate the pressure drop of different conditions of liquid and gas velocity. The experimental results were compared with the CFD and the ANN predictions of the pressure drop. They found that the CFD measurements were more accurate than the ANN evaluations.

Ekambara et al. [87] modelled the internal phase of a co-current air-water bubbly flow inside a horizontal pipe. They used CFD to study the effect of different volumetric superficial liquid and gas velocities on flow fields. They noticed that the predicted CFD model showed good agreement with the experimental results reported by other researchers [88-90].

Gupta et al. [91] created a numerical model to study the flow and heat transfer in a Taylor flow regime by using two different codes: ANSYS Fluent and TransAT. They used the volume of fluid approach (VOF) and level-set techniques to track the gas-liquid interface. They found that the data predicted using the two codes were very similar.

In another study, presented by Gupta et al. [92], ANSYS Fluent was used to model Taylor flow in a horizontal micro channel. The simulations in Fluent were carried out using the VOF method. The research suggested using fine meshes in order to capture the liquid film around the Taylor bubble. The results were compared with existing correlations and previous modelling data and found to be in good agreement.

Experimental and numerical simulation was introduced by Lu et al. [93] to investigate the characteristics of oil-gas flow in a horizontal pipe on a large scale. The simulation was carried out using the VOF technique to perform different flow regimes and their

transitions. The research compared the numerical simulations with the experimental results and reported good agreement.

He et al. [94] carried out a numerical simulation of gas-liquid slug flow and associated heat transfer without phase change in a micro tube. The authors found that the heat transfer rate depends strongly on the flow pattern. They also pointed out that the Nusselt number was as much as 2.4 times higher than that of the single-phase laminar flow.

de Sampaio et al. [95] reported on a numerical simulation and experimental study with a stratified gas-liquid, two-phase flow in horizontal circular pipes. The finite element method was used to solve the Reynolds averaged Navier-Stokes equations with the k-w turbulence model. The results showed that the k-w model was suitable for the numerical simulation of stratified gas-liquid flow.

Juric and Tryggvason [96] carried out a two-dimensional numerical simulation for liquid-vapour phase change. The effects of inter-phase mass transfer, latent heat, surface tension, and unequal material properties between liquid and vapour phases were studied. The authors compared the numerical results with a one-dimensional solution. They then compared a two-dimensional simulation of film boiling with experimental results. The results of the heat transfer rate and wall temperatures were compared with experimental results and found to be in good agreement.

A numerical and experimental investigation was introduced by Hu et al. [66] to study the freezing of a high-temperature phase-change medium outside of a two-phase closed thermosyphon by considering natural convection during the freezing. The phase-change medium was used as heat storage; then, the thermosyphon was used to transfer this stored heat. The authors compared the numerical and experimental results and reported good agreement.

Narain et al. [97] and Phan et al. [98] carried out a numerical investigation of two-dimensional problems of steady and unsteady laminar internal condensing flows of pure vapour inside a vertical tube and a channel. The investigators used FC-72 and R-113 as working fluids.

Lhuillier [99] developed a new version of a two-phase flow model for liquid-gas as well as liquid-liquid mixtures, numerically. The differences of pressure, temperature, and velocity between the two phases were considered.

Vidalain et al. [100] performed a thermally-enhanced conduction model for predicting a convection-dominated, solid-liquid phase change. Their model predicted the overall thermal behaviour of the system as well as the phase front position. The model was examined and compared with a CFD model for two test cases, namely freezing duct flow and melting inside an enclosure, and the results were found to be in good agreement. The study demonstrated that the enhanced conduction model was suitable for controlling real-time solid-liquid phase change processes that take place in industrial applications and storage systems.

5.2.3 Studies of CFD modelling of two-phase closed thermosyphons

Two-phase closed thermosyphons have been extensively used in many applications [57], such as heating, ventilation, and air conditioning (HVAC) systems [7], ground source heat pumps [8], water heating systems [9] and electronics thermal management [10]. However, only a limited number of CFD numerical simulation studies on two-phase closed thermosyphons has been published. This review is based on the most recently published CFD modelling studies.

Alizadehdakhel et al. [19] provided a two-dimensional model and experimental studies in which they investigated the effect of input heat flow and fill ratio of the working fluid on the performance of a two-phase closed thermosyphon. They validated their study using experimental results. Three input heat flow rates of 700, 500, and 350W and three fill ratios of 0.3, 0.5, and 0.8 were considered. Under these operating conditions, they found the performance of the thermosyphon improved when the input heat flow was increased from 350 to 500W. Further, they discovered the best performance was at a fill ratio of 0.5. The authors reported a term called “heat performance”, which they calculated by using the following equation for different fill ratios:

$$\eta = \frac{\dot{Q}_{out}}{\dot{Q}_{in}} x\ 100 \qquad (5\text{-}1)$$

However, this term is not usual in heat pipe publications as it is not reported in the literature. If $\dot{Q}_{in}$ is being applied to the evaporator section of the thermosyphon, $\dot{Q}_{in}$ will be dissipated in the condenser to change the internal energy of the system when assuming good insulation. In general, the thermal performance term used to characterize thermodynamics at different heat throughputs is the total thermal resistance.

Kafeel and Turan [17] numerically studied the effect of different pulsed increases in heat input at the evaporator zone on the behaviour of the thermosyphon. They used similar thermosyphon configurations to that of Amatachaya et al [101] to validate the simulation model, and an Eulerian model to simulate film condensation at the condenser zone with fill ratio of 30% of the evaporator zone. They reported the temperature and velocity profiles along the thermosyphon for two different heat flux inputs of 10% and 20% of the steady-state heat flux at the evaporator zone. However, the authors did not state the working fluid used to charge the thermosyphon. This model did not show the evaporation process of the liquid pool boiling that takes place in the evaporator zone. This study also did not include the phase change and the formation of bubbles in the liquid pool during the evaporation process. The authors did not report on the effect of different pulsed increases in heat input on the thermal performance of the thermosyphon.

Legierski et al. [3] provided CFD modelling and experimental measurements of heat and mass transfer in a horizontal wicked heat pipe. They investigated the effectiveness of the heat pipe thermal conductivity in a transient state during start-up of the pipe operation and during temperature increases. The authors used a heat pipe that was 200 mm long with 4 mm diameter and 25 mm length for the evaporator and condenser. They also used two containers, one for hot water (90 ^{o}C) at the evaporator section and one for cold water (ambient temperature) at the condenser section. They developed a three-dimensional CFD model to simulate the internal vapour flow. They found that the effective thermal conductivity of the wicked heat pipe depended on the time in the range between 15 x 10^3 and 30 x 10^3 W/m K, and achieved its steady-state value after approximately 20 to 30s. Figure 5.2 shows the CFD modelling of the heat pipe reported by the authors. However, the authors did not consider in the CFD modelling the phase

change from liquid phase to vapour phase, as well as condensation in the condenser section and pool boiling in the evaporator section.

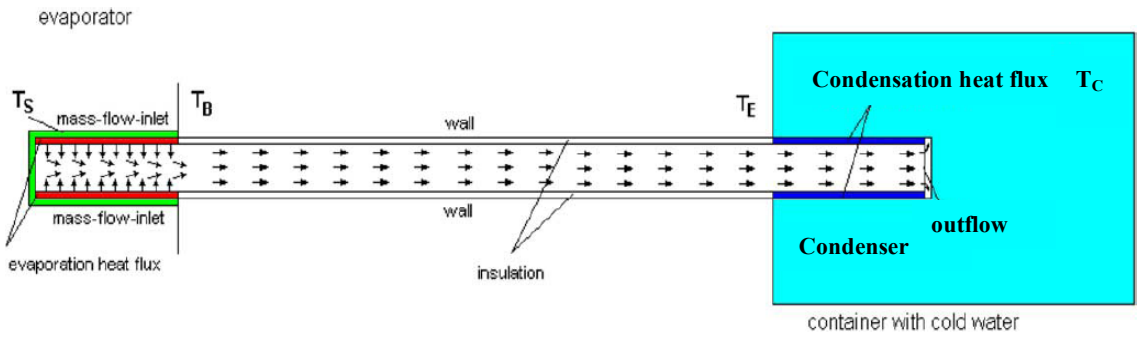

Figure 5.2: CFD modelling of wick heat pipe [3]

Zhang et al. [47] developed a two-dimensional heat and mass transfer model for a disk-shaped flat two-phase thermosyphon used in electronics cooling. The authors simulated the vapour flow inside the flat two-phase thermosyphon as a single-phase flow. They compared their predicted model with experimental results to determine the factors that affected the axial thermal resistance of a thermosyphon. This model was limited as it considered the flow inside the flat thermosyphon as a pure vapour phase only.

Joudi and Al-Tabbakh [102] numerically studied a two-phase thermosyphon solar domestic hot water system, by using a computer simulation. They used R-11 as a working fluid in the thermosyphon. Firstly, the authors validated the computer program and calculation procedure by comparing the results with those obtained with single-phase systems. They then performed calculations for the two-phase thermosyphon system. In their calculations, they evaluated mass flow rate, saturation pressure, and temperature in the collector and condenser, together with tank temperature and collector and condenser thermal efficiencies. The results of the study showed that the collector efficiency of the two-phase system was approximately 20% greater than in a single-phase system. Further, the response of the two-phase system in reaching maximum tank temperature and efficiency was faster than in a single phase system. This study was limited to a theoretical model and did not include a CFD model.

Annamalai and Ramalingam [18] carried out an experimental investigation and CFD analysis of a wicked heat pipe using ANSYS CFX. The authors considered the region

inside the heat pipe as a single phase of vapour and the wick region as the liquid phase. They compared the predicted surface temperature along the evaporator and condenser walls and the vapour temperature inside the heat pipe with the experimental data. This model treated the flow inside the heat pipe as a single-phase and did not include the evaporation, condensation and phase change processes.

De Schepper et al. [82] developed a model to simulate the evaporation process of a hydrocarbon feedstock in a heat exchanger. They used VOF to track the liquid-vapour interface, as well as user-defined functions (UDF) to simulate flow boiling including the phase change process. They proposed correlations and implemented them as UDF to calculate the mass and heat transfer between the phases, and were able to simulate the evaporation and boiling phenomena inside the convection section of a steam cracker. This model was for the convection section in a steam-cracking furnace; however, it did not include the heat pipe system.

Lin et al. [103] built a CFD model to predict the heat transfer capability of miniature oscillating heat pipes. The effects of different heat transfer lengths and inner diameters at different heat inputs were used to analyse the heat transfer capability of MOHPs. They compared the predicted model with experimental results. This model did not consider the internal phenomena of evaporation, condensation and phase change inside the MOHPs.

Ghajar et al. [44] developed a model to predict the behaviour of a micro loop heat pipe (MLHP) used in electronics cooling applications, including identifying the heat transfer to and from the microcompensation chamber (CC) by using CFD. A schematic diagram of a micro heat pipe reported by the authors is shown in Figure 5.3. The results showed that increasing the evaporator or the width of the vapour line and decreasing the length of the vapour line, increased the heat removal capability. This study was limited to a micro heat pipe and it did not include the evaporation, condensation and phase change processes.

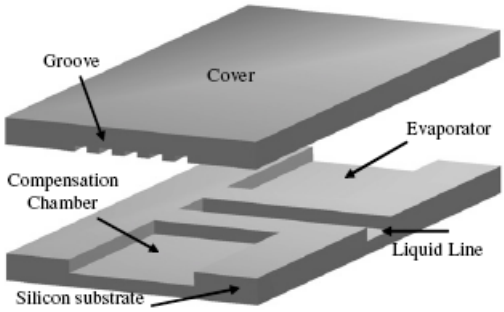

Figure 5.3: Schematic diagram of micro heat pipe [44]

Rahmat and Hubert [45] used ANSYS CFX to model a three-dimensional two-phase flow in a triangular micro heat pipe. The effective thermal conductivity, pressure, and velocity for both phases along the micro heat pipe, as well as the influence of the liquid filling ratio on the effective length of the heat pipe, were studied and results compared with those available in the literature. This model showed the ability of using ANSYS CFX to simulate heat transfer problems; however, the model is suitable only for a triangular micro heat pipe.

Riffat and Gan [63] investigated the effectiveness of a heat pipe heat exchanger (HPHX) for naturally ventilated buildings. The authors examined the performance of three types of heat pipe heat recovery units in a two-zone chamber with a horizontal dividing wall. The first type was a bank of seven externally finned heat pipes; the second type was a cylindrical spine fin, and the third type was made of two rows of staggered heat pipes. They used a commercial CFD package to calculate the pressure loss characteristics of HPHX units. Each row of heat pipes was modelled as one bank of rectangular cylinders. They also modelled the fins as uniformly distributed rectangular studs on each side of the heat pipes. The experimental results demonstrated that air velocity had a major influence on the effectiveness of heat pipe heat recovery. The authors found that, at the same velocity, the heat recovery was between 16% and 17% more efficient when double banks of heat pipes with plain fins had been used than when one bank was used. They suggested that, in naturally ventilated low rise buildings without the wind effect, the mean air velocity should be less than 1 m/s. This study did not investigate heat and mass transfer phenomena inside the HPHX.

5.2.4 Approaches of Modelling Multiphase Flow

There are two main methods to the numerical calculations of multiphase flows, which are the Euler-Lagrange method and the Euler-Euler method. The Euler-Lagrange method treats the fluid phase as a continuum and a dispersed phase such as bubbles or droplets as a second phase, in which the dispersed-phase volume fractions are not to exceed 10%. As the current application considers the volume fraction of the second phase exceeds 10%, the Euler-Euler approach has been adopted as it uses the idea of phasic volume fraction in which the volume of a phase cannot be occupied by the other phases. These volume fractions are assumed to be continuous functions of space and time [104]. From the available CFD model for multiphase flow in the CFD package, volume of fluid model has been used in the current study. This model is an Euler-Euler approach in which the grid cells fixed and the phases are summed to behave like a continuous media. The volume of fluid model is described in the next section.

5.2.5 Volume of fluid (VOF) model

Numerical solutions based on the finite volume method are more difficult for multiphase flows than for a single-phase flow. The reasons for this difficulty are that the interfaces between the phases are not stationary and physical properties at the interfaces such as density and viscosity change between the different phases, which requires an intensive computational effort. The volume of fluid (VOF) technique, therefore, has been used to solve these problems by determining the motion of all phases and indirectly from this result defining the motion of the interfaces [82,105,106]. A description of the VOF method was given by Hirt and Nichols [107]. Gopala and Wachem [108] also carried out an investigation of different numerical methods to track interfaces in multiphase flows, such as the front tracking method, the marker particle method, and the VOF method. They found that the VOF method has the advantage of being reasonably accurate and conceptually simple, and that phenomena such as coalescence and interface backup are included inherently.

The VOF technique can be applied to model two immiscible fluids with a clearly defined interface between the phases, and is used for surface-tracking applied to a fixed mesh. In the VOF model, one set of Navier-Stokes equations are solved through the computational domain and used to track the motion of the different phases by defining

the volume fraction of each phase [104]. The VOF model relies on the fact that each cell in the domain is occupied by one phase or a combination of the two phases. In other words, if α_l is a volume fraction of liquid and α_v is a volume fraction of vapour, the following three conditions are possible:

- $\alpha_l = 1$: The cell is fully occupied by liquid
- $\alpha_l = 0$: The cell is fully occupied by vapour
- $0 < \alpha_l < 1$: The cell is at the interface between the liquid and vapour phases

When the third condition occurs, the volume fractions of all phases sum to unity [104].

5.2.6 Navier-Stokes equations for VOF model

The governing equations of mass continuity, momentum and energy are used to describe the motion of the working fluid in a thermosyphon. This will be explained in the next section.

5.2.6.1 Continuity equation for VOF model (Volume fraction equation)

By applying the physical principle of conservation of mass to the fluid, the continuity equation has the following form [106]:

$$\nabla \cdot (\rho \, \mathbf{V}) = -\frac{\partial \rho}{\partial t} \tag{5-2}$$

where is the density, **V** is the velocity vector and *t* is the time.

Solution of the above equation for the volume fraction of one of the phases is used to track the interface between the phases. Thus, the continuity equation of the VOF model for the secondary phase (*l*) can be expressed as [104]:

$$\nabla \cdot (\alpha_l \, \rho_l \, \mathbf{V}) = -\frac{\partial}{\partial t}(\alpha_l \, \rho_l) + S_m \tag{5-3}$$

where S_m is the mass source term used to calculate the mass transfer during evaporation and condensation.

The continuity equation shown above can be called the volume fraction equation and this relation will not be solved for the primary phase as the volume fraction of the primary-phase is determined based on the following constraint [104]:

$$\sum_{l=1}^{n} {}_{l} = 1 \tag{5-4}$$

When the cell is not fully occupied by the primary phase (v) or the secondary phase (l), a mixture of the phases l and v exists. Thus, the density of the mixture is given as the volume-fraction-averaged density and takes the following form [104]:

$$= {}_{l}\,{}_{l} + \left(1 \quad {}_{l}\right) {}_{v} \tag{5-5}$$

5.2.6.2 Momentum equation for VOF model

The forces acting in the fluid were considered to be gravitational, pressure, friction and surface tension. In order to consider the effect of surface tension along the interface between the two phases, the continuum surface force (*CSF*) model proposed by Brackbill et al. [109] has been added to the momentum equation

$$\mathbf{F}_{CSF} = 2\sigma \frac{\alpha_l \rho_l C_v \nabla \alpha_v + \alpha_v \rho_v C_l \nabla \alpha_l}{\rho_l + \rho_v} \tag{5-6}$$

where σ is the surface tension coefficient and C is the surface curvature.

By taking into account the above forces, the momentum equation for the VOF model takes the following form [106]:

$$\frac{\partial}{\partial t}(\rho\,\mathbf{V}) + \nabla \cdot (\rho\,\mathbf{V}\,\mathbf{V}^{\boldsymbol{T}}) = \rho\,\mathbf{g} - \nabla p + \nabla \cdot \left[\mu\,(\nabla\,\mathbf{V} + (\nabla\,\mathbf{V})^{\boldsymbol{T}}) - \frac{2}{3}\mu\,(\nabla \cdot \mathbf{V})\boldsymbol{I}\right] + \mathbf{F}_{CSF} \tag{5-7}$$

where g is the acceleration of gravity, p is the pressure and $\boldsymbol{I}$ is the unit tensor.

The momentum equation depends on the volume fraction of all phases through the physical properties of density and viscosity [104]. Thus, the dynamic viscosity is given by

$$= {}_{l}\,{}_{l} + \left(1 \quad {}_{l}\right) {}_{v} \tag{5-8}$$

A single momentum equation is solved through the computational domain, and the calculated velocity is shared among the phases.

5.2.6.3 Energy equation for VOF model

The energy equation for the VOF model has the following form [106]:

$$\frac{\partial}{\partial t}(\rho E) + \nabla \cdot (\rho E \mathbf{V}) = \nabla \cdot (k \nabla T) + \nabla \cdot (p \mathbf{V}) + S_E \quad (5\text{-}9)$$

where S_E is the energy source term used to calculate the heat transfer during evaporation and condensation.

The VOF model treats the temperature T as a mass-averaged variable and the thermal conductivity k is calculated as [104]:

$$k = \alpha_l k_l + (1 - \alpha_l) k_v \quad (5\text{-}10)$$

The VOF model also treats the energy E as a mass-averaged variable in the following form [104]:

$$E = \frac{\alpha_l \rho_l E_l + \alpha_v \rho_v E_v}{\alpha_l \rho_l + \alpha_v \rho_v} \quad (5\text{-}11)$$

where E_l and E_v are based on the specific heat C_v of the phase and the shared temperature, given by the caloric equation of state [106]:

$$E_l = c_{v,l}(T - T_{sat}) \quad (5\text{-}12)$$

$$E_v = c_{v,v}(T - T_{sat}) \quad (5\text{-}13)$$

A single energy equation is also solved throughout the domain for both phases, and the calculated temperature is shared among the phases.

5.3 User-Defined Function (UDF)

5.3.1 What is a user-defined function?

A user-defined function (UDF) is a set of functions constructed in the C programing language, which can be linked to the FLUENT code in order to adjust the standard features of the code as illustrated in Figure 5.4. In particular, UDFs can be employed to specify custom source terms for the existing governing equations in FLUENT in order to determine mass, momentum and energy sources for the phases involved in the mass and heat transfer. UDFs can be used to enhance existing multiphase models, such as built-in mass transfer models. UDFs can also be used as a tool to be called at the beginning of every iteration to adjust flow variables, such as temperature, by using the User-defined ADJUST tool, as shown in Figure 5.4 [110].

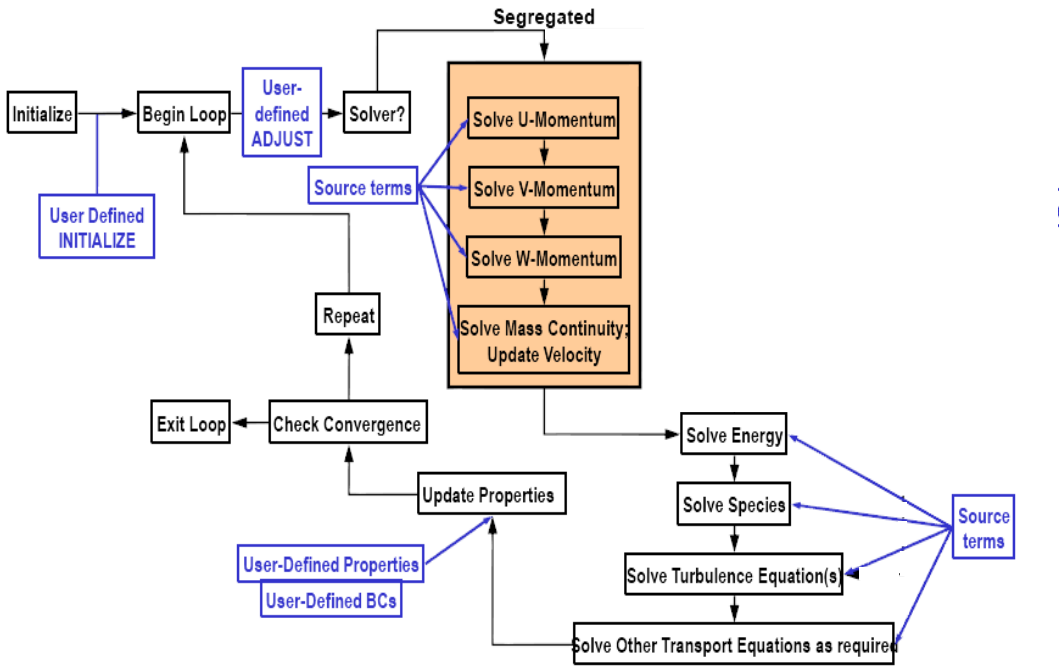

Figure 5.4: UDF access to the FLUENT solver [110]

5.3.2 CFD simulation of mass and heat transfer during the evaporation and condensation processes

During the thermosyphon operation, phase change occurs from liquid to vapour phase during the nucleate pool boiling in the evaporator section and from vapour to liquid phase during the liquid film condensation in the condenser section. In order to simulate these processes, user-defined functions (UDFs) are employed to specify customised source terms [82] for the existing governing equations in the FLUENT package. These UDFs are essentially required to calculate the mass and heat transfer between the liquid and vapour phases during the evaporation and condensation processes, determined by the source terms in the governing equations, particularly the volume fraction and energy equations.

The mass flow rate of vapour molecules into the liquid during condensation and the opposite process during evaporation, based on the kinetic theory of gases, have been reported by Knudsen [111] and given by:

$$m_f = \sqrt{\frac{M}{2\pi R_u}} \frac{p}{\sqrt{T}} \tag{5-14}$$

where m_f is the mass flux of molecules, R_u is the universal gas constant and M is the molecular weight.

By assuming that the interaction between the molecules at the vapour-liquid interface is under equilibrium conditions [25], the net mass flux at the vapour-liquid interface is given by:

$$m_f = a_c \sqrt{\frac{M}{2\pi R_u}} \frac{(p - p_{sat})}{\sqrt{T_{sat}}} \tag{5-15}$$

where a_c is the accommodation coefficient that expresses the portion of vapour molecules going into the liquid surface. This term can be empirically determined, and has the value of 1.0 under equilibrium [82].

The Clausius-Clapeyron equation relates the pressure to the temperature at saturation conditions [82], and is obtained by equating the vapour and liquid chemical potential:

$$\frac{dp}{dT} = \frac{h_{fg}}{T}\left(\frac{\rho_l \rho_v}{\rho_l - \rho_v}\right) \tag{5-16}$$

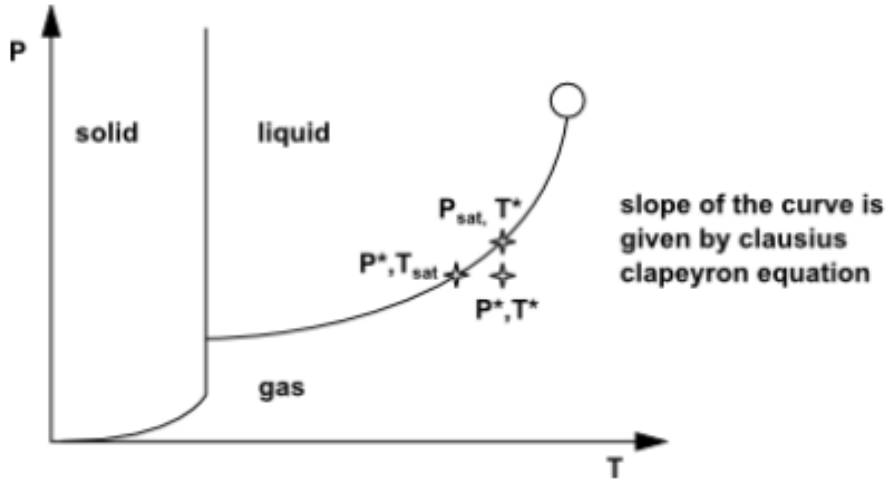

Figure 5.5: The stability phase diagram [104]

The above relation yields the following form, as long as the temperature and the pressure are close to the saturation conditions [82]:

$$(p - p_{sat}) = \frac{h_{fg}}{T_{sat}}\left(\frac{\rho_l \rho_v}{\rho_l - \rho_v}\right)(T_{sat} - T) \tag{5-17}$$

The net mass flux at the vapour-liquid interface can be expressed by substituting Eq. (5-17) into Eq. (5-15):

$$m_f = \sqrt{\frac{M}{2\pi R_u}}\frac{h_{fg}}{\sqrt{T_{sat}}}\left(\frac{\rho_l \rho_v}{\rho_l - \rho_v}\right)\left(\frac{T_{sat} - T}{T_{sat}}\right) \tag{5-18}$$

The above equation describes the mass transfer during evaporation and condensation processes and hence, this equation is introduced in the volume fraction equation (Eq. (5-3)) as a mass source term (i.e. S_M). However, Eq. (5-18) has units of kg/m^2.s, and in order to add this mass source term to Eq. (5-3), Eq. (5-18) should be expressed in

kg/m^3.s. Therefore, Eq. (5-18) is multiplied by the volumetric interfacial surface area. The volumetric interfacial surface area is related to the Sauter mean diameter, D_{sm} of the vapour bubble and the volume fraction of the vapour/liquid phase [104], and can be expressed as $\left(\frac{6\,\alpha}{D_{sm}}\right)$ [82].

Therefore, the expression for the mass source term is given by:

$$S_M = \frac{6}{D_{sm}}\sqrt{\frac{M}{2\pi R_u T_{sat}}}\left(\frac{h_{fg}}{\rho_l - \rho_v}\right)\left(\rho_l \rho_v \alpha \frac{T_{sat} - T}{T_{sat}}\right) \tag{5-19}$$

Based on the above equation, two parameters f_1 and f_2, which have units of s^{-1} and describe the mass transfer time relaxation during evaporation (Eq. (5-20)) and condensation (Eq. (5-21)), respectively, are introduced in the following forms:

$$f_1 = \frac{6}{D_{sm}}\sqrt{\frac{M}{2\pi R_u T_{sat}}}\left(\frac{\rho_v}{\rho_l - \rho_v}\right)\left(h_{fg}\right) \tag{5-20}$$

$$f_2 = \frac{6}{D_{sm}}\sqrt{\frac{M}{2\pi R_u T_{sat}}}\left(\frac{\rho_l}{\rho_l - \rho_v}\right)\left(h_{fg}\right) \tag{5-21}$$

Consequently, the mass source terms for evaporation and condensation are expressed in the following forms by substituting Eq. (5-20) and Eq. (5-21) into Eq. (5-19):

$$S_{M_1} = f_1\, \rho_l \alpha_l \frac{T_{sat} - T}{T_{sat}} \tag{5-22}$$

$$S_{M_2} = f_2\, \rho_v \alpha_v \frac{T_{sat} - T}{T_{sat}} \tag{5-23}$$

Eq. (5-22) and Eq. (5-23) represent the mass sources that determine the mass transfer during evaporation and condensation, respectively.

The heat flux at the vapour-liquid interface can be expressed by the product of the net mass flux with the latent heat of evaporation,

$$q_f = m_f\, x\, h_{fg} \tag{5-24}$$

The above equation expresses the heat transfer during evaporation and condensation. Thus, this equation is introduced in the energy equation (Eq. (5-9)) as an energy source term which can be expressed in the following forms:

$$S_{E_1} = S_{M_1}(h_{fg}) \tag{5-25}$$

$$S_{E_2} = S_{M_2}(h_{fg}) \tag{5-26}$$

Eq. (5-25) and Eq. (5-26) represent the energy sources that determine the heat transfer during evaporation and condensation, respectively.

It should be noted that, the vapour bubble diameter and the value of the parameters f_1 and f_2 is not very well known [104]. According to [82,104,112], the value of the parameters f_1 and f_2 may be set equal to 0.1 s^{-1} and it has been reported that too large values and too small values of f_1 and f_2 can lead to numerical convergence issues.

Mass sources, S_M in the volume fraction equation, and energy sources, S_E in the energy equation, used in the present work can be found in Table 5-1, where T_{mix} and T_{sat} are the mixture temperature and saturation temperature, respectively, and h_{fg} stands for latent heat of vaporisation.

Mass and energy sources in Table 5-1 have been implemented in the UDF and linked to the governing equations in FLUENT. The volume fraction for each phase in the cell has been defined by the VOF model. Therefore, the evaporation process required two mass sources for the calculation of the mass transfer, Eq. (5-27) describing the amount of mass taken from the liquid phase and Eq. (5-28) describing the amount of mass added to the vapour phase. The same procedure takes place for the condensation process, Eq. (5-29) and Eq. (5-30) describing the amount of mass transfer from vapour to liquid phase.

A single source term for both phases is required in the evaporation or condensation during the heat transfer process. Energy sources S_E in the energy equation used in the present study are determined by multiplying the calculated mass sources in Eq. (5-27)

and Eq. (5-29) by the latent heat of evaporation for the working fluid. As a result, Eq. (5-31) and Eq. (5-32) are introduced.

It is important to note that the temperature T_{mix} in the above equations is introduced as a mixture temperature rather than liquid or vapour temperature. The reason as mentioned before is that the VOF model associates some variables such as temperature and velocity with the mixture phase, not with a specific phase.

Table 5-1: Construction of mass and energy sources

Thermal Energy	Phase Change process	Temp. Condition	Phase	Source Term
Mass Transfer	Evaporation	$T_{mix} > T_{sat}$	Liquid	$S_{M1} = 0.1 \rho_L \rho_L \frac{T_{mix} - T_{sat}}{T_{sat}}$ (5-27)
			Vapour	$S_{M1} = 0.1 \rho_L \rho_L \frac{T_{mix} - T_{sat}}{T_{sat}}$ (5-28)
	Condensation	$T_{mix} < T_{sat}$	Liquid	$S_{M2} = 0.1 \rho_V \rho_V \frac{T_{sat} - T_{mix}}{T_{sat}}$ (5-29)
			Vapour	$S_{M2} = 0.1 \rho_V \rho_V \frac{T_{sat} - T_{mix}}{T_{sat}}$ (5-30)
Heat Transfer	Evaporation	$T_{mix} > T_{sat}$	$S_{E1} = 0.1 \rho_L \rho_L \frac{T_{mix} - T_{sat}}{T_{sat}} (h_{fg})$ (5-31)	
	Condensation	$T_{mix} < T_{sat}$	$S_{E2} = 0.1 \rho_V \rho_V \frac{T_{sat} - T_{mix}}{T_{sat}} (h_{fg})$ (5-32)	

5.4 Model Geometry

A two-dimensional model is developed to simulate the two-phase flow and heat transfer phenomena in a thermosyphon. According to the experimental conditions, a closed thermosyphon tube wall made of copper with a thickness of 0.9mm and a total length of 500 mm is used as the thermosyphon geometry, as can be seen in Figure 5.7. The evaporator and condenser sections of the thermosyphon model are taken to be 200mm in length, making the adiabatic section 100mm long. The outer and inner diameters are 22mm and 20.2mm, respectively.

The temperature distribution along the outer wall of the thermosyphon is monitored using eight different positions, which are the thermocouple positions shown in Figure 5.7. According to the experimental setup, Te_1 and Te_2 are used to record the average temperature of the evaporator section, while Tc_1 to Tc_5 are used to record the

average temperature of the condenser section. *Ta* is used to record the average temperature of the adiabatic section.

5.5 Mesh Generation

The two-dimensional geometry is constructed and meshed using GAMBIT's grid generation software. The solid region contains 15092 cells and 54000 cells for the fluid region. As a result, 69,092 Quad cells are generated. Near the left and right walls, fifteen layers of cells are used in order to capture the thin liquid film that develops near the wall, as shown in Figure 5.8. The first grid size was 0.01 mm and the growth ratio was 1.2. One cell layer with 36 cells has been used for the upper and bottom walls, as no heat conduction is considered through these walls, as shown in Figure 5.6.

Different mesh sizes are used to test grid independence as shown in Figure 5.9. The average temperature of the evaporator ($T_{e,av}$), adiabatic (T_a) and condenser ($T_{c,av}$) sections for different mesh sizes for the working fluids of water and R134a are monitored and shown in Table 5-2 and Table 5-3, respectively, In which, $T_{e,av} = \frac{T_{e1}+T_{e2}}{2}$ and $T_{c,av} = \frac{T_{c1}+T_{c2}+T_{c3}+T_{c4}+T_{c5}}{5}$, based on Figure 5.7.

From theses tables, it was found that almost the same average temperatures for the evaporator, adiabatic and condenser sections were obtained for different mesh sizes. As a result, the mesh size of 69,092 Quad, Map cells is selected for the simulation analysis.

Table 5-2: Grid-independence results for the thermosyphon charged with water for heat input of 173 W

Mesh size (cells)		19,603	69,092	87,800
$T_{e,av}$	K	378.71	378.37	378.19
T_a	K	362.71	362.41	362.32
$T_{c,av}$	K	326.54	326.96	327.79

Table 5-3: Grid-independence results for the thermosyphon charged with R134a for heat input of 30 W

Mesh size (cells)		19,500	69,276	129,944
$T_{e,av}$	K	303.66	302.31	302.47
T_a	K	299.18	299.01	299.64
$T_{c,av}$	K	294.63	294.80	295.62

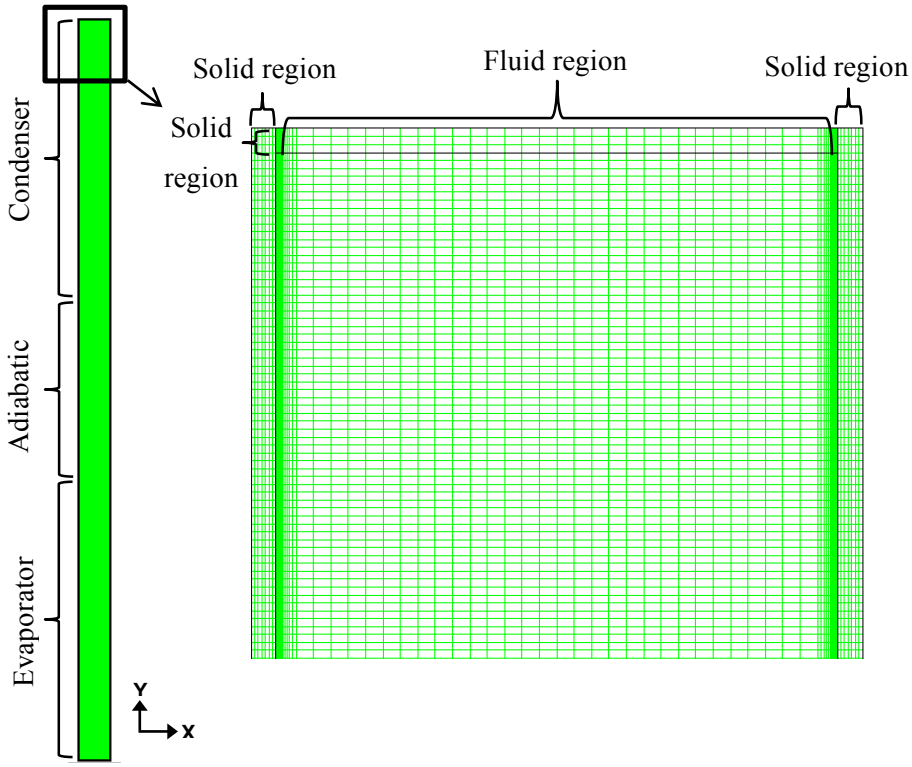

Figure 5.6: Mesh distribution

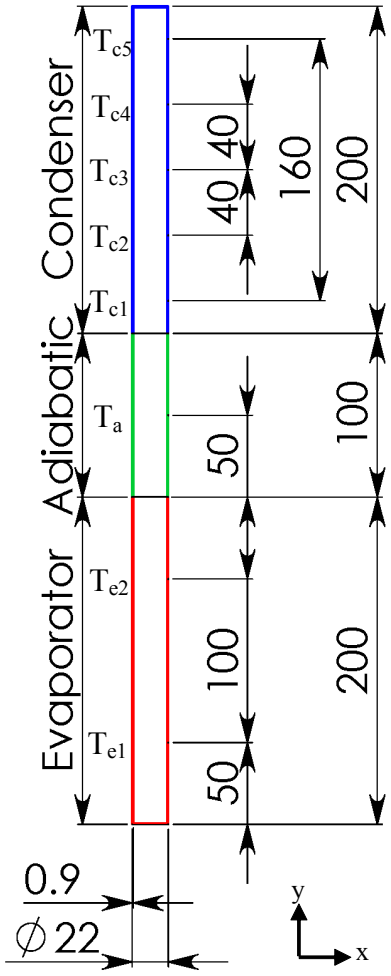

Figure 5.7: Geometry and dimensions

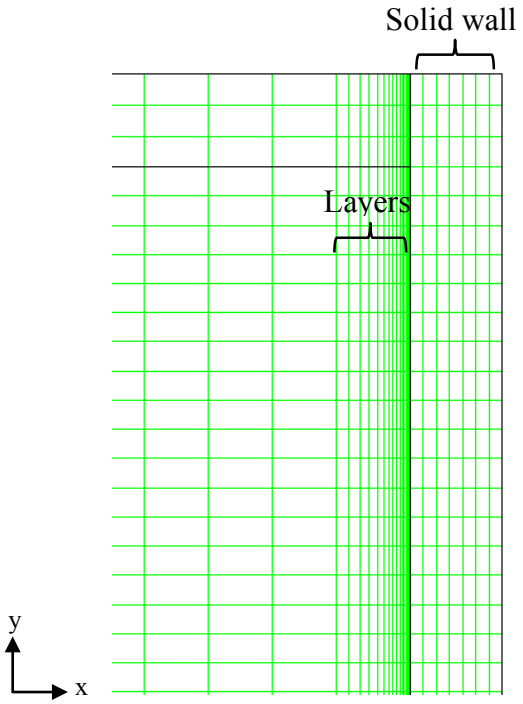

Figure 5.8: Layers near the right wall

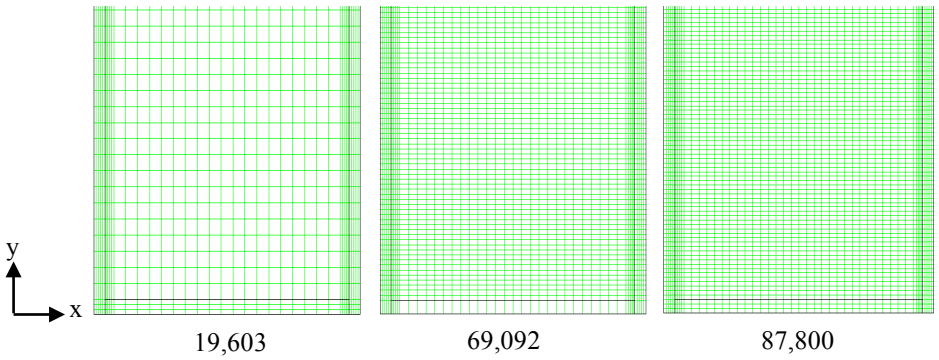

Figure 5.9: A section of the computational mesh

5.6 CFD Model Boundary Conditions

5.6.1 Heat transfer across the condenser section

The condenser section of the thermosyphon is cooled as a result of heat released when vapour condenses, using a double pipe heat exchanger, according to the experimental apparatus. The heat exchanger consists of two concentric pipes, where the saturated vapour flows through the condenser pipe and the cooling water flows in the same direction (parallel flow) through the annular space between the two pipes. The condenser heat exchanger is shown in Figure 5.10.

A forced convection heat transfer takes place between the condenser wall and the cooling fluid and can be explained in an analogous manner to Newton's law of cooling as:

$$\dot{Q}_c = h_c(2\pi r l_c)\,\Delta T_{lm} \tag{5-33}$$

where h_c is the overall heat transfer coefficient of the condenser section's heat exchanger, Q_c is the rate of heat transfer from the condenser, l_c is the condenser height, r is the radius of the condenser and ΔT_{lm} is the logarithm mean temperature difference.

The logarithm mean temperature difference is determined by tracing the actual temperature profile of the fluids along the condenser section's heat exchanger, as illustrated in Figure 5.10 and expressed in Eq. (5-34).

$$\Delta T_{lm} = \frac{\Delta T_1 - \Delta T_2}{ln\ (\frac{\Delta T_1}{\Delta T_2})} = \frac{T_{w,outlet} - T_{w,inlet}}{ln\ (\frac{T_{c,av} - T_{w,inlet}}{T_{c,av} - T_{w,outlet}})} \tag{5-34}$$

where $T_{c,av}$ is the condenser wall average temperature and, $T_{w,outlet}$ and $T_{w,inlet}$ are the cooling water inlet and outlet temperatures, respectively.

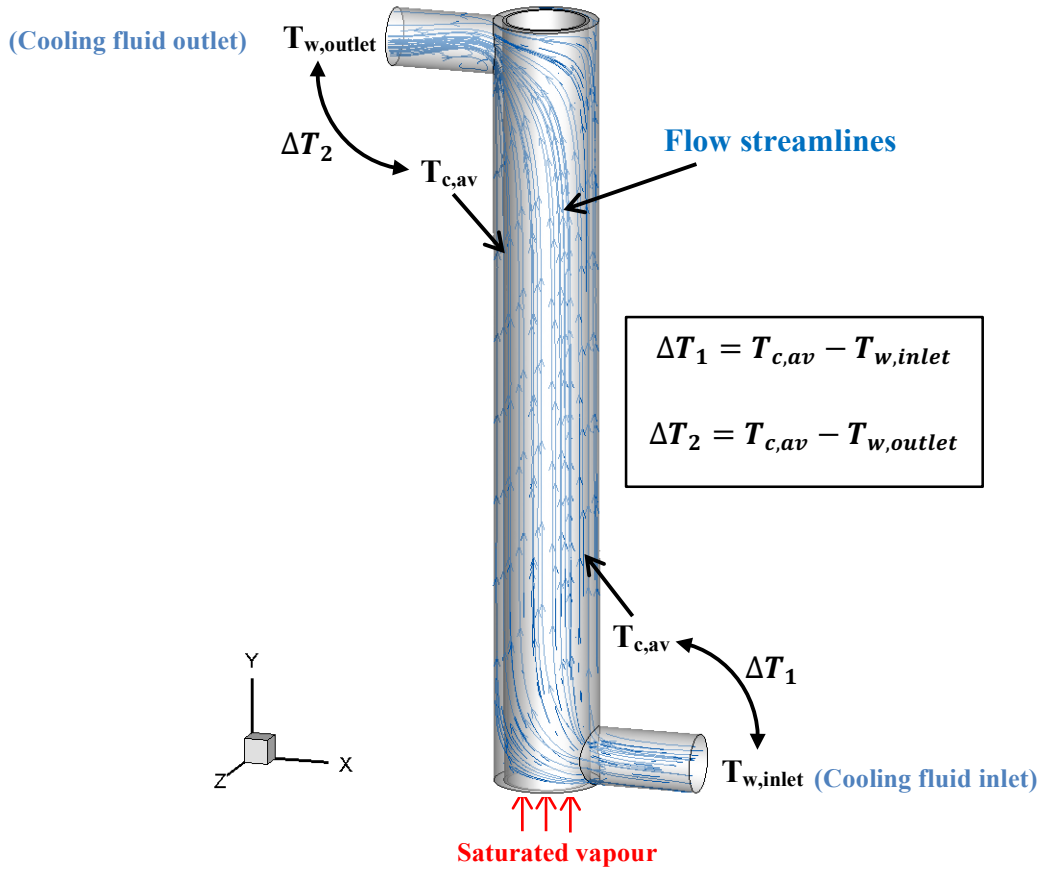

Figure 5.10: Schematic of the flow along the condenser section's heat exchanger

A three-dimensional CFD model has been developed to simulate the heat transfer across the condenser heat exchanger in order to predict the forced convection heat transfer between the condenser wall and the cooling water, $\dot{Q}_c$ and the outlet temperature of the cooling water, $T_{w,outlet}$. The corresponding heat transfer coefficients are then determined by using Eq. (5-33) and Eq. (5-34). Figure 5.11 shows the three-dimensional geometry of the CFD model of the condenser section's heat exchanger. A double pipe heat exchanger with a total length of 200mm and outer diameter of 27mm, as can be seen in the figure, is used as the heat exchanger geometry. The diameter of the inlet and outlet of the cooling fluid to the heat exchanger is 15mm.

The geometry is constructed and meshed using the GAMBIT grid generation software. A mesh of 639,331 cells is used for the simulation. Near the condenser wall, eight layers of cells are used in order to capture the forced convection heat transfer between

the condenser wall and the cooling water. Figure 5.12 shows the computational mesh of the condenser section's heat exchanger.

A steady simulation with a single-phase is carried out to model the condenser section's heat exchanger for the tested working fluids for different power throughputs. For the boundary conditions used in the model, the cooling water inlet is defined as a mass flow rate and is kept constant at 0.003 kg/s, while the cooling water outlet is defined as a pressure outlet. As the simulation at this stage is considered only the condenser section's heat exchanger, the evaporator section is not present and thus the saturated vapour is not simulated. In order to simulate the heat source in the condenser section's heat exchanger, a constant temperature is assumed at the inner wall of the condenser and a temperature boundary condition is defined. The developed three-dimensional CFD model, explained in Chapter 6, will be simulated both the two-phase flow inside the thermosyphon and the condenser section's heat exchanger and hence the saturated vapour will be simulated. Consequently, the inner wall of the condenser section will be defined as coupled wall boundary condition, so as to allow heat to transfer between the saturated vapour region and the condenser solid region. As mentioned earlier, the purpose of this simulation at this stage is to determine the heat transfer coefficients between the condenser wall and the cooling water by predicting the forced convection heat transfer and the temperature of the outlet cooling water in the condenser section's heat exchanger at the same experimental conditions. Hence, the experimental values of the condenser wall temperature and the inlet temperature of the cooling water have been used in this simulation. The experimental data used in the model for different power throughputs are illustrated in Table 5-4. The outer wall of the condenser section's heat exchanger is considered as adiabatic. Figure 5.11 shows the boundary conditions of the condenser section's heat exchanger.

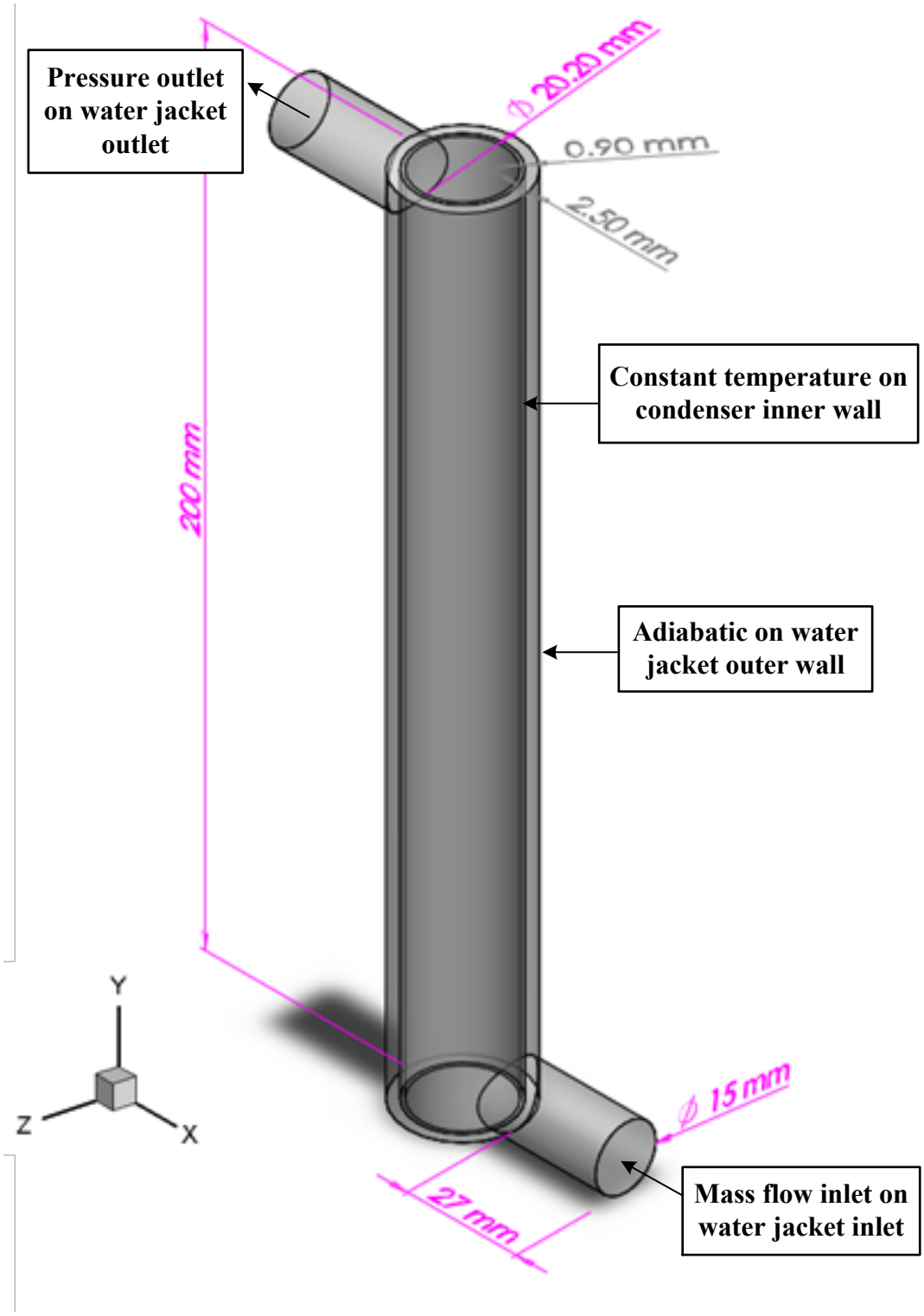

Figure 5.11: Dimensions and boundary conditions of the condenser section's heat exchanger

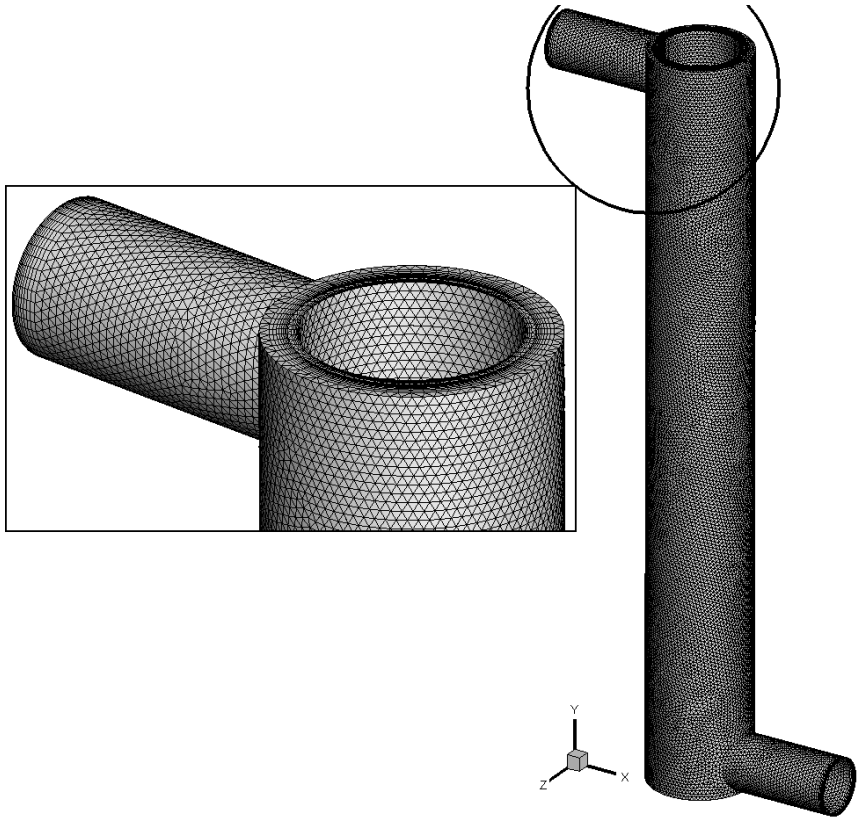

Figure 5.12: The computational mesh of the condenser section's heat exchanger

Table 5-4: Experimental data used in the model of the condenser section's heat exchanger

Water			
Q_c	$T_{c,av}$	$T_{w,inlet}$	$\dot{m}$
W	K	K	kg/s
95.1	312.41	294.75	0.003
162.6	318.1	294.35	0.003
192.2	320.5	294.55	0.003
236.6	325.9	294.85	0.003
254.8	326.15	295.15	0.003
336.6	330.33	294.65	0.003
R134a			
19.74	292.67	293.81	0.003
29.58	291.79	293.75	0.003
39.53	291.11	296.02	0.003
50.16	291.71	294.81	0.003
100.44	294.45	298.57	0.003
R404a			
19.88	300.3	297.74	0.003
29.04	298.7	295.18	0.003
40.66	299.4	294.82	0.003
49.61	301	295.39	0.003
100.65	304.5	294.89	0.003

In order to verify the sensitivity of the results to the value of the heat transfer coefficient, an empirical correlation proposed by Zukauskas [113] is used to determine the average Nusselt number for external forced convection over a circular pipe, defined as

$$Nu_{Zukauskas} = \frac{h_c \, x \, D_c}{k_l} = 0.683 \, Re^{0.466} \, Pr_l^{\frac{1}{3}} \qquad \text{(for } 40 \leq \text{Re} \geq 4000\text{)} \tag{5-35}$$

$$Re = \frac{U \, x \, D_c}{v_l} \tag{5-36}$$

where k_l, v_l and Pr_l are the thermal conductivity, kinematic viscosity and Prandtl number of the condenser cooling water, U is the inlet cooling water velocity and D_c is the condenser diameter.

Churchill and Bernstein [114] reported an additional correlation to determine the average Nusselt number, defined as

$$Nu_{Churchill} = \frac{h_c \, x \, D_c}{k_l} = 0.3 + \frac{Re^{0.5} \, Pr^{\frac{1}{3}}}{[1+(0.4/P_r)^{\frac{2}{3}}]^{\frac{1}{4}}} \left(1 + \left(\frac{Re}{282{,}000}\right)^{\frac{5}{8}}\right)^{\frac{4}{5}} (0.62) \tag{5-37}$$

In order to test the simulation results independence on the condenser heat transfer coefficients, correlations (5-33), (5-35) and (5-37) are checked for the heating power throughput of 30 W for the working fluid R134a. Thus, the average temperature of the evaporator, adiabatic and condenser sections are observed and shown in Table 5-5. From this observation, it is apparent that the average temperature for the evaporator, adiabatic and condenser are very close for different tested correlations. Consequently, the correlation (5-33) is selected to determine the heat transfer coefficients of the condenser's wall based on the CFD modelling results of the condenser section's heat exchanger, and are shown in Table 5-6.

Table 5-5: Average temperatures for the thermosyphon charged with R134a for different heat transfer coefficient correlations

Correlation of condenser heat transfer coefficient		Eq. (5-33)	Eq. (5-35)	Eq. (5-37)
h_c	W/m^2.K	418.3	592.3	654.6
$T_{e,av}$	K	302.5	302.3	302.2
T_a	K	299.7	299.8	299.7
$T_{c,av}$	K	295.6	295.2	295.0

Table 5-6: Heat transfer coefficients for the condenser's heat exchanger

Water				
Q_c	$T_{w,inlet}$	$T_{w,outlet}$	$T_{c,av}$	h_c
W	K	K	K	W/m^2.K
95.1	294.75	304.43	312.41	746.3
162.6	294.35	307.36	318.1	747.6
192.2	294.55	308.79	320.5	746.1
236.6	294.85	311.98	325.9	745.9
254.8	295.15	312.14	326.15	745.9
336.6	294.65	314.19	330.33	745.7
R134a				
19.74	292.67	293.81	296.1	418.3
29.58	291.79	293.75	297.6	418.3
39.53	291.11	296.02	301.5	464.9
50.16	291.71	294.81	300.8	420.5
100.44	294.45	298.57	306.7	418.1
R404a				
19.88	297.74	299.15	300.3	745.3
29.04	295.18	297.12	298.7	746.1
40.66	294.82	297.31	299.4	747.3
49.61	295.39	298.46	301	745.6
100.65	294.89	300.15	304.5	745.9

5.6.2 Boundary and operating conditions of the thermosyphon

A non-slip boundary condition is imposed at the inner walls of the thermosyphon. In order to simulate the heating and evaporation, a constant heat flux is defined at the wall boundaries of the evaporator section, depending on the power input. A zero heat flux is defined as boundary condition on the adiabatic section, assuming this section is insulated. The upper and lower caps of the thermosyphon are also defined as adiabatic. Based on the discussion in the previous section (section 5.6), a convection heat transfer is defined as boundary condition on the condenser's wall. The corresponding heat transfer coefficient values come from the CFD simulation of the condenser section's heat exchanger explained in the previous section and shown in Table 5-6. The interfaces (i.e. inner walls) between the solid and fluid regions of the heat pipe are defined as coupled wall boundary condition, so as to allow heat to transfer between the solid and fluid zones. Figure 5.13 illustrates the boundary conditions implemented to the computational model of the two-phase closed thermosyphon.

The model considered water, as well as R134a and R404, as the working fluids with different fill ratios (the ratio of initial liquid volume per total volume of the evaporator) for water-charger thermosyphon and a 100% filling ratio of the evaporator section (i.e. FR = 1.0) for R134a and R404a charged thermosyphon. The mesh adaption facility in FLUENT was used to define the fill ratio of the working fluid in the fluid region. Apart from the density of the liquid phase and surface tension, the physical properties of the working fluids are assumed to be temperature-independent to limit the calculation time. These properties are taken at 298.15 K using the NIST REFPROP program [74], and can be found in Table 5-7.

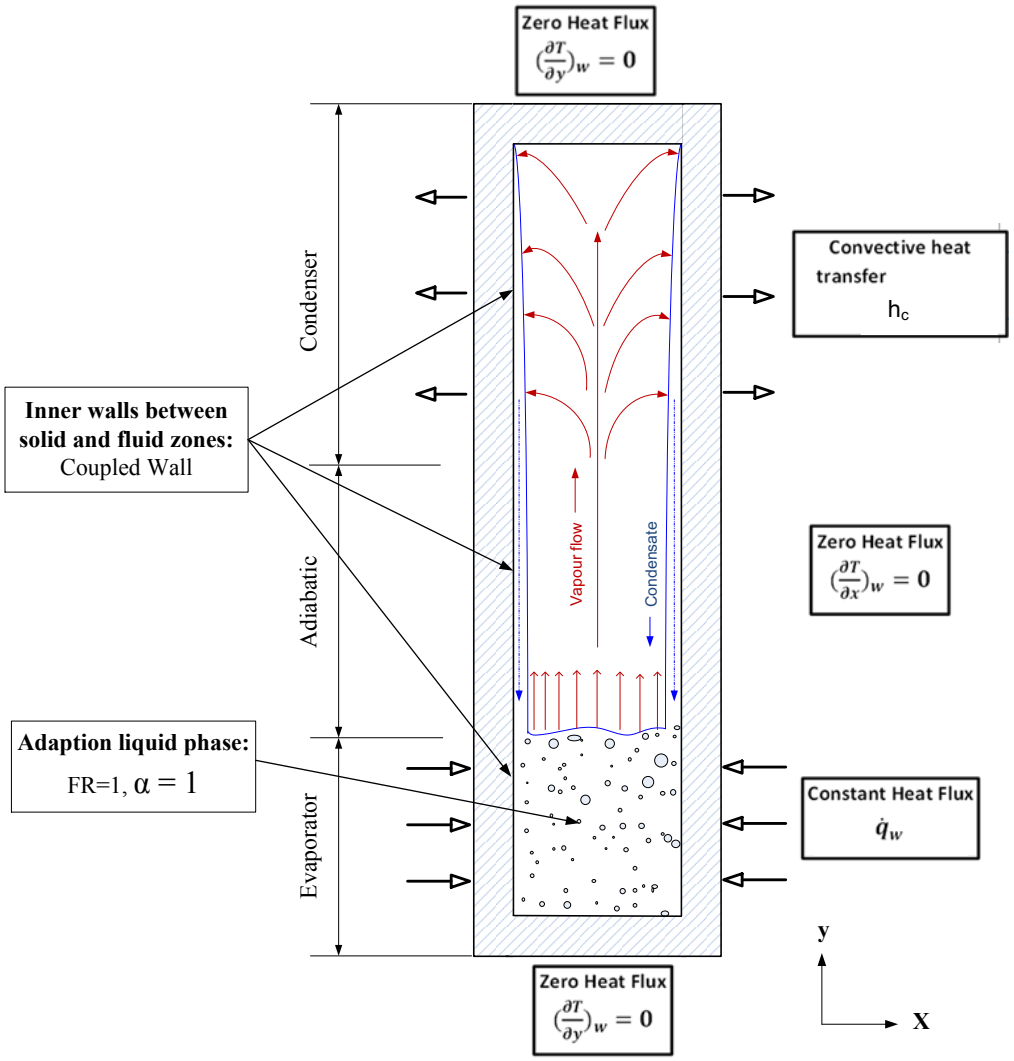

Figure 5.13: Boundary conditions of the thermosyphon

Table 5-7: Physical properties of the working fluids [74]

Physical property	Unit	Working fluid		
		Water	R134a	R404a
Latent heat of evaporation	kJ/kg	2441.7	177.79	140.25
Density of vapour phase	kg/m^3	0.02307	32.35	65.247
Specific heat of liquid phase	kJ/kg.K	4.1816	1.4246	1.5423
Specific heat of vapour phase	kJ/kg.K	1.9118	1.0316	1.2214
Thermal conductivity of liquid phase	W/m.K	0.60646	0.081134	0.063625
Thermal conductivity of vapour phase	W/m.K	0.018433	0.013825	0.015905
Viscosity of liquid phase	kg/m.s	$8.9004x10^{-04}$	$1.9489x10^{-04}$	$1.2827x10^{-04}$
Viscosity of vapour phase	kg/m.s	$9.7009x10^{-06}$	$1.1693x10^{-05}$	$1.2152x10^{-05}$
Molecular weight	kg/kmol	18.015	102.03	97.604
Critical temperature	K	647.1	374.21	345.27
Critical pressure	kPa	22064	40593	3734.9

The density of the liquid phase (ρ_l) of the working fluid is considered as temperature-dependent and fitted into the functions of temperature in the form of high-order polynomial, defined as:

$$\rho_l(T) = \sum_{i=0}^{n=4} C_i \,.\, T^i \tag{5-38}$$

where C_i is the density coefficients listed in Table 5-8.

The effect of surface tension (σ_{lv}) along the interface between the two phases is also considered as temperature-dependent and included in the model by using the following correlation.

$$\sigma_{lv}(T) = \sum_{i=0}^{n=3} B_i \, . \, T^i \tag{5-39}$$

where B_i is the surface tension coefficients listed in Table 5-8.

The data source of the thermophysical properties of the correlations listed in Table 5-8 is obtained using the NIST REFPROP program [74].

Table 5-8: Density and surface tension correlations of the working fluids

Working fluid	**Density ρ_l**				
	C_0	C_1	C_2	C_3	C_4
Water	717.85	2.3932	- 0.00572	2.794x10-06	0
R134a	3952.801	-25.9914	0.09482	$-1.290x10^{-04}$	0
R404a	- 23723.15	380.3528	- 2.14135	0.005318	$-4.965x10^{-06}$
	Surface tension σ_{lv}				
	B_0	B_1	B_2	B_3	-
Water	0.08343	$1.04637x10^{-04}$	$– 5.723x10^{-07}$	$3.104x10^{-10}$	
R134a	0.04929	$– 8.34x10^{-05}$	$– 3.95x10^{-07}$	$7.071x10^{-10}$	-
R404a	0.03121	$7.1086x10^{-05}$	$– 9.82x10^{-07}$	$1.485x10^{-09}$	-

5.7 Solution Strategy and Convergence Criterion

A transient simulation (i.e. time-dependent simulation) with a time step of 0.0005 s for the water-charged thermosyphon and 0.001 s for the R134a and R404a charged thermosyphon are carried out to model the dynamic behaviour of the two-phase flow and the pool boiling process. The time step has been selected based on the Courant number, which is the ratio of the time step to the time a fluid takes to move across a cell. Because the pool boiling process for water is unstable and in vigorous irregular motion, a small time step has been selected to simulate the pool boiling behaviour for the water-charged thermosyphon. In contrast, the pool boiling process for refrigerants is less vigorous and thus a larger time step has been selected to simulate the pool boiling behaviour for the refrigerants charged thermosyphon.

In the current CFD model, the continuity equation has been solved to track the interface between the two phases by determining the volume fraction of each phase, and the energy equation has been solved to observe the temperature distribution along the computational domain. The fluid is assumed to be laminar. For VOF models, the maximum Courant number allowed near the interface is 250 [26]. The Courant number is less than 3 for a time step of 0.0005 and about 1 for a time step of 0.001. The simulation reaches a steady-state within 60 s.

FLUENT provides different segregated types of algorithm for pressure-velocity coupling. For reduced CPU time and to avoid convergence difficulties, a combination of the SIMPLE algorithm for pressure-velocity coupling and a first-order upwind scheme for the determination of momentum and energy is included in the model. Geo-Reconstruct and PRESTO discretization for the volume fraction and pressure interpolation scheme, respectively, are also performed in the simulation. In the current work, the numerical computation is considered to have converged when the scaled residual is 10^{-5} for the variables volume fraction and velocity components and about 10^{-6} for the temperature variable. The governing equations are solved throughout the CFD computational domain. In particular, the variables appearing in the governing equations are determined by the presence of the phases in each cell in the computational domain. For example, the volume fraction of each phase is determined by tracking the interface between the different phases in each cell in the computational domain. Tracking of the interfaces between *N* different phases present in the computational domain is accomplished by solving the continuity equation for the volume fraction of *N-1* phases. The residual for each variable is calculated by averaging values computed in each cell.

The vapour phase of the working fluid is defined as the primary phase and liquid phase of the working fluid is defined as the secondary phase. For the calculation of the mass and heat transfer during the evaporation and condensation processes, the boiling temperatures and the latent heat of evaporation of the working fluids have been defined in the UDF code. When the simulation is started, the liquid pool in the evaporator is heated first. Once the saturation temperature defined in the UDF is reached, evaporation starts and phase change occurs due to boiling at the inner evaporator wall. The saturated

vapour is then flow upward, where it condenses along the cold walls of the condenser forming a thin liquid film.

5.8 CFD Simulation Results and Discussion

CFD has the ability to provide a comprehensive flow visualisation. Thus, the phase change phenomena occurs that from liquid to vapour phase during the pool boiling in the evaporator section, and from vapour to liquid phase during the liquid film condensation in the condenser section will be presented for the tested working fluids. The thermal performance for different working fluids, filling ratios and heating power inputs will be discussed. The wall temperature distribution profiles along the thermosyphon will also be discussed. The CFD simulation findings for water-filled thermosyphon have been published in [75] and for R134a and R404a filled thermosyphons have been published in [115].

5.9 CFD Simulation of Water-Charged Thermosyphon

It is known from classical working fluids such as water that the filling ratio has a non-negligible influence on the thermal performance of heat pipes [2]. The filling ratio is the ratio of the working fluid volume to the volume of the evaporator section. As shown in Figure 5.14, different working fluid filling ratios of 0.3, 0.5, 0.8 and 1.0 have been adopted to investigate the thermal performance of the water-charged thermosyphon at varying heat throughputs. Different contour plots will be generated to present the flow visualisation during the operation of the thermosyphon. The temperature distribution profiles along the water-charged thermosyphon with the fill ratio of 0.5 will be compared with experimental measurements for different heating throughputs. The thermal performance of the water-filled thermosyphon for the tested fill ratios will be discussed.

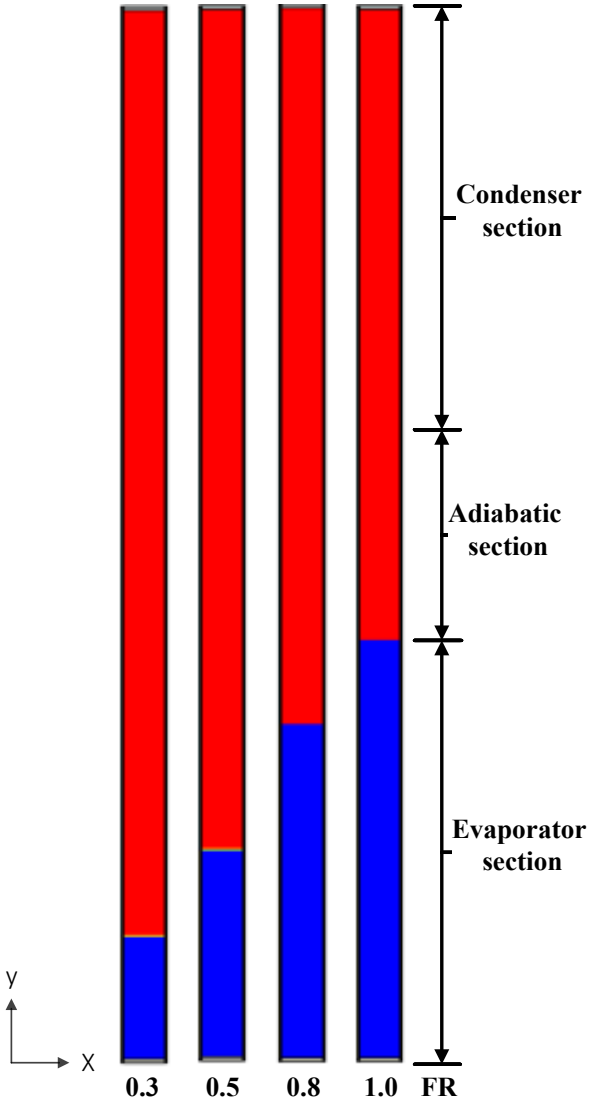

Figure 5.14: Tested fill ratio levels of the working fluid in the evaporator section for a water-filled thermosyphon

5.9.1 Flow visualisation of CFD simulation

In the following sub-sections, the CFD simulation findings from the tests will be visualised and an analysis of the nature of the heat transfer, pool boiling and liquid film condensation processes within the water-charged thermosyphon, will be discussed

5.9.1.1 Heat transfer process

In order to understand the heat transfer process during the thermosyphon operation, the temperature contours at different times have been observed during the start-up (heating) and steady-state operation. In this visual observation, the temperature distribution in the fluid region inside the evaporator, adiabatic and condenser sections has been recorded for different fill ratios. Two fill ratios (0.5 and 1.0) have been selected to demonstrate the heat transfer process for water and shown in Figure 5.15 and Figure 5.16, respectively. A heating power of 173 W is selected to compare the heat transfer process for both fill ratios.

At the beginning, the temperature in the evaporator section increased due to the constant heat flux throughput, which allows heat to transfer through the evaporator wall into the water pool, as shown in Figure 5.15 (0.5 s and 1 s). Due to the temperature difference between the wall and the working fluid within the thermosyphon, boiling heat transfer continues on the walls of the evaporator section. The region of high temperature in the evaporator section expands due to the vapour moving upward, as shown in Figure 5.15 (1.5 s - 3 s). As the heating power in the evaporator section continues, the vapour flows across the adiabatic section to the condenser section, as shown in Figure 5.15 (4 s and 5 s). Then, a high temperature region appears in the condenser section due to the vapour reaching this section, as shown in Figure 5.15 (10 s). As the vapour condenses along the inner surface of the condenser wall, a lower temperature is seen near the inner surface of the condenser wall. With the help of gravity, the condensed liquid falls back to the evaporator section. The above cycle describes the process of heat transfer during the operation of the thermosyphon. After that, the temperature distribution inside the thermosyphon becomes uniform as shown in Figure 5.15 (30 s - 60 s).

A similar heat transfer process for the water filling the total volume of the evaporator section (fill ratio 1.0) is observed to those of the half-filled evaporator section, as shown in Figure 5.16.

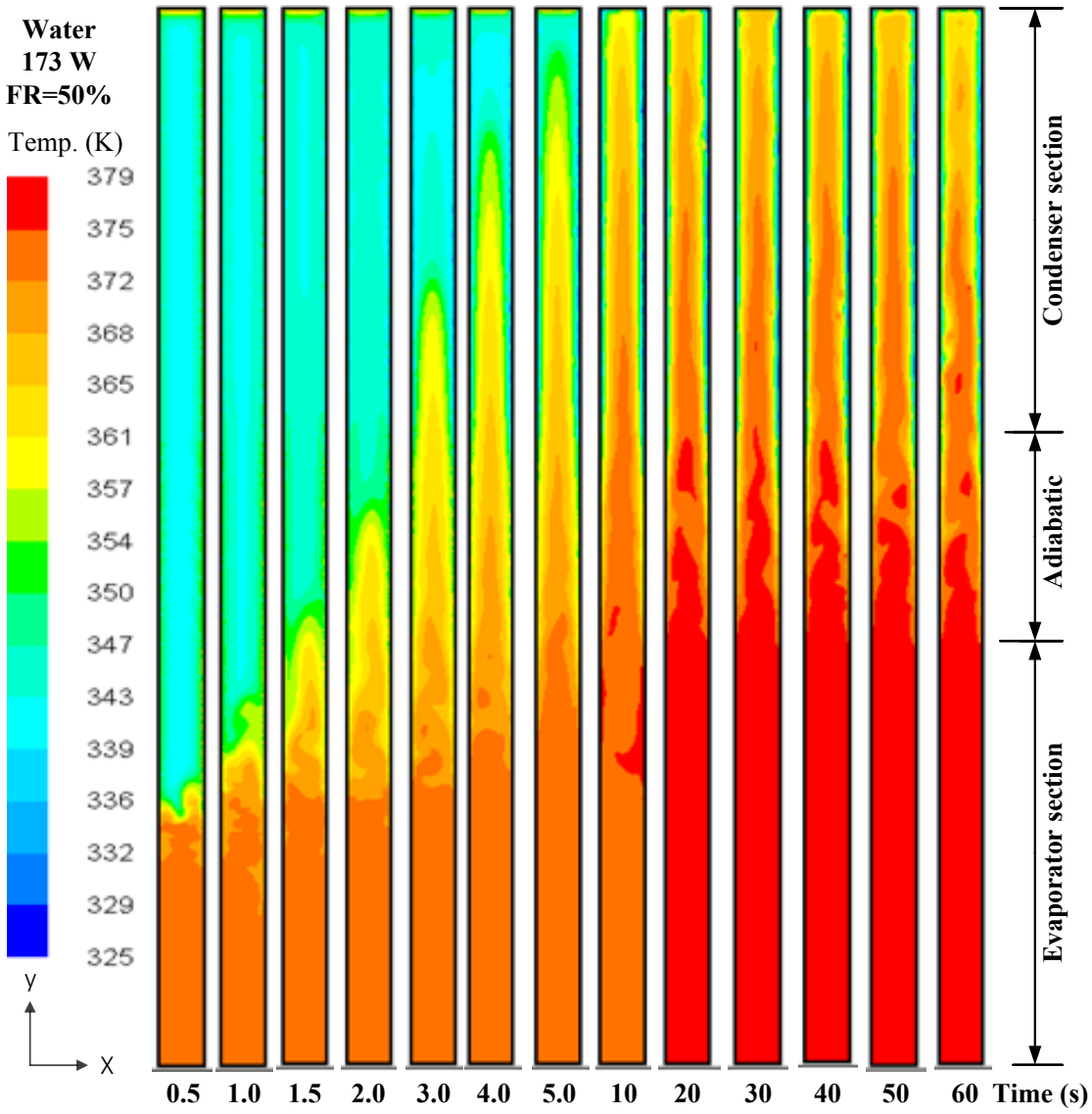

Figure 5.15: Temperature distribution contours of heat transfer process for water-filled thermosyphon at different times for 0.5 fill ratio

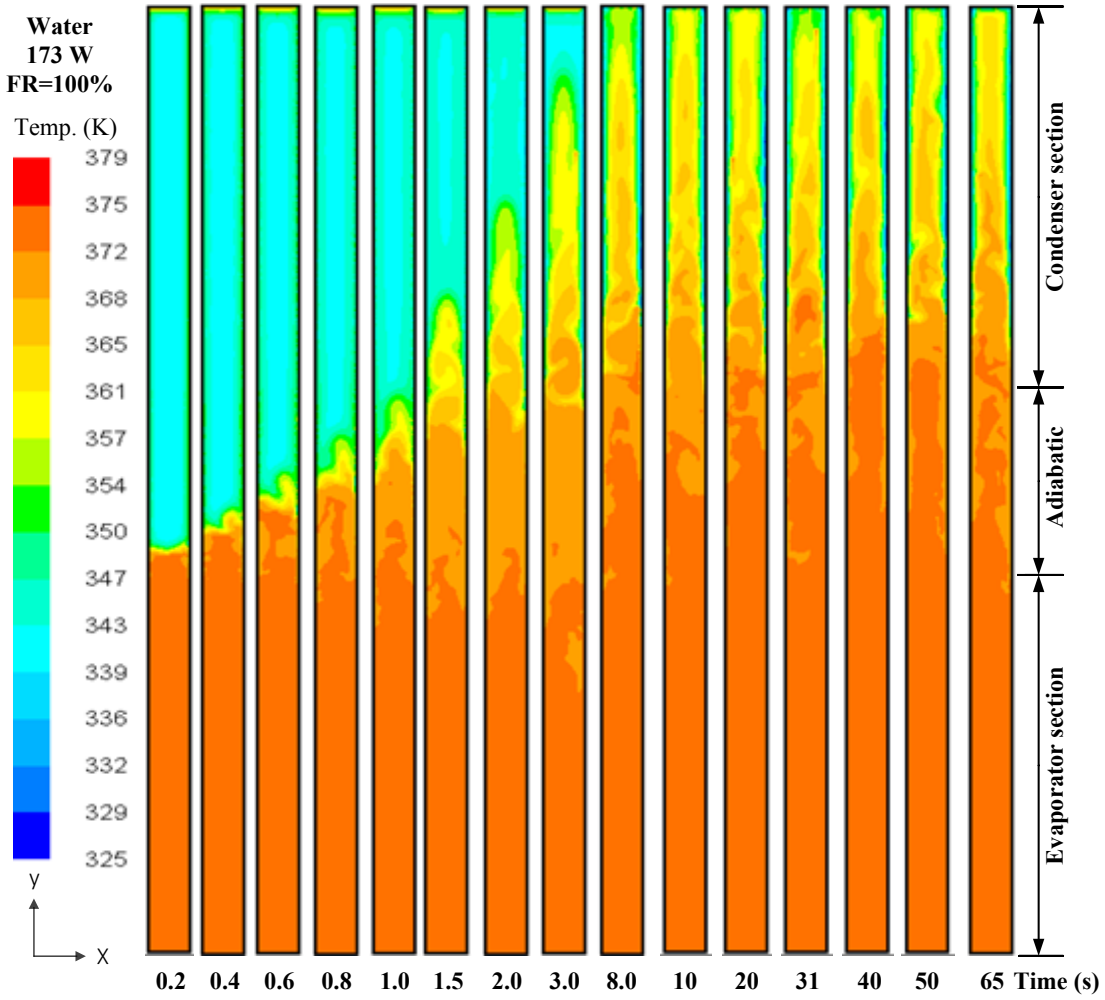

Figure 5.16: Temperature distribution contours of heat transfer process for water-filled thermosyphon at different times for 1.0 fill ratio

5.9.1.2 Evaporation process

The pool boiling phenomenon taking place inside the evaporator section has also been visualised. Figure 5.17 and Figure 5.18 show the volume fraction contours of water pool boiling in the evaporator with the fill ratios of 0.5 and 1.0, respectively, for a heating power of 173 W. A red colour illustrates the presence of only vapour (vapour volume fraction = 1), while a blue colour stands for the presence of only liquid (vapour volume fraction = 0). At the beginning of the process, the liquid pool that initially filled half of the evaporator for FR = 0.5 (Figure 5.17), and filled the total volume of the evaporator for FR = 1.0 (Figure 5.18), was heated by imposing a constant heat flux into the wall of the evaporator section. Heat is then conducted through the evaporator wall to the inner wall to be transferred into the saturated liquid by boiling. At positions where the liquid temperature exceeds the saturation temperature, the liquid begins to boil and phase change occurs. Hence, nucleation sites take place and vapour bubbles start to form at those positions, as shown in Figure 5.17 and Figure 5.18. Isolated vapour bubbles are formed due to continuous nucleation and transported toward the top region of the water pool where they break up and release their vapour content, as can be seen in the figures. This continuous boiling of liquid results in a decrease in the liquid volume fraction and an increase of the vapour volume fraction.

5.9.1.3 Condensation process

Following the evaporation process, where the liquid pool of the working fluid changes to vapour, the converse process takes place in the condenser section. Figure 5.19 illustrates the liquid film condensation phenomena that occur along the inner surface of the condenser wall and focus is made on the condensed liquid film region in the lower part of the condenser. After the boiling process, saturated vapour is transported upward to the condenser. As the vapour reaches the condenser's wall, where a convection heat transfer boundary condition is defined, the vapour condenses along the cold walls forming filmwise condensation as shown in Figure 5.19. As the condenser section is placed above the evaporator, the liquid film is returned by gravity and recharges the water pool in the evaporator section.

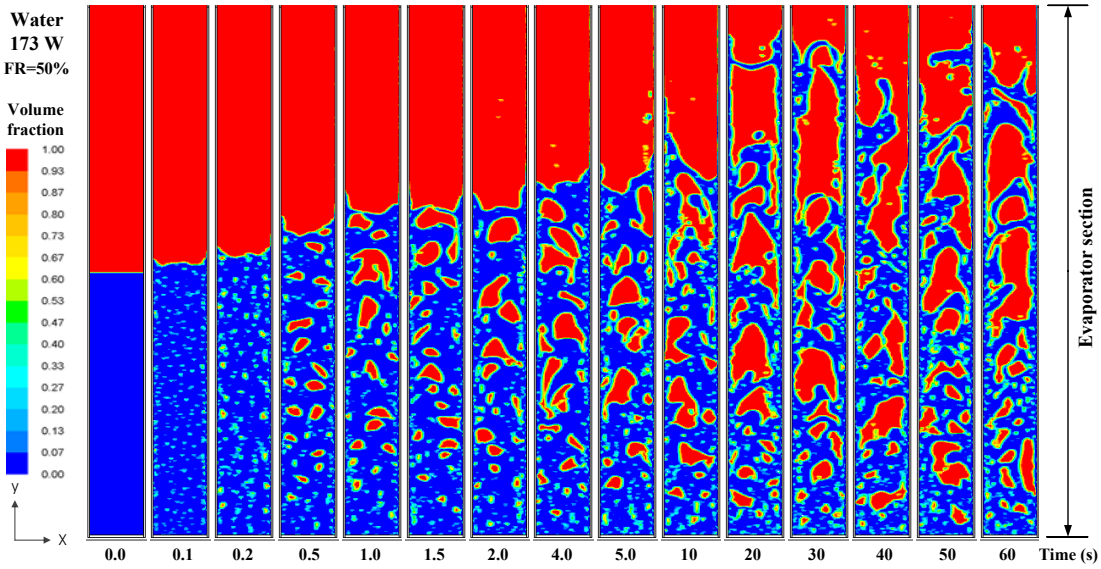

Figure 5.17: Volume fraction contours of pool boiling process in the evaporator section for water-filled thermosyphon with 0.5 fill ratio

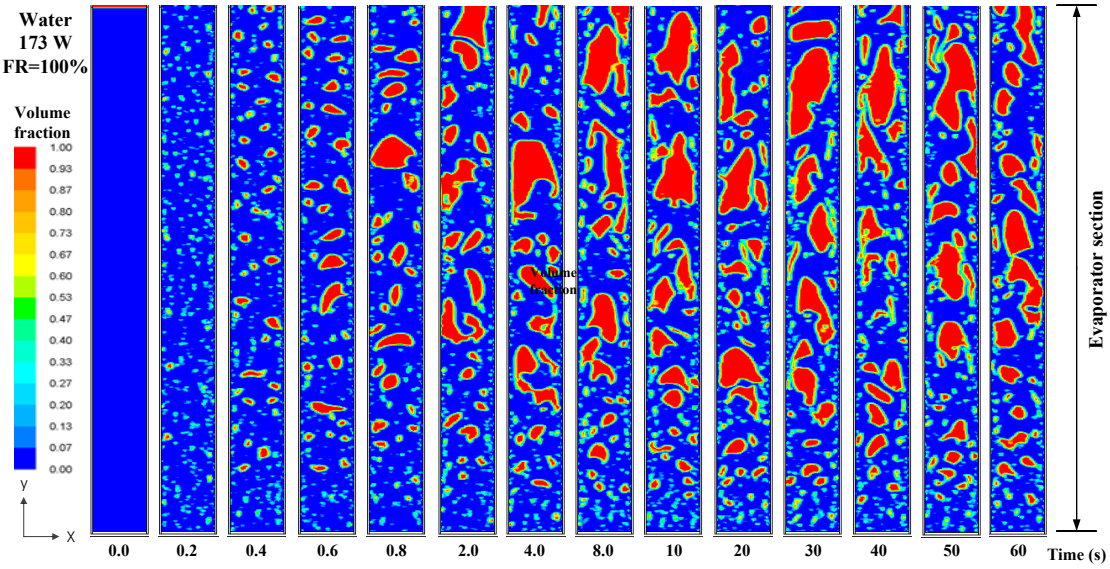

Figure 5.18: Volume fraction contours of pool boiling process in the evaporator section for water-filled thermosyphon with 1.0 fill ratio

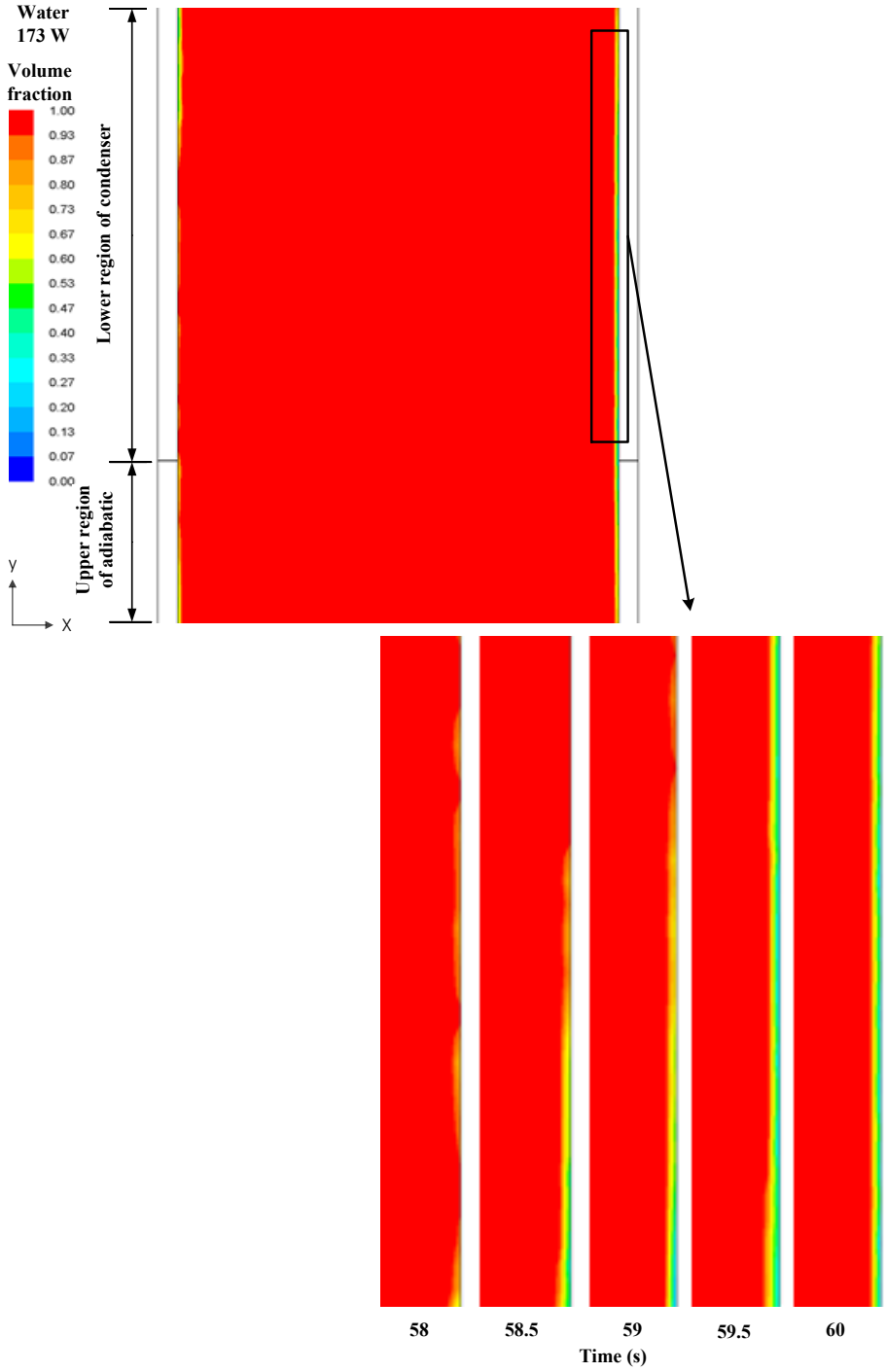

Figure 5.19: Volume fraction contours of liquid film condensation process for water-filled thermosyphon with 0.5 fill ratio

5.9.2 Temperature distribution of CFD simulation of thermosyphon

5.9.2.1 Heat pipe start-up characteristics

Heat pipe start-up characteristics have been categorised into four modes according to Chi [24]. These categories depend on a number of conditions, namely the pipe structure, the condenser cooling system, the thermal resistance between the condenser external surface and the heat sink and the vapour pressure of the working fluid. Figure 5.20 to Figure 5.23 reported by Chi [24] show the temperature distribution profiles along the heat pipe at varying heat loads.

Figure 5.20 illustrates schematically the failure start-up of a heat pipe due to the very low vapour pressure of the working fluid, as well as the thermal resistance between the condenser section and the heat sink. As a result, the increase in the heat load at the evaporator section fails to raise the temperature at the condenser section, as shown in the figure. Figure 5.21 illustrates another failure start-up of a heat pipe due to the presence of a non-condensable gas at the end of the condenser section. As a result, the temperature of the heat pipe remains uniform apart from the region of the non-condensable gas. As the heat load rises, a successful start-up can be achieved, as shown in the figure.

Figure 5.22 shows the successful start-up of a heat pipe and occurs when the vapour pressure of the working fluid is high. As a result, the pressure drop and the velocity of the vapour are small. As the temperature inside the heat pipe is corresponding to the vapour pressure, the temperature of the heat pipe remains uniform and increases with the increase of the heat load, as shown in the figure. Figure 5.23 shows another successful start-up of a heat pipe that occurs when the vapour pressure of the working fluid is low, while the thermal resistance between the condenser section and the heat sink is high. As a result, sonic flow may occur at low heat load. As the heat load rises, the vapour pressure increases and the temperature of the condenser section increases as well, due to the high thermal resistance. As a result, the temperature of the heat pipe remains uniform, as shown in the figure.

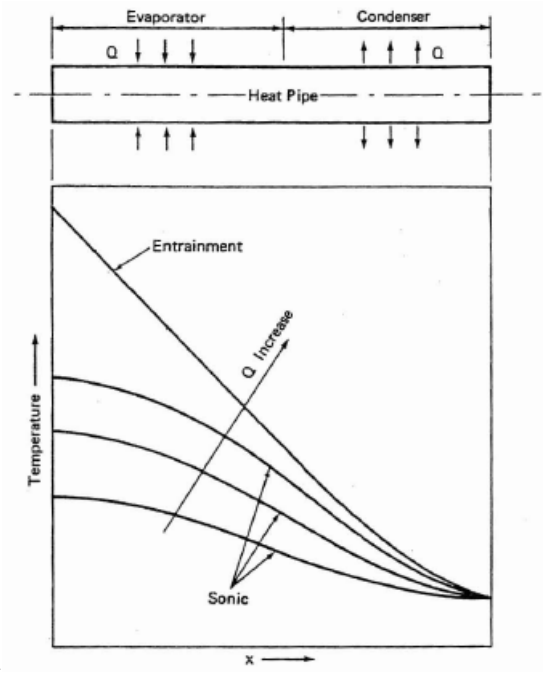

Figure 5.20: A first mode of temperature distribution along a heat pipe when vapour pressure and condenser thermal resistance are very low [24]

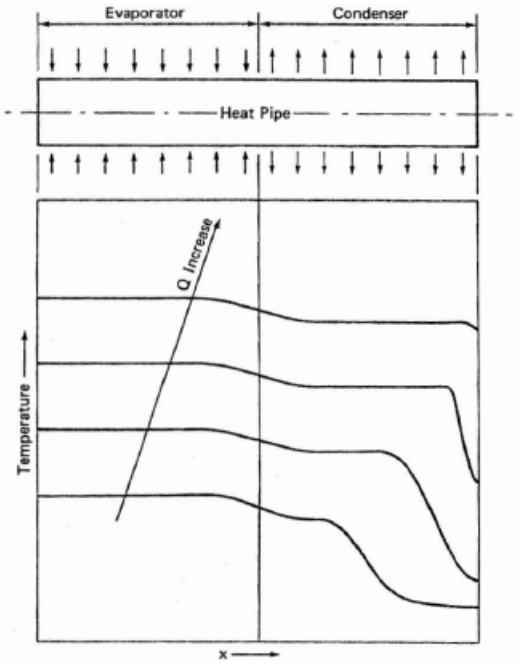

Figure 5.21: A second mode of temperature distribution along a heat pipe when a non-condensable gas is present in the condenser section [24]

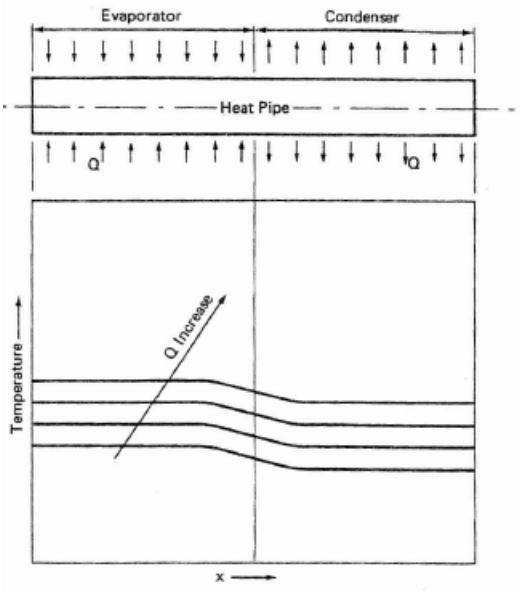

Figure 5.22: A third mode of temperature distribution along a heat pipe when vapour pressure is high [24]

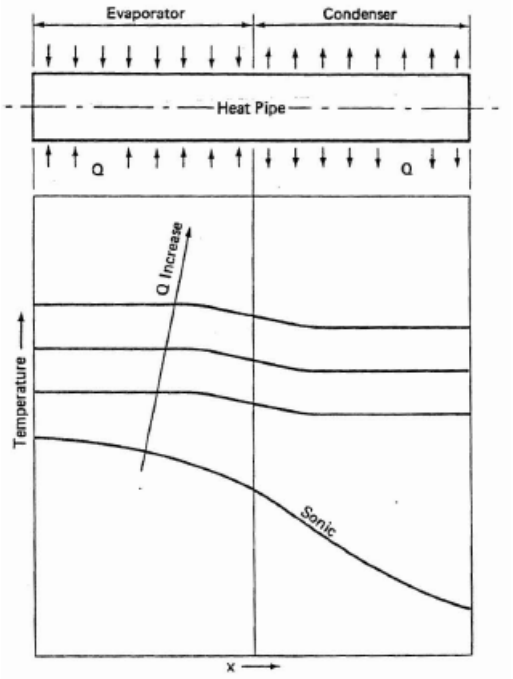

Figure 5.23: A fourth mode of temperature distribution along a heat pipe when vapour pressure is low and condenser thermal resistance is high [24]

5.9.2.2 Temperature distribution of CFD simulations of water-charged thermosyphon with different fill ratios

The simulation results of the boiling and condensation processes for a water-charged thermosyphon reached a quasi-steady state within 60 s. The CFD simulation of the water-charged thermosyphon with fill ratio of 0.5 is validated through comparison with experimental data, as explained in Chapter 4. The temperature distribution along the modelled thermosyphon for heating powers of 173 W and 376 W, with fill ratio of 0.5, are shown in Table 5-9 and Table 5-10, respectively. Eight different positions in the model have been used to monitor the average wall temperatures of the evaporator, adiabatic and condenser sections. Two positions, placed 40mm and 160mm from the bottom, are used to monitor the evaporator section and one position is used at the centre of the adiabatic section. Five evenly spaced positions are used to monitor the condenser section. These five positions are used to confirm the absence of non-condensable gases which, if present, would be swept by the vapour towards the top area of the condenser section where they would accumulate and reduce the thermal performance. Thus, non-condensable gases are neglected in the current CFD model.

Table 5-11 shows the wall average temperatures in the evaporator (Te_{av}), adiabatic (Ta) and condenser (Tc_{av}) sections, in addition to the thermal resistance of the system and the relative error (RE) between CFD simulation (CFD) and experimental results (EXP).

The CFD simulation results of temperature distribution profiles have been compared with the experimental data by determining the average relative error (ARE), which is the absolute percentage different between CFD simulation and experimental average wall temperature results and can be expressed as,

$$ARE = \left[\frac{T_{CFD_{av}}}{T_{EXP_{av}}} - 1\right] * 100 \tag{5-40}$$

The average relative error of evaporator, adiabatic and condenser average wall temperatures are 7.9%, 9.9% and 1.9%, respectively. The CFD simulation results of the thermosyphon with fill ratio of 0.5 showed the same trend as the experimental data. It should be noted that as the power throughput is increased the ARE decreases, as shown

in Table 5-11, and the reason behind this is believed to be the nature of boiling in the evaporator section for the power ratings considered.

Figure 5.24 illustrates the experimental and CFD simulation temperature profiles along the water-charged thermosyphon with fill ratio of 0.5 for varying applied heat loads. The distance between 0 and 200mm indicates the evaporator section. The distance between 200 and 300mm indicates the adiabatic section, while the distance between 300 and 500mm indicates the condenser section. Based on the discussion in the previous section, the predicted CFD temperature distribution are approximately uniform along the evaporator and condenser sections for each respective heat load.

A mathematical model was developed by Shabgard et al. [116] to investigate the thermal characteristics of a closed thermosyphon under different filling conditions. The developed mathematical model was validated through comparison with experimental data reported by Jouhara and Robinson [51] and Baojin et al. [33] Experimental data reported by Baojin et al were used to validate the developed mathematical model and the results illustrated that the evaporator average temperature difference between the predicted and experimental data for the power throughput 331 W was 4.0 K. For the adiabatic and condenser sections, the average temperature difference between the predicted and experimental data was 1.0 K.

In contrast to the present study, the predicted CFD average temperature of the evaporator section has higher differences than the experimental measurements. This can be partially explained by the fact the way of wrapping the evaporator section in the experiment is different to the CFD model, making the CFD evaporator average temperature different from the experimental measurements. In particular, a constant heat power input, in the CFD model, has been applied along the whole length of the evaporator section where, in the experiment, the evaporator section is wrapped by a wire heater, which does not cover the whole length of the evaporator section, and thus less heat is delivered to the evaporator section. Furthermore, the limitations of the CFD model in the present work may also explain some of the differences between prediction and experiment. In particular, enhanced boiling in the evaporation section and fully developed flow, in the experiments, are considered, which is limited in the current CFD model. In the present work, the CFD model managed to take into account the boiling

regimes based on certain functions, however additional development of the user-defined-functions will be required to simulate the bubble generation in the evaporation section in more detail. Hence, very developed boiling could be achieved and the CFD results may be much closer to the experimental data.

As shown in Figure 5.24, the condenser section temperature shows better agreement with the experimental results. As a result of no heat loss in the adiabatic section, the temperature is raised in the surface of this section due to the axial conduction heat transfer.

For the CFD simulations carried out to predict the thermal behaviour of the water-charged thermosyphon for the fill ratios of 0.3, 0.8 and 1.0, Figure 5.25 shows the CFD simulation results of the temperature distribution along the thermosyphon for varying heat loads. The temperature rise of the upper part of the evaporator section in the thermosyphon with 0.3 fill ratio, Figure 5.25 (a), is much higher than the thermosyphon with 0.8 and 1.0 fill ratios. This can be explained by the fact that the amount of working fluid in the evaporator is insufficient to perform enough liquid in the condenser and the return rate of the liquid to the evaporator will be insufficient. It is observed in Figure 5.25 (b) and (c) that the temperature distributions of the thermosyphon with 0.8 and 1.0 fill ratios, respectively, are similar and approximately uniform. For all filling ratios, the temperature distributions of the condenser section are almost uniform except for the lower part for the thermosyphon with 1.0 fill ratio.

Table 5-9: Comparison between experimental data and CFD simulation for heat input of 173 W with 0.5 fill ratio

Section	**Position**	T_{EXP}	T_{CFD}	$\Delta T_{CFD-EXP}$	RE	$T_{EXP\ av}$	$T_{CFD\ av}$	ARE
		K	K	K	%	K	K	%
Evaporator	Te_1	345.75	378.33	32.58	9.42	341.6	378.37	10.78
	Te_2	337.45	378.40	40.95	12.14			
Adiabatic	Ta	327.45	362.41	34.96	10.68			10.68
Condenser	Tc_1	320.55	329.54	8.99	2.80	318.07	326.96	2.80
	Tc_2	318.85	326.54	7.69	2.41			
	Tc_3	317.95	325.95	8.00	2.52			
	Tc_4	317.05	325.64	8.59	2.71			
	Tc_5	315.95	327.13	11.18	3.54			

Table 5-10: Comparison between experimental data and CFD simulation for heat input of 376 W with 0.5 fill ratio

Section	**Position**	T_{EXP}	T_{CFD}	$\Delta T_{CFD-EXP}$	RE	$T_{EXP\ av}$	$T_{CFD\ av}$	ARE
		K	K	K	%	K	K	%
Evaporator	Te_1	376.75	385.14	8.39	2.23	370.2	385.05	4.01
	Te_2	363.65	384.97	21.32	5.86			
Adiabatic	Ta	342.75	370.11	27.36	7.98			7.98
Condenser	Tc_1	328.95	327.12	1.83	0.56	330.33	323.96	1.92
	Tc_2	325.55	323.66	1.89	0.58			
	Tc_3	332.45	323.15	9.3	2.80			
	Tc_4	331.35	322.70	8.65	2.61			
	Tc_5	333.35	323.17	10.18	3.05			

Table 5-11: Comparison between experimental data and CFD simulation for different heat loads with 0.5 fill ratio

Source	**Evaporator**			**Adiabatic**			**Condenser**			**Thermal Resistance**	
Q_{in}	Te_{av} EXP	Te_{av} CFD	ARE	Ta EXP	Ta CFD	ARE	Tc_{av} EXP	Tc_{av} CFD	ARE	R_{EXP}	R_{CFD}
W	K	K	%	K	K	%	K	K	%	K/W	K/W
100.41	343	376.18	9.67	321.25	363.25	13.07	312.412	328.35	5.10	0.3046	0.4763
172.87	341.6	378.37	10.76	327.45	362.41	10.68	318.07	326.96	2.80	0.1361	0.2974
225.25	348.1	379.92	9.14	331.05	364.94	10.24	320.55	323.47	0.91	0.1223	0.2506
275.6	356.1	381.6	7.16	335.55	365.62	8.96	325.95	327.36	0.43	0.1094	0.1967
299.52	358.75	382.41	6.60	336.25	365.46	8.69	323.91	324.81	0.28	0.1163	0.1923
376.14	370.2	385.06	4.01	342.75	370.11	7.98	330.33	323.96	1.93	0.1060	0.1624
Average relative error %			7.89			9.94			1.91		

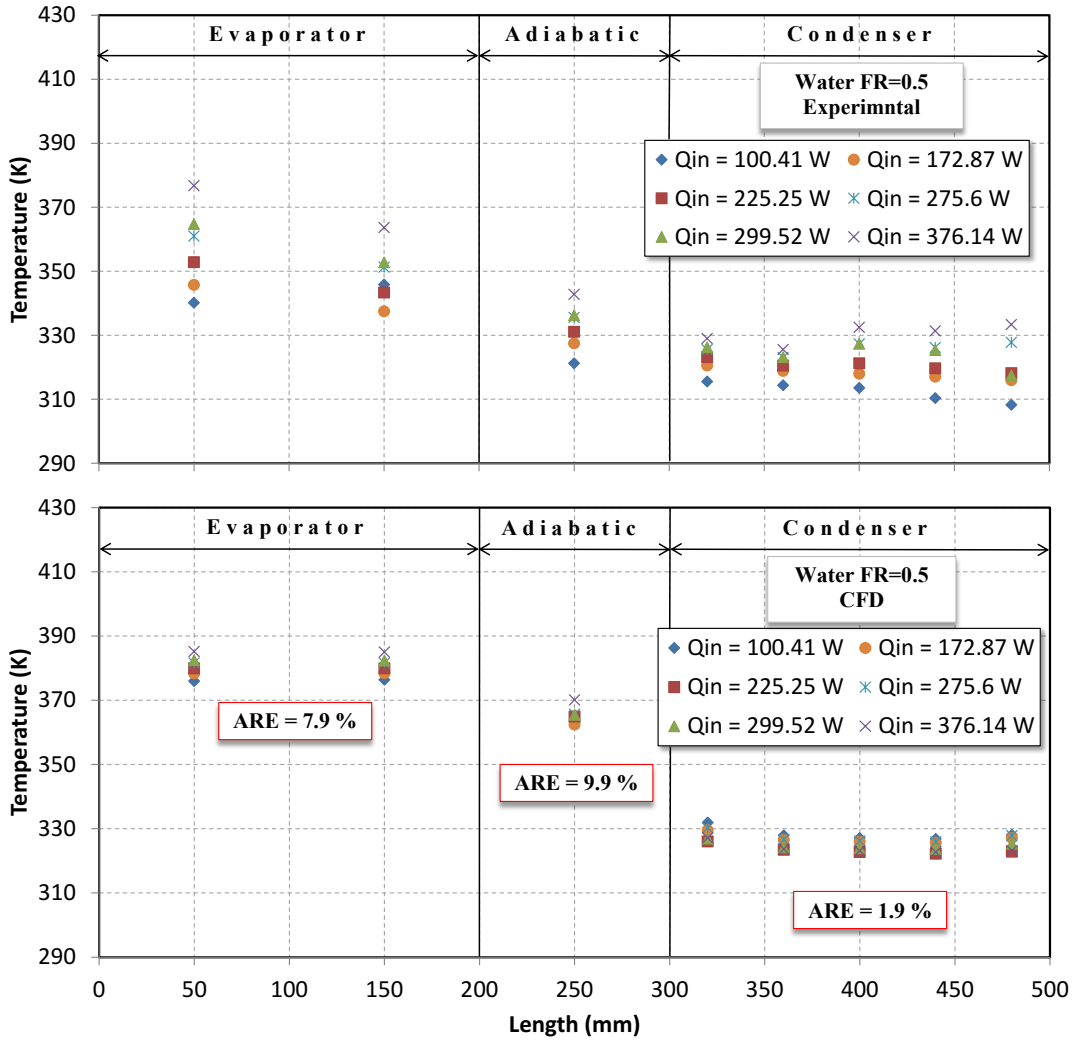

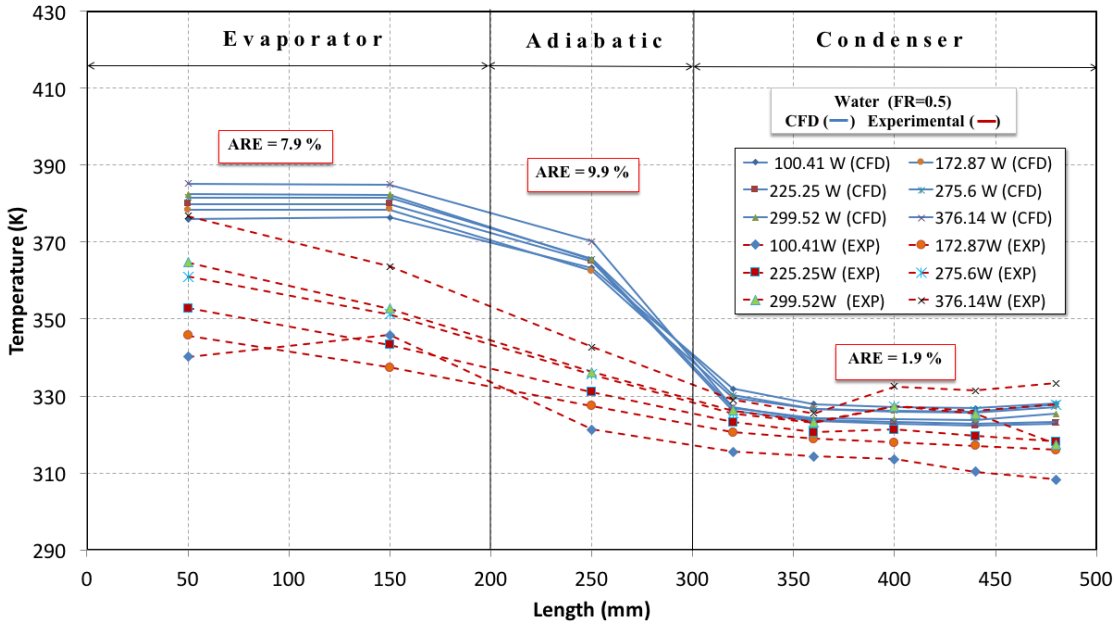

Figure 5.24: Temperature distribution profiles for experiments and CFD simulations along water-filled thermosyphon with 0.5 fill ratio for different heat loads

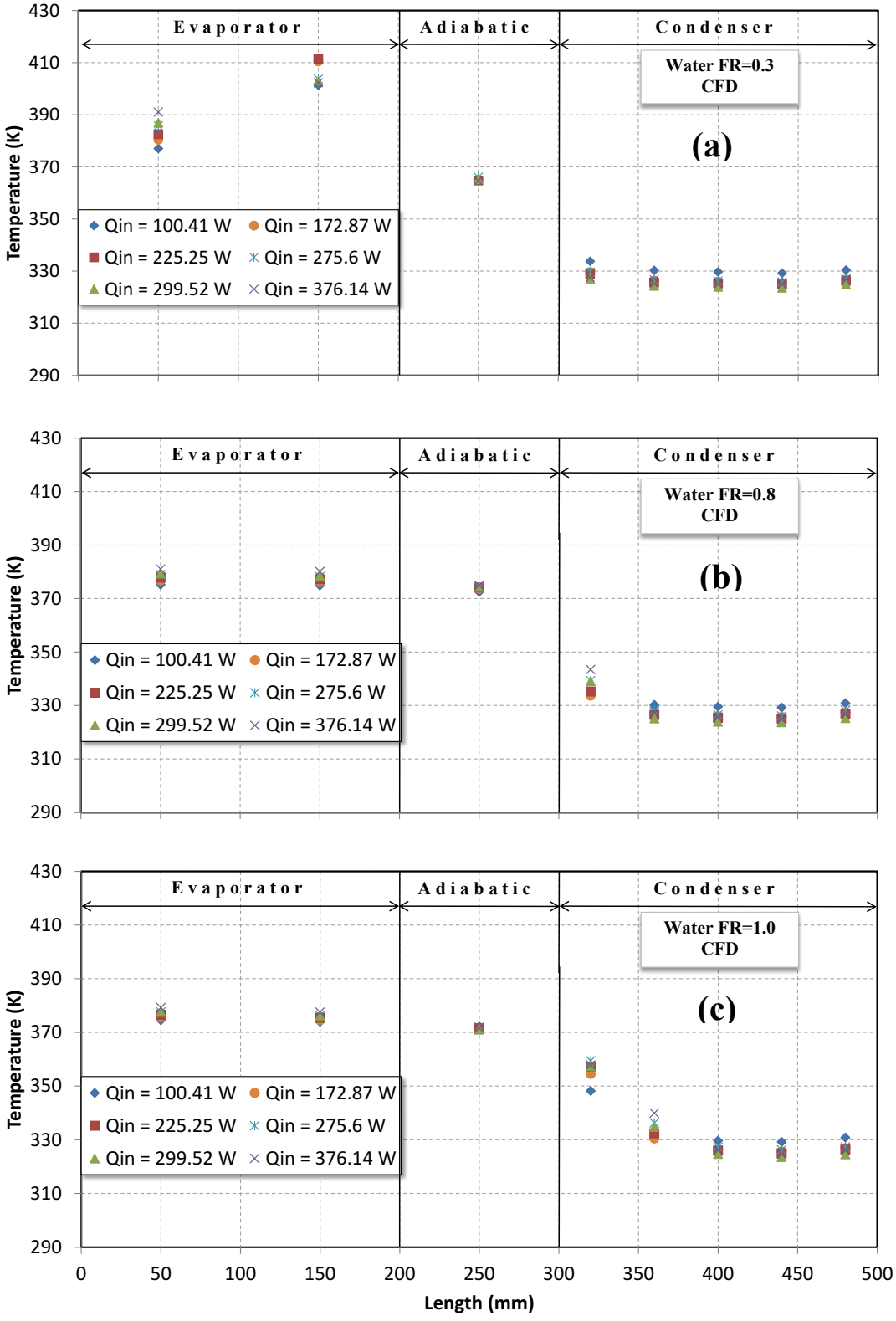

Figure 5.25: Temperature distribution profiles for CFD simulations along water-filled thermosyphon with 0.3 (a), 0.8 (b) and 1.0 (c) fill ratios for different heat loads

5.9.3 Thermal performance of CFD simulation of thermosyphon

The performance of the CFD simulation of thermosyphon can be characterised by the overall thermal resistance (R_{CFD}). The overall rate of heat transfer to the system is proportional to the effective temperature difference between the evaporator and condenser, and inversely proportional to the equivalent thermal resistance to heat transfer between the two regions. The overall rate of heat transfer can be defined as:

$$Q = \frac{\Delta T_{evp-cond}}{R_{eq}} \tag{5-41}$$

The above expression for the overall rate of heat transfer is analogous to the relation for electric current flow $I_{electric}$, expressed as:

$$I_{electric} = \frac{\Delta V_{vol}}{R_{eq}} \tag{5-42}$$

where ΔV_{vol} is the voltage difference.

Consequently, the overall thermal resistance of the CFD simulation of the thermosyphon can be calculated by rearranging Eq. (5-41) to the form,

$$R_{CFD} = \frac{Te_{CFD} - Tc_{CFD}}{Q} \tag{5-43}$$

here $Te_{CFD} = (T_{e1} + T_{e2})/2$ and $Tc_{CFD} = \sum_{j=1\to5} \frac{T_{cj}}{5}$ are the evaporator and condenser average wall temperatures, respectively, and Q is the power throughput.

Figure 5.26 shows the predicted thermal resistance compared with the experimental data. The figure illustrates that the thermal resistance of the thermosyphon decreases with increasing heating power load. For heating powers above 170 W, the thermal resistance stays relatively independent of the heating power input rate. For lower heating inputs, the thermal resistance tends to increase. It is thus suggested that the suppressed activity of the nucleate boiling taking place in the evaporator is the main cause of the deteriorating thermal resistance with decreasing the power loads. In summary, the CFD simulation results are able to show the variation trends of the thermal performance of the thermosyphon for different heat throughputs.

Figure 5.26 also illustrates a comparison of thermal resistances for different filling ratios for the water-charged thermosyphon at different heating powers. For all filling ratios, the figure indicates that lower values of thermal resistance can be obtained for higher heat loads, specifically for the heat load above 300 W. For lower heat loads, the thermal resistance values increase, especially for the fill ratio of 0.3. It is also observed in the figure that the thermal resistance decreased with increasing filling ratio at each same heating power. Thus, the trends observed in the figure are similar for each fill ratio. The fill ratio of 1.0 shows better results in terms of reduced temperature difference across the evaporator and condenser sections and consequently decreased thermal resistance.

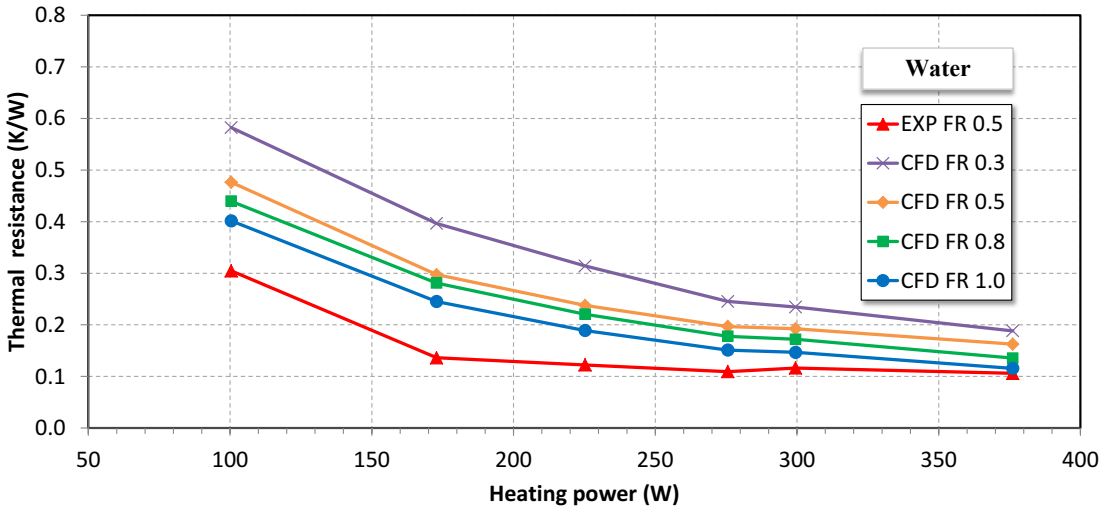

Figure 5.26: CFD simulation and experimental thermal resistance versus heating power for water-filled thermosyphon for different fill ratios

5.10 CFD Simulations of R134a and R404a Charged Thermosyphons

A CFD simulation of a thermosyphon charged with refrigerants that considers all the details of heat transfer phenomena inside the heat pipe will be discussed. Refrigerants R134a and R404a are chosen as the working fluids and filled the total volume of the evaporator section (i.e. FR = 1.0). Similar to the water-charged thermosyphon, the temperature distribution profiles along R134a and R404a charged thermosyphons will be compared with experimental measurements for different heating throughputs for the fill ratio of 1.0. The two-phase flow and heat transfer phenomena will be visualised and the thermal performance will also be discussed.

5.10.1 Flow visualisation of CFD simulation

In the following sub-sections, the CFD simulation findings from the tests will be visualised and an analysis of the nature of the heat transfer, pool boiling and liquid film condensation processes within the R134a and R404a charged thermosyphons for the fill ratio of 1.0 will be discussed.

5.10.1.1 Heat transfer process

In order to understand the heat transfer process during the thermosyphon operation, the temperature distribution in the fluid region inside the evaporator, adiabatic and condenser sections has been recorded for both R134a and R404a. The results for R134a and R404a are shown in Figure 5.27 and Figure 5.28, respectively. A heating power of 30 W is selected to compare the heat transfer process for both working fluids.

At the beginning of the heating procedure, the operating pressure and temperature of the working fluid were set to the saturation values at the initial temperature of the heat pipe (around 298K for both cases), as shown in Figure 5.27 and Figure 5.28 at 0.2 s. Between 2.0 s and 8.0 s, the temperature in the evaporator section increased as a constant heat flux is applied to the outer wall of the evaporator section, which allows the heat to transfer through the evaporator wall into the liquid pool, as shown in Figure 5.27 and Figure 5.28. Boiling heat transfer continues on the walls of the evaporator section due to the temperature difference between the wall and the saturated working fluid within the thermosyphon. The generated vapour then moves upward, as

shown at 20 s and this vapour flows through the adiabatic section to the condenser section, as can be seen at 30 s, 40 s and 50 s in Figure 5.27 and Figure 5.28. Then, a high temperature region appears in the condenser section between 60 s and 90 s due to the vapour reaching this section. The region near the inner wall of the condenser section has a lower temperature than the middle region, as a result of vapour condensing along the inner surface of the condenser wall. Eventually, between 100 s and 120 s, the temperature distribution inside the thermosyphon becomes uniform as shown in Figure 5.27 and Figure 5.28. The above described procedure shows the heat transfer process during the operation of thermosyphons charged with R134a and R404a.

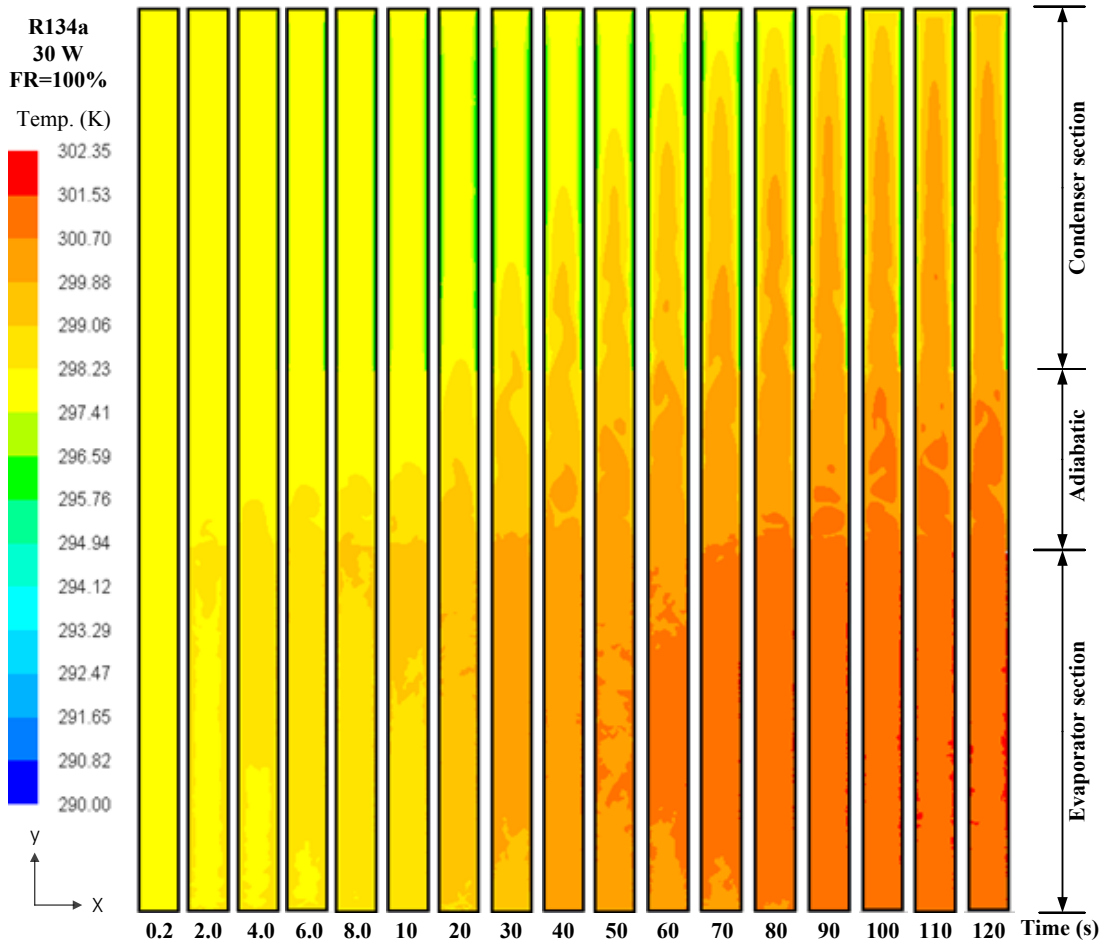

Figure 5.27: Temperature distribution contours of heat transfer process for R134a-filled thermosyphon at different times

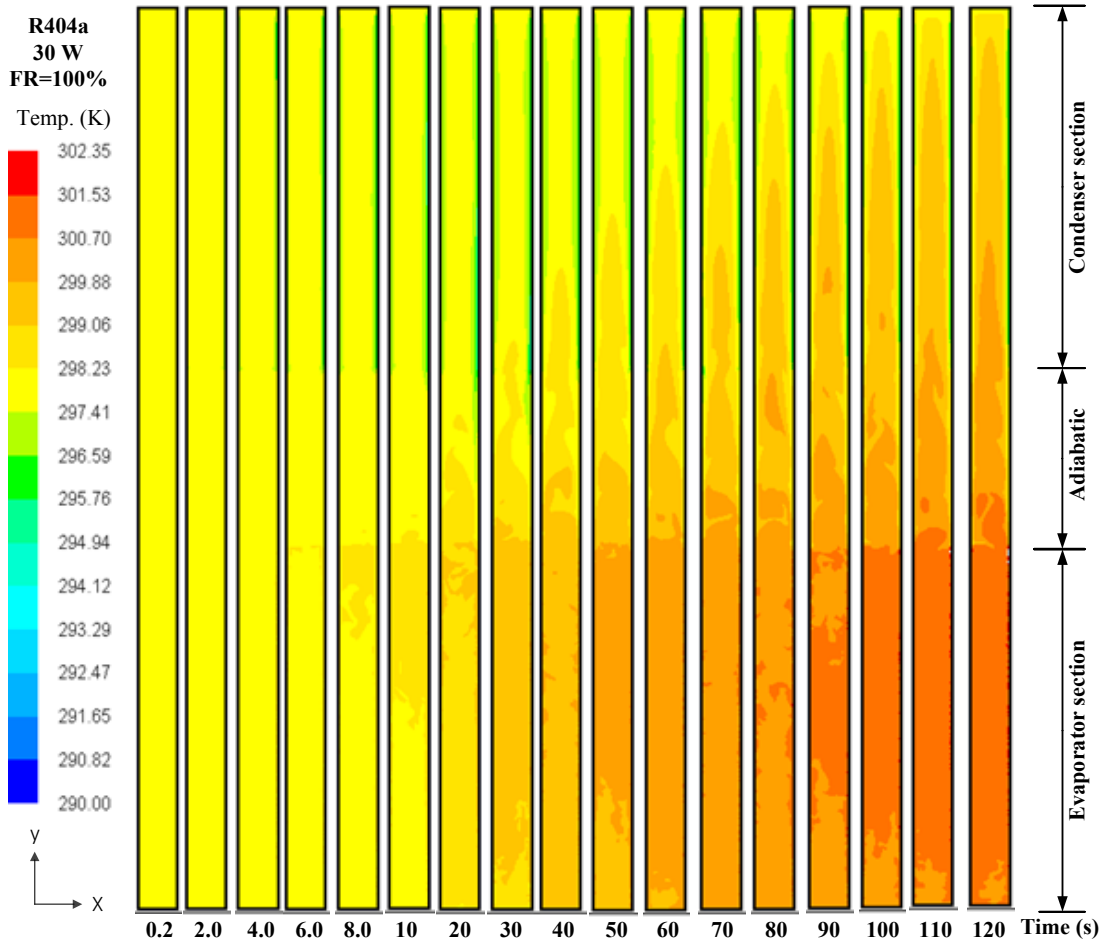

Figure 5.28: Temperature distribution contours of heat transfer process for R404a-filled thermosyphon at different times

5.10.1.2 Evaporation process

The pool boiling phenomena taking place inside the evaporator section has also been visualised during the evaporation process. Figure 5.29 and Figure 5.30 show the volume fraction contours of the liquid pool in the evaporator section for R134a and R404a, for a power throughput of 30 W. The liquid pool of the tested working fluid is represented by a blue colour, which takes the value of 0 of the vapour volume fraction, and the vapour is represented by a red colour, which takes the value of 1 of the vapour volume fraction.

The working fluids have initially filled the total volume of the evaporator section, as shown in Figure 5.29 and Figure 5.30 at 0.0 s. By applying a constant heat flux onto the wall of the evaporator section, heat is then conducted through the evaporator wall to the inner wall to be transferred into the saturated liquid by boiling. Due to the weight of the working fluid column, localised natural convection currents at the lower half of the evaporator section can be seen due to the slight increase in the saturation pressure/temperature of the working fluid. The liquid starts to boil at a position where the liquid temperature at the wall exceeds the saturation temperature (at the adjacent liquid film that is stuck on the inner wall of the evaporator), hence local nucleation sites critical radiuses are exceeded so continuous nucleation takes place. Vapour bubbles then start to form at those positions where the liquid boils, as shown in Figure 5.29 and Figure 5.30 between 2.0 s and 10.0 s. By continuous nucleation, isolated vapour bubbles form and rise all the way up to the top region of the liquid pool before breaking up and releasing their vapour content. This is illustrated in Figure 5.29 and Figure 5.30 at time 20 s and above. During the evaporation process described above, the liquid volume fraction decreases and the vapour volume fraction increases.

It is clear from Figure 5.29 and Figure 5.30 that the pool boiling behaviour of R134a and R404a is significantly different to that of water (Figure 5.18), as very small bubbles grow during the pool boiling. This can be explained by the fact that water requires an amount of heat for evaporation equal to about 2.4 MJ/kg, which is high amount of energy required to evaporate 1 kg of water comparing to R134a and R404a (about 0.2 MJ/kg). The results for both water and the refrigerants have been validated visually using transparent glass wickless heat pipes. This provides evidence that the CFD model

has the ability to reproduce the difference in pool boiling behaviour between different working fluids.

5.10.1.3 Condensation process

Following the boiling process, the converse process takes place in the condenser section. The CFD model predicts the condensate film configuration as illustrated in Figure 5.31 for the R404a charged thermosyphon that was undergoing a power throughput of 30 W.

After the pool boiling process, the saturated vapour flows through the adiabatic section and into the condenser section. As the saturated vapour contacts the condenser's surface, where the temperature is below the saturation temperature of the vapour, the vapour condenses along the cold walls forming a liquid film as shown in Figure 5.31 at the condenser zone. This liquid film will then fall down under gravity through the adiabatic section, as can be seen in Figure 5.31 at the adiabatic zone. Eventually, the liquid pool in the evaporator section will be charged by a continuous thin liquid film as shown in Figure 5.31 at the evaporator zone. During the above cycle, heat in the form of the latent heat that was absorbed in the evaporator section is released by the vapour and transferred through the liquid film to the condenser wall, where a convection heat transfer boundary condition is defined.

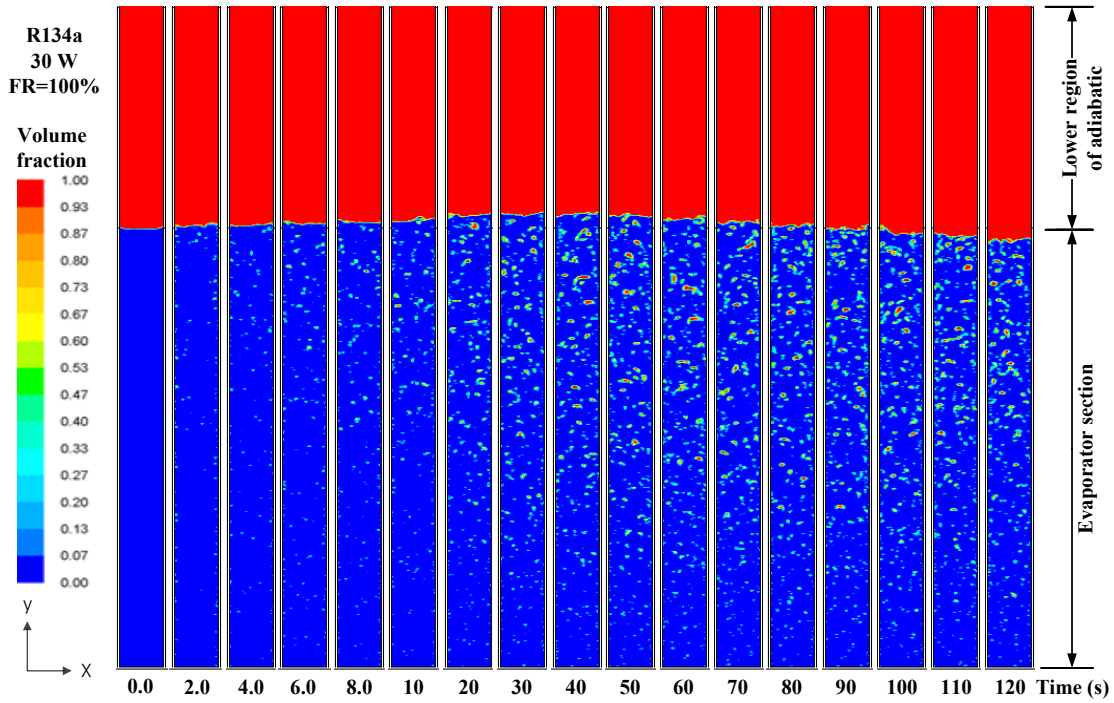

Figure 5.29: Volume fraction contours of pool boiling process in the evaporator section for R134a-filled thermosyphon

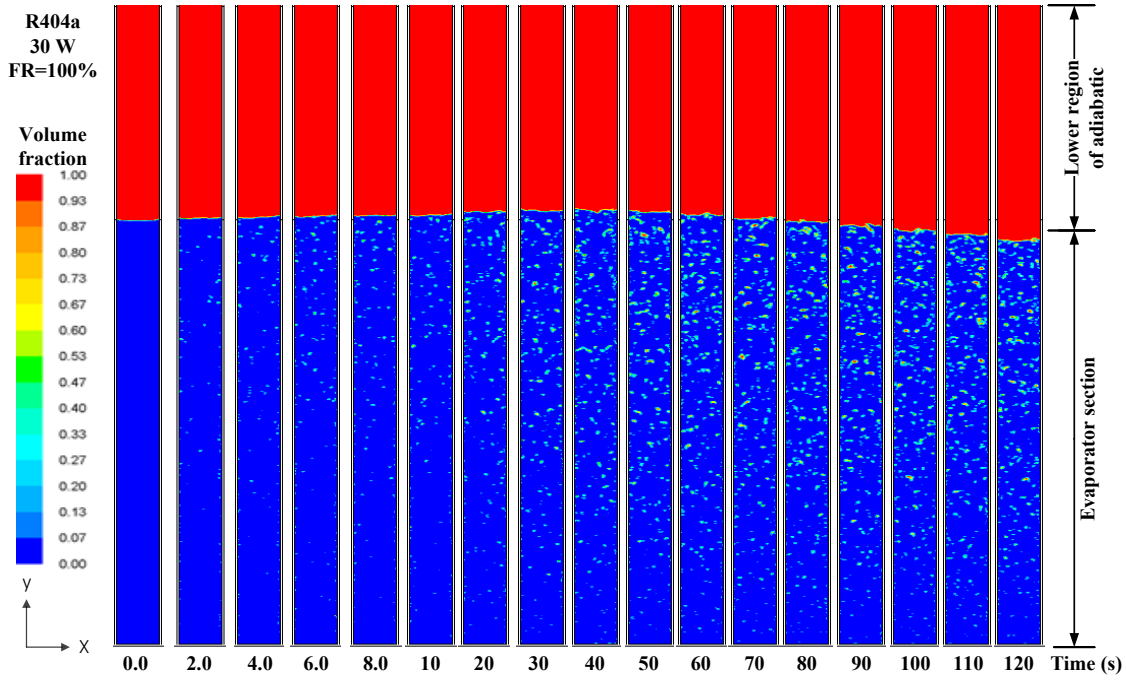

Figure 5.30: Volume fraction contours of pool boiling process in the evaporator section for R404a-filled thermosyphon

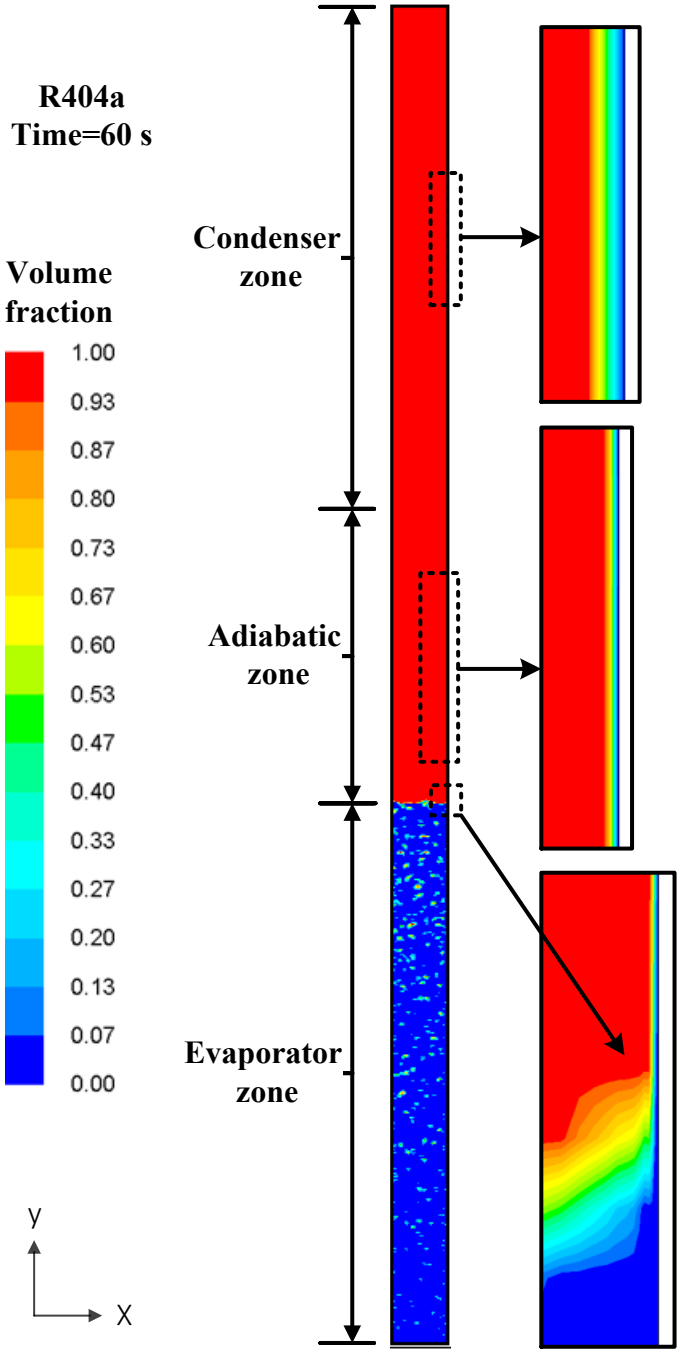

Figure 5.31: Volume fraction contours of liquid film condensation process for R404a-filled thermosyphon

5.10.2 Temperature distribution of CFD simulation of thermosyphon

In order to investigate the thermal performance of the refrigerant-filled thermosyphon, the temperature distribution profiles along the thermosyphon have been observed under different power throughputs. Eight different positions have been used to monitor the average wall temperature for the evaporator, adiabatic and condenser sections. Two positions are used to monitor the evaporator section and one position is used at the centre of the adiabatic section. Five evenly spaced positions are used to monitor the condenser section.

Figure 5.32 and Figure 5.33 illustrate the experimental and CFD simulation temperature distributions along the R134a and R404a charged thermosyphons, respectively, for varying applied heat loads. The distance between 0 and 200mm indicates the evaporator section, while the distance between 300 and 500mm indicates the condenser section. The middle section is the adiabatic region. The CFD simulation results of temperature distribution profiles have been compared with the experimental data by determining the average relative error (*ARE*). As depicted in Figure 5.32 and Figure 5.33, the CFD simulation results also showed the same trend as the experimental results.

Referring to Figure 5.32 and Figure 5.33, the CFD simulation results of the refrigerant-based thermosyphon showed very good agreement with the temperature profiles of the experimental data for the lower heat loads. The average wall temperatures of the evaporator, adiabatic and condenser are close to those obtained in the experiments. As a result, the *ARE* of evaporator, adiabatic and condenser average wall temperatures are 1.19%, 0.66% and 0.71%, respectively for R134a, and 2.64%, 0.78% and 0.47%, respectively for R404a. For heat loads above approximately 60 W, the predicted CFD evaporator average temperature has deviated from the experimental results due to the consideration of a continuous heat power input along the length of the evaporator section where, in the experiment, the evaporator section was equally wrapped by a wire heater to ensure the heater was not directly contacted with the thermocouple.

Furthermore, by comparing the temperature distribution profiles for refrigerants-filled thermosyphon with the temperature distribution profiles for the water-filled thermossypghon (Figure 5.24, Figure 5.32 and Figure 5.33), it appears that the *ARE* for the refrigerants-filled thermosyphon is much better. The reason behind this is believed to be the critical nucleation site radiuses, as very small bubbles grow during the pool boiling of the refrigerants–filled thermosyphon, as refrigerants require very low latent heat of vaporisation in order to evaporate 1 kg of refrigerant (i.e. h_{fg}=0.2MJ/kg) compared to water, which requires much higher latent heat of vaporisation (i.e. h_{fg}=2.3MJ/kg), as clearly seen in Figure 5.18 and Figure 5.29.

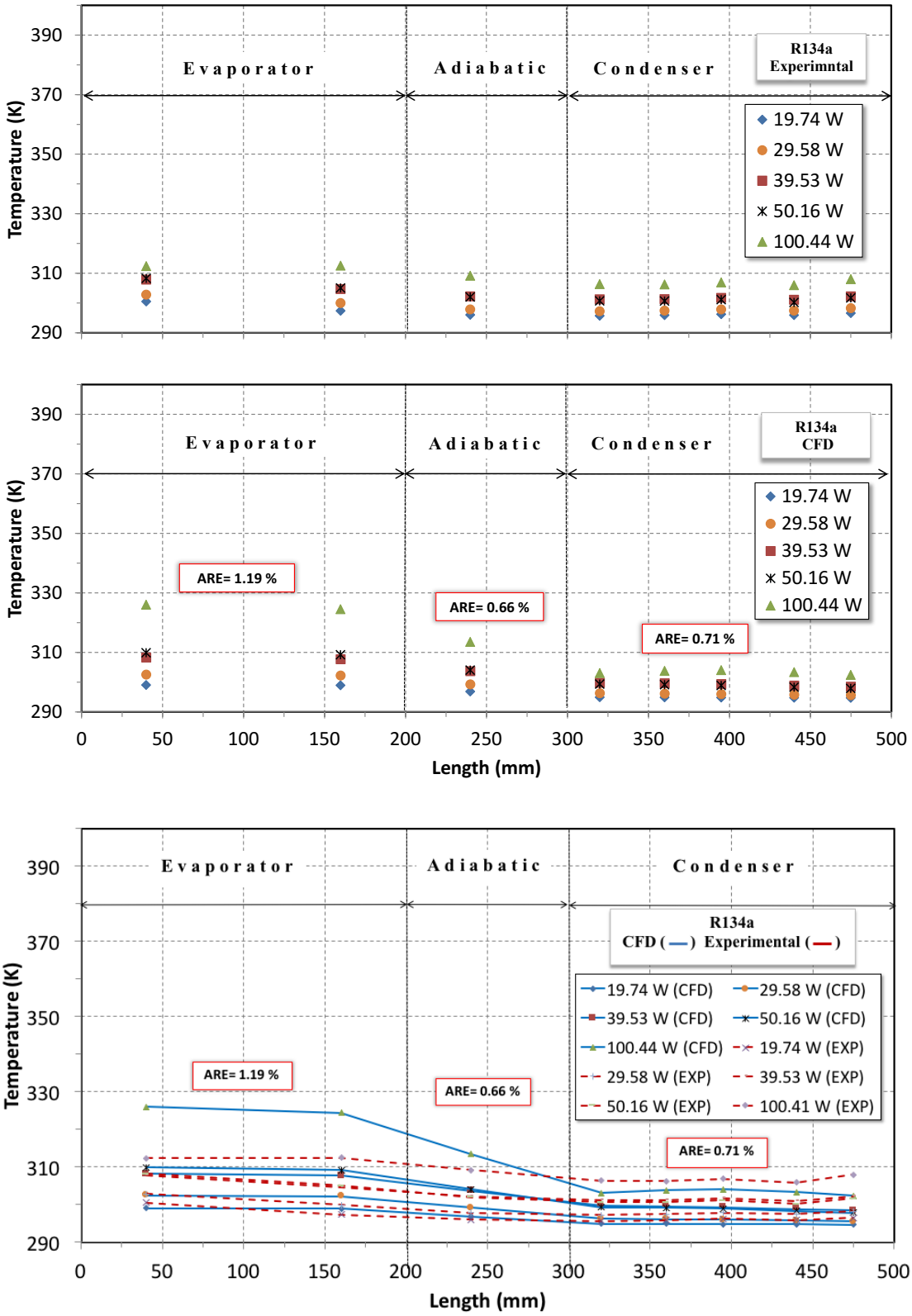

Figure 5.32: Temperature distribution profiles for experiments and CFD simulations along R134a-filled thermosyphon for different heat loads

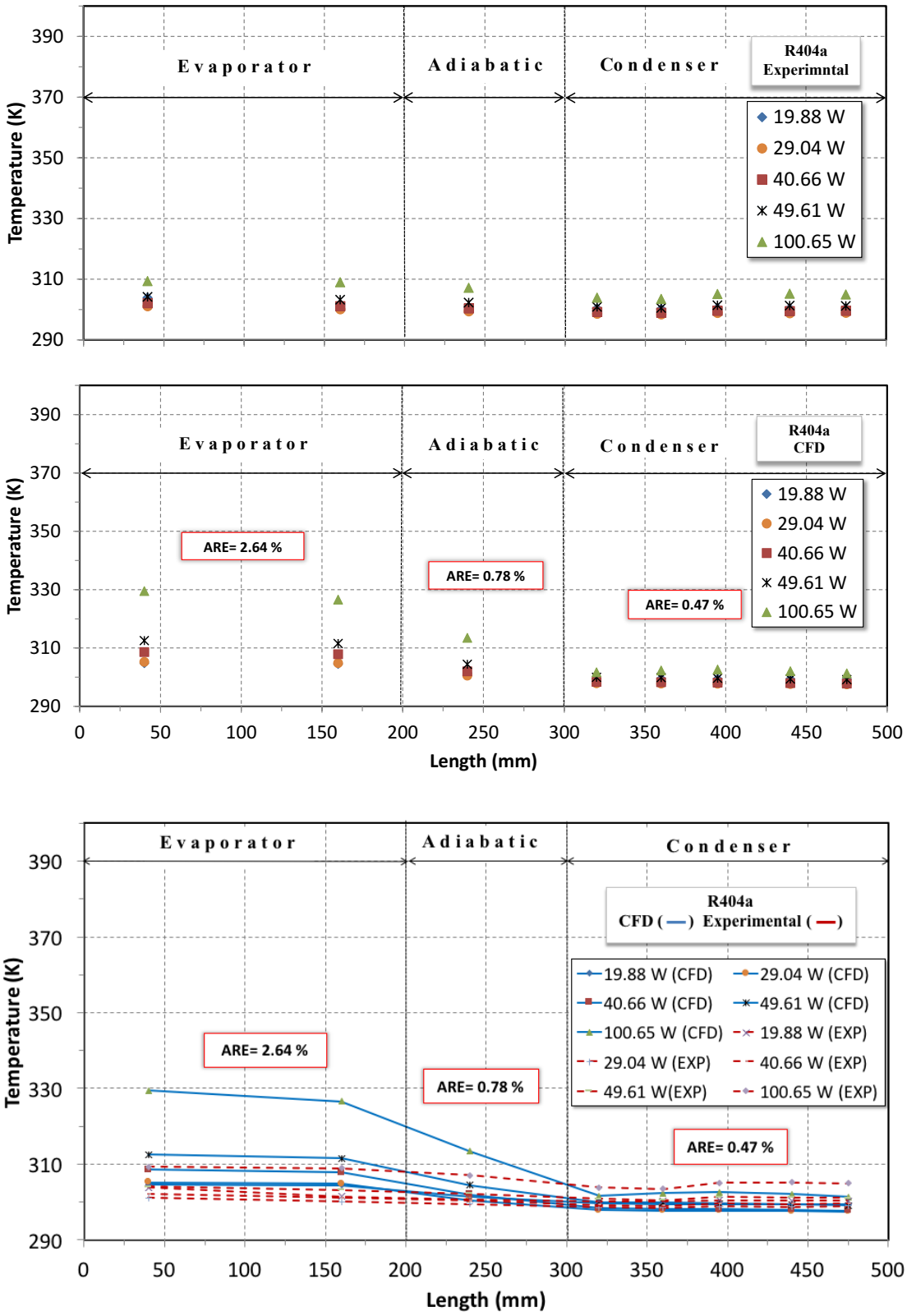

Figure 5.33: Temperature distribution profiles for experiments and CFD simulations along R404a-filled thermosyphon for different heat loads

5.10.3 Thermal performance of CFD simulation of thermosyphon

A series of tests have been performed to study the overall thermal resistance of the thermosyphon under different power throughputs. Eq. (5-43) has been used to determine the overall thermal resistance for CFD simulations of R134a and R404a charged thermosyphon, as shown in Figure 5.34. The experimental results of the thermal resistance have been used to validate the CFD results, in order to assess the accuracy of the CFD simulations. The CFD simulation results of the refrigerant-based thermosyphon showed good agreement with the temperature profiles of the experimental data, although the predicted CFD overall thermal resistance tends to over predict the experimental thermal resistance, as shown in Figure 5.34. This can be explained by the fact that the overall thermal resistance is very sensitive to the temperature difference between the evaporator and condenser sections, as shown by Eq. (5-43), however the predicted CFD overall thermal resistance follow the same trends of the experimental data.

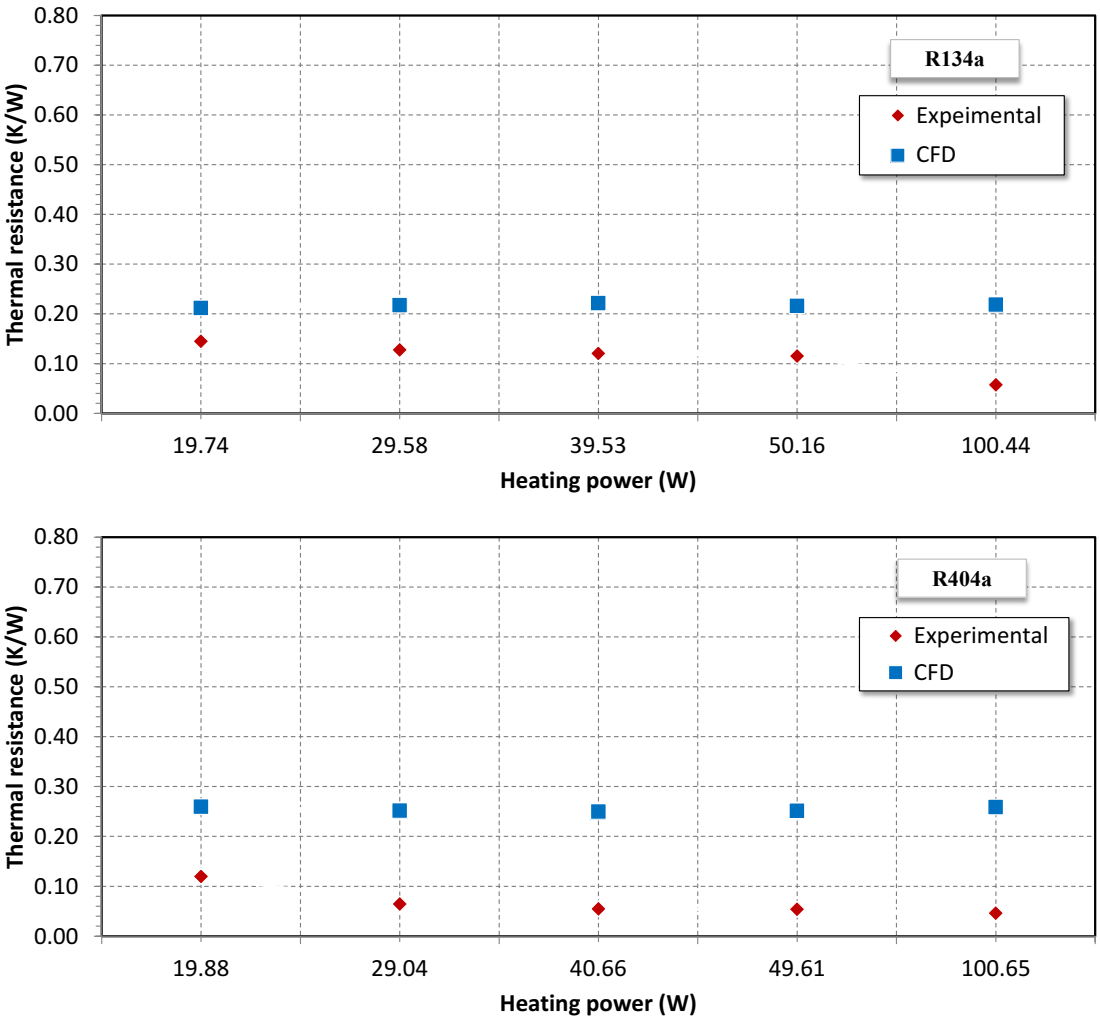

Figure 5.34: CFD simulation and experimental thermal resistance versus heating power for R134a and R404a filled thermosyphon

CHAPTER 6 THREE-DIMENSIONAL CFD MODELLING OF TWO-PHASE FLOW IN A THERMOSYPHON

The main goal of this chapter is to extend the two-dimensional CFD simulation of the two-phase flow in a thermosyphon in combination with the three-dimensional CFD simulation of the condenser water jacket described in Chapter 5, in order to create a comprehensive three-dimensional CFD model of a two-phase closed thermosyphon, including the simulation of both the complex two-phase heat and mass transfer characteristics of boiling and condensation and the heat transfer charteristcs of the cooling fluid. In this form, the CFD simulation should be able to predict with greater accuracy the heat transfer coefficients between the condenser wall and the cooling fluid in the condenser's heat exchanger. For reduced CPU time, an experimental investigation of a small thermosyphon carried out by Jouhara and Robinson [20] has been selected for this simulation. The pool boiling behaviour will be investigated for different working fluids, namely water and R134a. The CFD model will also attempt to predict and visualise the geyser boiling phenomenon, which has not been reported before in previous studies. The effects of high and low power throughput on the characteristics of the geyser boiling will also be investigated.

Consequently, this chapter will be focused on the flow visualisation of the two-phase flow during the operation of a thermosyphon. Due to the large time required to simulate the three–dimensional two-phase flow inside the thermosyphon, where two seconds of operation required two weeks of simulation time, only two power throughputs have been tested for the thermosyphon filled with water and one for the thermosyphon filled with R134a.

6.1 Model Geometry and Computational Mesh

A three-dimensional model was developed to simulate the two-phase flow in a thermosyphon. According to the experimental configuration described in [20], the specifications of a small two-phase closed thermosyphon for this model are as follows:

- Material: copper
- Working fluid: water
- Evaporator section length: 40mm
- Adiabatic section length: 100mm
- Condenser section length: 60mm
- Inner diameter: 6mm
- Outer diameter: 12mm
- Wall thickness: 3mm

Figure 6.1 shows the three-dimensional model geometry and dimensions.

The computational mesh used in the simulation of the two-phase closed thermosyphon with water jacket is illustrated in Figure 6.2. At the near inner wall of the thermosyphon, ten layers of cells are used in order to capture the thin liquid film that develops in that region. Another ten layers of cells are also used near the outer wall of the condenser section in order to capture the forced convection heat transfer between the condenser section and the cooling water, as shown in Figure 6.2. As a result, 370,702 cells are used for the simulation analysis.

Due to the limitation of the computing resources used in the present work, optimization of the geometry and mesh need to be addressed for a more detailed visualisation of the fluid flow and further investigation of multiphase flow and heat transfer over greater operating ranges/configurations.

6.2 Boundary Conditions and CFD Solution Procedure

A transient simulation is carried out to model the dynamic behaviour of the two-phase flow. A variable time stepping technique has been used in order to automatically change the time-step based on the maximum Courant number near the interface. A combination of the SIMPLE algorithm for pressure-velocity coupling and a first-order upwind scheme for the determination of momentum and energy is selected in the model.

PRESTO and Geo-Reconstruct discretization for the pressure and volume fraction interpolation scheme, respectively, are also performed in the model.

The vapour phase of the working fluid is defined as the primary phase and the liquid phase is defined as the secondary phase. The VOF method and UDFs have been employed in the model, as explained in Chapter 5. The boiling temperature and the latent heat of evaporation of the working fluid have been defined in the UDF code in order to calculate the mass and energy transfer during the evaporation and condensation processes.

A non-slip boundary condition is imposed at the inner walls of the thermosyphon. Heat is applied to the thermosyphon by defining a constant heat flux at the wall of the evaporating section. A zero heat flux is defined as boundary condition on the adiabatic section.

The condenser section is a double pipe heat exchanger, cooled by a flow of water, as can be seen in Figure 6.1. The heat exchanger consists of two concentric pipes, where the saturated vapour flows through the condenser pipe and the cooling fluid flows through the annular space between the two pipes, as described in Chapter 5, section 5.6. According to the experimental configuration, the flow rate of the cooling water is kept constant at 0.001329 kg/s [20]. Water has been used as the working fluid and filled the total volume of the evaporator section (i.e. FR=1.0). The thermophysical properties of the working fluid are assumed constant to limit the calculation time.

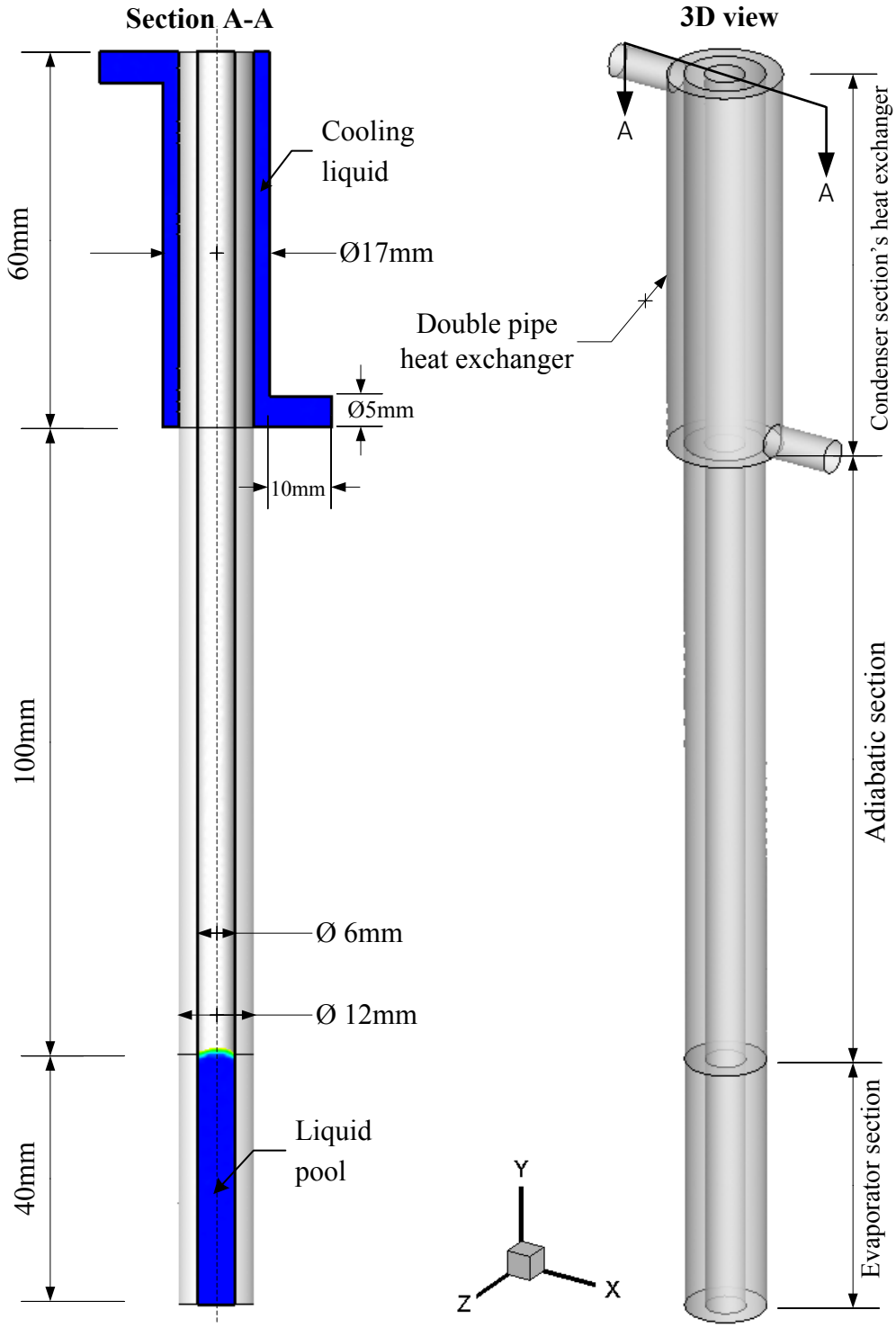

Figure 6.1: 3D model geometry and dimensions of two-phase closed thermosyphon with water jacket

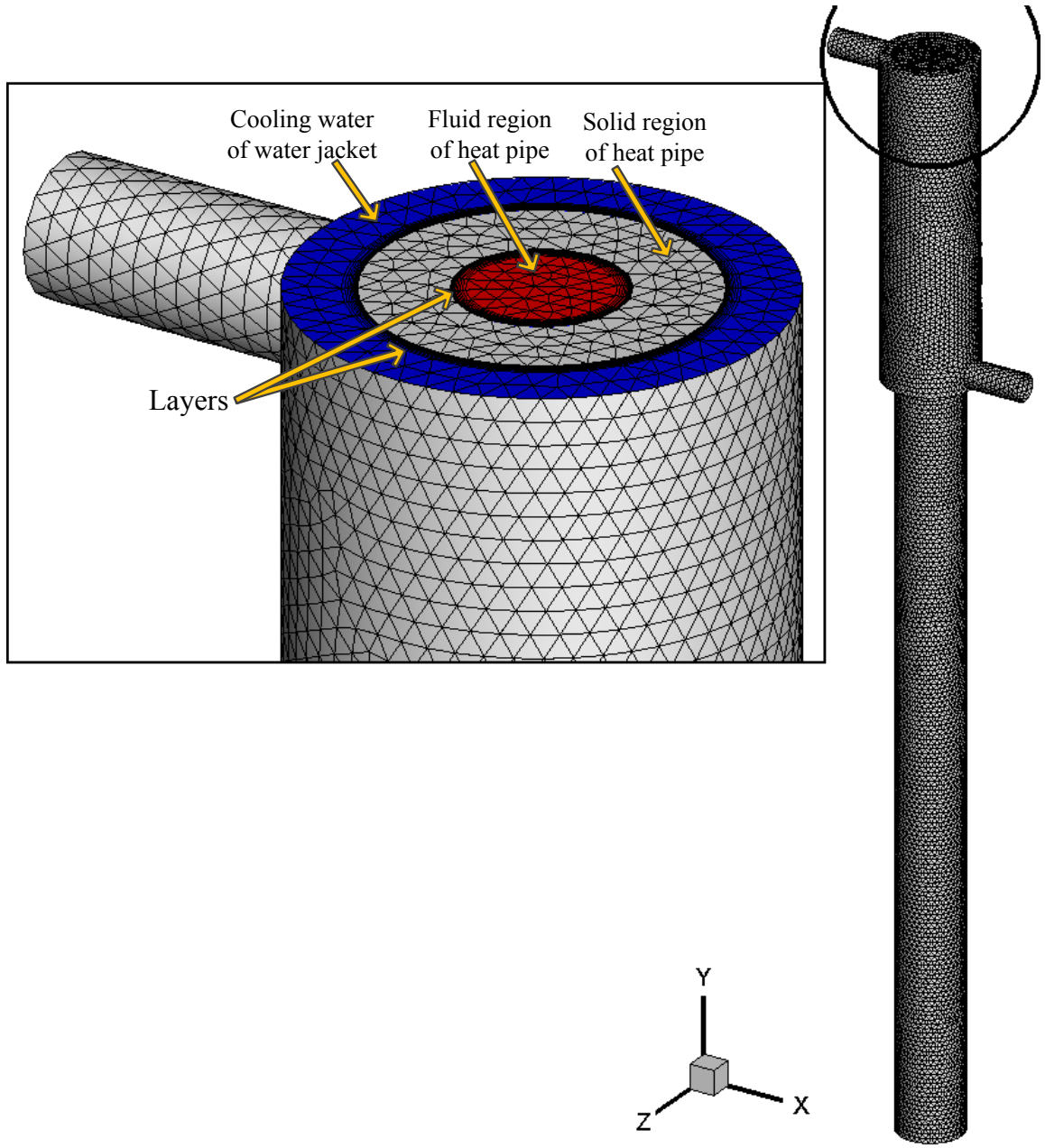

Figure 6.2: The computational mesh used in the simulation of a two-phase closed thermosyphon with water jacket

6.3 Flow Visualisation of CFD Simulation Results

First of all, the flow visualisation of the three-dimensional CFD modelling of the thermosyphon reproduced the same findings of the two-phase flow phenomena of boiling and condensation as that for the two-dimensional CFD modelling of the thermosyphon described in Chapter 5, providing further validation of the simpler two-dimensional CFD model.

Furthermore, during the flow visualisation of the boiling process, a flow pattern has been noticed at low power throughput. This pattern is then compared with the actual experimental work described in Chapter 4 and a type of boiling known as geyser boiling is observed, as shown in Figure 6.3. This figure shows the temperature profile in two locations in the evaporator section, T_{e1} and T_{e2}, at different power throughputs. The data from the two thermocouples that measure the wall temperatures T_{e1} and T_{e2} are used to collect the wall temperature in the pool boiling and nucleate film boiling regions. The boiling pattern that is noticed at low power throughput into the thermosiphon is known as geyser boiling. This boiling mode, which will be discussed in more detail in a later section, is observed when there is boiling water at low heat fluxes and relatively smooth surfaces where the number of active nucleation sites is limited. As it can be seen in Figure 6.3, typical geyser boiling regime is evident at low heat fluxes where the wall that surrounds the pool boiling regime experienced superheating until the nucleation site is activated. This effect on the wall that surrounds the nucleate film boiling region is also clear, especially when a large vapour bubble departs the pool boiling area.

Comparing the characteristics of the geyser boiling with the flow visualisation of the CFD modelling, as will be discussed in later sections, it can be noticed that, for the first time to the best of our knowledge, the three-dimensional CFD simulation has successfully modelled geyser boiling in a thermosyphon at low power throughput.

Consequently, in the following sub-sections, the geyser boiling phenomenon will be briefly described, the CFD simulation findings will be visualised and the geyser boiling process within the water-filled thermosyphon will be discussed, for a high and a low power throughput, will be discussed.

6.3.1 Geyser boiling

Geyser boiling is a phenomenon affected by many factors, such as heat load and filling ratio, and occurs in two-phase thermosyphons when the liquid fill ratio in the evaporator section is large and heat input is insufficient. Figure 6.4 presents a schematic of the geyser boiling phenomenon [117]. When the liquid pool in the evaporator section is gradually heated until it becomes superheated, a vapour bubble grows and expands to the size of the inner diameter of the thermosyphon. This bubble then blow-up suddenly, pushing all the liquid above it, causing the evaporator wall temperature in the pool boiling section to suddenly drop while that in the nucleate film boiling and the condenser is suddenly raised due to the pushed hot liquid coming from the lower half of the evaporator. This hot liquid then starts to fall back to the evaporator, causing the condenser wall temperature to drop. The geyser boiling phenomenon can be recognised by a special sound. The falling liquid from the condenser then reaches the evaporator and gradually heats up again and starts another cycle of geyser boiling. Thus, a zigzag temperature variation in the evaporator wall has been observed, as clearly seen in Figure 6.3.

While the above behaviour can be interpreted using the thermocouples measurements, an experimental visual validation is required to corroborate the CFD findings. To facilitate the visual validations, a transparent glass thermosyphon filled with water has been used to visualise the phenomena of geyser boiling and comparing with the flow visualisation findings of the three-dimensional CFD simulation.

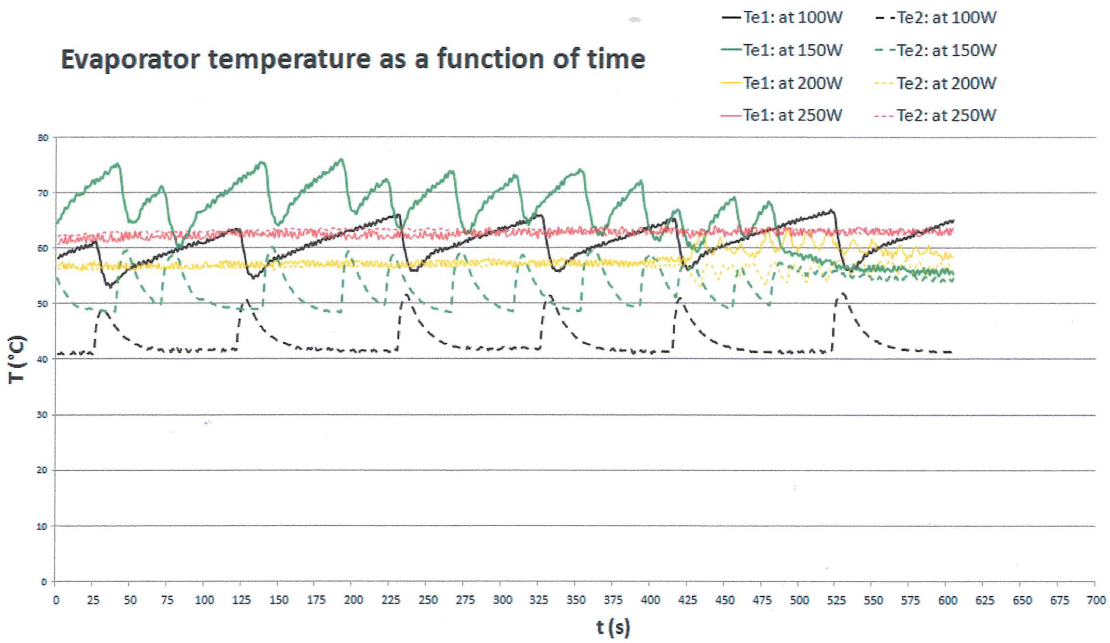

Figure 6.3: Evaporator temperatures for water-filled thermosyphon at different power throughputs from the experiments carried out for validation, explained in Chapter 4

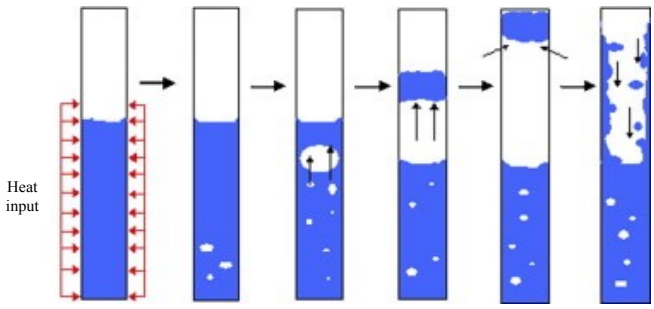

Figure 6.4: Schematic of geyser boiling process in a thermosyphon [117]

6.3.2 Three-dimensional CFD simulation of water-filled thermosyphon

The geyser boiling phenomenon generated inside the thermosyphon occurs when the water is superheated near the bottom of the evaporator, creating a nucleation site and leading to a large vapour bubble which expands to the size of the inner diameter of the thermosyphon. When the buoyancy of that bubble becomes higher than the weight of the water column above the bubble, the bubble quickly pushes the entire water column above it and produces a strange sound in the thermosyphon [118].

The process of geyser boiling described above is observed in the CFD flow visualisation shown in Figure 6.5. In this visual observation, the volume fraction contours of the fluid region in the thermosyphon for a power throughput of 30 W has been monitored for different times. Vapour bubbles that appear in the evaporator section during the geyser boiling process and take the size of the inner diameter of the evaporator are shown in Figure 6.6.

The water pool is represented by a blue colour and the vapour is represented by a red colour, as can be seen in Figure 6.5 and Figure 6.6. The water has initially filled the total volume of the evaporator section, as shown in Figure 6.5 at t=0.0 s. The water is heated and at a certain time, vapour bubbles start to form in the evaporator, as shown in Figure 6.5 at t=0.12 s. Vapour bubbles then grow and expand almost to the size of the inner diameter of the thermosyphon, specially at the top region of the evaporator section, which is clearly shown in Figure 6.6. As a result, the geyser boiling regime starts and the bubble quickly expels the water above it, as shown in Figure 6.5 at t=3.0 s. The water expelled by the bubble then starts to fall back and the geyser boiling cycle is completed, as shown in Figure 6.5 at t=3.1 s. Later, another cycle of geyser boiling starts as the next bubble appears and grows, as seen in Figure 6.5 at t=4.0 s and 5.0 s. It should be noted that the CFD flow visualisation does not show the pushed water at the top of the condenser section, as shown in Figure 6.4. The main reason behind this is the limitation of the computational mesh in the present study and thus optimization of the mesh needs to be addressed for a more detailed visualisation of the fluid flow.

Furthermore, by comparing Figure 6.5 described above with Figure 5.18 described in Chapter 5, it appears that the same boiling behaviour is observed in the two figures. It is observed from the figures that the surface of the water pool has been raised due to the bubbles forming at a large number of nucleation sites, which form continuous columns of vapour bubbles in the liquid pool.

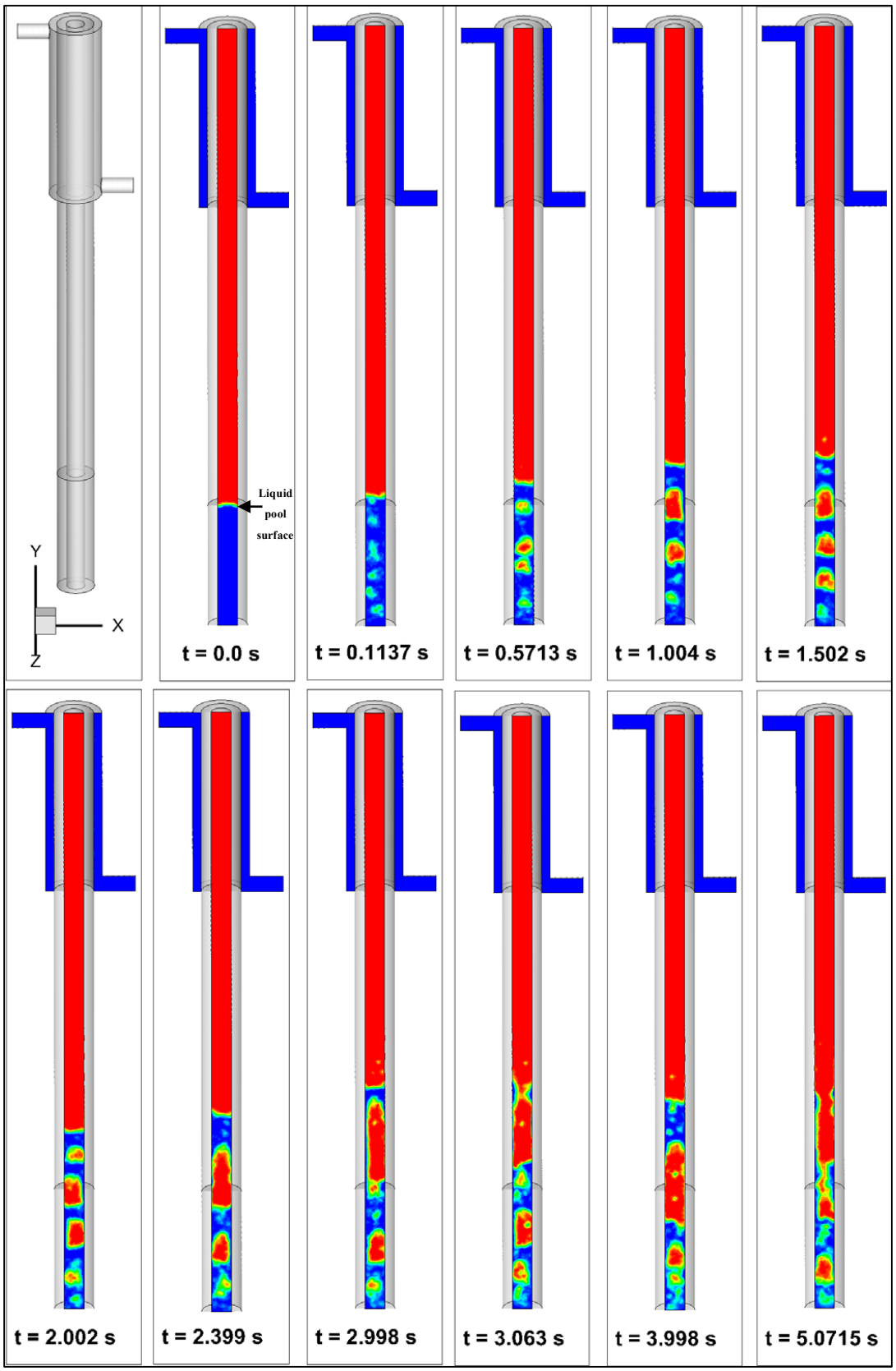

Figure 6.5: Geyser boiling process in a thermosyphon for a power throughput of 30 W

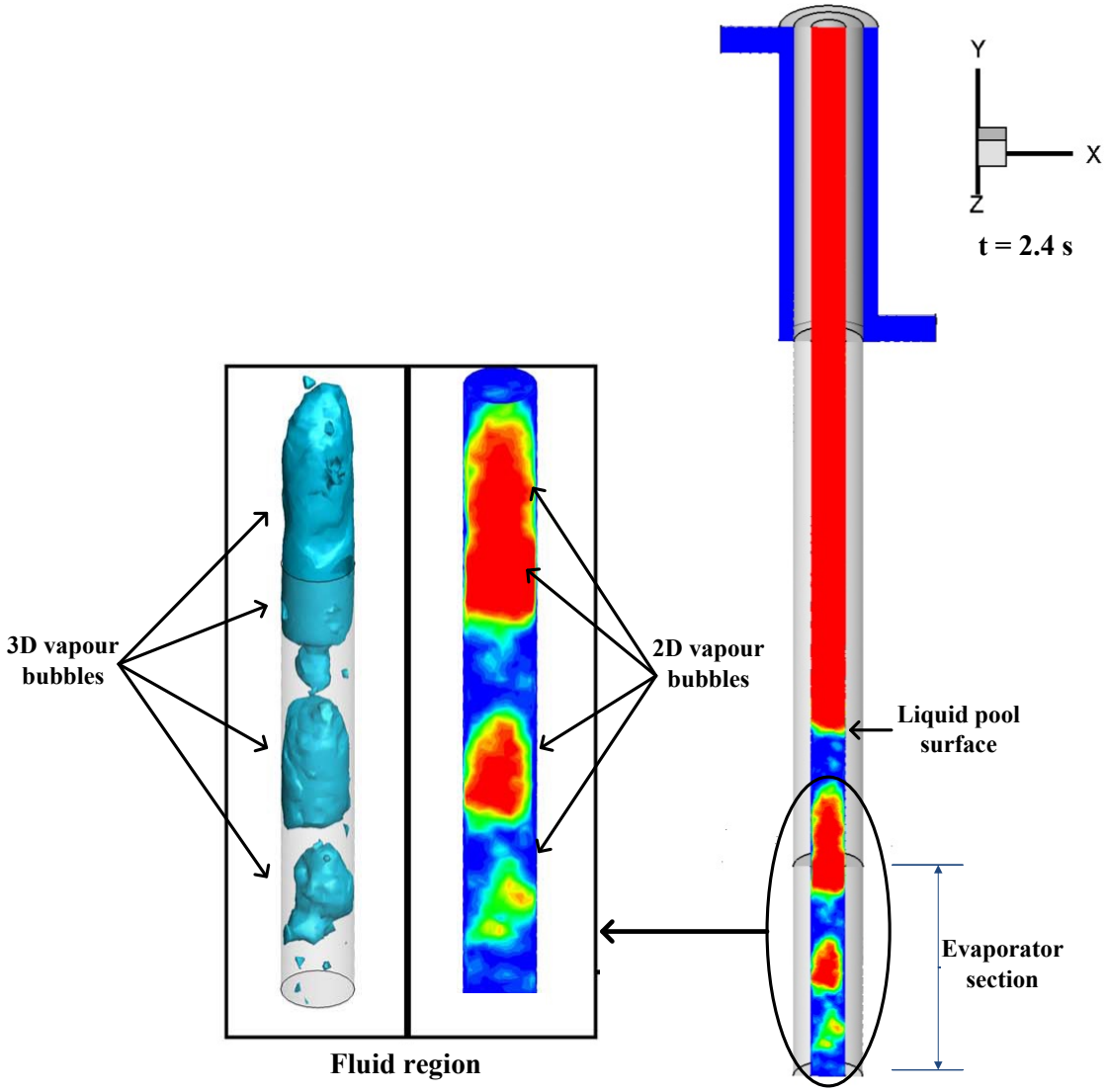

Figure 6.6: Size of the vapour bubbles in the evaporator section for a power throughput of 30 W

In order to understand the effects of the power throughput on the boiling characteristics, flow visualisation of the pool boiling at a high power throughput is also conducted for the water-filled thermosyphon. Figure 6.7 shows the volume fraction contours of the fluid region in the evaporator and in the lower adiabatic region for a power throughput of 220W. The figure includes both the three-dimensional vapour bubbles in the liquid pool and a cross-section of the evaporator and the lower adiabatic region for different simulation times.

The water is heated and at a certain time, vapour bubbles start to form in the evaporator, as shown at 0.02 s. It can also be noted from the figure that a high number of small bubble nucleation sites is observed on the evaporator inner wall, as can be seen between 0.02 s and 0.05 s. This can be explained by the fact that the evaporator wall at high power throughput is superheated well above the temperature required for the onset of nucleate boiling. As a result of this, the water pool is unstable and in vigorous irregular motion, which is clearly shown in the figure between 0.02 s and 0.05s at the upper region of the evaporator. In contrast, for the low power throughput, the water pool is stable and been in quiescent condition, as shown in Figure 6.5 at 0.1 s. Between 0.07 s and 0.15 s (Figure 6.7), a large number of vapour bubbles are formed and move upward to the water pool surface where they break up and release their vapour content. Furthermore, it is observed from the figure that some large vapour bubbles are formed later in the liquid pool and, as a result, the water pool surface raises upward, as shown in the figure between 0.16 s and 0.2 s.

The above discussion refers to the short period of time between 0.0 s and 0.2 s, and that is explained by the high frequency of the evaporator wall temperature profiles given in Figure 6.3 for high power throughputs of 200W and 250W, while the temperature profile for low power throughput has low frequency of bubble formation, as shown in Figure 6.3 for 100W and 150W. It should be noted that the geyser boiling phenomenon disappears with the high power throughput and this is due to the presence of a large number of vapour bubbles in the liquid pool, which move upward fast; hence, a very large size vapour bubble, as shown in Figure 6.6, has not been observed. Furthermore, the same boiling characteristics has been observed in the two-dimensional CFD simulation explained in Chapter 5 and shown in Figure 5.17 and Figure 5.18.

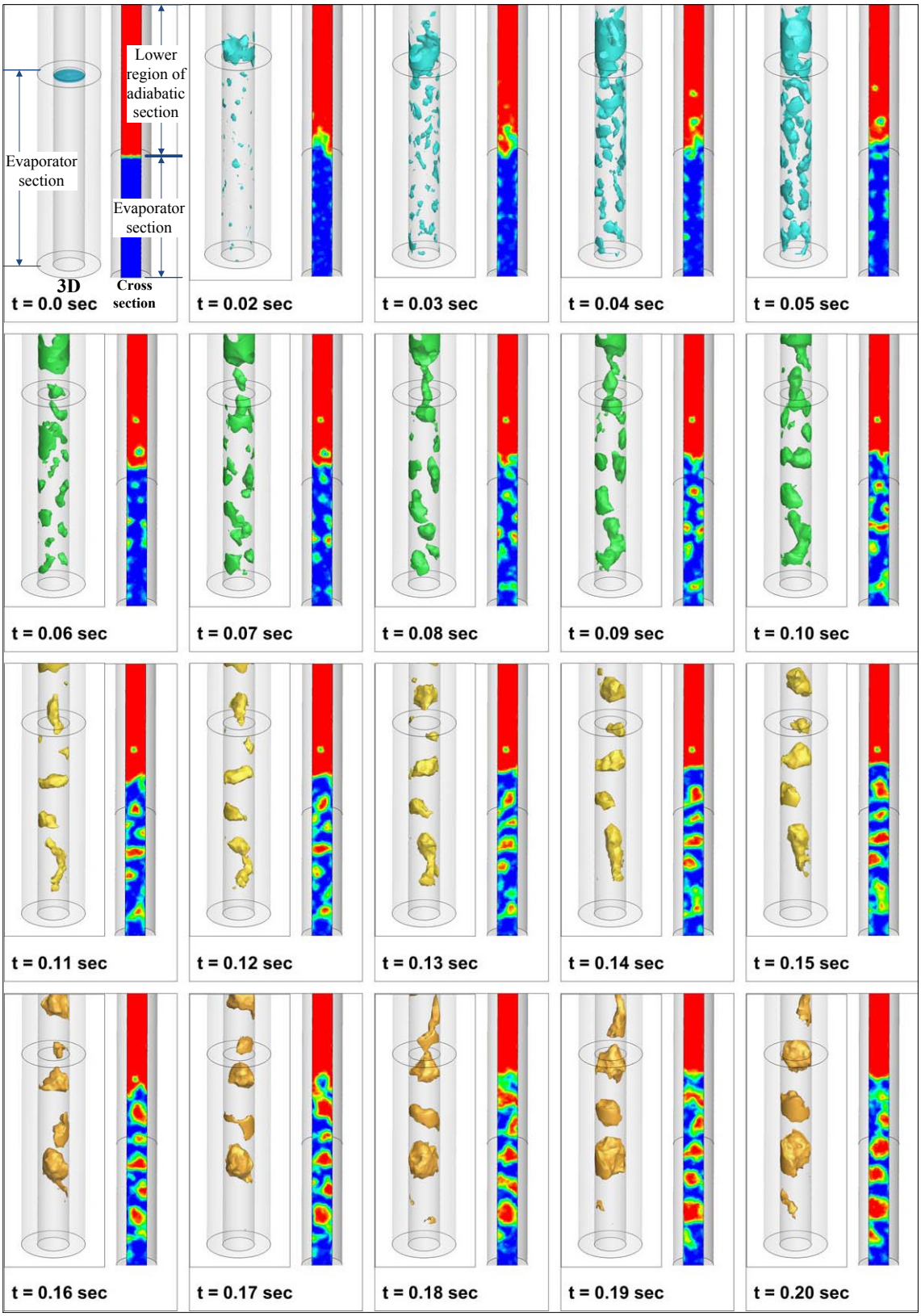

Figure 6.7: Pool boiling process in a thermosyphon for a power throughput of 220 W

6.3.3 A transparent glass thermosyphon

In order to show that the three-dimensional CFD simulation has successfully modelled the geyser boiling phenomenon in a thermosyphon at low power throughput, a transparent glass thermosyphon charged with water has been used to observe and visualise the process. The visualisation of the geyser boiling is carried out by immersing the glass thermosyphon into a flask containing boiling water to supply heat to the evaporator section. The glass thermosyphon is then kept immersed in the flask until the geyser boiling phenomenon takes place, which is monitored using a digital camera recorder. Geyser boiling continues to occur until all the energy of the boiling water in the flask is dissipated.

The footage frames recorded during the geyser boiling process in the evaporator section of the glass thermosyphon are shown in Figure 6.8. The initial stage of the geyser boiling process is known as the quiescent period, where the temperature of the water pool in the evaporator section gradually increases as it absorbs heat, as shown in Figure 6.8 (a). The water then becomes superheated and a nucleation site is created and as a result, a single vapour bubble appeared at the bottom of the evaporator section, as shown in Figure 6.8 (b). This bubble then grows quickly to a large size, equal to the inner diameter of the evaporator section, and suddenly the growing bubble pushes up the water above it from the evaporator to the condenser producing a special sound, as shown in Figure 6.8 (c). Consequently, a very small volume of the water pool remains in the evaporator section, as shown in Figure 6.8 (d). The pushed water then falls down from the condenser and a liquid film can be seen on the inner wall, as shown in Figure 6.8 (e). The above described process then repeats again once the returned water is heated for another cycle, as shown in Figure 6.8 (f). It should be noted that due to the limitation of the resolution of the digital camera, Figure 6.8 (c) is not clearly visualised in the very small period of time when the water is pushed upward in the evaporator section.

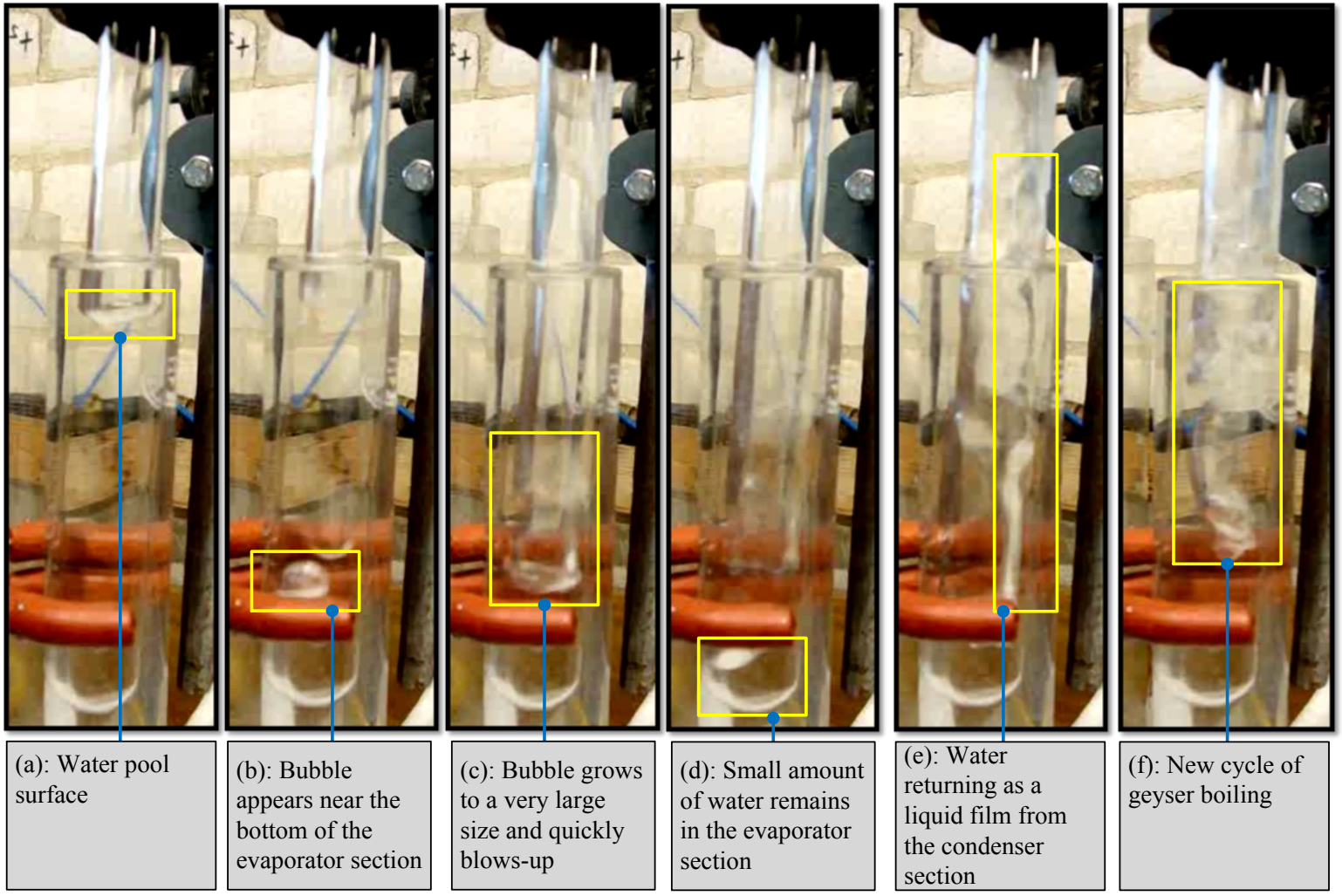

Figure 6.8: Visualisation of geyser boiling using transparent glass thermosyphon

6.4 Three-Dimensional CFD Simulation of R134a-Filled Thermosyphon

In order to show that the developed three-dimensional CFD model has the ability to reproduce the difference in pool boiling behaviour between different working fluids, refrigerant R134a has been simulated and a three-dimensional flow visualisation of pool boiling and film condensation during the operation of the R134a-filled thermosyphon was observed and shown in Figure 6.9.

In this case, three phases have been defined for the CFD simulation of the thermosyphon filled with R134a and cooled by water through the condenser section's heat exchanger. In particular, the two main phases defined in the CFD model are the liquid phase of R134a (filled the total volume of the evaporator section) and the vapour phase of R134a. These phases have been adopted in the fluid region of the thermosyphon, where phase change occurs between them during the boiling and condensation processes. The third phase is the cooling fluid of the condenser section's heat exchanger, which is water. This phase has been adopted in the annular space of the heat exchanger, as shown in Figure 6.1 (Section A-A), where forced convection heat transfer takes place between the condenser wall and the cooling fluid.

In order to show the three-dimensional pool boiling, three-dimensional vapour bubbles and the surface liquid pool in the evaporator section have been visualised, as illustrated in Figure 6.9. Heat is applied through the evaporator section where a liquid pool of R134a exists, as shown in Figure 6.9 at t=0.0 s. Vapour bubbles are then generated in the evaporator section and moved to the liquid pool surface releasing their content of vapour, as shown in Figure 6.9 at t=0.12 s. In the condenser section, the saturated vapour condenses along the inner wall and gravity then returns the condensate back to the evaporator section as a falling liquid film, as clearly seen in Figure 6.9 at t=0.21 s and 0.56 s. The continuous liquid film then recharges the liquid pool in the evaporator section, as shown in Figure 6.9 at t= 3.5 s to 5.8 s.

Furthermore, due to the critical nucleation site radiuses, the pool boiling behaviour of R134a is significantly different to that of water, as very small bubbles grow during the pool boiling of R134a–filled thermosyphon. As a result, the position of the liquid pool surface is not raised, as clearly seen in Figure 6.6 and Figure 6.9. For this reason, it can be noted that geyser boiling is not observed in this case.

By comparing the CFD flow visualisation of evaporation and condensation processes for the two-dimensional CFD model described in Chapter 5 (Figure 5.29 and Figure 5.31) with the three-dimensional CFD model, it appears that the same findings related to fluid flow and thermal fields are observed for the two models.

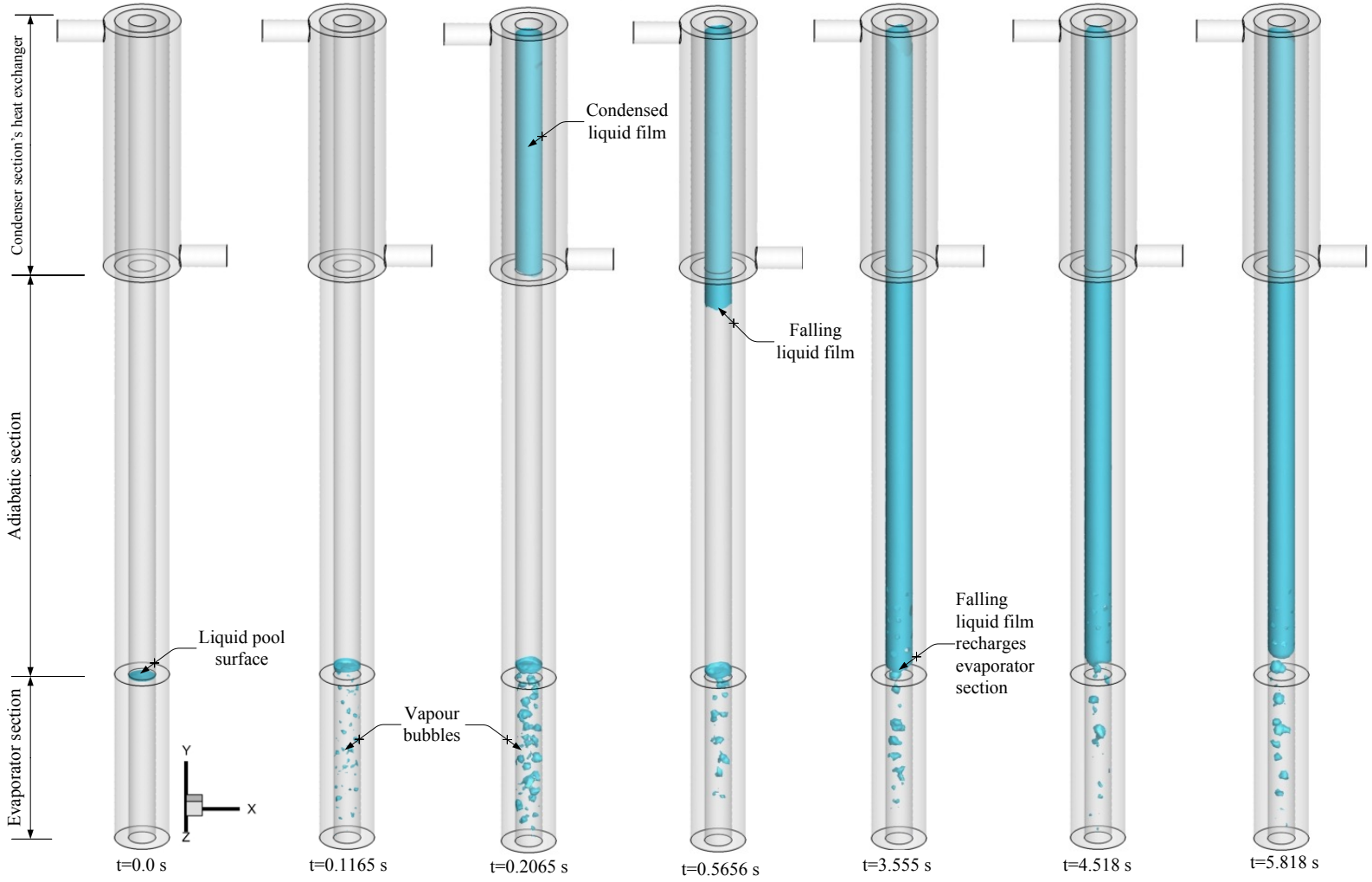

Figure 6.9: Three-dimensional CFD modelling of evaporation and condensation for a thermosyphon charged with R134a for a power throughput of 30 W

CHAPTER 7 CONCLUSIONS AND RECOMMENDATIONS FOR FUTURE WORK

7.1 Conclusions

Heat pipe technology is receiving increased attention nowadays and the optimisation of heat pipe performance is of great interest. Wickless heat pipe systems are more desirable than conventional systems due to their passive operation, reliability, efficiency and the cost and ease of manufacturing. However, up to now, computational studies developed on wickless heat pipes, displaying the complex two-phase flow inside the heat pipe are at an early stage. In this study, a novel CFD model has been developed that allows the detailed study of the two-phase flow and heat transfer phenomena during the operation of a wickless heat pipe. Three working fluids: water, R134a and R404a were investigated. This thesis describes the CFD procedure employed to study the evaporation and condensation phenomena and evaluate the performance of these fluids as working fluids in the wickless heat pipe. Temperature profiles along the wickless heat pipe have been determined and the two-phase flow characteristics have been visualised.

The ANSYS FLUENT CFD simulation package was used to visualise the evaporation, condensation and heat transfer processes during the start-up and steady state process of a wickless heat pipe. The phase change process occurring during the evaporation and condensation was simulated in FLUENT, due to the flexibility and accuracy of the finite volume method. An in-house code was developed using user-defined functions (UDFs) to enhance the ability of FLUENT to simulate the phase change during the operation of a wickless heat pipe.

The work carried out as part of this thesis can be summarised into the following stages:

- A literature review of heat pipe technology, benefits, applications, the basic theory of heat pipe operation and numerical and experimental studies of different types of heat pipes was presented in Chapter 2.
- The theoretical physics behind the multiphase flow and heat transfer phenomena of boiling and condensation during the operation of wickless heat pipes, the correlations of the wickless heat pipe evaporator and condenser heat transfer characteristics and the theoretical model containing calculations of heat transfer coefficients and thermal resistance of the wickless heat pipe was presented in Chapter 3.
- For the purpose of validating the proposed CFD model of the wickless heat pipe and the theoretical calculations, an experimental apparatus was built and presented in Chapter 4.
- The CFD theory and numerical approaches for modelling the multiphase flow, the computational studies of wickless heat pipes, the developed UDF techniques to simulate the phase change during the evaporation and condensation processes, model geometry and computational mesh, boundary and operating conditions and CFD solution procedure were described in Chapter 5.
- The two-phase flow visualisation and an analysis of the nature of the heat transfer, pool boiling and film condensation processes, temperature distribution profiles and thermal performance of CFD simulations of wickless heat pipe filled with water, R134a and R404a was also presented in Chapter 5.
- A comprehensive three-dimensional CFD modelling of a two-phase wickless heat pipe, combining the simulation of the two-phase flow phenomena of boiling and condensation and the simulation of the condenser section' heat exchanger, was presented in Chapter 6.
- A three-dimensional CFD flow visualisation of boiling vapour bubbles and liquid film condensation was reported in Chapter 6.
- An experimental test carried out with a transparent glass thermosyphon to validate the three dimensional CFD simulation findings was also presented in Chapter 6.

In a first step, this study provides evidence that the proposed CFD model of a wickless heat pipe with a two-dimensional geometry has successfully reproduced both the characteristics of fluid flow as well as thermodynamics, in spite of its simplicity. The model includes the complex physical phenomena of both the heat transfer process of evaporation and condensation and the mass transfer process of phase change from liquid to vapour phase during the pool boiling and from vapour to liquid phase during the film condensation. The results of this study have also demonstrated the abilities of the CFD model to simulate the characteristics of multiphase flow for different working fluids. A good agreement has been observed between the predicted CFD temperature profiles along the wickless heat pipe and the experimental results at the same condition. The predicted CFD thermal performance of the wickless heat pipe has also successfully emphasised the variation trends of the experimental measurements for different power throughputs.

Next, a comprehensive three-dimensional CFD model of a wickless heat pipe has been successfully developed for the first time, to the best of our knowledge, capable of reproducing both the complex multiphase heat and mass transfer characteristics of boiling and condensation. The results closely agreed with those previously reported for the two-dimensional CFD model, and the simulation of heat transfer characteristics of the cooling fluid in the cooling system heat exchanger. The three-dimensional CFD simulation has successfully modelled and visualised the multiphase flow characteristics of pool boiling and film condensation for water and R134a, emphasising the difference in pool boiling behaviour between these working fluids. The three-dimensional CFD simulation has also successfully predicted and visualised, for the first time, a flow pattern that takes place with water at low power throughput, known as geyser boiling phenomenon. Furthermore, modelling the complicated multiphase flow of boiling and condensation has been carried out and validated for a simple three-dimensional configuration, however boiling and condensation specially boiling does not depend on the actual shape of the surface. Therefore, the proposed CFD model can be applied for more complicated heat exchanger designs.

Finally, the developed CFD model can reduce the amount of experimental work. In other words, instead of investing substantial human and financial resources on building experimental setups to test a certain configuration, the same configuration can be built using reduced computational resources and the proposed CFD model applied to predict the performance of the system, which can then be optimised. The performance of the final optimised model can then be verified through experiments, substantially reducing the design costs.

7.2 Recommendations for Future Work

In the course of the present study, some potential improvements have been realised and recommended for future work.

The following are recommendations for future work:

1. Due to the limitation of the computing resources used in the present work, optimization of the geometry and mesh for the three-dimensional CFD model described in Chapter 6 is needed for more detailed CFD flow visualisation and further investigation of multiphase flow and heat transfer over greater operating ranges/configurations of a wickless heat pipe.
2. Further simulations of the three-dimensional CFD model over a long time period is also needed to predict the temperature profiles along the wickless heat pipe and compare the predicted results with the experimental measurements carried out by Jouhara and Robinson [20].
3. Further CFD investigations on the two-phase flow patterns in a wickless heat pipe, including the geyser boiling phenomenon, are needed for the effects of filling ratio, heat flux and heat pipe inclination on the geyser boiling period.
4. Heat exchangers with helical flow path offer certain advantages. For instance, a helical flow path heat exchanger creates uniform flow velocity inside the tube, which reduces the fouling issue and enhances convective heat transfer coefficients [119]. Further, a helical shape offers uniform heat distribution as the fluid tend to flow in a turbulent manner, which results in better heat distribution. Therefore, enhancement of the CFD geometry of the heat exchanger cooling system for the condenser section by introducing a helical flow path heat exchanger can also be investigated.

5. Non-condensable gases (NCGs) have a significant influence on the thermal performance of a wickless heat pipe. If present, they would be swept by the vapour towards the top area of the condenser section where they would accumulate and reduce the thermal performance [40]. Therefore, CFD modelling of a wickless heat pipe in the presence of NCGs need to be investigated by testing the effect of different NCGs, for instance air and helium, on the thermal performance of the heat pipe.

It should be noted that the presence of NCGs in the condenser section would increase the level of complexity of the multiphase flow characteristics, leading to more complex and sophisticated CFD models. In particular, the gas phase in the condenser section could be treated as a mixture region, consisting of two species, which are the vapour phase of the working fluid and the NCG. Hence, in addition to the VOF model, the species model in the CFD package would need to be applied to the model, in order to compute the mass and heat transfer of species during the condensation process. This would require additional developments of UDFs by determining the mass/mole fraction of each species in the mixture phase and adding them to the mass and heat sources of the condensation process.

REFERENCES

[1] Chi SW. *Heat pipe theory and practice :a sourcebook*. Hemisphere Pub. Corp.: Washington, 1976.

[2] Reay D, Kew P. *Heat Pipes: Theory, Design and Applications*. Elsevier Science & Technology: UK, 2009;367.

[3] Legierski J, Wiecek B, de Mey G. Measurements and simulations of transient characteristics of heat pipes. *Microelectronics and Reliability* 2006; 46: 109-115.

[4] Jouhara H, Ezzuddin H. Thermal performance characteristics of a wraparound loop heat pipe (WLHP) charged with R134A. *Energy* 2013; 61: 128-138.

[5] Jouhara H, Robinson AJ. An experimental study of small-diameter wickless heat pipes operating in the temperature range 200^{o}C to 450^{o}C. *Heat Transfer Engineering* 2009; 30: 1041-1048.

[6] United Nations Framework Convention on Climate Change. Web Site. http://unfccc.int/kyoto_protocol/items/2830.php.

[7] Kerrigan K, Jouhara H, O'Donnell GE, Robinson AJ. Heat pipe-based radiator for low grade geothermal energy conversion in domestic space heating. *Simulation Modelling Practice and Theory* 2011; 19: 1154-1163.

[8] Jouhara H, Meskimmon R. Experimental investigation of wraparound loop heat pipe heat exchanger used in energy efficient air handling units. *Energy* 2010; 35: 4592-4599.

[9] Mathioulakis E, Belessiotis V. A new heat-pipe type solar domestic hot water system. *Solar Energy* 2002; 72: 13-20.

[10] Weng Y-, Cho H-, Chang C-, Chen S-. Heat pipe with PCM for electronic cooling. *Applied Energy* 2011; 88: 1825-1833.

[11] Jouhara H. Economic assessment of the benefits of wraparound heat pipes in ventilation processes for hot and humid climates. *International Journal of Low-Carbon Technologies* 2009; 4: 52-60.

[12] Parand R, Rashidian B, Ataei A, Shakiby K. Modeling the transient response of the thermosyphon heat pipes. *Journal of Applied Sciences* 2009; 9: 1531-1537.

[13] Ochsner K. Carbon dioxide heat pipe in conjunction with a ground source heat pump (GSHP). *Applied Thermal Engineering* 2008; 28: 2077-2082.

[14] Du J, Bansal P, Huang B. Simulation model of a greenhouse with a heat-pipe heating system. *Applied Energy* 2012; 93: 268-276.

[15] Cengel YA. *Heat Transfer : A Practical Approach*. McGraw-Hill: Boston ; Toronto, 2003.

[16] Savino R, Cecere A, Di Paola R. Surface tension-driven flow in wickless heat pipes with self-rewetting fluids. *International Journal of Heat and Fluid Flow* 2009; 30: 380-388.

[17] Kafeel K, Turan A. Simulation of the response of a thermosyphon under pulsed heat input conditions. *International Journal of Thermal Sciences* 2014; 80: 33-40.

[18] Annamalai AS, Ramalingam V. Experimental investigation and computational fluid dynamics analysis of an air cooled condenser heat pipe. *Thermal Science* 2011; 15: 759-772.

[19] Alizadehdakhel A, Rahimi M, Alsairafi AA. CFD modeling of flow and heat transfer in a thermosyphon. *International Communications in Heat and Mass Transfer* 2010; 37: 312-318.

[20] Jouhara H, Robinson AJ. Experimental investigation of small diameter two-phase closed thermosyphons charged with water, FC-84, FC-77 and FC-3283. *Applied Thermal Engineering* 2010; 30: 201-211.

[21] Kirby R. *Fluid Services and Heat Transfer Equipment*. Brunel University: Middlesex, 2005.

[22] ESDU. Heat pipes - performance of two-phase closed thermosyphons. *ESDU Manual 81038 1983*.

[23] ESDU. Heat pipes - general information on their use, operation and design. *ESDU Manual 80013 1980*.

[24] Chi SW. *Heat Pipe Theory and Practice: A Sourcebook*. Hemisphere Publishing Corporation: Washington, 1976;239.

[25] Faghri A. *Heat Pipe Science and Technology.* Taylor & Francis: Washington, D.C., 1995.

[26] Jouhara H, Ezzuddin H. Thermal performance characteristics of a wraparound loop heat pipe (WLHP) charged with R134A. *Energy* 2012; 61: 128-138.

[27] Advanced Cooling Technologies Inc. Web Site. http://www.1-act.com/hvac/products/.

[28] Bassanina s.r.l Via dell Artigianato. Web Site http://www.bassanina.com/dett-categorie_eng.html?id=4.

[29] The Hardware Info. Web Site http://uk.hardware.info/productgroup/19/cpu-coolers.

[30] Memsys. Web Site http://www.memsys.eu/projects-details/solar-driven-desalination-at-marina-barrage-singapore.html.

[31] Anderson WG. Intermediate temperature fluids for heat pipes and loop heat pipes. *Collection of Technical Papers - 5th International Energy Conversion Engineering Conference* 2007; 2: 1147-1164.

[32] Anderson WG, Dussinger PM, Bonner RW, Sarraf DB. High temperature titanium-water and Monel-water heat pipes. *Collection of Technical Papers - 4th International Energy Conversion Engineering Conference* 2006; 2: 828-839.

[33] Baojin Q, Li Z, Hong X, Yan S. Heat transfer characteristics of titanium/water two-phase closed thermosyphon. *Energy Conversion and Management* 2009; 50: 2174-2179.

[34] Anderson WG, Bonner RW, Dussinger PM, Hartenstine JR, Sarraf DB, Locci IE. Intermediate temperature fluids life tests - Experiments. *Collection of Technical Papers - 5th International Energy Conversion Engineering Conference* 2007; 2: 926-941.

[35] Tarau C, Sarraf DB, Locci IE, Anderson WG. Intermediate Temperature Fluids Life Tests - Theory. *Proceedings, STAIF 2007, AIP Conference Proceedings* 2007; 880: 137-146.

[36] Sarraf DB, Anderson W,G. High-Temperature Water Heat Pipes. *IMAPS International Conference and Exhibition on High Temperature Electronics* 2006; 1: 549-556.

[37] Dussinger PM, Anderson WG, Sunada ET. Design and testing of titanium/cesium and titanium/potassium heat pipes. *Collection of Technical Papers - 3rd International Energy Conversion Engineering Conference* 2005; 2: 1088-1096.

[38] Yau YH, Foo YC. Comparative study on evaporator heat transfer characteristics of revolving heat pipes filled with R134a, R22 and R410A. *International Communications in Heat and Mass Transfer* 2011; 38: 202-211.

[39] Devarakonda A, Anderson WG. Thermo-physical properties of intermediate temperature heat pipe fluids. *Space Technology and Applications International Forum (STAIF-05)* 2005; 746: 179-186.

[40] Mantelli MBH, Ângelo WB, Borges T. Performance of naphthalene thermosyphons with non-condensable gases - Theoretical study and comparison with data. *International Journal of Heat and Mass Transfer* 2010; 53: 3414-3428.

[41] Sarraf DB, Anderson WG. Heat pipes for high temperature thermal management. *2007 Proceedings of the ASME InterPack Conference, IPACK 2007* 2007; 1: 707-714.

[42] ESDU. Heat pipes - performance of capillary-driven designs. *ESDU Manual 79012 1980*.

[43] Wide Work. Web Site http://www.widework.co.jp.

[44] Ghajar M, Darabi J, Crews N. A hybrid CFD-mathematical model for simulation of a MEMS loop heat pipe for electronics cooling applications. *Journal of Micromechanics and Microengineering* 2005; 15: 313-321.

[45] Rahmat M, Hubert P. Two-phase simulations of micro heat pipes. *Computers and Fluids* 2010; 39: 451-460.

[46] Yarin LP, Ekelchik LA, Hetsroni G. Two-phase laminar flow in a heated microchannels. *International Journal of Multiphase Flow* 2002; 28: 1589-1616.

[47] Zhang M, Liu Z, Ma G, Cheng S. Numerical simulation and experimental verification of a flat two-phase thermosyphon. *Energy Conversion and Management* 2009; 50: 1095-1100.

[48] Maydanik YF. Loop heat pipes. *Applied Thermal Engineering* 2005; 25: 635-657.

[49] Gerasimov YF, Maidanik YF, Shchegolev GT, Filippov GA, Starikov LG, Kiseev VM, Dolgirev YE. Low-temperature heat pipes with separate channels for vapor and liquid. *Journal of engineering physics* 1975; 28: 683-685.

[50] Wan JW, Zhang JL, Zhang WM. The effect of heat-pipe air-handling coil on energy consumption in central air-conditioning system. *Energy and Buildings* 2007; 39: 1035-1040.

[51] Jouhara H, Robinson AJ. Experimental investigation of small diameter two-phase closed thermosyphons charged with water, FC-84, FC-77 and FC-3283. *Applied Thermal Engineering* 2010; 30: 201-211.

[52] Jouhara H, Merchant H. Experimental investigation of a thermosyphon based heat exchanger used in energy efficient air handling units. *Energy* 2012; 39: 82-89.

[53] Nguyen-Chi H, Groll M. Entrainment or flooding limit in a closed two-phase thermosyphon. *Journal of Heat Recovery Systems* 1981; 1: 275-286.

[54] Jiao B, Qiu LM, Gan ZH, Zhang XB. Determination of the operation range of a vertical two-phase closed thermosyphon. *Heat and Mass Transfer/Waerme- und Stoffuebertragung* 2012; 48: 1043-1055.

[55] Dunn P, Reay DA. *Heat Pipes*. Pergamon Press: New York, 1994;343.

[56] Kalogirou SA, Papamarcou C. Modelling of a thermosyphon solar water heating system and simple model validation. *Renewable Energy* 2000; 21: 471-493.

[57] Jiao B, Qiu LM, Zhang XB, Zhang Y. Investigation on the effect of filling ratio on the steady-state heat transfer performance of a vertical two-phase closed thermosyphon. *Applied Thermal Engineering* 2008; 28: 1417-1426.

[58] Abreu SL, Colle S. An experimental study of two-phase closed thermosyphons for compact solar domestic hot-water systems. *Solar Energy* 2004; 76: 141-145.

[59] Nayak AK, Lathouwers D, Hagen THJJvd, Schrauwen F, Molenaar P, Rogers A. A numerical study of boiling flow instability of a reactor thermosyphon system. *Applied Thermal Engineering* 2006; 26: 644-653.

[60] Yau YH. Application of a heat pipe heat exchanger to dehumidification enhancement in a HVAC system for tropical climates-a baseline performance characteristics study. *International Journal of Thermal Sciences* 2007; 46: 164-171.

[61] Yau YH. Experimental thermal performance study of an inclined heat pipe heat exchanger operating in high humid tropical HVAC systems. *International Journal of Refrigeration* 2007; 30: 1143-1152.

[62] Yau YH. The use of a double heat pipe heat exchanger system for reducing energy consumption of treating ventilation air in an operating theatre-A full year energy consumption model simulation. *Energy and Buildings* 2008; 40: 917-925.

[63] Riffat SB, Gan G. Determination of effectiveness of heat-pipe heat recovery for naturally-ventilated buildings. *Applied Thermal Engineering* 1998; 18: 121-130.

[64] Jouhara H, Martinet O, Robinson AJ. Experimental study of small diameter thermosyphons charged with water, FC-84, FC-77 & FC-3283. *The Proceeding of the 5th European Thermal-Sciences Conference* 2008;.

[65] Park YJ, Kang HK, Kim CJ. Heat transfer characteristics of a two-phase closed thermosyphon to the fill charge ratio. *International Journal of Heat and Mass Transfer* 2002; 45: 4655-4661.

[66] Hu H, Wu C, Gu W. Calculation of a combined high-temperature phase-change medium freezing outside of a two-phase closed thermosyphon. *Heat Transfer - Asian Research* 2001; 30: 54-62.

[67] Rohsenow WM. A method of correlating heat transfer data for surface boiling of liquids. *Trans.ASME* 1952; 74: 969-976.

[68] Shiraishi M, Kikuchi K, Yamanishi T. Investigation of heat transfer characteristics of a two-phase closed thermosyphon. *Journal of Heat Recovery Systems* 1981; 1: 287-297.

[69] Labuntsov DA. Heat transfer problems with nucleate boiling of liquids. *Thermal Engineering (English translation of Teploenergetika)* 1972; 19: 21-28.

[70] Kruzhilin GN. Free-convection transfer of heat from a horizontal plate and boiling liquid. *Dokl.AN SSSR (Rep.USSR Acad.Sci.)* 1947; 58: 1657-1660.

[71] Imura H, Kusuda H, Ogata J, Miyazaki T, Sakamoto N. Heat transfer in two-phase closed-type thermosyphons. *Heat Transfer - Japanese Research* 1979; 8: 41-53.

[72] Kutateladze SS. *Heat Transfer and Hydrodynamic Resistance*. Publishing House: Moscow, Russia, 1990.

[73] Hashimoto H, Kaminaga F. Heat transfer characteristics in a condenser of closed two-phase thermosyphon: Effect of entrainment on heat transfer deterioration. *Heat Transfer - Asian Research* 2002; 31: 212-225.

[74] Lemmon EW, Huber ML, McLinden MD. NIST Standard Reference Database 23: Reference Fluid Thermodynamics and Transport Properties-REFPROP. *National Institute of Standards and Technology, Standard Reference Data Program, Gaithersburg* 2013; Version 9.1.

[75] Fadhl B, Wrobel LC, Jouhara H. Numerical modelling of the temperature distribution in a two-phase closed thermosyphon. *Applied Thermal Engineering* 2013; 60: 122-131.

[76] Taylor JR. *An Introduction to Error Analysis: The Study of Uncertainties in Physical Measurements*. University Science Books, 1997.

[77] Barbour SL, Krahn J. Numerical modelling - prediction or process?. *Geotechnical News* 2004; December Issue: 44-52.

[78] Thompson DE. Verification, validation, and solution quality in computational physics: CFD methods applied to ice sheet physics 2005; NASA/TM-2005-213453.

[79] Zikanov O. *Essential Computational Fluid Dynamics*. John Wiley and Sons: New Jersey, 2010;302.

[80] Sayma A. *Computational Fluid Dynamics*. Ventus Publishing ApS: Denmark, 2009;133.

[81] De Schepper SCK, Heynderickx GJ, Marin GB. CFD modeling of all gas–liquid and vapor–liquid flow regimes predicted by the Baker chart. *Chemical Engineering Journal* 2008; 138: 349-357.

[82] De Schepper SCK, Heynderickx GJ, Marin GB. Modeling the evaporation of a hydrocarbon feedstock in the convection section of a steam cracker. *Computers & Chemical Engineering* 2009; 33: 122-132.

[83] Ghorai S, Nigam KDP. CFD modeling of flow profiles and interfacial phenomena in two-phase flow in pipes. *Chemical Engineering and Processing* 2006; 45: 55-65.

[84] Parvareh A, Rahimi M, Alizadehdakhel A, Alsairafi AA. CFD and ERT investigations on two-phase flow regimes in vertical and horizontal tubes. *International Communications in Heat and Mass Transfer* 2010; 37: 304-311.

[85] Liu S, Li J, Chen Q. Visualization of flow pattern in thermosyphon by ECT. *Flow Measurement and Instrumentation* 2007; 18: 216-222.

[86] Alizadehdakhel A, Rahimi M, Sanjari J, Alsairafi AA. CFD and artificial neural network modeling of two-phase flow pressure drop. *International Communications in Heat and Mass Transfer* 2009; 36: 850-856.

[87] Ekambara K, Sanders RS, Nandakumar K, Masliyah JH. CFD simulation of bubbly two-phase flow in horizontal pipes. *Chemical Engineering Journal* 2008; 144: 277-288.

[88] Kocamustafaogullari G, Wang Z. An experimental study on local interfacial parameters in a horizontal bubbly two-phase flow. *International Journal of Multiphase Flow* 1991; 17: 553-572.

[89] Kocamustafaogullari G, Huang WD. Internal structure and interfacial velocity development for bubbly two-phase flow. *Nuclear Engineering and Design* 1994; 151: 79-101.

[90] Iskandrani A, Kojasoy G. Local void fraction and velocity field description in horizontal bubbly flow. *Nuclear Engineering and Design* 2001; 204: 117-128.

[91] Gupta R, Fletcher DF, Haynes BS. CFD modelling of flow and heat transfer in the Taylor flow regime. *Chemical Engineering Science* 2010; 65: 2094-2107.

[92] Gupta R, Fletcher DF, Haynes BS. On the CFD modelling of Taylor flow in microchannels. *Chemical Engineering Science* 2009; 64: 2941-2950.

[93] Lu G, Wang J, Jia Z. Experimental and numerical investigations on horizontal oil-gas flow. *Journal of Hydrodynamics, Ser.B* 2007; 19: 683-689.

[94] He Q, Hasegawa Y, Kasagi N. Heat transfer modelling of gas-liquid slug flow without phase change in a micro tube. *International Journal of Heat and Fluid Flow* 2010; 31: 126-136.

[95] de Sampaio PAB, Faccini JLH, Su J. Modelling of stratified gas-liquid two-phase flow in horizontal circular pipes. *International Journal of Heat and Mass Transfer* 2008; 51: 2752-2761.

[96] Juric D, Tryggvason G. Computations of boiling flows. *International Journal of Multiphase Flow* 1998; 24: 387-410.

[97] Narain A, Phan LA, Wang X, Kurita JH, Siemionko A, Tian WN, Kulkarni SD. Direct computational simulations and experiments for film condensation inside tubes and channels. *Annals of the New York Academy of Sciences* 2006; 1077: 471-507.

[98] Phan L, Wang X, Narain A. Effects of exit-condition, gravity, and surface-tension on stability and noise-sensitivity issues for steady condensing flows inside tubes and channels. *International Journal of Heat and Mass Transfer* 2006; 49: 2058-2076.

[99] Lhuillier D. A mean-field description of two-phase flows with phase changes. *International Journal of Multiphase Flow* 2003; 29: 511-525.

[100] Vidalain G, Gosselin L, Lacroix M. An enhanced thermal conduction model for the prediction of convection dominated solid-liquid phase change. *International Journal of Heat and Mass Transfer* 2009; 52: 1753-1760.

[101] Amatachaya P, Srimuang W. Comparative heat transfer characteristics of a flat two-phase closed thermosyphon (FTPCT) and a conventional two-phase closed thermosyphon (CTPCT). *International Communications in Heat and Mass Transfer* 2010; 37: 293-298.

[102] Joudi KA, Al-Tabbakh AA. Computer simulation of a two phase thermosyphon solar domestic hot water heating system. *Energy Conversion and Management* 1999; 40: 775-793.

[103] Lin Z, Wang S, Shirakashi R, Winston Zhang L. Simulation of a miniature oscillating heat pipe in bottom heating mode using CFD with unsteady modeling. *International Journal of Heat and Mass Transfer* 2013; 57: 642-656.

[104] ANSYS FLUENT Theory Guide (Release 13.0). *Multiphase Flows*. ANSYS, Inc., November 2010, (chapter 17), pp. 455-568.

[105] Versteeg HK, Malalasekera W. *An Introduction to Computational Fluid Dynamics; The Finite Volume Method, Second Edition*. Pearson Education: Glasgow, 2007;495.

[106] Anderson JD. *Computational Fluid Dynamics The Basics with Applications*. McGraw-Hill: New York, 1995.

[107] Hirt CW, Nichols BD. Volume of fluid (VOF) method for the dynamics of free boundaries. *Journal of Computational Physics* 1981; 39: 201-225.

[108] Gopala VR, van Wachem BGM. Volume of fluid methods for immiscible-fluid and free-surface flows. *Chemical Engineering Journal* 2008; 141: 204-221.

[109] Brackbill JU. A continuum method for modeling surface tension. *Journal of Computational Physics* 1992; 100: 335-354.

[110] ANSYS FLUENT UDF Manual (Release 13.0). *User Defined Function*. ANSYS, Inc., November 2010, pp. 1-501.

[111] Knudsen M. The kinetic theory of gases. Some modern aspects. *Methuen's Monographs on Physical Subjects* 1934;.

[112] Wu HL, Peng XF, Ye P, Eric Gong Y. Simulation of refrigerant flow boiling in serpentine tubes. *International Journal of Heat and Mass Transfer* 2007; 50: 1186-1195.

[113] Žukauskas A. *Heat Transfer from Tubes in Crossflow*. Advances in Heat Transfer. Elsevier:93-160.

[114] Churchill SW, Bernstein M. Correlating equation for forced convection from gases and liquids to a circular cylinder in crossflow. *Journal of Heat Transfer* 1977; 99: 300-306.

[115] Fadhl B, Wrobel LC, Jouhara H. CFD modelling of a two-phase closed thermosyphon charged with R134a and R404a. *Applied Thermal Engineering* 2015; 78: 482-490.

[116] Shabgard H, Xiao B, Faghri A, Gupta R, Weissman W. Thermal characteristics of a closed thermosyphon under various filling conditions. *International Journal of Heat and Mass Transfer* 2014; 70: 91-102.

[117] Khazaee I, Hosseini R, Noie SH. Experimental investigation of effective parameters and correlation of geyser boiling in a two-phase closed thermosyphon. *Applied Thermal Engineering* 2010; 30: 406-412.

[118] Lin TF, Lin WT, Tsay YL, Wu JC, Shyu RJ. Experimental investigation of geyser boiling in an annular two-phase closed thermosyphon. *International Journal of Heat and Mass Transfer* 1995; 38: 295-307.

[119] Master BI, Chunangad KS, Pushpanathan V. Fouling mitigation using helixchanger heat exchangers. *ECI Conference on Heat Exchanger Fouling and Cleaning* 2003; RP1.

APPENDICES

Appendix A: Experimental Results

This appendix provides the experimental data obtained from the thermocouples, which are used to validate the CFD simulation results. Eight thermocouples, as described in Chapter 4, are used to monitor the temperatures of the evaporator, adiabatic and condenser sections. Two thermocouples are also used to monitor the temperatures of the input and output of the water jacket. The voltage and current readings for the heater, as well as the average wall temperatures for each tested power throughput, are presented in the tables below.

Table A-1: Experimental data for water-charged thermosyphon

Heater			**Evaporator**		**Adia.**	**Condenser**					**Water Jacket**		
I	V	Q_{in}	T_{e1}	T_{e2}	T_a	T_{c1}	T_{c2}	T_{c3}	T_{c4}	T_{c5}	$T_{w,in}$	$T_{w,out}$	$\dot{V}$
amp	volt	W	°C	°C	°C	°C	°C	°C	°C	°C	°C	°C	L/min
0.649	77.2	50.10	58.8	58.9	36.1	33.8	31.5	28.2	25.6	25.1	25.9	21.4	0.165
0.796	94.8	75.46	64.2	67.5	44.2	39.2	34.7	32	27.8	26.9	27.9	21.6	0.165
0.917	109.5	100.41	67	72.7	48.1	42.4	41.2	40.4	37.21	35.1	29.9	21.6	0.165
1.022	122	124.68	60.3	74.8	49.9	44.5	43.2	42.4	39	37.2	30.6	21.6	0.165
1.111	133.6	148.43	69.2	61	52.1	45.9	44.6	45	43.4	40	33.3	21	0.165
1.198	144.3	172.87	72.6	64.3	54.3	47.4	45.7	44.8	43.9	42.8	35.4	21.2	0.165
1.287	155.2	199.74	76.9	67.1	56	48.8	46.1	47.2	45.4	43.5	37.3	21.4	0.165
1.366	164.9	225.25	79.7	70.2	57.9	50	47.4	48.1	46.5	45	38.2	21.4	0.165
1.437	174	250.04	83.8	73.2	59.5	50.8	48.2	51.7	48.2	47.9	40.4	21.6	0.165
1.506	183	275.6	87.8	78.1	62.4	52.4	49.9	54.1	53	54.6	42.4	21.7	0.165
1.569	190.9	299.52	91.6	79.6	63.1	53.1	50	54.2	52.2	44.3	44.3	22	0.165
1.631	198.1	323.1	96.1	83.4	65.9	55.4	52.5	58	54	53.9	47.5	22.4	0.165
1.693	206.3	349.27	99.8	86.7	67.5	56.2	52.7	58	56.6	57.2	49.2	21.5	0.165
1.756	214.2	376.14	103.6	90.5	69.6	55.8	52.4	59.3	58.2	60.2	51	21.5	0.165

Table A-2: Experimental data for R134a-charged thermosyphon

Heater			Evaporator		Adia.	Condenser					Water Jacket		
I	V	Q_{in}	T_{e1}	T_{e2}	T_a	T_{c1}	T_{c2}	T_{c3}	T_{c4}	T_{c5}	$T_{w,in}$	$T_{w,out}$	$\dot{V}$
amp	volt	W	°C	°C	°C	°C	°C	°C	°C	°C	°C	°C	L/min
0.322	61.3	19.74	27.3	24.2	22.8	22.5	22.7	23.1	22.7	23.4	19.5	20.9	0.2
0.449	65.8	29.58	29.6	26.8	24.6	24.1	24.3	24.6	24.3	25.1	18.6	19.4	0.2
0.517	76.4	39.53	34.7	31.5	29.1	28.1	28.1	28.5	27.9	29.1	17.9	18.6	0.2
0.649	77.2	50.16	35.1	31.8	28.8	27.5	27.5	27.9	27.1	28.5	18.5	19.3	0.2
0.917	109.5	100.4	39.2	39.4	36.1	33.2	33.1	33.7	32.7	34.8	21.3	25.8	0.2

Table A-3: Experimental data for R404a-charged thermosyphon

Heater			Evaporator		Adia.	Condenser					Water Jacket		
I	V	Q_{in}	T_{e1}	T_{e2}	T_a	T_{c1}	T_{c2}	T_{c3}	T_{c4}	T_{c5}	$T_{w,in}$	$T_{w,out}$	$\dot{V}$
amp	volt	W	°C	°C	°C	°C	°C	°C	°C	°C	°C	°C	L/min
0.324	61.35	19.88	30.7	28.4	27.5	27.1	27.0	27.3	27.2	27.2	24.6	25.8	0.2
0.442	65.71	29.04	28.0	26.9	26.3	25.5	25.3	25.7	25.6	25.8	22.0	24.2	0.2
0.519	78.34	40.66	28.9	27.9	27.2	26.1	25.8	26.4	26.3	26.4	21.7	24.2	0.2
0.643	77.16	49.61	31.0	30.1	29.1	27.7	27.3	28.2	28.1	28.0	22.2	25.4	0.2
0.918	109.64	100.64	36.2	35.8	34.0	30.7	30.3	31.9	32.0	31.8	21.7	26.5	0.2

Appendix B: Errors and Uncertainties Calculation

This appendix provides a sample calculation of errors and uncertainties for one set of the experimental readings for the water-charged thermosyphon. The same procedure has been obtained for the other sets of readings. The set of the experimental readings for Q_{in} = 100.41 W has been selected and presented in Table B-1.

Table B-1: Results of the experimental readings for Q_{in} =100.41 W

Heater		
$I_{electric}$	amp	0.917
V_{vol}	volt	109.5
Q_{in}	W	100.41
Evaporator section		
T_{e1}	^{o}C	67
T_{e2}	^{o}C	72.7
$T_{e,av}$	^{o}C	69.85
Adiabatic section		
T_a	^{o}C	48.1
Condenser section		
T_{c1}	^{o}C	42.4
T_{c2}	^{o}C	41.2
T_{c3}	^{o}C	40.4
T_{c4}	^{o}C	37.21
T_{c5}	^{o}C	35.1
$T_{c,av}$	^{o}C	39.26
Water jacket		
T_{w1}	^{o}C	21.6
T_{w2}	^{o}C	29.9
ΔT_w	^{o}C	8.3
$\dot{V}$	m^3/s	$2.75*10^{-6}$
Q_{out}	W	95.11
Thermal resistance		
ΔT_{e-c}	^{o}C	30.58
R	K/W	0.3046

Each reading presented in the above table will have an error associated with it and, as a result, each of these will need to be determined. The errors for quantities obtained by sums or differences can be determined as

$$S_y = \sqrt{(S_a)^2 + (S_b)^2} \tag{B-1}$$

The errors for quantities obtained from products and quotients can be determined as

$$S_y = y\sqrt{\left(\frac{S_a}{a}\right)^2 + \left(\frac{S_b}{b}\right)^2} \tag{B-2}$$

The error for the voltage (V_{vol}) and current ($I_{electric}$) readings can be determined as

$$\pm(1.2\%.rdg) \tag{B-3}$$

The error for the temperature readings can be determined as

$$\pm(0.05\%.rdg + 0.3\ ℃) \tag{B-4}$$

Based on Eq. (B-1), the error for the calculated average wall temperature of the evaporator and condenser sections can be determined using Eq. (B-5) and Eq. (B-6), respectively,

$$S_{T_{e,av}} = \sqrt{\left(S_{T_{e1}}\right)^2 + \left(S_{T_{e2}}\right)^2} \tag{B-5}$$

$$S_{T_{c,av}} = \sqrt{\left(S_{T_{c1}}\right)^2 + \left(S_{T_{c2}}\right)^2 + \left(S_{T_{c3}}\right)^2 + \left(S_{T_{c4}}\right)^2 + \left(S_{T_{c5}}\right)^2} \tag{B-6}$$

The error for the calculated temperature difference between the cooling water inlet and outlet and the calculated temperature difference between the average wall temperature of the evaporator and condenser sections can be determined using Eq. (B-7) and Eq. (B-8), respectively,

$$S_{\Delta T_w} = \sqrt{\left(S_{T_{w,inlet}}\right)^2 + \left(S_{T_{w,outlet}}\right)^2} \tag{B-7}$$

$$S_{\Delta T_{e-c}} = \sqrt{\left(S_{T_{e,av}}\right)^2 + \left(S_{T_{c,av}}\right)^2} \tag{B-8}$$

Based on Eq. (B-2), the error for the calculated heat load (Q_{in}) to the evaporator section and the calculated heat rejected (Q_{out}) from the condenser section can be determined using Eq. (B-9) and Eq. (B-10), respectively,

$$S_{Q_{in}} = Q_{in}\sqrt{\left(\frac{S_{I_{electric}}}{I_{electric}}\right)^2 + \left(\frac{S_{V_{vol}}}{V_{vol}}\right)^2} \tag{B-9}$$

$$S_{Q_{out}} = Q_{out}\sqrt{\left(\frac{S_{\Delta T_w}}{\Delta T_w}\right)^2 + \left(\frac{S_{\dot{V}}}{\dot{V}}\right)^2} \tag{B-10}$$

Eventually, the error for the calculated thermal resistance (R) can be determined as

$$S_R = R\sqrt{\left(\frac{S_{\Delta T_{e-c}}}{\Delta T_{e-c}}\right)^2 + \left(\frac{S_{Q_{in}}}{Q_{in}}\right)^2} \tag{B-11}$$

Based on the above discussion, the results for the errors and uncertainties for the set of readings for Q_{in} = 100.41 W have been tabulated in Table B-2.

Table B-2: Results of error and uncertainty analysis for the set of readings for Q_{in}=100.41 W

Heater			$S_y \pm$	$Error \pm$
$I_{electric}$	amp	0.917	0.011004	1.20%
V_{vol}	volt	109.5	1.314	1.20%
Q_{in}	W	100.41	1.7040	1.70%
Evaporator section				
T_{e1}	°C	67	0.3335	0.50%
T_{e2}	°C	72.7	0.33635	0.46%
$T_{e,av}$	°C	69.85	0.47365	0.68%
Adiabatic section				
T_a	°C	48.1	0.32405	0.67%
Condenser section				
T_{c1}	°C	42.4	0.3212	0.76%
T_{c2}	°C	41.2	0.3206	0.78%
T_{c3}	°C	40.4	0.3202	0.79%
T_{c4}	°C	37.21	0.31861	0.86%
T_{c5}	°C	35.1	0.31755	0.90%
$T_{c,av}$	°C	39.26	0.71472	1.82%
Water jacket				
T_{w1}	°C	21.6	0.3108	1.44%
T_{w2}	°C	29.9	0.31495	1.05%
ΔT_w	°C	8.3	0.44248	5.33%
$\dot{V}$	m^3/s	$2.75*10^{-6}$	$5.5*10^{-8}$	2.00%
Q_{out}	W	95.11	5.41566	5.69%
Thermal resistance				
ΔT_{e-c}	°C	30.58	0.85743	2.80%
R	K/W	0.3046	0.00998	3.28%

Appendix C: Working Fluids Thermodynamic Properties

This appendix provides the saturation properties of the tested working fluids. The NIST REFPROP program [74] has been used to obtain the thermodynamics properties, which are listed in the tables below.

Table C-1: Water saturation properties

T_{sat}	P_v	ρ_l	ρ_v	$C_{p,l}$	h_{fg}	k_l	μ_l	Pr_l	σ_{lv}
K	**Pa**	**kg/m^3**	**kg/m^3**	**J/kg.K**	**J/kg**	**W/m.K**	**kg/m.s**	**-**	**N/m**
274.15	657.09	999.9	0.0051965	4216.6	2498600	0.55811	0.0017312	13.08	0.075508
279.15	935.36	999.9	0.0072657	4203.2	2486700	0.57001	0.0014716	10.851	0.074799
284.15	1313	999.6	0.010021	4194	2474800	0.58079	0.0012692	9.1654	0.074075
289.15	1818.8	998.9	0.013645	4187.8	2463000	0.59064	0.0011081	7.8568	0.073337
294.15	2488.2	998.0	0.018354	4183.7	2451200	0.59971	0.00097756	6.8197	0.072584
299.15	3363.9	996.7	0.024406	4181.2	2439300	0.60808	0.00087012	5.983	0.071818
304.15	4496.9	995.3	0.032102	4179.9	2427400	0.61584	0.00078054	5.2977	0.071037
309.15	5947.9	993.6	0.04179	4179.5	2415500	0.62305	0.00070498	4.7291	0.070242
314.15	7787.8	991.8	0.053871	4179.7	2403600	0.62973	0.00064063	4.2521	0.069434
319.15	10099	989.8	0.068803	4180.6	2391600	0.63594	0.00058533	3.8479	0.068611
324.15	12978	987.5	0.087103	4181.8	2379500	0.64169	0.00053745	3.5025	0.067776
329.15	16533	985.2	0.10935	4183.5	2367400	0.64701	0.00049569	3.2051	0.066927
334.15	20888	982.6	0.1362	4185.6	2355200	0.65191	0.00045906	2.9474	0.066065
339.15	26183	980.0	0.16835	4188	2342900	0.6564	0.00042673	2.7226	0.06519
344.15	32575	977.2	0.20661	4190.8	2330500	0.66051	0.00039806	2.5256	0.064302
349.15	40239	974.2	0.25184	4194	2318100	0.66424	0.00037252	2.3521	0.063402
354.15	49367	971.1	0.30498	4197.6	2305500	0.66761	0.00034966	2.1985	0.062489
359.15	60173	967.9	0.36706	4201.7	2292800	0.67062	0.00032913	2.0621	0.061565
364.15	72890	964.6	0.43918	4206.2	2279900	0.67328	0.00031061	1.9405	0.060628
369.15	87771	961.2	0.52254	4211.3	2266900	0.67559	0.00029386	1.8318	0.059679
374.15	105090	957.6	0.61841	4216.8	2253800	0.67758	0.00027866	1.7342	0.058719
379.15	125150	954.0	0.72816	4223	2240400	0.67924	0.00026481	1.6464	0.057747
384.15	148260	950.2	0.85325	4229.7	2226900	0.68059	0.00025217	1.5672	0.056765
389.15	174770	946.3	0.99522	4237.1	2213200	0.68163	0.0002406	1.4956	0.055771
394.15	205050	942.3	1.1557	4245.2	2199300	0.68237	0.00022998	1.4308	0.054766
399.15	239470	938.2	1.3365	4253.9	2185200	0.68281	0.00022021	1.3719	0.053751
404.15	278460	934.0	1.5394	4263.5	2170800	0.68296	0.0002112	1.3184	0.052726
409.15	322450	929.7	1.7664	4273.8	2156200	0.68283	0.00020286	1.2697	0.051691
414.15	371890	925.2	2.0196	4284.9	2141300	0.68242	0.00019515	1.2253	0.050646
419.15	427260	920.7	2.301	4296.8	2126100	0.68175	0.00018798	1.1848	0.049592
424.15	489070	916.1	2.613	4309.7	2110600	0.68081	0.00018132	1.1478	0.048528
429.15	557840	911.3	2.9581	4323.6	2094800	0.67961	0.0001751	1.114	0.047455

434.15	634120	906.5	3.3387	4338.4	2078700	0.67846	0.0001693	1.0826	0.046374
439.15	718480	901.5	3.7576	4354.3	2062300	0.67694	0.00016387	1.0541	0.045284
444.15	811520	896.4	4.2176	4371.3	2045400	0.67514	0.00015878	1.0281	0.044186
449.15	913840	891.2	4.7217	4389.5	2028200	0.67309	0.000154	1.0043	0.04308
454.15	102610	885.9	5.273	4409	2010600	0.6708	0.0001495	0.98264	0.041967
459.15	114890	880.5	5.875	4429.7	1992600	0.66828	0.00014526	0.96289	0.040847
464.15	128300	875.0	6.5312	4452	1974100	0.66553	0.00014126	0.94494	0.039719
469.15	142900	869.3	7.2453	4475.7	1955200	0.66255	0.00013747	0.92865	0.038586
474.15	158770	863.5	8.0214	4501.1	1935800	0.65936	0.00013388	0.91393	0.037446
479.15	175980	857.6	8.8638	4528.2	1915900	0.65595	0.00013047	0.90068	0.036301
484.15	194610	851.5	9.777	4557.2	1895500	0.65232	0.00012723	0.88883	0.03515
489.15	214730	845.3	10.766	4588.2	1874600	0.64848	0.00012414	0.87832	0.033994
494.15	236430	838.9	11.836	4621.5	1853000	0.64444	0.00012119	0.86908	0.032834
499.15	259780	832.4	12.993	4657.1	1830900	0.64018	0.00011837	0.86108	0.03167

Table C-2: R134a saturation properties

T_{sat}	P_v	ρ_l	ρ_v	$C_{p,l}$	h_{fg}	k_l	μ_l	Pr_l	σ_{lv}
K	**Pa**	**kg/m^3**	**kg/m^3**	**J/kg.K**	**J/kg**	**W/m.K**	**kg/m.s**	**-**	**N/m**
193.15	3671.9	1529	0.2342	1198.1	249670	0.13154	0.0010203	9.292	0.02356
194.15	3985.6	1526.3	0.2530	1199.1	249080	0.13098	0.0009953	9.1119	0.023401
195.15	4321.7	1523.6	0.2730	1200.2	248500	0.13042	0.0009713	8.9383	0.02324
196.15	4681.6	1520.9	0.2943	1201.3	247910	0.12987	0.00094824	8.7716	0.023079
197.15	5066.5	1518.2	0.3170	1202.4	247330	0.12931	0.00092607	8.6112	0.022918
198.15	5477.7	1515.5	0.3411	1203.6	246740	0.12876	0.00090473	8.4569	0.022758
199.15	5916.8	1512.8	0.3667	1204.7	246160	0.12821	0.00088418	8.3083	0.022598
200.15	6385.1	1510.1	0.3939	1205.9	245580	0.12766	0.00086438	8.1652	0.022437
201.15	6884.3	1507.3	0.4227	1207.1	244990	0.12712	0.00084529	8.0272	0.022278
202.15	7415.8	1504.6	0.4533	1208.4	244410	0.12657	0.00082688	7.8941	0.022118
203.15	7981.4	1501.9	0.4856	1209.6	243820	0.12603	0.0008091	7.7656	0.021959
204.15	8582.6	1499.1	0.5199	1210.9	243240	0.12549	0.00079194	7.6416	0.021799
205.15	9221.3	1496.4	0.5561	1212.2	242650	0.12495	0.00077535	7.5217	0.02164
206.15	9899.2	1493.7	0.5943	1213.5	242070	0.12441	0.00075931	7.4059	0.021482
207.15	10618	1490.9	0.6347	1214.8	241480	0.12388	0.0007438	7.2938	0.021323
208.15	11380	1488.2	0.6728	1216.1	240890	0.12335	0.00072879	7.1854	0.021165
209.15	12187	1485.4	0.7221	1217.5	240300	0.12281	0.00071426	7.0805	0.021007
210.15	13041	1482.6	0.7694	1218.8	239720	0.12229	0.00070019	6.9788	0.020849
211.15	13944	1479.9	0.8192	1220.2	239130	0.12176	0.00068655	6.8803	0.020691
212.15	14899	1477.1	0.8716	1221.6	238540	0.12123	0.00067333	6.7849	0.020534
213.15	15906	1474.3	0.9267	1223	237950	0.12071	0.00066051	6.6923	0.020377
214.15	16970	1471.6	0.9846	1224.5	237350	0.12019	0.00064807	6.6025	0.02022
215.15	18091	1468.8	1.0454	1225.9	236760	0.11967	0.00063599	6.5154	0.020063
216.15	19273	1466	1.1092	1227.4	236170	0.11915	0.00062427	6.4308	0.019907
217.15	20518	1463.2	1.1762	1228.9	235570	0.11863	0.00061288	6.3486	0.019751
218.15	21828	1460.4	1.2463	1230.4	234980	0.11812	0.00060182	6.2688	0.019595

219.15	23206	1457.6	1.3198	1231.9	234380	0.1176	0.00059106	6.1912	0.019439
220.15	24655	1454.8	1.3968	1233.4	233780	0.11709	0.0005806	6.1157	0.019284
221.15	26176	1452	1.4773	1234.9	233180	0.11658	0.00057043	6.0424	0.019128
222.15	27774	1449.1	1.5616	1236.5	232580	0.11607	0.00056053	5.971	0.018973
223.15	29451	1446.3	1.6496	1238.1	231980	0.11557	0.00055089	5.9016	0.018819
224.15	31209	1443.5	1.7416	1239.6	231370	0.11506	0.00054151	5.834	0.018664
225.15	33051	1440.6	1.8377	1241.3	230770	0.11456	0.00053237	5.7682	0.01851
226.15	34982	1437.8	1.938	1242.9	230160	0.11406	0.00052346	5.7041	0.018356
227.15	37003	1434.9	2.0427	1244.5	229550	0.11356	0.00051479	5.6416	0.018202
228.15	39117	1432.1	2.1518	1246.2	228940	0.11306	0.00050633	5.5807	0.018049
229.15	41329	1429.2	2.2655	1247.8	228330	0.11256	0.00049808	5.5214	0.017896
230.15	43640	1426.4	2.384	1249.5	227710	0.11207	0.00049003	5.4635	0.017743
231.15	46055	1423.5	2.5074	1251.2	227100	0.11157	0.00048217	5.4071	0.01759
232.15	48577	1420.6	2.6359	1252.9	226480	0.11108	0.00047451	5.352	0.017437
233.15	51209	1417.7	2.7695	1254.6	225860	0.11059	0.00046703	5.2983	0.017285
234.15	53955	1414.8	2.9085	1256.4	225240	0.1101	0.00045972	5.2459	0.017133
235.15	56817	1411.9	3.0529	1258.1	224610	0.10961	0.00045258	5.1947	0.016982
236.15	59801	1409	3.2031	1259.9	223980	0.10913	0.00044561	5.1447	0.01683
237.15	62908	1406.1	3.359	1261.7	223350	0.10864	0.0004388	5.0959	0.016679
238.15	66144	1403.1	3.5209	1263.5	222720	0.10816	0.00043213	5.0482	0.016528
239.15	69512	1400.2	3.689	1265.4	222090	0.10768	0.00042562	5.0016	0.016378
240.15	73015	1397.3	3.8633	1267.2	221450	0.1072	0.00041925	4.9561	0.016227
241.15	76658	1394.3	4.0441	1269.1	220810	0.10672	0.00041302	4.9116	0.016077
242.15	80444	1391.4	4.2316	1271	220170	0.10624	0.00040692	4.8681	0.015927
243.15	84378	1388.4	4.4259	1272.9	219530	0.10576	0.00040095	4.8255	0.015778
244.15	88463	1385.4	4.6271	1274.8	218880	0.10529	0.00039511	4.7839	0.015629
245.15	92703	1382.4	4.8356	1276.7	218230	0.10482	0.00038939	4.7431	0.01548
246.15	97104	1379.5	5.0514	1278.7	217580	0.10434	0.00038379	4.7033	0.015331
247.15	101670	1376.5	5.2748	1280.7	216920	0.10387	0.0003783	4.6643	0.015182
248.15	106400	1373.4	5.5059	1282.7	216260	0.1034	0.00037292	4.6261	0.015034
249.15	111300	1370.4	5.745	1284.7	215600	0.10293	0.00036765	4.5888	0.014886
250.15	116390	1367.4	5.9922	1286.8	214930	0.10246	0.00036249	4.5522	0.014739
251.15	121650	1364.4	6.2477	1288.8	214270	0.102	0.00035742	4.5163	0.014592
252.15	127100	1361.3	6.5117	1290.9	213590	0.10153	0.00035246	4.4812	0.014445
253.15	132730	1358.3	6.7845	1293	212920	0.10107	0.00034758	4.4469	0.014298
254.15	138570	1355.2	7.0662	1295.2	212240	0.10061	0.00034281	4.4132	0.014151
255.15	144600	1352.1	7.3571	1297.3	211560	0.10014	0.00033812	4.3802	0.014005
256.15	150840	1349	7.6574	1299.5	210870	0.099684	0.00033352	4.3479	0.013859
257.15	157280	1345.9	7.9673	1301.7	210180	0.099225	0.000329	4.3162	0.013714
258.15	163940	1342.8	8.287	1304	209490	0.098767	0.00032456	4.2851	0.013569
259.15	170820	1339.7	8.6168	1306.2	208790	0.09831	0.00032021	4.2546	0.013424
260.15	177920	1336.6	8.9568	1308.5	208090	0.097854	0.00031593	4.2248	0.013279
261.15	185240	1333.4	9.3074	1310.8	207390	0.097398	0.00031173	4.1955	0.013135
262.15	192800	1330.3	9.6688	1313.2	206680	0.096944	0.00030761	4.1668	0.012991
263.15	200600	1327.1	10.041	1315.6	205970	0.096491	0.00030355	4.1386	0.012847
264.15	208640	1323.9	10.425	1318	205250	0.096039	0.00029956	4.111	0.012704

265.15	216930	1320.8	10.82	1320.4	204530	0.095588	0.00029565	4.0839	0.012561
266.15	225480	1317.6	11.227	1322.9	203810	0.095138	0.00029179	4.0573	0.012418
267.15	234280	1314.3	11.646	1325.4	203080	0.094689	0.000288	4.0312	0.012275
268.15	243340	1311.1	12.077	1327.9	202340	0.094241	0.00028428	4.0056	0.012133
269.15	252680	1307.9	12.521	1330.4	201600	0.093794	0.00028061	3.9804	0.011991
270.15	262280	1304.6	12.978	1333	200860	0.093347	0.00027701	3.9558	0.01185
271.15	272170	1301.4	13.448	1335.7	200110	0.092902	0.00027346	3.9316	0.011709
272.15	282340	1298.1	13.931	1338.3	199360	0.092457	0.00026996	3.9078	0.011568
273.15	292800	1294.8	14.428	1341	198600	0.092013	0.00026653	3.8845	0.011427
274.15	303560	1291.5	14.939	1343.8	197840	0.09157	0.00026314	3.8616	0.011287
275.15	314620	1288.1	15.465	1346.6	197070	0.091128	0.00025981	3.8391	0.011147
276.15	325980	1284.8	16.005	1349.4	196300	0.090687	0.00025653	3.817	0.011008
277.15	337660	1281.4	16.56	1352.3	195520	0.090246	0.00025329	3.7954	0.010869
278.15	349660	1278.1	17.131	1355.2	194740	0.089806	0.00025011	3.7741	0.01073
279.15	361980	1274.7	17.717	1358.1	193950	0.089367	0.00024697	3.7532	0.010592
280.15	374630	1271.3	18.319	1361.1	193160	0.088929	0.00024388	3.7327	0.010454
281.15	387610	1267.9	18.938	1364.1	192360	0.088491	0.00024083	3.7126	0.010316
282.15	400940	1264.4	19.573	1367.2	191550	0.088054	0.00023783	3.6928	0.010178
283.15	414610	1261	20.226	1370.4	190740	0.087618	0.00023487	3.6734	0.010041
284.15	428630	1257.5	20.896	1373.6	189920	0.087182	0.00023195	3.6543	0.009904
285.15	443010	1254	21.584	1376.8	189100	0.086747	0.00022907	3.6356	0.009768
286.15	457760	1250.5	22.29	1380.1	188270	0.086312	0.00022622	3.6173	0.009632
287.15	472880	1246.9	23.015	1383.5	187430	0.085878	0.00022342	3.5992	0.009496
288.15	488370	1243.4	23.758	1386.9	186590	0.085444	0.00022066	3.5815	0.009361
289.15	504250	1239.8	24.522	1390.3	185740	0.085011	0.00021793	3.5642	0.009226
290.15	520520	1236.2	25.305	1393.9	184890	0.084579	0.00021524	3.5471	0.009092
291.15	537180	1232.6	26.109	1397.5	184030	0.084147	0.00021258	3.5304	0.008954
292.15	554240	1229	26.934	1401.1	183160	0.083715	0.00020996	3.514	0.008824
293.15	571710	1225.3	27.78	1404.9	182280	0.083284	0.00020737	3.4979	0.008691
294.15	589590	1221.7	28.648	1408.7	181400	0.082854	0.00020481	3.4821	0.008558
295.15	607890	1218	29.539	1412.5	180510	0.082423	0.00020228	3.4666	0.008422
296.15	626620	1214.2	30.452	1416.5	179610	0.081993	0.00019979	3.4514	0.008241
297.15	645780	1210.5	31.389	1420.5	178700	0.081564	0.00019732	3.4365	0.008162
298.15	665380	1206.7	32.35	1424.6	177790	0.081134	0.00019489	3.4219	0.008031
299.15	685430	1202.9	33.335	1428.8	176870	0.080705	0.00019248	3.4076	0.007900
300.15	705920	1199.1	34.346	1433.1	175940	0.080277	0.0001901	3.3936	0.00777
301.15	726880	1195.2	35.382	1437.5	175000	0.079848	0.00018775	3.3799	0.00764
302.15	748300	1191.4	36.445	1441.9	174050	0.07942	0.00018542	3.3665	0.007510
303.15	770200	1187.5	37.535	1446.5	173100	0.078992	0.00018313	3.3533	0.007381
304.15	792570	1183.5	38.653	1451.1	172130	0.078564	0.00018085	3.3405	0.007252
305.15	815430	1179.6	39.799	1455.9	171160	0.078136	0.00017861	3.3279	0.007124
306.15	838780	1175.6	40.974	1460.8	170180	0.077709	0.00017638	3.3157	0.006996
307.15	862630	1171.6	42.18	1465.8	169180	0.077281	0.00017418	3.3037	0.006869
308.15	886980	1167.5	43.416	1470.9	168180	0.076853	0.000172	3.292	0.006742
309.15	911850	1163.4	44.683	1476.1	167170	0.076426	0.00016985	3.2806	0.006615
310.15	937240	1159.3	45.983	1481.5	166150	0.075998	0.00016772	3.2694	0.006489

311.15	963150	1155.1	47.316	1487	165120	0.075571	0.00016561	3.2586	0.006364
312.15	989600	1151	48.683	1492.6	164070	0.075143	0.00016352	3.2481	0.006239
313.15	1016600	1146.7	50.085	1498.4	163020	0.074716	0.00016145	3.2378	0.006119
314.15	1044100	1142.5	51.523	1504.4	161950	0.074288	0.0001594	3.2279	0.005990
315.15	1072200	1138.2	52.998	1510.5	160880	0.07386	0.00015737	3.2182	0.005867
316.15	1100900	1133.8	54.512	1516.7	159790	0.073432	0.00015536	3.2089	0.005744
317.15	1130100	1129.5	56.064	1523.2	158690	0.073003	0.00015337	3.1999	0.005621
318.15	1159900	1125.1	57.657	1529.8	157580	0.072575	0.00015139	3.1912	0.005499
319.15	1190300	1120.6	59.292	1536.7	156450	0.072146	0.00014943	3.1828	0.005378
320.15	1221300	1116.1	60.969	1543.7	155310	0.071717	0.00014749	3.1748	0.005257
321.15	1252900	1111.5	62.69	1550.9	154160	0.071287	0.00014557	3.1671	0.005136
322.15	1285100	1106.9	64.458	1558.4	152990	0.070857	0.00014366	3.1597	0.005017
323.15	1317900	1102.3	66.272	1566.1	151810	0.070427	0.00014177	3.1527	0.004897
324.15	1351300	1097.6	68.134	1574.1	150620	0.069996	0.0001399	3.1461	0.004779
325.15	1385400	1092.9	70.047	1582.4	149410	0.069565	0.00013803	3.1398	0.004660
326.15	1420100	1088.1	72.012	1590.9	148180	0.069133	0.00013619	3.134	0.004542
327.15	1455500	1083.2	74.03	1599.7	146940	0.0687	0.00013435	3.1285	0.004426
328.15	1491500	1078.3	76.104	1608.9	145680	0.068267	0.00013253	3.1234	0.004309
329.15	1528200	1073.4	78.235	1618.4	144410	0.067834	0.00013072	3.1188	0.004193
330.15	1565600	1068.3	80.426	1628.2	143120	0.067399	0.00012893	3.1147	0.004078
331.15	1603600	1063.2	82.679	1638.4	141800	0.066964	0.00012715	3.111	0.003964
332.15	1642300	1058.1	84.996	1649.1	140470	0.066528	0.00012538	3.1078	0.003850
333.15	1681800	1052.9	87.379	1660.2	139120	0.066091	0.00012361	3.1051	0.003737
334.15	1721900	1047.6	89.832	1671.7	137750	0.065654	0.00012187	3.103	0.003624
335.15	1762800	1042.2	92.358	1683.8	136360	0.065215	0.00012013	3.1015	0.003512
336.15	1804400	1036.8	94.958	1696.4	134950	0.064776	0.00011839	3.1006	0.003401
337.15	1846700	1031.2	97.637	1709.5	133520	0.064336	0.00011667	3.1003	0.003290
338.15	1889800	1025.6	100.4	1723.4	132060	0.063894	0.00011496	3.1007	0.003180
339.15	1933700	1020	103.24	1737.9	130570	0.063452	0.00011326	3.1019	0.003071
340.15	1978300	1014.2	106.18	1753.1	129060	0.063009	0.00011156	3.1039	0.002963
341.15	2023700	1008.3	109.21	1769.1	127530	0.062564	0.00010987	3.1067	0.002855
342.15	2069800	1002.3	112.34	1786	125960	0.062118	0.00010818	3.1105	0.002749
343.15	2116800	996.25	115.57	1803.9	124370	0.061672	0.00010651	3.1153	0.002642
344.15	2164600	990.06	118.91	1822.8	122740	0.061224	0.00010483	3.1212	0.002537
345.15	2213200	983.76	122.37	1842.9	121090	0.060775	0.00010316	3.1283	0.002433
346.15	2262700	977.33	125.95	1864.3	119390	0.060324	0.0001015	3.1367	0.002329
347.15	2313000	970.78	129.65	1887.1	117670	0.059873	0.000099831	3.1465	0.002227
348.15	2364100	964.09	133.49	1911.5	115900	0.059421	0.000098169	3.1579	0.002125
349.15	2416100	957.25	137.48	1937.6	114100	0.058967	0.000096508	3.1711	0.002024
350.15	2469000	950.26	141.62	1965.7	112250	0.058513	0.000094846	3.1863	0.001925
351.15	2522800	943.1	145.93	1996.1	110360	0.058058	0.000093182	3.2037	0.001826
352.15	2577600	935.77	150.41	2029	108420	0.057602	0.000091516	3.2236	0.001728
353.15	2633200	928.24	155.08	2064.8	106420	0.057147	0.000089846	3.2464	0.001631
354.15	2689800	920.51	159.95	2104	104380	0.056691	0.00008817	3.2723	0.001536
355.15	2747300	912.56	165.05	2147	102270	0.056235	0.000086487	3.302	0.001441
356.15	2805800	904.37	170.38	2194.5	100100	0.055781	0.000084794	3.3359	0.001348

357.15	2865300	895.91	175.97	2247.3	97854	0.055329	0.00008309	3.3749	0.001256
358.15	2925800	887.16	181.85	2306.4	95536	0.05488	0.000081372	3.4198	0.001165
359.15	2987400	878.1	188.05	2373	93134	0.054435	0.000079637	3.4716	0.001076
360.15	3049900	868.68	194.59	2448.8	90639	0.053997	0.000077882	3.5319	0.000988
361.15	3113600	858.86	201.52	2535.8	88042	0.053568	0.000076102	3.6025	0.000901
362.15	3178300	848.6	208.89	2636.9	85330	0.053153	0.000074293	3.6857	0.000816
363.15	3244200	837.83	216.76	2755.9	82487	0.052755	0.00007245	3.7848	0.000733
364.15	3311200	826.47	225.2	2898.3	79495	0.052383	0.000070565	3.9043	0.000652
365.15	3379300	814.43	234.31	3071.9	76330	0.052047	0.000068628	4.0506	0.000572
366.15	3448700	801.58	244.22	3288.6	72961	0.051762	0.000066629	4.2331	0.000495
367.15	3519300	787.75	255.08	3566.9	69344	0.051551	0.000064551	4.4664	0.000420
368.15	3591200	772.7	267.14	3938.5	65423	0.05145	0.000062373	4.7746	0.000347
369.15	3664500	756.09	280.73	4460.2	61111	0.051514	0.000060062	5.2003	0.000278
370.15	3739100	737.34	296.41	5247.5	56271	0.051838	0.000057567	5.8275	0.000211

Table C-3: R404a saturation properties

T_{sat}	P_v	ρ_l	ρ_v	$C_{p,l}$	h_{fg}	k_l	μ_l	Pr_l	σ_{lv}
K	**Pa**	**kg/m^3**	**kg/m^3**	**J/kg.K**	**J/kg**	**W/m.K**	**kg/m.s**	**-**	**N/m**
230	113180	1296.8	6.085	1257.6	198480	0.09067	0.0003220	4.4655	0.013708
231	118610	1293.7	6.3601	1259.7	197820	0.09024	0.0003173	4.4289	0.01356
232	124240	1290.5	6.6448	1261.7	197150	0.08981	0.0003127	4.3931	0.013412
233	130080	1287.4	6.9394	1263.9	196490	0.08938	0.0003082	4.3582	0.013265
234	136130	1284.3	7.2441	1266	195810	0.08895	0.0003038	4.3239	0.013117
235	142400	1281.1	7.5592	1268.2	195140	0.08852	0.0002995	4.2905	0.01297
236	148890	1278	7.885	1270.4	194460	0.08810	0.0002952	4.2577	0.012824
237	155600	1274.8	8.2217	1272.7	193790	0.08767	0.0002911	4.2256	0.012678
238	162550	1271.6	8.5695	1275	193100	0.08725	0.0002870	4.1942	0.012532
239	169740	1268.4	8.9288	1277.4	192410	0.08683	0.0002830	4.1634	0.012386
240	177170	1265.2	9.2998	1279.8	191720	0.08641	0.0002791	4.1333	0.012241
241	184850	1262	9.6828	1282.2	191020	0.08599	0.0002752	4.1038	0.012096
242	192790	1258.8	10.078	1284.7	190320	0.08557	0.0002714	4.0749	0.011952
243	200980	1255.5	10.486	1287.2	189610	0.08515	0.0002677	4.0466	0.011807
244	209440	1252.3	10.907	1289.7	188900	0.08474	0.0002640	4.0188	0.011664
245	218170	1249	11.341	1292.4	188190	0.08432	0.0002604	3.9916	0.01152
246	227180	1245.7	11.788	1295	187470	0.08391	0.0002569	3.965	0.011377
247	236470	1242.4	12.249	1297.7	186750	0.08350	0.0002534	3.9388	0.011234
248	246050	1239.1	12.725	1300.4	186020	0.08309	0.0002500	3.9132	0.011092
249	255930	1235.8	13.214	1303.2	185290	0.08268	0.0002467	3.888	0.01095
250	266110	1232.4	13.719	1306.1	184550	0.08227	0.0002434	3.8634	0.010808
251	276590	1229.1	14.239	1308.9	183810	0.08186	0.0002401	3.8392	0.010667
252	287380	1225.7	14.774	1311.9	183070	0.08145	0.0002369	3.8155	0.010526
253	298500	1222.3	15.325	1314.9	182310	0.08105	0.0002338	3.7922	0.010385
254	309940	1218.9	15.892	1317.9	181550	0.08064	0.0002307	3.7694	0.010245
255	321710	1215.5	16.476	1321	180790	0.08024	0.0002276	3.747	0.010105

256	333810	1212.1	17.077	1324.1	180020	0.07984	0.0002246	3.7251	0.009965
257	346260	1208.6	17.695	1327.3	179250	0.07944	0.0002217	3.7035	0.009826
258	359060	1205.1	18.331	1330.6	178460	0.07904	0.0002187	3.6823	0.009687
259	372220	1201.6	18.985	1333.9	177680	0.07864	0.0002159	3.6616	0.009549
260	385740	1198.1	19.658	1337.3	176880	0.07824	0.0002130	3.6412	0.009411
261	399630	1194.6	20.35	1340.7	176080	0.07784	0.0002103	3.6212	0.009274
262	413890	1191.1	21.062	1344.2	175280	0.07745	0.0002075	3.6016	0.009137
263	428530	1187.5	21.793	1347.8	174470	0.07705	0.0002048	3.5823	0.009000
264	443570	1183.9	22.545	1351.4	173650	0.07666	0.0002021	3.5634	0.008864
265	459000	1180.3	23.318	1355.1	172820	0.07627	0.0001995	3.5449	0.008728
266	474830	1176.7	24.112	1358.9	171990	0.07587	0.0001969	3.5267	0.008592
267	491070	1173	24.929	1362.7	171150	0.07548	0.0001944	3.5088	0.008457
268	507720	1169.3	25.768	1366.7	170300	0.07509	0.0001918	3.4913	0.008323
269	524800	1165.6	26.629	1370.7	169450	0.07470	0.0001893	3.4741	0.008189
270	542300	1161.9	27.515	1374.8	168590	0.07431	0.0001869	3.4573	0.008055
271	560250	1158.2	28.425	1378.9	167720	0.07393	0.0001845	3.4407	0.007921
272	578630	1154.4	29.359	1383.2	166840	0.07354	0.0001821	3.4245	0.007789
273	597470	1150.6	30.319	1387.6	165960	0.07315	0.0001797	3.4086	0.007656
274	616760	1146.8	31.305	1392	165060	0.07277	0.0001774	3.393	0.007524
275	636510	1142.9	32.318	1396.6	164150	0.07238	0.0001751	3.3777	0.007393
276	656740	1139	33.359	1401.2	163240	0.07200	0.0001728	3.3627	0.007262
277	677450	1135.1	34.427	1406	162320	0.07161	0.0001705	3.348	0.007131
278	698640	1131.2	35.524	1410.8	161390	0.07123	0.0001683	3.3337	0.007001
279	720320	1127.2	36.652	1415.8	160460	0.07085	0.0001661	3.3196	0.006871
280	742510	1123.2	37.809	1420.9	159510	0.07047	0.0001639	3.3058	0.006742
281	765200	1119.2	38.998	1426.1	158550	0.07009	0.0001618	3.2923	0.006614
282	788410	1115.1	40.219	1431.5	157580	0.06971	0.0001597	3.2791	0.006485
283	812140	1111	41.473	1437	156600	0.06933	0.0001576	3.2663	0.006358
284	836410	1106.9	42.761	1442.6	155610	0.06895	0.0001555	3.2537	0.006231
285	861210	1102.7	44.084	1448.4	154610	0.06857	0.0001535	3.2414	0.006104
286	886550	1098.5	45.443	1454.3	153590	0.06819	0.0001514	3.2294	0.005978
287	912460	1094.3	46.839	1460.4	152570	0.06781	0.0001494	3.2177	0.005852
288	938920	1090	48.273	1466.7	151530	0.06744	0.0001474	3.2064	0.005727
289	965950	1085.7	49.746	1473.2	150480	0.06706	0.0001455	3.1953	0.005603
290	993570	1081.3	51.26	1479.8	149420	0.06668	0.0001435	3.1845	0.005479
291	1021800	1076.9	52.815	1486.6	148350	0.06631	0.0001416	3.1741	0.005355
292	1050600	1072.5	54.413	1493.7	147260	0.06593	0.0001397	3.164	0.005232
293	1080000	1068	56.056	1500.9	146150	0.06556	0.0001378	3.1542	0.005110
294	1110000	1063.4	57.744	1508.4	145040	0.06518	0.0001359	3.1448	0.004988
295	1140600	1058.8	59.48	1516.1	143920	0.06481	0.0001340	3.1357	0.004867
296	1171800	1054.2	61.264	1524.1	142770	0.06443	0.0001322	3.1269	0.004746
297	1203700	1049.5	63.099	1532.4	141610	0.06406	0.0001304	3.1185	0.004626
298	1236300	1044.8	64.986	1540.9	140430	0.06368	0.0001286	3.1105	0.004507

299	1269500	1040	66.927	1549.8	139240	0.06331	0.0001268	3.1029	0.004388
300	1303300	1035.1	68.924	1559	138030	0.06293	0.0001250	3.0957	0.004270
301	1337800	1030.2	70.98	1568.5	136810	0.06256	0.0001232	3.0889	0.004153
302	1373000	1025.2	73.095	1578.4	135570	0.06218	0.0001214	3.0825	0.004036
303	1408900	1020.2	75.273	1588.7	134300	0.06181	0.0001197	3.0766	0.003920
304	1445500	1015.1	77.516	1599.4	133020	0.06144	0.0001180	3.0711	0.003804
305	1482800	1009.9	79.826	1610.6	131720	0.06106	0.0001163	3.0662	0.003690
306	1520900	1004.6	82.207	1622.2	130390	0.06069	0.0001145	3.0618	0.003576
307	1559600	999.29	84.661	1634.4	129050	0.06031	0.0001128	3.0579	0.003462
308	1599100	993.89	87.191	1647.1	127690	0.05994	0.0001112	3.0546	0.003350
309	1639400	988.4	89.801	1660.4	126290	0.05956	0.0001095	3.052	0.003238
310	1680400	982.82	92.494	1674.4	124880	0.05919	0.0001078	3.05	0.003127
311	1722200	977.15	95.275	1689.1	123440	0.05881	0.0001062	3.0487	0.003016
312	1764700	971.39	98.147	1704.6	121980	0.05844	0.0001045	3.0482	0.002907
313	1808100	965.54	101.11	1720.9	120490	0.05806	0.0001029	3.0486	0.002798
314	1852200	959.57	104.18	1738.1	118970	0.05768	0.0001012	3.0498	0.002690
315	1897200	953.5	107.36	1756.3	117410	0.05731	0.0000996	3.052	0.002583
316	1943000	947.31	110.64	1775.6	115830	0.05693	0.0000980	3.0553	0.002477
317	1989600	941.01	114.05	1796.2	114220	0.05655	0.0000963	3.0597	0.002372
318	2037100	934.57	117.58	1818	112560	0.05618	0.0000947	3.0654	0.002266
319	2085500	928	121.24	1841.4	110880	0.05580	0.0000931	3.0725	0.002164
320	2134700	921.28	125.04	1866.5	109150	0.05542	0.0000915	3.0812	0.002061
321	2184800	914.41	128.99	1893.4	107390	0.05504	0.0000899	3.0916	0.001960
322	2235900	907.38	133.1	1922.4	105570	0.05466	0.0000883	3.104	0.001859
323	2287800	900.17	137.38	1953.8	103720	0.05428	0.0000866	3.1185	0.001760
324	2340700	892.77	141.84	1988	101820	0.05391	0.0000850	3.1356	0.001661
325	2394500	885.17	146.51	2025.2	99850	0.05353	0.0000834	3.1555	0.001564
326	2449300	877.36	151.38	2066.1	97830	0.05315	0.0000818	3.1786	0.001468
327	2505100	869.3	156.49	2111.2	95760	0.05278	0.0000801	3.2055	0.001374
328	2561900	860.99	161.85	2161.1	93610	0.05241	0.0000785	3.2368	0.001280
329	2619700	852.4	167.49	2217	91390	0.05204	0.0000768	3.2733	0.001188
330	2678600	843.5	173.43	2279.7	89090	0.05168	0.0000752	3.316	0.001097
331	2738500	834.25	179.72	2351	86700	0.05132	0.0000735	3.366	0.001008
332	2799500	824.62	186.38	2432.7	84210	0.05098	0.0000718	3.4251	0.000920
333	2861600	814.56	193.46	2527.3	81620	0.05064	0.0000700	3.4953	0.000834
334	2924900	804.01	201.03	2638.5	78890	0.05032	0.0000683	3.5796	0.000750
335	2989300	792.9	209.16	2771.2	76030	0.05003	0.0000665	3.6819	0.000667
336	3055000	781.13	217.94	2932.6	73000	0.04977	0.0000646	3.808	0.000587
337	3121900	768.59	227.48	3133.6	69770	0.04955	0.0000627	3.9661	0.000508
338	3190000	755.12	237.95	3391	66320	0.04941	0.0000607	4.1692	0.000432
339	3259500	740.49	249.57	3733.4	62570	0.04936	0.0000587	4.4386	0.000358
340	3330400	724.38	262.66	4212	58460	0.04946	0.0000565	4.8117	0.000281

Appendix D: Theoretical Model Calculation

This appendix provides the procedures for applying the theoretical model, explained in Chapter 3, sections 3.3 and 3.4, used to calculate the heat transfer coefficients, which are used to predict the thermal resistance in the evaporator and condenser section. A summary of the theoretical model calculation for the thermosyphon charged with R134a is presented in Table D-1.

Table D-1: Theoretical model calculation for R134a-charged thermosyphon

		Power throughput, $\dot{Q}$				
		19.74 W	**29.58 W**	**39.53 W**	**50.16 W**	**100.4 W**
Thermodynamic properties	**Unit**					
Latent heat of vaporisation, h_{fg}	J/kg	179157	177356	173664	173664	166895
Liquid Dynamic Viscosity, μ_l	N.s/m^2	2.0278 x10^{-04}	1.9802 x10^{-04}	1.8861 x10^{-04}	1.8861 x10^{-04}	1.7245 x10^{-04}
Liquid density, ρ_l	kg/m^3	1220.6	1213.0	1197.2	1197.2	1167.9
Vapour density, ρ_v	kg/m^3	32.48	34.42	38.39	38.39	45.86
Liquid thermal conductivity, k_l	W/m.K	0.08192	0.08105	0.07933	0.07933	0.07632
Surface tension, σ	N/m	0.00827	0.00801	0.00749	0.00749	0.00661
Liquid kinematic viscosity, v_l	m^2/s	1.6613 x10^{-07}	1.6325 x10^{-07}	1.5754 x10^{-07}	1.5754 x10^{-07}	1.4767 x10^{-07}
Liquid specific heat, $C_{p,l}$	J/kg.K	1265.13	1268.83	1276.47	1276.47	1290.63
Liquid Prandlt Number, Pr_l	-	3.2541	3.2235	3.1629	3.1629	3.0540
Vapour Pressure, P_v	Pa	624844	663374	745773	745773	908202
Atmospheric Pressure, P_{atm}	Pa	101325	101325	101325	101325	101325
Geometric parameters						
Inner diameter, D_{in}	m	0.0202	0.0202	0.0202	0.0202	0.0202
Evaporator length, l_e	m	0.2	0.2	0.2	0.2	0.2
Condenser length, l_c	m	0.2	0.2	0.2	0.2	0.2
Evap. surface area, A_e ($\pi.D_{in}.l_e$)	m^2	0.01269	0.01269	0.01269	0.01269	0.01269
Cond. surface area, A_c ($\pi.D_{in}.l_c$)	m^2	0.01269	0.01269	0.01269	0.01269	0.01269
Average wall temperatures						
Adiabatic section, T_a, T_v, T_{sat}	K	296.15	298.15	302.15	302.15	309.15
Condenser section, $T_{c,av}$	K	296.06	297.63	301.49	300.86	306.69
Evaporator section, $T_{e,av}$	K	298.93	301.39	306.25	306.63	312.43
Nucleate pool poiling heat transfer coefficients (h_{NPB})						
C_{sf} (taken from [4])	-	0.013	0.013	0.013	0.013	0.013
n (taken from [4])	-	1	1	1	1	1
Heat flux, q	W/m^2	1428.05	2139.91	2859.73	3628.73	7266.15
h_{NPB}, Labuntsov's Correlation, Eq. (3-6)	W/m^2.K	455.433	614.324	789.838	926.481	1636.09
h_{NPB}, Rohsenow's Correlation, Eq. (3-4)	W/m^2.K	716.394	952.538	1192.37	1397.54	2354.41

h_{NPB}, Imura's Correlation, Eq. (3-8)	W/m^2.K	879.56	1038.90	1178.76	1296.58	1745.44
h_{NPB}, Shiraishi's Correlation, Eq. (3-5)	W/m^2.K	4441.72	5224.42	5879.38	6467.02	8586.56
h_{NPB}, Kruzhilin's Correlation, Eq. (3-7)	W/m^2.K	4184.79	5366.53	6164.64	7282.98	10696.2
h_{NPB}, Kutateladze's Correlation,Eq. (3-9)	W/m^2.K	1379.38	1876.35	2425.53	2865.56	5176.38
Thermal resistance of the evaporator section (*Re*), Eq. (3-2)						
R_e ,Labuntsov's Correlation	K/W	0.17299	0.12825	0.09975	0.08504	0.04815
R_e ,Rehesenow's Correlation	K/W	0.10998	0.08271	0.06607	0.05637	0.03346
R_e ,Imura's Correlation	K/W	0.08957	0.07583	0.06684	0.06076	0.04514
R_e ,Shiraishi's Correlation	K/W	0.01773	0.01508	0.01340	0.01218	0.00917
R_e ,Kruzhilin's Correlation	K/W	0.01882	0.01468	0.01278	0.01081	0.00736
R_e ,Kutateladze's Correlation	K/W	0.05711	0.04199	0.03248	0.02749	0.01522
Liquid film heat transfer coefficients (h_{film})						
$h_{film,}$ Nusselt's Correlation , Eq. (3-13)	W/m^2.K	4174.08	2670.49	2474.25	2092.58	1726.69
$h_{film,}$ Jouhara's Correlation , Eq. (3-15)	W/m^2.K	4380.75	2928.77	2813.68	2437.00	2184.37
$h_{film,}$ Hashimoto's Correlation , Eq. (3-14)	W/m^2.K	2765.49	1848.88	1776.23	1538.44	1378.95
$h_{film,EXP}$, Eq. (3-20)	W/m^2.K	17281.1	4481.90	4719.00	3063.62	3216.91
Film Reynolds Number						
Re_{film} , Eq. (3-19)	-	34.2482	53.0896	76.0682	96.5237	219.954
Nusselt Number (*Nu*)						
Nu Nusselt	-	10190.7	6589.37	6237.88	5275.64	4524.72
Nu Jouhara	-	10695.3	7226.65	7093.61	6143.97	5724.03
Nu Hasimoto	-	6751.77	4562.07	4478.08	3878.59	3613.48
Nu Experimental	-	42190.7	11058.9	11897.1	7723.75	8429.74
Thermal resistance of the condenser section (R_c), Eq. (3-11)						
R_c ,Nusselt's Correlation	K/W	0.01887	0.02950	0.03184	0.03765	0.04563
R_c ,Jouhara's Correlation	K/W	0.01798	0.02690	0.02800	0.03233	0.03606
R_c ,Hashimoto's Correlation	K/W	0.02849	0.04261	0.04435	0.05121	0.05713
Overall Predicted Thermal Resistance (R_{HP}), Eq. (3-1)						
R_e ,Labuntsov + R_c ,Jouhara	K/W	0.19098	0.15516	0.12776	0.11737	0.08423